UNIVERSITÉ DE MONTRÉAL

MODÉLISATIONS ET INVERSIONS TRI-DIMENSIONNELLES EN PROSPECTIONS GRAVIMÉTRIQUE ET ÉLECTRIQUE

OLIVIER BOULANGER
DÉPARTEMENT DES GÉNIES CIVIL, GÉOLOGIQUE ET DES MINES
ÉCOLE POLYTECHNIQUE DE MONTRÉAL

THÈSE PRÉSENTÉE EN VUE DE L'OBTENTION
DU DIPLÔME DE PHILOSOPHIÆ DOCTOR (Ph. D.)
(GÉNIE MINÉRAL)
MAI 2004

Your file Votre référence
ISBN: 0-612-98175-4
Our file Notre référence
ISBN: 0-612-98175-4

UNIVERSITÉ DE MONTRÉAL

ÉCOLE POLYTECHNIQUE DE MONTRÉAL

Cette thèse intitulée:

MODÉLISATIONS ET INVERSIONS TRI-DIMENSIONNELLES EN PROSPECTIONS GRAVIMÉTRIQUE ET ÉLECTRIQUE

présentée par: BOULANGER Olivier

en vue de l'obtention du diplôme de: Philosophiæ Doctor

a été dûment acceptée par le jury d'examen constitué de:

M. MARCOTTE Denis, Ph.D., président

M. CHOUTEAU Michel, Ph.D., membre et directeur de recherche

M. SAUCIER Antoine, Ph.D., membre

M. TABBAGH Alain, Ph.D., membre externe

A mes parents Rose et Michel

A mes frères Pascal et Emmanuel

A ma femme Mayana

A mon fils Axel

Remerciements

Avant de remercier les acteurs les plus proches qui étaient dans le feu de l'action, je voudrai saluer ma famille pour m'avoir encouragé tout au long de ma thèse. Avant d'arriver au Canada, plusieurs professeurs ont forgé ma façon de penser pendant mes années passées en physique théorique à l'université de Besançon, notamment Claude Girardet, Georges Jolicard et Daniel Robert. En me baignant dans la géophysique, j'ai rencontré avec enthousiasme d'autres professeurs (Marc Daignières, Jean Chery et Roger Bayer) et d'autres aspects de la physique au laboratoire de géophysique de Montpellier.

En arrivant au Canada, j'ai rencontré avec joie mon directeur de thèse Michel Chouteau au laboratoire de géophysique appliquée de l'école Polytechnique de Montréal. Je lui suis extrêmement reconnaissant de m'avoir proposé une thèse qui m'a permis de me dépasser une fois de plus. Remise en question, rigueur, acharnement et autonomie sont les principales qualités que mon directeur de recherche m'a transmis. Je tiens à lui exprimer toute ma gratitude.

Je tiens à remercier en toute sympathie le professeur Klaus Spitzer qui sans le savoir a induit mes travaux de recherche dans une direction particulière que je n'aurai pas pu prédire au commencement de ma thèse.

Je tiens aussi à remercier les membres du jury pour avoir pris le temps nécessaire

pour lire et commenter avec intérêt mon travail. Je remercie Alain Tabbagh, professeur à l'université Pierre et Marie Curie (Paris, France), pour la qualité et la pertinence de ses remarques. Je voudrais remercier Denis Marcotte pour sa disponibilité au laboratoire de géostatistique et de géophysique, et pour la qualité de son enseignement. J'ai apprécié les nombreuses discussions enjouées avec le professeur Antoine Saucier au salon des professeurs. Je remercie le professeur Yves Goussard pour m'avoir éclairé sur certains aspects de l'optimisation et entrainé dans de nombreuses séances de remise en condition en escalade.

Je tiens aussi à remercier le Natural Science and Engineering Research Council of Canada (NSERC) et le Centre de Recherche en Calcul Appliqué (CERCA) pour avoir contribué au financement de ma thèse.

L'ambiance du laboratoire de géophysique a suffit pour m'entraîner et me persuader d'arriver à mes fins. Je voudrai remercier tous ceux qui ont contribué indirectement à mon projet de thèse et en particulier Bernard Giroux (co-équipier privilégié en escalade), Gilles Bellefleur, Erwan Gloaguen, Pierrick Chasseriau, Benoît Tournerie, Stefka Krivochieva, Stéphane Rondenay, Gervais Perron, Keyvan Safai Naraghi, Erensin Pierre Sangala, Maria Annecchione, Circé Malo-Lalande, Erick Adam, Emmanuel Henry, Mathieu Gagné, Jean-Luc Arsenault, Iván Marroquín, Isabelle D'Amours, Mihu Rucareanu.

Je remercie finalement Mayana et Axel pour leur patience jusqu'à l'éclosion de ma thèse...

Résumé

Cette thèse porte sur l'application des méthodes gravimétriques et électriques pour la prospection des gisements miniers. Les objectifs visés de la recherche sont : (1) la mise au point d'une technique d'inversion gravimétrique rapide pour des données prises en surface ; (2) le développement d'un outil numérique pour modéliser le potentiel électrique mesuré en surface et en forage lorsque le milieu est hétérogène ; et (3) le développement d'une technique d'inversion stochastique permettant d'estimer les résistivités du sous-sol à partir du potentiel électrique.

La première technique concerne l'élaboration d'un programme d'inversion 3D permettant d'interpréter des données gravimétriques en utilisant un ensemble de contraintes telles que la distance minimum, la courbure minimum et la compacité. Ces contraintes sont intégrées dans une formulation Lagrangienne. Une méthode d'inversion multi grille est mise en oeuvre pour résoudre séparément les courtes et les longues ondes gravimétriques. Le domaine est décomposé en une multitude de prismes rectangulaires juxtaposés. Le problème est résolu en calculant le modèle des paramètres, i.e. la densité de chaque prisme. Des poids sont assignés à chaque bloc en fonction de la profondeur, de l'information *a priori* sur la densité et de l'intervalle autorisé pour la région investiguée. Le programme est testé sur des données synthétiques. Les avantages et les comportements de chaque contrainte

sont comparés pour une reconstruction 3D. La distribution des densités estimées du modèle dépend de l'ensemble des contraintes utilisées. La meilleure combinaison de contraintes pour le multi corps semble être le minimum de courbure couplée avec le minimum de volume. La méthode d'inversion est également testée sur des données réelles.

Le deuxième outil développé dans cette thèse est un programme de modélisation du potentiel électrique 3D pour interpréter des données de surface et de forage. Basé sur une équation intégrale, le programme calcule les densités de charge causées par les gradients de conductivité à chaque interface de la maille, permettant ainsi l'estimation du potentiel avec exactitude en un point donné. La modélisation génère une matrice imposante constituée des intégrales des fonctions de Green. Cette matrice est stockée en utilisant une méthode de compression pyramidale. Le potentiel est comparé avec des solutions analytiques et des solutions numériques obtenues par un code de modélisation par différences finies. La comparaison a été faite pour deux modèles simples. La méthode intégrale est plus précise autour du point source et aux limites du domaine pour le calcul du potentiel en utilisant une configuration pôle-pôle. Une technique est proposée pour calculer la matrice de sensibilité (Jacobien) et les matrices Hessiennes en 3D. Elle est basée sur la dérivation du potentiel électrique par rapport à un bloc de conductivité en utilisant l'équation intégrale ; elle nécessite de calculer seulement le champ électrique au point source. Une extension directe de cette technique permet de déterminer les dérivées secondes. La technique est comparée avec des solutions analytiques et avec la méthode de calcul de la sensibilité utilisant le produit scalaire des densités de courant calculées aux points source et récepteur. Les résultats sont très précis pour le calcul du potentiel et le calcul des sensibilités quand la fonction de Green incluant l'image de la

source est utilisée. Le calcul des trois composantes du champ électrique sur les interfaces de la maille est fait simultanément et rapidement en tirant avantage de la compression matricielle.

Le troisième outil développé consiste à interpréter les mesures de potentiel électrique à partir d'une approche géostatistique non linéaire incluant de nouvelles contraintes. Cette méthode estime un modèle de covariance analytique pour les résistivités à partir des données de potentiel. Les paramètres de résistivité sont obtenus en cokrigeant les données de potentiel électrique mesuré, les paramètres fixés le long des forages et les gradients de résistivité connus dans le sous-sol. Le code est testé sur plusieurs modèles synthétiques. Les données sont recueillies en configuration pôle-pôle dans un plan incluant les forages émetteur et récepteur. De forts contrastes de résistivité sont retrouvés en utilisant cette méthode. Pour les applications réelles, l'ajustement de la matrice de covariance est facilité par l'information géologique disponible et les cas d'études menés sur les sites. Le code est testé sur deux cas réels. Les géométries et les résistivités sont en accord avec l'information géologique disponible.

Abstract

The aim of this thesis is the application of gravity and resistivity methods for mining prospecting. The objectives of the present study are: (1) to build a fast gravity inversion method to interpret surface data; (2) to develop a tool for modelling the electrical potential acquired at surface and in boreholes when the resistivity distribution is heterogeneous; and (3) to define and implement a stochastic inversion scheme allowing the estimation of the subsurface resistivity from electrical data.

The first technique concerns the elaboration of a three dimensional (3D) inversion program allowing the interpretation of gravity data using a selection of constraints such as the minimum distance, the flatness, the smoothness and the compactness. These constraints are integrated in a Lagrangian formulation. A multi-grid technique is also implemented to resolve separately large and short gravity wavelengths. The subsurface in the survey area is divided into juxtaposed rectangular prismatic blocks. The problem is solved by calculating the model parameters, i.e. the densities of each block. Weights are given to each block depending on depth, *a priori* information on density, and density range allowed for the region under investigation. The present code is tested on synthetic data. Advantages and behaviour of each method are compared in the 3D reconstruction. Recovery of geometry (depth, size) and density distribution of the original model

is dependent on the set of constraints used. The best combination of constraints experimented for multiple bodies seems to be flatness and minimum volume for multiple bodies. The inversion method is tested on real gravity data.

The second tool developed in this thesis is a three-dimensional electrical resistivity modelling code to interpret surface and subsurface data. Based on the integral equation, it calculates the charge density caused by conductivity gradients at each interface of the mesh allowing an exact estimation of the potential. Modelling generates a huge matrix made of Green's functions which is stored by using the method of pyramidal compression. The potential is compared with the analytical and the numerical solutions obtained by finite differences codes for two models. The integral method is more accurate around the source point and at the limits of the domain for the potential calculation using a pole-pole array. A technique is proposed to calculate the sensitivity matrix and the Hessian matrices in 3D. It is based on the derivative with regards to the block conductivity of the potential computed using integral equation; it only needs to compute the electrical field at the source location. A direct extension of this technique allows the determination of the second derivatives. The technique is compared with the analytical solutions and with the calculation of the sensitivity according to the method using the inner product of the current densities calculated at the source and receiver points. Results are very accurate when the Green's function that includes the source image is used. The calculation of the three components of the electric field on the interfaces of the mesh is made simultaneously and quickly in taking advantage of matrix compression.

The third method consists to interpret electrical potential measurements from a non-linear geostatistical approach including new constraints. This method es-

timates an analytical covariance model for the resistivity parameters from the potential data. The resistivity parameters are obtained by cokriging the measured electrical potential data, the fixed resistivity parameters along the boreholes and the known resistivity gradients in the subsurface. The code is tested on various synthetic models. The data here is collected in the pole-pole array in a plane including the transmitter and receiver boreholes. High resistivity contrasts are recovered using this method. In real applications, the adjustment of the covariance matrix is aided by available geological information and the case histories on the sites. The code is tested on two real cases. Geometries and resistivity agree with the available geological information.

Table des matières

Liste des figures

Liste des tableaux

Chapitre 1

INTRODUCTION ET REVUE DE LITTÉRATURE

Problématique

Les réserves minérales au Canada diminuent considérablement en métaux tel que le cuivre, l'or et le zinc. Une exploitation à faible coût est généralement obtenue lorsque la mine est à ciel ouvert. De nos jours, il est peu probable de dénicher des gisements en surface, puisqu'ils sont déjà majoritairement en exploitation. Les gisements à grande profondeur offrent un potentiel économique plus attrayant. Cependant le mort-terrain reste un obstacle pour certaines mesures effectuées en surface, c'est le cas de mesures électriques. Il est donc nécessaire de forer le terrain pour contourner cet obstacle. Avec une source d'émission dans l'un des forages, on est capable de mesurer le potentiel électrique dans les autres forages. La reconstruction des propriétés physiques du milieu à partir de ces données est appelée tomographie électrique. Une autre technique de prospection consiste à mesurer le

potentiel gravimétrique en surface pour déceler les variations de densité dans le sous-sol. Les variations de densité indiquent la présence de gisements plus denses que la roche encaissante. Les mesures gravimétriques de surface et aéroportées ne sont pas gênées par le mort terrain, mais elles perdent en résolution au fur et à mesure que l'on s'éloigne de la surface de la terre.

La proposition d'une thèse en imageries gravimétrique et de résistivité électrique 3D est ainsi guidée par deux objectifs : détecter des gisements et minimiser les coûts d'exploitation. On propose une revue de la littérature sur les méthodes de modélisations gravimétrique et électrique et sur les différentes méthodes d'inversion pour pouvoir définir par la suite nos objectifs et notre méthodologie.

Dans cette thèse, nous avons mis au point deux méthodes d'interprétation automatique des données gravimétriques et électriques. La première technique correspond à l'inversion des données gravimétriques acquises en surface par un opérateur. Actuellement les méthodes d'inversion sont souvent limitées par le stockage des matrices jacobiennes. Dans le cas particulier d'une topographie plane, l'inversion proposée inclut plusieurs façons de contraindre la solution, tout en minimisant l'espace mémoire requis pour le calcul sur ordinateur. A ce jour, il n'y a pas de publications utilisant la symétrie des coefficients de sensibilité pour optimiser le problème de l'inversion gravimétrique.

La deuxième technique consiste à interpréter des données de potentiel électrique prises en mode tomographique. Pour y parvenir, il est nécessaire d'avoir un outil de modélisation aussi précis que possible car l'erreur peut se propager sur les résultats de l'inversion. La méthode intégrale en est un et a été retenue, mais elle demande beaucoup d'espace mémoire. Pour palier cet inconvénient, on utilise une méthode de compression matricielle. Pour la première fois, la méthode intégrale est utilisée

pour modéliser un milieu de conductivité arbitraire composé d'une multitude de prismes. Le processus inverse consistant à interpréter le potentiel électrique, pour retrouver une distribution tri-dimensionnelle de la conductivité, est fait à partir d'une méthode géostatistique appelée cokrigeage. Notre approche nouvelle, dans le cadre de la géophysique, consiste à déduire la structure du sous-sol à partir des données observées, en définissant un modèle de covariance des paramètres.

Revue de la littérature

Dans de nombreux domaines de la physique appliquée, nous sommes tendus vers le même objectif : déterminer la distribution spatiale des propriétés physiques à partir de mesures directes ou indirectes (Demoment *et al.*, 2001). La résolution d'un tel problème nécessite qu'il soit décomposé en trois étapes :

- un problème d'instrumentation où l'on doit recueillir des données en minimisant le bruit des instruments et les erreurs de mesures directes ;
- un problème direct où, connaissant la distribution spatiale des propriétés physiques du milieu et le modèle mathématique régissant le problème physique à résoudre, on calcule numériquement les données directes et/ou indirectes. Ce modèle mathématique doit être relativement simple pour pouvoir être implémenté assez facilement tout en fournissant une description correcte du problème physique ;
- et un problème inverse où l'on doit reconstruire la distribution spatiale des propriétés physiques du milieu à partir des mesures.

Une bonne estimation des propriétés physiques s'effectue correctement à condition de bien cerner les trois étapes précédentes. On se propose de montrer l'état actuel de la recherche pour les problèmes direct et inverse en gravimétrie et en résistivité électrique, en classant les références par type de modélisation et par type d'inversion.

Problème direct en gravimétrie

Dans le tableau 1.1, on a regroupé les trois types de modélisation les plus utilisées en gravimétrie. La modélisation avec un prisme rectangulaire droit est facile à mettre en oeuvre. En général, elle ne tient pas compte de la topographie, à moins de discrétiser le domaine plus finement en surface. Le prisme polygonal droit et le polyèdre permettent de modéliser des corps plus réalistes. Cependant, la mise en oeuvre pour l'inversion gravimétrique est plus fastidieuse.

TAB. 1.1: Méthodes de modélisation en gravimétrie et en magnétisme

Méthodes	**Références**
Prisme rectangulaire droit	Sorokin (1951); Haáz (1953); Plouff (1966); Nagy (1966); Sharma (1966); Mufti (1973); Plouff (1976)
Prisme polygonal droit	Talwani et Ewing (1960); Talwani (1965); Plouff (1976); Cady (1980); Kwok (1989)
Le polyèdre	Paul (1974); Barnett (1976); Okabe (1979); Strakhov *et al.* (1986); Götze et Lahmeyer (1988); Pohánka (1988); Holstein et Ketteridge (1996); Li et Chouteau (1998)

Problème direct en électrique

Dans le tableau 1.2, on regroupe les références principales liées aux différentes méthodes de modélisation électrique (méthode analytique, méthode des milieux

alpha harmoniques, méthode par équation intégrale, méthode par différences finies et méthode par éléments finis). Les méthodes analytique et intégrale permettent de modéliser des corps simples et servent de base fiable pour vérifier la justesse des autres méthodes. La méthode des milieux alpha harmoniques permet de modéliser des corps 3D rapidement sans être trop coûteuse en temps calcul. Les méthodes par éléments finis et par différences finies sont plus coûteuses, mais plus précises. Une étude comparative pour les méthodes par différences finies a été faite par Spitzer et Wurmstich (1999). Bien que le but ne soit pas de calculer le potentiel électrique, on a ajouté au tableau 1.2 les auteurs qui ont contribué à l'évaluation analytique ou numérique de la matrice de sensibilité (Jacobienne).

Problème inverse en électrique et en gravimétrie

On peut trouver les bases de l'inversion en géophysique parmi les auteurs Marquardt (1970); Jackson (1972); Tikhonov et Arsénine (1974); Jackson (1979); Oristaglio et Worthington (1980); Tarantola et Valette (1982); Lines et Treitel (1984); Menke (1984); Scales (1987); Meju (1994); Parker (1994); VanDecar et Snieder (1994) et plus généralement les méthodes d'optimisation dans Luenberger (1969, 1973); Avriel (1976); Bazaraa (1979); Bertsekas (1982); Culioli (1994); Shewchuk (1994); Bertsekas (1995); Gauvin (1995*a*); Nocedal et Wright (2000). On classe le tableau 1.3 par type d'inversion en résistivité électrique (DC), en gravimétrie (GRAVI) et les autres méthodes (AUTRE). Ce tableau donne une idée de la fonctionnelle minimisée, du nom donné dans la littérature et de la solution dans les cas les plus simples. Lorsque la méthode ne peut être résumée en deux lignes, le lecteur devra se référer à l'article cité.

Objectif de la recherche

Cette thèse a pour but de contribuer à la détection et à la quantification des gisements miniers par le développement de méthodes numériques capables d'estimer les propriétés physiques du sol. Les trois objectifs visés par le présent travail sont :

- la mise au point d'une technique d'inversion rapide permettant de prendre en charge des données gravimétriques de surface pour l'estimation des densités du sous-sol ;
- le développement d'un code de modélisation permettant de simuler le potentiel électrique pour des mesures prises en surface et en forage ;
- le développement d'une technique d'inversion permettant d'estimer les résistivités électriques du milieu à partir des mesures de potentiel électrique.

Méthodologie proposée

Pour atteindre les objectifs énoncés, notre démarche propose les trois directions suivantes :

La modélisation et l'inversion gravimétrique 3D

Le principal objectif de l'inversion gravimétrique est de cartographier le sous-sol avec une distribution 3D des densités. Pour parvenir à nos fins, le sous-sol est discrétisé en une multitude de prismes rectangulaires. La mesure gravimétrique issue d'un prisme est donnée par une solution analytique. La mesure en un point de la surface est la somme des effets de chacun des prismes à ce point. En supposant que la densité est constante à l'intérieur de chaque prisme, le problème

de modélisation directe devient très simple et peut être formulé sous une forme matricielle. Connaissant les densités du sous-sol, la modélisation directe permet de calculer l'anomalie gravimétrique. Connaissant maintenant l'anomalie observée (mesures de terrain), l'inversion consiste à retrouver la distribution des densités qui génère celle-là. Le problème d'inversion adopté ici est basé sur la formulation du Lagrangien. A l'intérieur de cette formulation, plusieurs contraintes sont introduites. Une des contraintes combine à la fois les dérivées premières et la contrainte de volume minimum. Ces contraintes permettent de stabiliser la solution et offrent un éventail d'option à l'utilisateur. On a choisi d'inverser des données sur une topographie plane pour minimiser l'espace mémoire sans pour autant exclure la possibilité d'inclure une topographie.

La modélisation électrique 3D

L'objectif principal est de simuler le potentiel électrique généré par un dipôle de courant dans un sol présentant une distribution de résistivités électriques. Pour des questions pratiques et analytiques, le domaine est décomposé à l'aide de prismes rectangulaires. L'approche adoptée pour modéliser le potentiel est basée sur le calcul des densités de charges surfaciques s'accumulant aux interfaces des prismes lorsque l'on injecte un courant électrique. Le calcul du potentiel se décompose en deux étapes. La première consiste à résoudre un système linéaire compressé pour en déduire la distribution 3D des densités de charges surfaciques. La seconde étape consiste à multiplier les densités de charges surfaciques avec une matrice géométrique composée d'intégrales de surface pour calculer le potentiel électrique à une position exacte du récepteur. Cette méthode tient compte de la conductivité du milieu où se trouve l'électrode de courant. Dans le but d'inverser les données de

potentiel électrique, une autre méthode de calcul des sensibilités est proposée pour un domaine 3D. Sur la même lancée, on dérive aussi les coefficients constituant la matrice Hessienne, lorsque la linéarisation du problème inverse se fait au deuxième ordre pour un domaine 3D.

L'inversion électrique 3D

L'inversion des données électriques étant la suite logique après la modélisation électrique, on propose de mettre en place une méthode géostatistique basée sur l'analyse des données observées. En effet, la formulation du problème inverse correspond à un cokrigeage non linéaire permettant d'inclure autant de variables secondaires possibles, sachant que la variable primaire est la résistivité électrique. Le problème électrique étant non linéaire, on estime au premier ordre le calcul du potentiel électrique pour formuler le cokrigeage itératif. Les contraintes utilisées dans le cokrigeage sont les données observées, les résistivités échantillonnées ou estimées le long des forages et les gradients discrets de résistivité entre deux unités lithologiques. La solution du cokrigeage peut s'écrire sous forme primale donnant accès à la variance des paramètres ou sous forme duale. On démontre que la forme duale est similaire à la méthode du maximum *a posteriori* dans le cas Gaussien et qu'elle ne permet pas d'accéder à la variance de cokrigeage.

Contributions originales de la thèse

De l'avis de l'auteur les contributions principales de cette thèse sont :

Pour la méthode gravimétrique

- la programmation d'un code d'inversion 3D mettant en oeuvre une nouvelle contrainte combinant la régularisation classique de Tikhonov et une contrainte locale de volume minimum ;
- la minimisation de l'espace mémoire pour stocker la matrice de sensibilité souvent contraignant en optimisation.

Pour la méthode électrique

- la programmation d'un code de modélisation du potentiel électrique à partir de la méthode intégrale pour une distribution arbitraire 3D de la resistivité ;
- une nouvelle écriture des coefficients de la matrice Jacobienne et des coefficients de la matrice Hessienne pour un domaine 3D ;
- la programmation d'un code d'inversion du potentiel électrique à partir d'une méthode de cokrigeage ;
- l'incorporation des contraintes de gradient de résistivité imposées comme mesures dans le processus d'inversion.

Les travaux ont fait l'objet de publications (Boulanger et Chouteau, 2001, 2004; Boulanger *et al.*, 2004).

Plan de la thèse

Le premier chapitre décrit la méthode d'imagerie gravimétrique 3D prenant en compte les données de surface sur une grille régulière. On propose en premier lieu un calcul de l'anomalie gravimétrique issue d'une cellule. Une analyse de la symétrie des coefficients de sensibilité permet de minimiser de l'espace mémoire. Une étude

de la sensibilité aide à mieux comprendre le comportement du programme d'inversion gravimétrique. Une formulation intégrant plusieurs contraintes est présentée avec plusieurs tests synthétiques à l'appui. Finalement, un test sur des données réelles du camp minier de Rouyn-Noranda (Abitibi, Québec) fournit une structure de densité et est comparée avec l'information géologique connue.

Le deuxième chapitre présente la modélisation électrique par la méthode intégrale. La première partie est consacrée au développement du système linéaire discret pour le calcul de la densité de charge. Une partie du chapitre évalue les coefficients de sensibilité suivant deux méthodes. La troisième partie est dédiée à la compression matricielle pour stocker de larges matrices et pour accélérer les calculs. La dernière partie est orientée sur le calcul du champ électrique. Le code est testé avec les réponses de modèles simples.

Le troisième chapitre présente la méthode d'inversion électrique en utilisant la formulation du cokrigeage. La première partie de l'article présente la notation et la théorie, ainsi que les méthodes utilisées pour l'estimation de la résistivité électrique. Une comparaison est faite entre le maximum a posteriori et le cokrigeage. Une méthode est proposée pour déterminer le modèle de covariance des paramètres. La deuxième partie de l'article consiste à tester la méthode d'inversion. La troisième partie présente des applications de la méthode pour des cas réels.

Le quatrième chapitre fait la synthèse de l'étude, suivi de la conclusion.

TAB. 1.2: Méthodes de modélisation électrique et calcul de la sensibilité

Méthodes	**Références**
Intégrales et autres	Webb (1931); Evjen (1938); Muskat et Evinger (1941); Van Nostrand (1953); Cook et Van Nostrand (1954); Roman (1959, 1963); Onodera (1963); Budak *et al.* (1964); Mooney *et al.* (1966); Keller et Frischknecht (1966); Nabighian (1966); Dieter *et al.* (1969); Merkel et Alexander (1971); Merkel (1971); Large (1971); Snyder et Merkel (1973); Hohmann (1975); Snyder (1976); Lee (1975); Nabighian et Elliot (1976); Edwards (1977); Daniels (1977); Dobecki (1980); Wait (1982); Lytle (1982); Lytle et Hanson (1983); Daniels et Dyck (1984); Schulz (1985); Xu *et al.* (1988); LaBrecque et Ward (1990); Telford *et al.* (1990); Apparao *et al.* (1992); Zhdanov et Keller (1994); Hvozdara (1994); Straub (1995*a*,*b*); Hvozdara et Kaikkonen (1998); Boulanger et Chouteau (2004)
Milieux alpha harmoniques	Stefanescu (1970); Stefanescu et Stefanescu (1974); Petrick *et al.* (1981); Shima (1990, 1992)
Différences finies	Brewitt-Taylor et Weaver (1976); Mufti (1978); Dey et Morrison (1979*b*,*a*); Scriba (1981); Mundry (1984); Wurmstich et Morgan (1994); Spitzer (1995); Zhang *et al.* (1995); Zhao et Yedlin (1996); Spitzer et Wurmstich (1999); Wang et Mezzatesta (2001)
Eléments finis	Coggon (1971); Pridmore *et al.* (1981); Murai et Kagawa (1985); Sasaki (1992, 1994); LaBrecque *et al.* (1996, 1999); Lesur *et al.* (1999*a*); Bing et Greenhalgh (2001)
Calcul de la sensibilité	Geselowitz (1971); Barker (1979); Chave (1984); Boerner et West (1989); McGillivray et Oldenburg (1990); Park et Van (1991); Li et Oldenburg (1991); Szarka (1992); Shima (1992); Li et Oldenburg (1992); McGillivray (1992); McGillivray *et al.* (1994); Spies et Habashy (1995); Loke et Barker (1995, 1996*a*); Spitzer (1998*b*,*a*)

TAB. 1.3: Méthodes d'inversion

Méthodes et Fonctionnelles minimisées	**Solutions et Descriptions. Inverse généralisée G^{-g} et $R = G^{-g}G$; $N = GG^{-g}$; $C_{mm} = G^{-g}G^{-g^T}$**	**Références**
Moindres carrés $minE = \|\|(d - Gm)\|\|^2$	$m = [G^TG]^{-1}G^Td$, solution surdéterminée. $G^{-g} = [G^TG]^{-1}G^T$, $N = G[G^TG]^{-1}G^T$, $R = I$, $C_{mm} = [G^TG]^{-1}$	**DC** : Dines et Lytle (1981); Daily et Owen (1991)
Longueur minimum $minE =$ $\|\|m\|\|^2 + \lambda^T(d - Gm)$	$m = G^T[GG^T]^{-1}d$, solution sousdéterminée, λ multiplicateur de Lagrange. $G^{-g} = G^T[GG^T]^{-1}$, $R = G^T[GG^T]^{-1}G$, $N = I$, $C_{mm} = G^T[GG^T]^{-2}G^T$	-
Moindres carrés amortie $minE =$ $\|\|d - Gm\|\|^2 + \epsilon\|\|m\|\|^2$	$m = [G^TG + \epsilon I]^{-1}G^Td$, solution mixte biaisée pour cas surdéterminé et sousdéterminé évitant la partition du problème($\epsilon \to 0$). $G^{-g} = [G^TG + \epsilon I]^{-1}G^T$	**DC** : Inman (1975); Petrick *et al.* (1977); Pelton *et al.* (1978); Oristaglio et Worthington (1980); Petrick *et al.* (1981); Shima (1990); Tong et Yang (1990); Dabas *et al.* (1994); Lehmann (1995); Olayinka et Yaramanci (2000)
Moindres carrés pondérée $minE = \|\|W_d(d - Gm)\|\|^2$	$m = [G^TW_dG]^{-1}G^TW_dd$, solution surdéterminée. $G^{-g} = [G^TW_dG]^{-1}G^TW_d$	**DC** : Tripp *et al.* (1984)
Longueur minimum pondérée amortie / m_0 $minE = \|\|W_m^{-1/2}(m - m_0)\|\|^2 + (d - G(m - m_0))^T\lambda$	$m =$ $m_0 + W_mG^T[GW_mG^T]^{-1}d$, solution sous déterminée. λ multiplicateur de Lagrange. $G^{-g} =$ $W_mG^T[GW_mG^T]^{-1}$	**GRAVI** :Boulanger et Chouteau (2001)

Méthodes et Fonctionnelles minimisées	**Solutions et Descriptions. Inverse généralisée**	**Références**
Moindres carrés pondérée amortie / m_0 $minE = ||W_d^{1/2}(d-G(m-m_0))||^2 + \epsilon||W_m^{1/2}(m-m_0)||^2$	$m = m_0 + [G^T W_d G + \epsilon W_m]^{-1} G^T W_d d$, solution mixte. $G^{-g} = [G^T W_d G + \epsilon W_m]^{-1} G^T W_d$	**DC** : Lytle *et al.* (1980); Smith et Vozoff (1984); Daniels et Dyck (1984); Constable *et al.* (1987); Yorkey *et al.* (1987); Sasaki (1989); de Groot-Hedlin et Constable (1990); Daily et Owen (1991); Li et Oldenburg (1992); Kallman et Berryman (1992); Meju (1992); Narayan (1992); Sasaki (1992); Ramirez *et al.* (1993); Meju (1994); Ellis et Oldenburg (1994); Narayan *et al.* (1994); Sasaki (1994); Liu (1994); Loke et Barker (1995, 1996*a*,*b*); LaBrecque *et al.* (1996); Borcea *et al.* (1996); Shi *et al.* (1997); Cohen-Bacrie *et al.* (1997); Vauhkonen *et al.* (1998); LaBrecque et Ward (1990); LaBrecque *et al.* (1999); Lesur *et al.* (1999*b*); Bing et Greenhalgh (2000); Zhou *et al.* (2000); Ramirez et Daily (2001); Jackson *et al.* (2001) **GRAVI** :Last et Kubik (1983); Guillen et Menichetti (1984); Barbosa et Silva (1994); Li et Oldenburg (1996); Pilkington (1997); Li et Oldenburg (1998)

Méthodes et Fonctionnelles minimisées	**Solutions et Descriptions. Inverse généralisée**	**Références**
Subspace Algorithms $minE = ||d - Gm||^2 + ||m||^2$		Skilling et Bryan (1984); Kennett et Sambridge (1998); McGillivray (1992); Oldenburg *et al.* (1993); Oldenburg et Li (1994)
Minimisation d'une norme L_1 $minE = ||d - Gm||^2 + ||\nabla m||_{L_1}$	$m^{k+1} = m^k + \tau \frac{\partial E(m,d)}{\partial m}$	**DC** : Dobson et Santosa (1994) **GRAVI** :Bertete-Aguirre *et al.* (1998); Portniaguine et Zhdanov (1999) **AUTRE** :Acar et Vogel (1994)
Maximum a posteriori $maxP = exp - [(d - Gm)^T C_{dd}^{-1}(d - Gm) + (m - m_0)^T C_{mm}^{-1}(m - m_0)]$	$m = m_0 + [G^T C_{dd}^{-1} G + C_{mm}^{-1}]^{-1} G^T C_{dd}^{-1}(d - Gm_0)$, solution mixte. $G^{-g} = [G^T C_{dd}^{-1} G + C_{mm}^{-1}]^{-1} G^T C_{dd}^{-1}$	**DC** : Pous *et al.* (1987); Mackie *et al.* (1988); Park et Van (1991); Zhang *et al.* (1995, 1996); Yang et LaBrecque (1998); Maillol *et al.* (1999) **GRAVI** :Lee et Biehler (1991); Zeyen et Pous (1991, 1993); Camacho *et al.* (1997)
Moindre carrés avec SVD $minE = ||(d - Gm)||^2$	$\Delta m = V L^{-1} U^T \Delta d$, solution surdéterminée. V,U et L matrices vecteurs propres des données, des paramètres et des valeurs propres	**DC** : Inman *et al.* (1973); Weidelt (1975)
Lagrangien augmenté pondéré $minL = ||W_m^{1/2} m||^2 + (d - Gm)^T \lambda + c||(d - Gm)||^2$	$m = [W_m + cG^T G]^{-1} G^T (cd + \lambda)$, solution mixte. λ multiplicateur de Lagrange.	**DC** : Bertsekas (1982, 1995); Gauvin (1995*a*)
Rétroprojections $(d - Gm)$	$m = W(QG)^T m_a$. matrice $W_{ii} = 1/\sum_j G_{ij}$, Q matrice de pondération, m_a résistivité apparente.	**DC** : Wexler *et al.* (1985); Noel et Xu (1991); Shima (1992); Cosentino *et al.* (1998)

Méthodes et Fonctionnelles minimisées	**Solutions et Descriptions. Inverse généralisée**	**Références**
Autres rétroprojections	-	**DC** : Santosa et Vogelius (1990); Barker (1992)
SIRT $minE = \|\|(d - Gm)\|\|^2$	$m^{k+1} =$ $m^k + WG^T(m_a - m_a^k)$. matrice $W_{ii} = 1/\sum_j G_{ij}$, m_a résistivité apparente.	**DC** : Dines et Lytle (1979, 1981); Brunner *et al.* (1999)
Recuit Simulé et Algorithme Génétique	-	**DC** : Sen *et al.* (1993); Chunduru *et al.* (1995, 1996); Kishimoto *et al.* (1996)
Principe de Fermat	-	**DC** : Berryman et Kohn (1990); Kallman et Berryman (1992)
Programmation linéaire ; Cokrigeage et Simulation ; Autres	-	**GRAVI** : Mottl et Mottlová (1972); Safon *et al.* (1978); Rene (1986); Xia et Sprowl (1992); Garcia-Abdeslem (1995); Boschetti *et al.* (1997); Asli *et al.* (2000) **DC** :Boulanger *et al.* (2004) **AUTRE** :Gloaguen *et al.* (2004)

Chapitre 2

MODÉLISATION ET INVERSION GRAVIMÉTRIQUE

2.1 Introduction

Ce chapitre échafaude la première méthode d'interprétation géophysique pour la recherche de gisements miniers. On présente l'article "Constraints in 3D gravity inversion", dont le texte est publié dans la revue Geophysical Prospecting (Boulanger et Chouteau, 2001). Cet article constitue un tout en regroupant d'une part la modélisation directe, et d'autre part l'inversion gravimétrique.

Le but de l'inversion est de déterminer le modèle des paramètres à partir d'observations. Bien qu'une solution satisfaisant les données observées puisse être obtenue facilement, la non unicité des méthodes potentielles est causée par la nature du problème physique et la sous-détermination du problème. Pour composer avec cette non-unicité en utilisant un très grand nombre de cellules contigues de densité inconnue, plusieurs auteurs ajoutent de l'information *a priori* pour contraindre la

solution. Green (1975) utilise une matrice de pondération appropriée pour fixer certains paramètres lorsque de l'information géologique ou la densité est disponible. D'autres auteurs comme Li et Oldenburg (1996, 1998); Pilkington (1997) contrecarrent la décroissance de la sensibilité des cellules avec la profondeur en les pondérant avec une fonction inverse de la profondeur. Last et Kubik (1983) cherchent une solution compacte avec sa contrainte de volume minimum. Guillen et Menichetti (1984) et Barbosa et Silva (1994) concentrent la solution le long d'axes d'inertie. Une contrainte globale appelée "lissage" est utilisée pour trouver un modèle avec un minimum de structures (Djeridane, 1996; Li et Oldenburg, 1996).

Dans ce qui suit, on propose en premier lieu un calcul de l'anomalie gravimétrique issue d'une cellule ; celui-là permet une analyse de la symétrie des coefficients de sensibilité conduisant à une minimisation de l'espace mémoire. Le comportement de la sensibilité est présenté pour aider à mieux comprendre l'aboutissement d'un modèle d'inversion. Puis, le problème inverse basé sur une formulation lagrangienne nous permet d'insérer toutes les contraintes d'égalité avec une norme pondérée comme fonction coût. Les troisième et quatrième parties sont réservées à la solution de la formulation lagrangienne et à une application de la technique multigrille, respectivement. Des tests sont exécutés en utilisant différentes combinaisons de contraintes sur des données modélisées. Finalement, un test sur des données réelles du camp minier de Rouyn-Noranda (Abitibi, Québec) fournit une structure de densité qui est comparée à l'information géologique connue.

2.2 Résumé

Un programme d'inversion pour des géométries tridimensionnelles (3D) est developpé afin d'interpréter des données gravimétriques, utilisant un ensemble de contraintes. Cet ensemble comporte les contraintes de distance minimum, de courbure minimum, de rugosité et de compacité, qui peuvent être combinées par le biais d'une formulation Lagrangienne. Une technique de multigrille est aussi mise en oeuvre pour résoudre séparément les longues et les courtes ondes gravimétriques. Le sous-sol dans l'aire d'étude est divisé en blocs prismatiques rectangulaires, et le problème est résolu en calculant le modèle des paramètres, i.e. la densité de chaque bloc. Des poids sont assignés à chaque bloc en fonction de la profondeur, de l'information *a priori* sur la densité et de l'intervalle autorisé pour la région investiguée. Le présent code est testé sur des données modélisées pour un dyke incliné et un multi-corps. Les résultats, combinant différentes contraintes et un poids dépendant de la profondeur, sont exposés pour le dyke incliné. Les avantages et les comportements de chaque méthode sont comparés pour une reconstruction 3D. La récupération de la géométrie (profondeur, taille) et de la distibution des densités du modèle original sont dépendants de l'ensemble des contraintes utilisées. Par expérimentation, la meilleure combinaison de contraintes pour le multi-corps semble être le minimum de courbure couplé avec la contrainte de volume minimum. La méthode d'inversion est testée sur des données réelles du camp minier de Rouyn-Noranda (Québec). Le modèle d'inversion 3D pour les dix premiers kilomètres est en accord avec les contacts lithologiques majeurs affleurant à la surface ; ceci nous permet de déterminer la géométrie des plutons et des roches intrusives situés en profondeur.

2.3 Constraints in 3D gravity inversion

2.3.1 Abstract

A three dimensional (3D) inversion program is developed to interpret gravity data using a selection of constraints. This selection include minimum distance, flatness, smoothness and compactness constraints, which can be conbined using a Lagrangian formulation. A Multi-grid technique is also implemented to resolve separately large and short gravity wavelengths. The subsurface in the survey area is divided into rectangular prismatic blocks and the problem is solved by calculating the model parameters, i.e. the densities of each block. Weights are given to each block depending on depth, a priori information on density and density range allowed for the region under investigation. The present computer code is tested on modeled data for a dipping dyke and multiple bodies. Results combining different constraints and a weight depending on depth are shown for the dipping dyke. Advantages and behavior of each method are compared in the 3D reconstruction. Recovery of geometry (depth, size) and density distribution of the original model is dependent on the set of constraints used. The best combination of constraints experimented for multiple bodies seems to be flatness and minimum volume for multiple bodies. The inversion method is tested on real gravity data from the Rouyn-Noranda (Quebec) mining camp. The 3D inversion model for the first 10 km is in agreement with the known major lithological contacts at the surface; it allows the determination of the geometry of plutons and intrusive rocks at depth.

Key words : gravity, three-dimensional, depth weighting, surface sensitivity, inversion, multi-grid, Abitibi.

2.3.2 Introduction

The goal of inverse theory is to determine the model parameters from the observations. Although a solution that satisfies the observed data can easily be found, its non-uniqueness in potential methods is caused by the nature of the physics and the underdetermination of the problem. To deal with non-uniqueness using models composed of a large number of contiguous cells of unknown density, many authors add a priori information to constrain the solution. Green (1975) uses an appropriate weighting matrix to fix some of the parameters when geological or density information are available. Others authors (Li et Oldenburg, 1996, 1998; Pilkington, 1997) counteract the decreasing sensitivities of cells with depth by weighting them with an inverse function of depth. Last et Kubik (1983) find a compact solution with a minimum volume constraint. Guillen et Menichetti (1984) and Barbosa et Silva (1994) concentrate the solution along inertial axes. A global constraint called "smoothing" is used to find a model with a minimum structure (Li et Oldenburg, 1996; Djeridane, 1996).

In the following article we first propose an analytical calculation of the gravity anomaly derived from a cell model; it allows analysis of the symmetry of the sensitivity coefficients leading to minimization of the amount of memory storage. The behavior of sensitivity is presented to help understand the convergence to a model in the inverse problem. A simple analytical relation is developed from the sensitivity of a spheric cell to automatically choose the dimensions of the model domain. Then, the inverse problem based on a Lagrangian formulation allows us to insert all equality constraints with a weighted norm cost function. Third and fourth parts are devoted to the solution of the Lagrangian formulation and to an application of multi-grid technique respectively. Tests are performed by using different combina-

tions of constraints on modeled data. Finally a test on real data from the mining camp of Rouyn-Noranda (Abitibi, Quebec) yields a density structure of the upper 10 km which is compared with the known geological information.

2.3.3 Gravity modeling

The purpose of forward modeling is to compute the gravimetric response g at the surface due to a density distribution of the subsurface. This calculated anomaly is compared with the observed anomaly g^{obs} in the survey area. For convenience we decide to discretize the subsurface as an ensemble of rectangular prisms (figure 2.1). This classic method can consume huge memory space for large set of observations, however we will use the symmetry of the kernel to minimize the amount of memory. Thus the attraction g at each surface station is due to the sum of the responses of each block. The solution for the gravitational attraction $g_i \equiv g(x_i, y_i, z_i)$ of a j^{th} right rectangular prism with dimensions described by the limits $x'_1 \leq x' \leq x'_2$, $y'_1 \leq y' \leq y'_2$ and $z'_1 \leq z' \leq z'_2$ using Cartesian coordinate is given by :

$$g_i = -\gamma \rho_j \int_{x'_1}^{x'_2} dx' \int_{y'_1}^{y'_2} dy' \int_{z'_1}^{z'_2} dz' \, \frac{(z_i - z')}{((x_i - x')^2 + (y_i - y')^2 + (z_i - z')^2)^{3/2}} \qquad (2.1)$$

The density ρ_j is assumed to be constant within the prism. A solution of this integral was first developed by Haáz (1953) and used by others authors (Nagy, 1966; Banerjee et Gupta S.P., 1977; Bear *et al.*, 1995). A synthetic development is made by Li et Chouteau (1998) and a proof is given for the validity of the equation 2.2 when gravity is calculated outside, on the boundary and inside the prism.

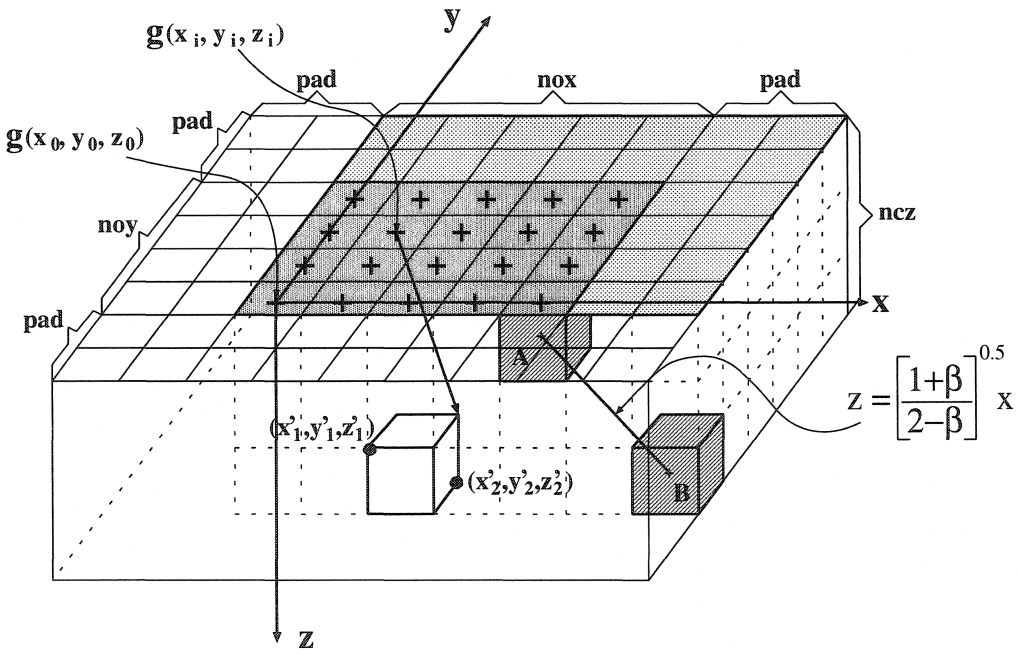

Figure 2.1: Discretization of the subsurface with prisms. Gravity stations $g(x_i, y_i, z_i)$ are located at the center of the upper face of prisms in the top layer. The stations lie on a horizontal grid at a constant elevation $z_i(= z_0)$. Increments in x, y and z directions are δx, δy and δz. nox and noy are the number of observations in x and y directions respectively, and $ncx = nox+2*pad$, $ncy = noy+2*pad$, ncz the number of cells in x, y, z directions. pad indicates the cells added around the domain of observation. Line linking cells A and B indicates the maximum of sensitivity $G^{MAX}_{s,\beta}$. The gray zone delimits the domain above a minimum sensitivity, used to calculate the gravity data.

$$\frac{g_i}{\rho_j} = -\gamma \sum_{p=1}^{2}\sum_{q=1}^{2}\sum_{s=1}^{2} \mu_{pqs}\left[a_p\ ln(b_q + r_{pqs}) + b_q\ ln(a_p + r_{pqs}) - c_s\ arctan(\frac{a_p b_q}{c_s r_{pqs}})\right] \tag{2.2}$$

where :

- g_i is the gravitational attraction measured at point (x_i, y_i, z_i)
- ρ_j is the contrast of density for the j^{th} prism
- γ is the universal gravitational constant
- $\mu_{pqs} = (-1)^p(-1)^q(-1)^s$ with $p, q, s = 1, 2$
- $a_p = x_i - x'_p$, $b_q = y_i - y'_q$ and $c_s = z_i - z'_s$
- (x'_p, y'_q, z'_s) are the coordinates of the eight corners of the j^{th} prism
- $r_{pqs} = (a_p^2 + b_q^2 + c_s^2)^{1/2}$ is the distance between one corner of the prism and the observation site (x_i, y_i, z_i) as displayed in figure 2.1

The term at the right side of the equality, noted G_{ij}, is the kernel. This response is valid only at the station g_i and for one prism ρ_j. Gravity stations $g(x_i, y_i, z_i)$ are located at the center of the upper face of prisms in the top layer with a constant elevation z_i depending on the observation points with regards to the ground level (typically $z_i = z_0 = -0.1$ m). This is to take account of the actual height of the instrument above the ground. To obtain the total response at each station g_i $(i = 1, N)$, we sum the gravity response of $M = ncx * ncy * ncz$ prisms :

$$g_i = \sum_{j=1}^{M} G_{ij}\ \rho_j \tag{2.3}$$

In matrix notation as $\boldsymbol{g} = \boldsymbol{G\rho}$ where $\boldsymbol{G}$ is also called the sensitivity matrix

relating the gravimetric acceleration $\boldsymbol{g}$ and the contrast of density $\boldsymbol{\rho}$. To avoid exponent in units, we use the $g.cm^{-3}$ ($\equiv 1000\ kg.m^{-3}$) for the contrast of density and the $mGal$ ($\equiv 10^{-5}\ m.s^{-2}$) for the gravitational attraction. In the next section, properties of the kernel are used to minimize memory storage and to determine the dimensions of the model domain with a simple analytical relation.

2.3.4 Sensitivity matrix

The aim of this section is to show the symmetry and the behavior of the kernel G when it is normalized by weighting coefficients. Finally, a relation for determining the dimensions of our domain and a choice of cell size is proposed.

2.3.4.1 Symmetry and storage optimization

Figure 2.2 shows for one station g_i that the kernel is symmetric with respect to the vertical z axis. This pattern is identically the same for all stations located at coordinates (x_i, y_i, z_i). The product $G_{ij}\ \rho_j$ is just a spatial convolution of $G_{i,j}$ with the $3D$ density distribution ρ_j. Thus the model can be split into four quadrants using its symmetry to calculate only the sensitivity of the first quadrant (figure 2.2a). If we choose the coordinates (x_0, y_0, z_0) for the station g at the corner of the 2D data grid (see gray zone in figure 2.1), we need to calculate only the first row of the matrix $\boldsymbol{G}$ (G_{1j} with $j = 1, \mathtt{M}$). The rest of the elements of G_{ij} can be called by finding the appropriate value of j. In fact, we store G_{1j} in a three dimensional array $G(ig, jg, kg)$ where $ig = [1, nox + pad]$, $jg = [1, noy + pad]$ and $kg = [1, ncz]$. Indices associated to the observations are $io = [1, nox]$ and $jo = [1, noy]$ and to the parameters are $ip = [1, ncx]$, $jp = [1, ncy]$ and $kp = [1, ncz]$. Five nested loops operating on jo, io, kp, jp, ip indices respectively are used to compute the

sensitivity terms. These indices serve to determine, among other things, the indices $ig = |(ip - pad) - io| + 1$, $jg = |(jp - pad) - jo| + 1$ and $kg = kp$ which call the appropriate value of sensitivity. The amount of memory to store for $G(ig, jg, kg)$ is just a (`1xM`) vector with $M = (nox + pad) * (noy + pad) * ncz$ instead of a (`NxM`) matrix. *pad* is the numbers of cells of padding used to extend the model domain and is discussed in the next paragraph.

2.3.4.2 Weighting the sensitivity matrix

We now analyze the behavior of the sensitivity G_{ij}, normalized by the universal gravitational constant γ, when it is weighted by a factor depending on the mean depth of the cell ρ_j ($\frac{1}{<z_j+\epsilon>}$ where ϵ is a small number to avoid singularity at the surface). This artifice is used by some authors (Li et Oldenburg, 1996; Pilkington, 1997) to give an equi-probability to each cell during the inversion process and to desensitize cells at surface. Figure 2.2b shows a cross-section of the contributions of each cell to gravity observation at the surface. Obviously the sensitivity is highest on near-surface cells. Thus every density distribution will be preferably determined at the surface if the matrix $\boldsymbol{G}$ is not altered. Figures 2.2 and 2.3 show how the kernel calculated with equation 2.2 reacts when weighted by $\frac{1}{<z_j+\epsilon>^\beta}$ with three distinct values of β. For $\beta = 0.0$ the form is "natural" and pictured as a shallow hemisphere. In the case of $\beta = 0.8$ the pattern is spread like a bulb (figure 2.3 a) giving more emphasis to intermediate depths. For $\beta = 1.9$ the sensitivity is practically constant just under the station g_i at coordinate $(0, 0, -0.1)$. A consequence would be to yield extreme density contrast and concentrate the solution at depth. On these figures, we see that the maximum sensitivity with depth lies approximately on the straight line $z = [\frac{1+\beta}{2-\beta}]^{\frac{1}{2}}\ x$ calculated with a simple spheric model. Proof is given in the

next section "*Model domain for inversion*". Numerous tests on synthetic inversion indicate that a weight depending on a power β like $\frac{1}{<z_j+\epsilon>^\beta}$ is appropriate for adjusting the reconstruction of synthetic bodies. The best value found in our tests is $\beta = 0.9$ and an acceptable range is $[0.5, 1.0]$. Li et Oldenburg (1998) use a weighting function which take account of the elevation z_0 of the gravity station ($w(z) =< z + z_0 >^{-\beta/2}$). In our case, data are always inverted at elevation $z_0 \ll \delta z$ and results are not affected by our depth weighting function. Inclusion of the elevation z_0 in the weighting function will be made if needed.

2.3.4.3 Model domain for inversion

A way is proposed to choose automatically the dimensions of the inversion domain in the x and y directions by padding (*pad*) the gravity data grid with cells around, therefore avoiding possible distortion in the reconstruction along the boundary. To obtain an analytical formulation, the subsurface is modeled by a network of spheres of radius r_s. The associated analytical kernel G_s is :

$$G_s = \gamma \frac{4}{3} \pi r_s^3 \frac{(z+\epsilon)}{(x^2+y^2+(z+\epsilon)^2)^{\frac{3}{2}}} \tag{2.4}$$

We want to know the influence of a cell B on a reference cell A located at the surface (see figure 2.1). As the inversion reconstruction favors the cells at the surface, a weight Q is introduced depending on the inverse mean depth for each cell like :

$$Q = \frac{1}{< z+\epsilon >^\beta} \tag{2.5}$$

The sensitivity kernel G_s is weighted with the scalar Q giving a new one noted

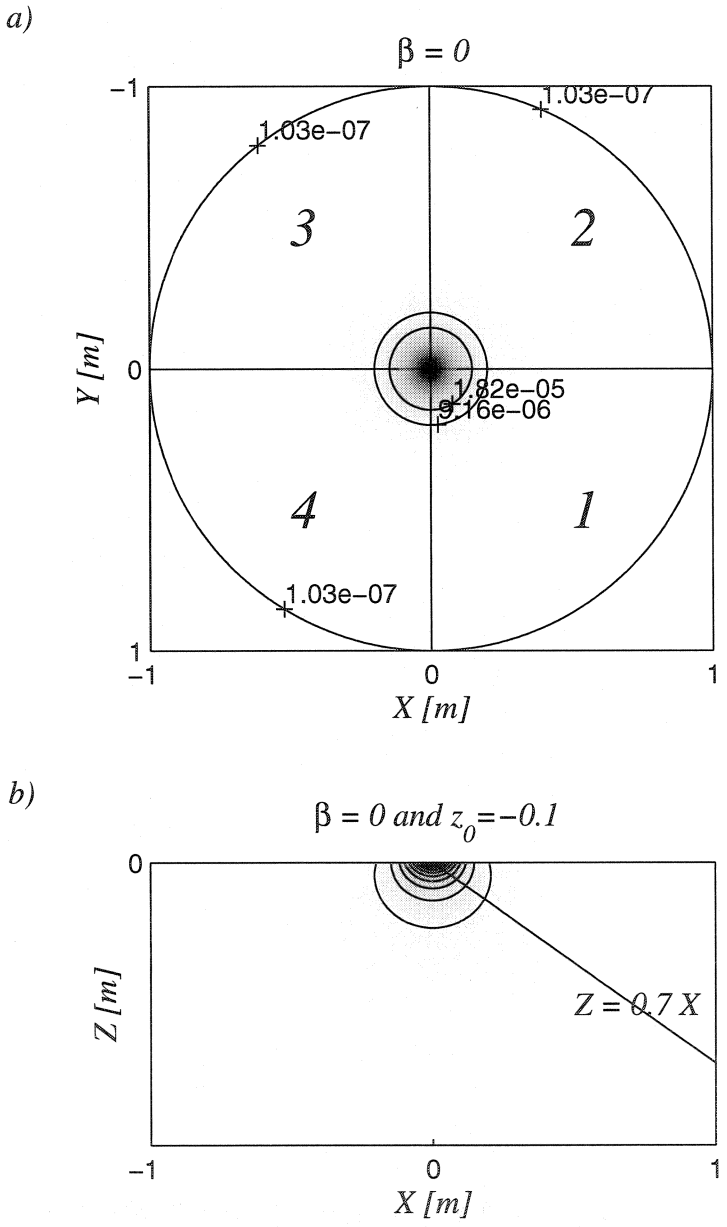

Figure 2.2: Normalized sensitivity coefficients G/γ for $\beta = 0$ and for a station located at $z_0 = -0.1\ m$. a) plan view at the surface. Numbers 1 to 4 delimits the four quadrants. b) section at $Y = 0\ m$. Equation 3.8 of maximum sensitivity for $\beta = 0$ is plotted as a dipping black line.

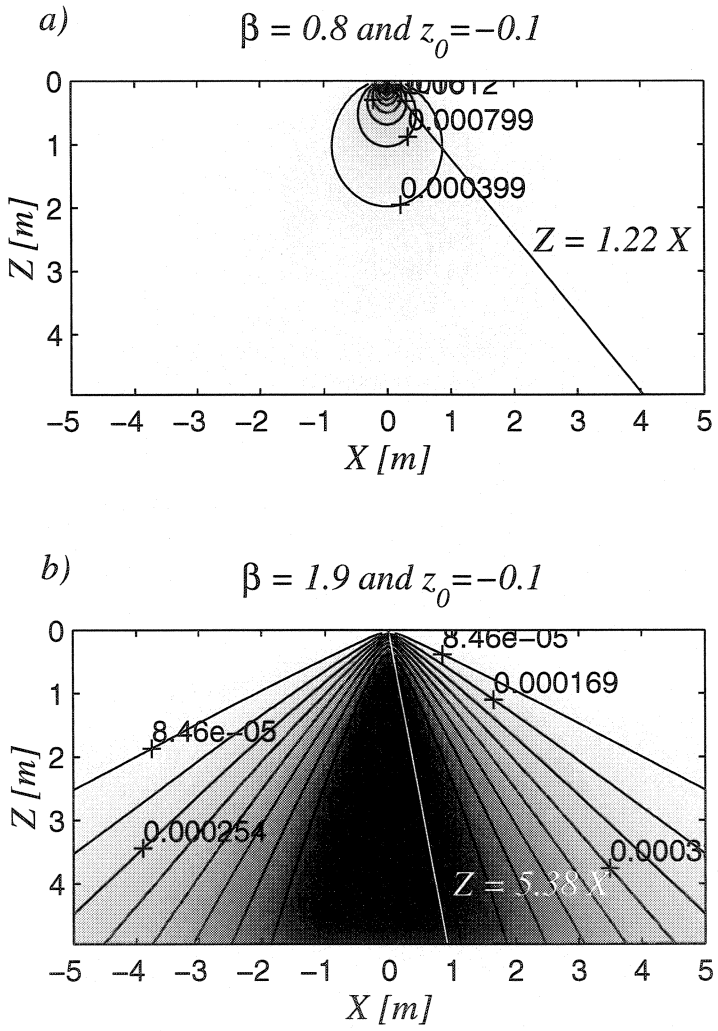

Figure 2.3: Section at $Y = 0\ m$ of the normalized sensitivity coefficients $\boldsymbol{G}/\gamma$ for a station located at $z_0 = -0.1\ m$ and for a) $\beta = 0.8$ and b) $\beta = 1.9$. Equation 3.8 for the selected β is plotted as a dipping line.

$G_{s,\beta} = G_s\ Q^{-1}$. The maximum of the function $G_{s,\beta}$ according to z ($\frac{\partial G_{s,\beta}}{\partial z} = 0$) leads to :

$$(z+\epsilon) = (\frac{1+\beta}{2-\beta})^{\frac{1}{2}}\ d \tag{2.6}$$

where $d = [x^2+y^2]^{\frac{1}{2}}$ is the polar distance in $x-y$ plane. Along this straight line (equation 2.6), we have the maximum of sensitivity with depth $G_{s,\beta}$ (For $\beta = 0$, without weighting, the relation is $z = 0.7 * x$ in the plane $x - z$). If we replace equation 2.6 in the function $G_{s,\beta}$ we obtain $G_{s,\beta}^{MAX}$:

$$G_{s,\beta}^{MAX} = \gamma \frac{4}{3}\pi r_s^3 \frac{(1+\beta)^{\frac{1+\beta}{2}}\ (2-\beta)^{\frac{2-\beta}{2}}}{3\sqrt{3}\ d^{2-\beta}} \tag{2.7}$$

Now we compare the influence of the sensitivity $G_{s,\beta}^B$ of a cell B (figure 2.1) to the sensitivity $G_{s,\beta}^A$ of a reference cell A located at the surface along the line define by equation 2.6. In such a way we define an admissible threshold q chosen like $\frac{G_{s,\beta}^B}{G_{s,\beta}^A} \leq q\ \%$ with $G_{s,\beta}^A = \gamma\ \frac{4}{3}\pi r_s^3\ (r_s)^{\beta-2}$ at $(x_j, y_j, z_j) = (0, 0, r_s)$ and $G_{s,\beta}^B = G_{s,\beta}^{MAX}$. We find an inequality for the polar distance d :

$$d \geq \frac{(1+\beta)^{\frac{1+\beta}{4-2\beta}}\ (2-\beta)^{\frac{1}{2}}}{(3\sqrt{3} * \frac{q}{100})^{\frac{1}{2-\beta}}}\ r_s \tag{2.8}$$

Practically we replace r_s by the increment of the prism in z direction ($\delta z = 2r_s$) and divide the length d by the minimum between the two increments δx and δy. Thus the number of extra cells to add around the domain is $pad = \frac{d}{min\{\delta x, \delta y\}}$. As a result, the minimum storage for the sensitivity matrix is equal to $((nox + pad) * (noy + pad) * ncz)$, where nox and noy are the number of observations in x and y directions, and ncz the number of cells in z direction.

2.3.4.4 Cell size

The determination of the optimum cell size for a given problem is fundamental in inversion. Two competing criterion have to be considered : (1) a sufficiently small cell size such that short wavelength present in the observed data can be modeled ; (2) a sufficiently large cell size such that the total number of parameters to invert for remains limited and allows computation to take place within a reasonable time. In appendix 2.4.3, we develop the necessary formulation to address the problem. We come to the conclusion that the maximum cell size which is able to fit the shortest wavelength in the data should be less than 1.2 δx where δx is the distance between gravity observations. In the inversion code discussed here, we always take a cell size equal to δx. This is a general rule used by others authors as well (Li et Oldenburg, 1996).

2.3.5 Formulation

The formulation of an inverse problem consists in finding an acceptable model closest to an initial guess (Backus et Gilbert, 1967). The inversion using the criterion of minimum distance as proposed by Green (1975) consists in minimizing the distance of an acceptable model from an initial one subject to an equality constraint $(\boldsymbol{g}^{obs} - \boldsymbol{g}) = \boldsymbol{G}\ (\boldsymbol{\rho} - \boldsymbol{\rho}^{\mathbf{0}}))$ imposed through the Lagrange multipliers. We rewrite here the Lagrangian function $L(\boldsymbol{\rho}, \boldsymbol{\theta})$ which minimize the semi-norm $\frac{1}{2}\|\boldsymbol{W}(\boldsymbol{\rho} - \boldsymbol{\rho}^{\mathbf{0}})\|_2^2$ subject to equality constraints $\boldsymbol{A}(\boldsymbol{\rho} - \boldsymbol{\rho}^{\mathbf{0}}) = \boldsymbol{b}$ in a standard form (Gauvin, 1995b) as :

$$L(\boldsymbol{\rho}, \boldsymbol{\theta}) = \frac{1}{2}\ (\boldsymbol{\rho} - \boldsymbol{\rho}^{\mathbf{0}})^T \boldsymbol{W}^T \boldsymbol{W} (\boldsymbol{\rho} - \boldsymbol{\rho}^{\mathbf{0}}) + (\boldsymbol{b} - \boldsymbol{A}(\boldsymbol{\rho} - \boldsymbol{\rho}^{\mathbf{0}}))^T\ \boldsymbol{\theta} \tag{2.9}$$

The Lagrangian function $L(\boldsymbol{\rho}, \boldsymbol{\theta})$ is composed of augmented matrix (Jackson, 1979; Pilkington, 1997) :

- $\boldsymbol{A}^T = [\boldsymbol{G}^T | \boldsymbol{H}^T]$ where $\boldsymbol{G}_{\mathtt{NxM}}$ is the sensitivity matrix and $\boldsymbol{H}_{\mathtt{MxM}}$ is the first centered derivative ($\xi_H\ \partial$) or the second derivative ($\xi_H\ \partial^2$) matrix. ξ_H is a coefficient giving more or less importance to the matrix $\boldsymbol{H}$. The first and the second derivates are usually referred to as "flatness" and "smoothness" constraints in the literature. Practically we choose ξ_H as the square norm of the matrix $\|\boldsymbol{Gx}\|^2$ with $\|\boldsymbol{x}\| = 1$ (Golub et Van Loan, 1996) multiplied by a small number μ_H ($\xi_H = \mu_H\ \|\boldsymbol{Gx}\|^2$). In the tests presented in this paper $\mu_H = 10^{-4}$ was used. If the balancing coefficient ξ_H is too large when the conjugate gradient is running, we choose to decrease ξ_H iteratively by a factor to ensure convergence.
- $\boldsymbol{b}^T = [\boldsymbol{\Delta g}^T | \boldsymbol{0}^T]$ where the vector $\boldsymbol{b}_{\mathtt{1x(N+M)}}$ consists of $\boldsymbol{\Delta g}$ which is the difference between the observed $\boldsymbol{g}^{\boldsymbol{obs}}$ and calculated $\boldsymbol{g}$ anomaly, and a null vector $\boldsymbol{0}$.
- $\boldsymbol{\theta}^T = [\boldsymbol{\alpha}^T | \boldsymbol{\zeta}^T]$ where $\boldsymbol{\theta}_{\mathtt{1x(N+M)}}$ is a Lagrange multiplier associated to equality constraints and splitted in two others ($\boldsymbol{\alpha}$ for $\boldsymbol{\Delta g}$ and $\boldsymbol{\zeta}$ for $\boldsymbol{0}$)
- $\boldsymbol{\rho^0}$ is the vector of initial contrasts of density.
- $\boldsymbol{W}_{\mathtt{MxM}} = \boldsymbol{P}^{-1}\boldsymbol{Q}\boldsymbol{\mathcal{V}}$ is equal to a product of three diagonal matrix $\boldsymbol{P}$,$\boldsymbol{Q}$ and $\boldsymbol{\mathcal{V}}$.
- $\boldsymbol{P}$ is the matrix of the "hard" constraint, where P_{jj} is fixed to $\eta \approx 10^{-2}$ or 1 whether the value of the j^{th} initial contrast of density ρ_j^0 is fixed by geological information or not, respectively. Moreover, if ρ_j takes a value beyond the global limits defined by $\rho_{min} \leq \rho_j \leq \rho_{max}$, P_{jj} is fixed to η.
- $\boldsymbol{Q}$ is the depth weighting matrix with diagonal elements $Q_{jj} = \frac{1}{<z_j+\epsilon>^{\beta}}$
- The matrix $\boldsymbol{\mathcal{V}}$ is a minimum volume constraint where $\mathcal{V}_{jj} = \frac{max\{|\rho_j|\}}{\alpha_{\mathcal{V}}(|\rho_j|+10^{-5})}$. $\alpha_{\mathcal{V}}$ is a coefficient giving more or less importance to the minimum volume constraint. For $\alpha_{\mathcal{V}} = 1$, $\mathcal{V}_{jj}$ takes value between 0 and 1. The scalar $max\{|\rho_j|\}$ avoid huge

increase of $\mathcal{V}_{jj}$ and numerical instability. When all ρ_j are equal to zero, we assign $\mathcal{V}_{jj} = 1$. Behavior of this constraint is to concentrate the solution in a minimum volume by decreasing the amplitude of small contrast of density ρ_j. The constraint of Last et Kubik (1983), which minimize the volume or maximize the compactness, is formulated as $V_{jj} = \frac{1}{\rho_j^2+\epsilon}$ and differ from $\mathcal{V}_{jj}$. But global aim of $\mathcal{V}_{jj}$ and V_{jj} is the same. $\boldsymbol{\mathcal{V}} \equiv \boldsymbol{I}$ if we don't use the minimum volume constraint.

Minimization of the objective function $L(\boldsymbol{\rho}, \boldsymbol{\theta})$ with respect to the contrast of density $\boldsymbol{\rho}$ and the Lagrange multipliers $\boldsymbol{\theta}$ vectors give, after some manipulations, a system of two equations. This system is solved iteratively and can be written as :

$$(\boldsymbol{A}\boldsymbol{W}^{-1})(\boldsymbol{A}\boldsymbol{W}^{-1})^T\, \boldsymbol{\theta}^k = \boldsymbol{b}^k \tag{2.10}$$

$$\boldsymbol{\rho}^{k+1} = \boldsymbol{\rho}^k + \boldsymbol{W}^{-1}(\boldsymbol{A}\boldsymbol{W}^{-1})^T\, \boldsymbol{\theta}^k \tag{2.11}$$

$\boldsymbol{W}$ is modified at each iteration k. At each iteration k, we find a solution $\boldsymbol{\theta}^k$ of equation 2.10 with a rms^k_{CG} error $\leq 10^{-1} * rms^0_{CG}$ (CG for Conjugate Gradient). $\boldsymbol{\theta}^k$ is replaced in equation 2.11 to give the solution $\boldsymbol{\rho}^{k+1}$. The anomaly $\boldsymbol{g}^{k+1}$ and the vector $\boldsymbol{\Delta g}^{k+1}$ are calculated to estimate a global rms_{GL} error or a χ^2 magnitude ($\chi^2 = ||\frac{g_i^{obs} - g_i}{\sigma_i}||_2^2$ where σ_i is the error standard deviation). The program stop when it reaches the rms^k_{GL} error target $\leq 10^{-2} * rms^0_{GL}$ or $\chi^2 \leq N + \sqrt{2N}$, and/or a maximum of iterations. Successive solutions can be viewed as an increment $\boldsymbol{\Delta\rho}^k$ added to the current contrast of density $\boldsymbol{\rho}^k$ yielding $\boldsymbol{\rho}^{k+1} = \boldsymbol{\rho}^k + \boldsymbol{\Delta\rho}^k$. $\boldsymbol{\Delta\rho}^k$ can be expressed as :

$$\Delta\rho^k = W^{-1}(AW^{-1})^T((AW^{-1})(AW^{-1})^T)^{-1}\, b^k \tag{2.12}$$

The code works with absolute value of density in the input file, and a background density value ρ_B is asked to the user. ρ_B is subtracted from the density of all prisms to obtain contrasts of density. The code is stable with respect to background density variations since contrasts of density are added at each iteration around ρ^0.

Equation 2.10 can be written explicitly as :

$$\begin{bmatrix} GW^{-1} \\ HW^{-1} \end{bmatrix} \begin{bmatrix} W^{-1}G^T & W^{-1}H^T \end{bmatrix} \begin{bmatrix} \alpha \\ \zeta \end{bmatrix} = \begin{bmatrix} \Delta g \\ 0 \end{bmatrix} \tag{2.13}$$

First implementation of the problem didn't make use of flatness/smoothness constraint ($A \equiv G$). It was solved using the singular value decomposition of the product $(GW^{-1})(GW^{-1})^T = VLV^T$ where L and V correspond to the eigenvalue and eigenvector matrix respectively. The system to resolve is $VLV^T\,\alpha = \Delta g$ and the solution of the estimated Lagrange multiplier α is given by (Lines et Treitel, 1984) :

$$[\hat{\alpha}] = VL\left(L^2 + \lambda\, I\right)^{-1} V^T \Delta g \tag{2.14}$$

with λ the Marquardt's damping factor. But this solution is not tractable when the number of data is large. Therefore we use the conjugate gradient method (Golub et Van Loan, 1996) to resolve the system of equations 2.13. A special case was made to solve equation 2.14 with the conjugate gradient when $A \equiv G$. In fact the product $U = (GW^{-1})(GW^{-1})^T$ is a square positive definite matrix and if we scale it with its diagonal ($U_d = diag(U)$), we obtain the scaled system :

$$\boldsymbol{U_s}\ \boldsymbol{\alpha_s} = \boldsymbol{\Delta g_s} \tag{2.15}$$

with $\boldsymbol{U_s} = \boldsymbol{U_d}^{-1/2}\boldsymbol{U}\boldsymbol{U_d}^{-1/2}$, $\boldsymbol{\alpha} = \boldsymbol{U_d}^{-1/2}\boldsymbol{\alpha_s}$ and $\boldsymbol{\Delta g_s} = \boldsymbol{U_d}^{-1/2}\boldsymbol{\Delta g}$. Thus the particularity of the matrix $\boldsymbol{U_s}$ is its symmetry which allows to obtain all its elements only with the first row of $\boldsymbol{U_s}$. The amount of memory to storage becomes a vector of length (`1xN`) instead of a (`NxN`) matrix. Furthermore updating and resolution of the system become very fast.

2.3.6 Multi-grid

Multi-grid technique is generally used to resolve discretized differential equations with iterative or relaxation methods. A good tutorial can be found in Briggs (1987) and a more detailed analysis in Hackbusch et Trottenberg (1982). The aim of our approach is to use this technique for the under-determined inverse problem. Thus we decide to sample gravity observations in x and y directions for solving first long anomaly wavelengths and then short wavelengths. We need for this to decompose the observation set in several levels. The first level is the finest composed of all data and the last one is the coarsest. In the case of two levels, we solve the system of equations 2.10 and 2.11 with $\boldsymbol{A} \equiv \boldsymbol{G}$ for the coarse level. The density found for this level is transferred by a tri-linear interpolation to the finest level. The same equations are now solved for the finest level giving the final density result. The same global rms_{GL} error or χ^2 magnitude is used for each level. If the number of levels is greater than two, we run these levels in different manner by designing a cycle. More details about how we use the multi-grid method is given in appendix 2.4.4.

2.3.7 Modeled data

2.3.7.1 Dipping dyke

For testing the program, we use a simple dipping dyke model of density 0.2 $g.cm^{-3}$ placed in a background of $\rho_B = 0\ g.cm^{-3}$ (see figure 2.4). This synthetic model is geometrically the same as the one used in the article of Li et Oldenburg (1996, 1998). Figure 2.5 show the anomaly calculated from this synthetic model. The subsurface is divided into 21x21x10=4410 cubic cells of $1km$ edge. Gravity effects g_i are computed at the surface straight above the center of the cells at $z_i = -0.1m$. The data have been contaminated by uncorrelated Gaussian noise of maximum amplitude 0.5 mGal. We generate the noise vector v_n added to g^{obs} as $v_n = [0.5\%\ var(g^{obs})]^{\frac{1}{2}} * N(0,1) \simeq 0.12 * N(0,1)$ where N(0,1) is a normally distributed random numbers with maximum amplitude of ± 5. $var(g^{obs})$ is the variance of the observed data g^{obs}. In each figure a cross section at $x = 0\ km$ and a plane at $z = 4.5\ km$ are shown. The starting model for inversion is an homogeneous ground with density $\rho^0 = 0$ and the initial penalty matrix $\boldsymbol{P} = \boldsymbol{I}$. Positivity of $\boldsymbol{\rho}^k$ is imposed here during the inversions on synthetic data by cutting densities beyond the global limits $[\rho_{min}, \rho_{max}]$ chosen to be 0 and 0.2 $g.cm^{-3}$ respectively, otherwise small negative amplitude of $\boldsymbol{\rho}^k$ are observed around the dike. For all inversion tests, the coefficient β in the weighting criterion $\boldsymbol{Q}$ is fixed at 0.9 and $\alpha_V = 1$ to compare all techniques. The program stops when $\chi^2 \leq 470$. $\sigma_i = 0.5\ mGal$ for all stations.

Figure 2.6 shows the results of inversion using only the minimum distance constraint (Green, 1975) for recovering density model. We find a density value of 0.185 $g.cm^{-3}$ and a good estimate of the depth to the top of the dyke, but its slope cannot be recovered (the white line contours the initial dyke model in figures 2.6 to

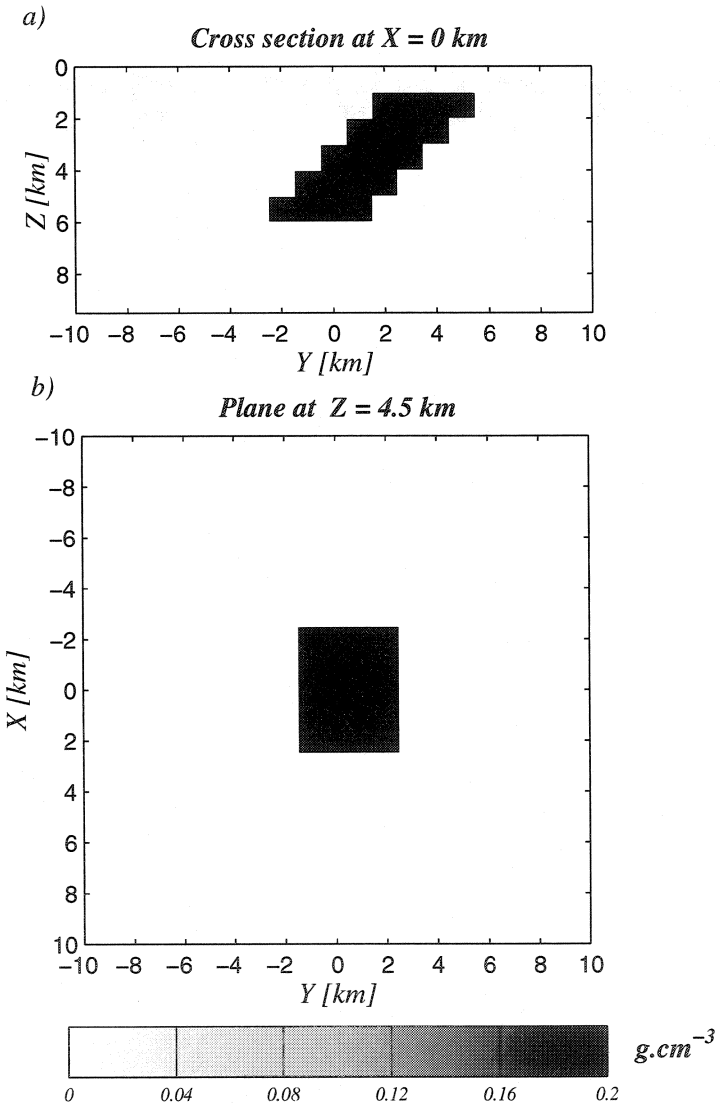

Figure 2.4: Model of dipping dyke set in a grid of 21x21x10 cells of 1 km side. a) Cross section at $X = 0\ km$. b) Plane at $Z = 4.5\ km$. Contrast of density of the dyke is $0.2\ g.cm^{-3}$.

2.10). This behavior is due to the sensitivity pattern presented in figure 2.3 which spreads the solution as depth increases. For compact bodies without anisotropy, this type of inversion gives good results with a good spatial resolution only in x and y directions. Tests have been made for different value of the coefficient β in the range $[0.5, 1]$ and the effect is to slightly move the solution vertically. Figure 2.7 shows the resulting model for the multi-grid technique with a FMV cycle with a maximum level equal to 3. The reconstruction shows a compact image with a maximum density value of 0.185 $g.cm^{-3}$. The solution is not perfect, but attractive because it is quickly obtained by taking advantage of the matrix symmetry explained in equation 2.15. This technique is not really appropriate for synthetic model with only one body, but could be an interesting technique in the case of multiple bodies for which mixture of long and short wavelengths are expected. Moreover, experience shows that the coefficient β must be chosen at 0.8 to best replace the top of bodies. Tests were made by using jointly the multi-grid technique and the flatness constraint, but improvement was found to be not significant. A reconstruction is found when using only the flatness operator giving a good estimate of the density 0.185 $g.cm^{-3}$ (see figure 2.8). The two last inversions use the criterion of minimum volume in conjunction with depth weighting. Figure 2.9 lead to a better solution with maximum density of 0.2 $g.cm^{-3}$. The limits of the dyke are better restricted eliminating the "natural" diffuse behavior visible in preceding figures. By using this time the minimum volume criterion and the flatness operator, the solution of the last test (figure 2.10) gives a good density estimate of 0.2 $g.cm^{-3}$. The two last inversions seem to best recover the geometry and density value for the dyke model.

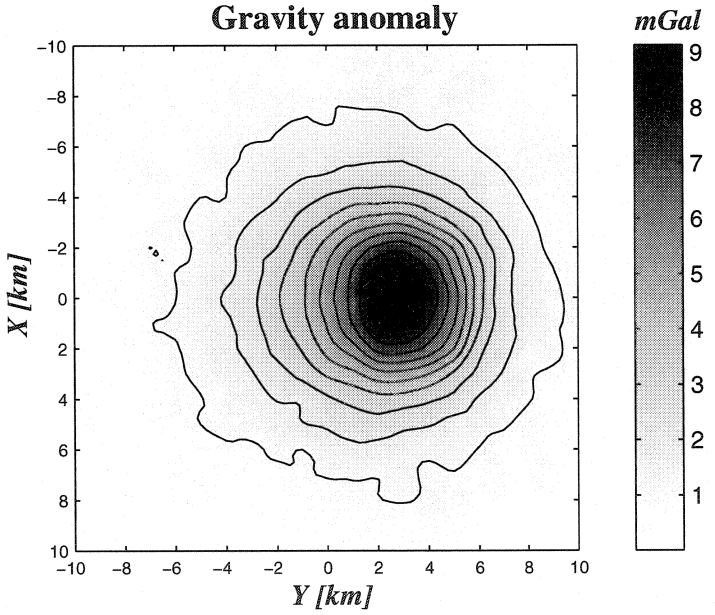

Figure 2.5: Anomaly due to the synthetic model shown in figure 2.4 and contaminated by uncorrelated Gaussian noise.

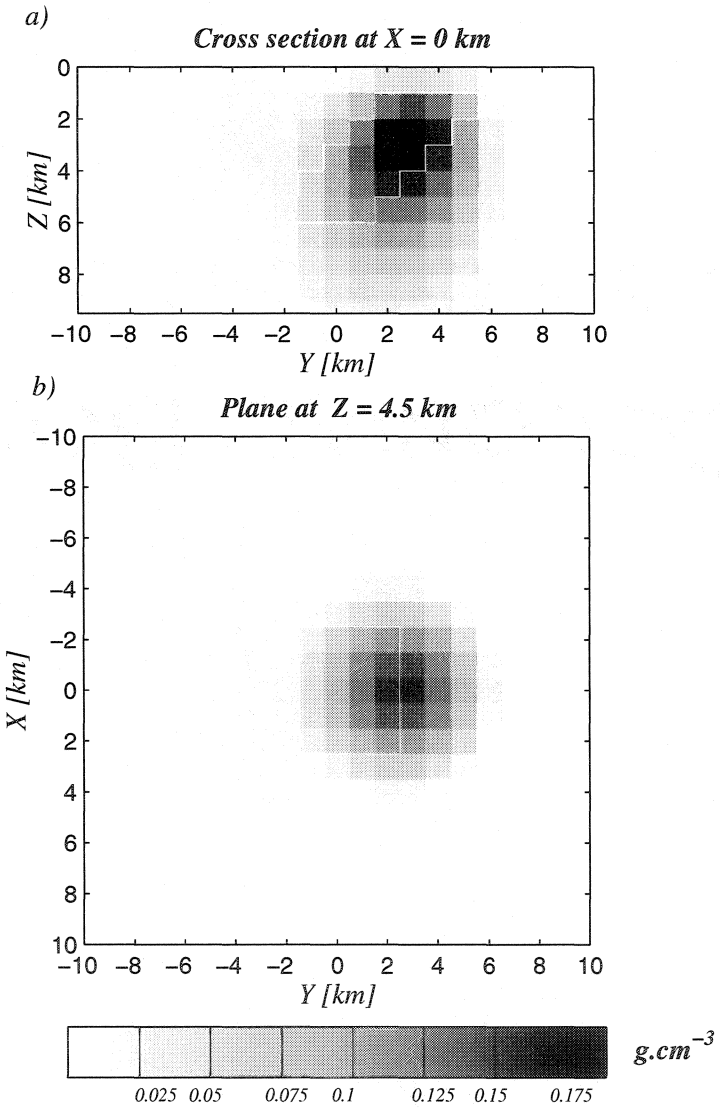

Figure 2.6: Density model obtained from inverting data of figure 2.5 using only the minimum distance formulation. $\beta = 0.9$ and a global misfit $\chi^2 = 470$ are used.

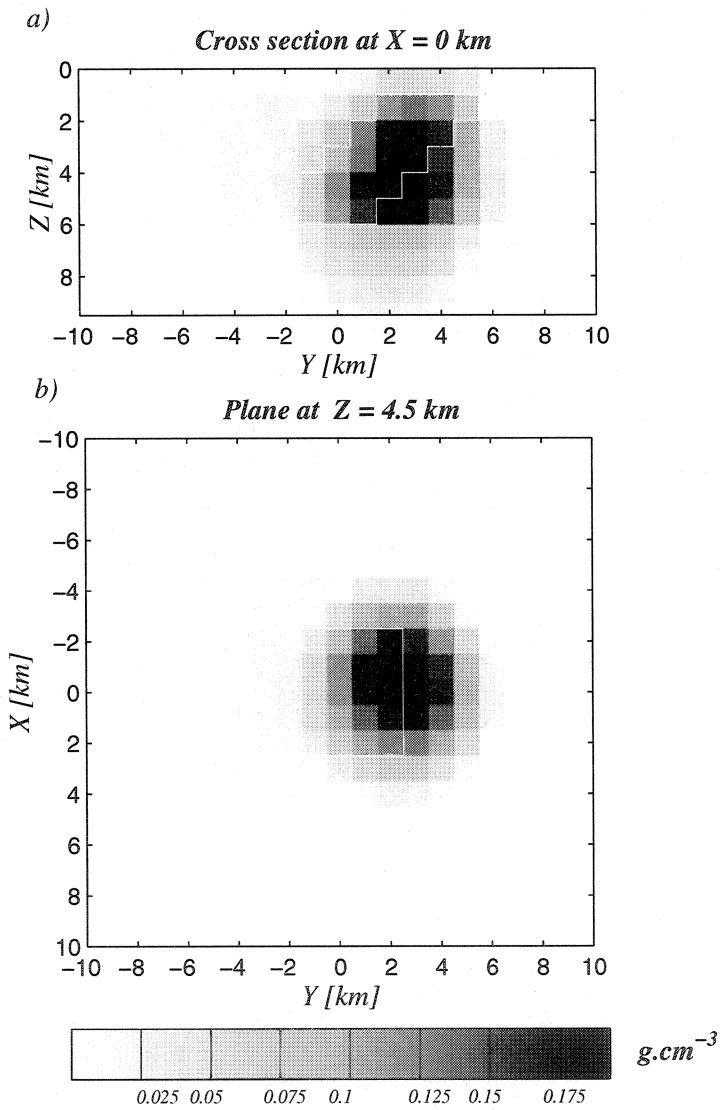

Figure 2.7: Density model obtained from inverting data of figure 2.5 using only the multi-grid technique (FMV cycle with a maximum level of 3). $\beta = 0.9$ and a global misfit $\chi^2 = 470$ are used.

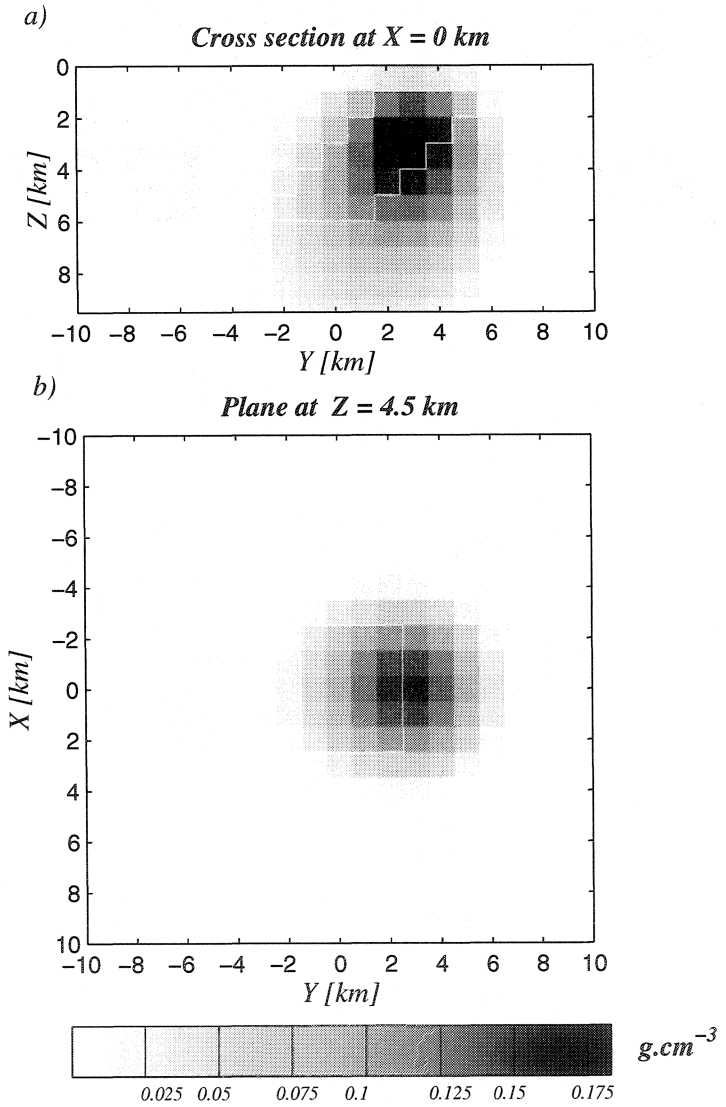

Figure 2.8: Density model obtained from inverting data of figure 2.5 using only the flatness constraint without the minimum volume constraint. $\beta = 0.9$ and a global misfit $\chi^2 = 470$ are used.

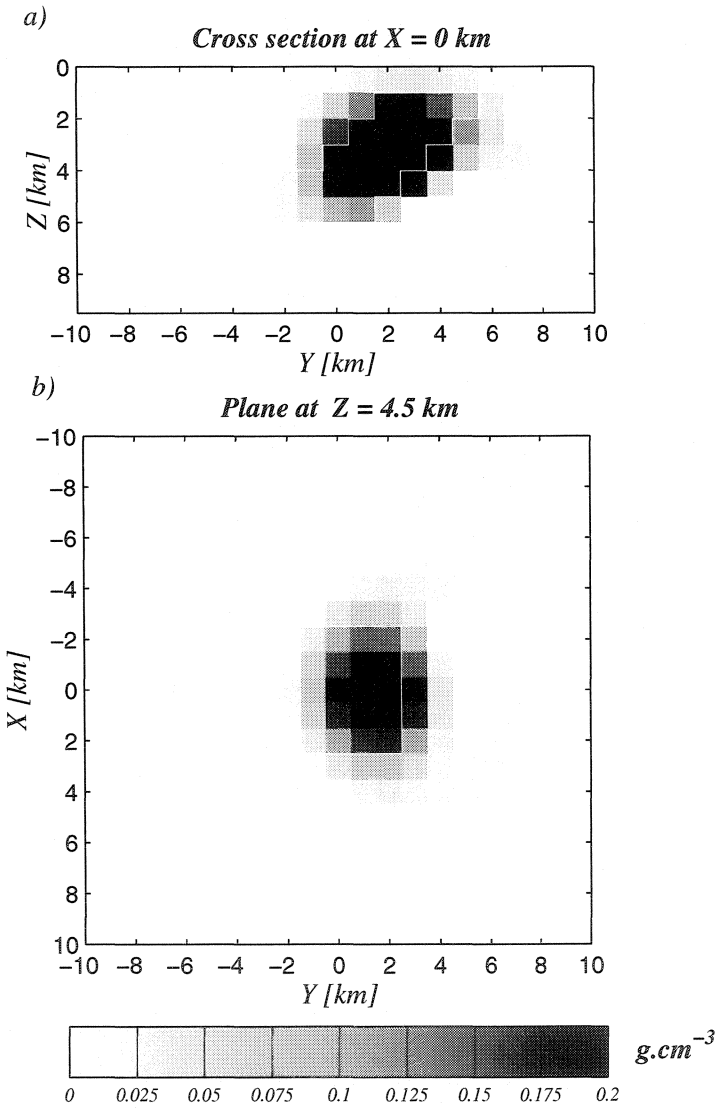

Figure 2.9: Density model obtained from inverting data of figure 2.5 using only the minimum volume constraint. $\beta = 0.9$ and a global misfit $\chi^2 = 470$ are used.

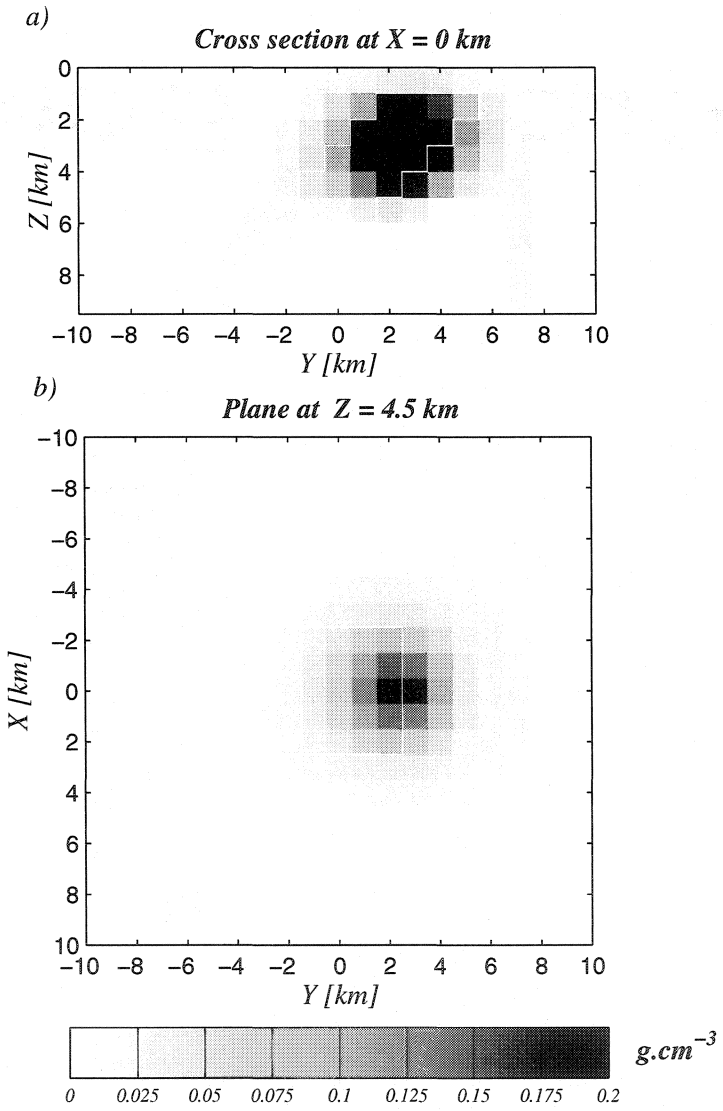

Figure 2.10: Density model obtained from inverting data of figure 2.5 using flatness and minimum volume constraints. $\beta = 0.9$ and a global misfit $\chi^2 = 470$ are used.

2.3.7.2 Multiple bodies

With this modeled data, we want to explore the ability and limitation of the current formulation to recover more complex structures from gravity data, i.e. contiguous bodies with various depths, sizes and geometries. Figure 2.11 shows a plan view and a vertical section of the modeled structures consisting of blocks lighter ($-0.2\ g.cm^{-3}$) and denser ($0.18\ g.cm^{-3}$) than the background ($2.82\ g.cm^{-3}$). Figure 2.12 displays the gravity anomaly contaminated by uncorrelated Gaussian noise of maximum amplitude 0.5 mGal and computed from the model at the surface (29x36 stations and 35x42x10 parameters). Inversion was performed using alternative constraints as on the previous dyke model. Figure 2.13 shows the resulting model for inversion using compactness ($\alpha_\mathcal{V} = 1$) and flatness constraint with $\beta = 0.9$. Convergence has been reached after 3 iterations. CPU time on a Sparc Ultra-1 143 MHz SUN workstation took 35 minutes. The horizontal position of all the bodies is well recovered in the two results. Depths to the top are also generally close to the ones of the model. Only extensions of the largest bodies appear to be overestimated in figure 2.13. This could be probably caused by the lack of sensitivity of the response to the deeper part of the model. Also the data set presented in figure 2.12 is a limited window over the complete anomaly ; truncation of the anomalies may play a role in blurring the reconstructed model. However, this test on multiple bodies allows to estimate the resolving power of the inversion method in real applications where geology is definitively more complex than the dyke model. This is particularly true for the next application in Abitibi.

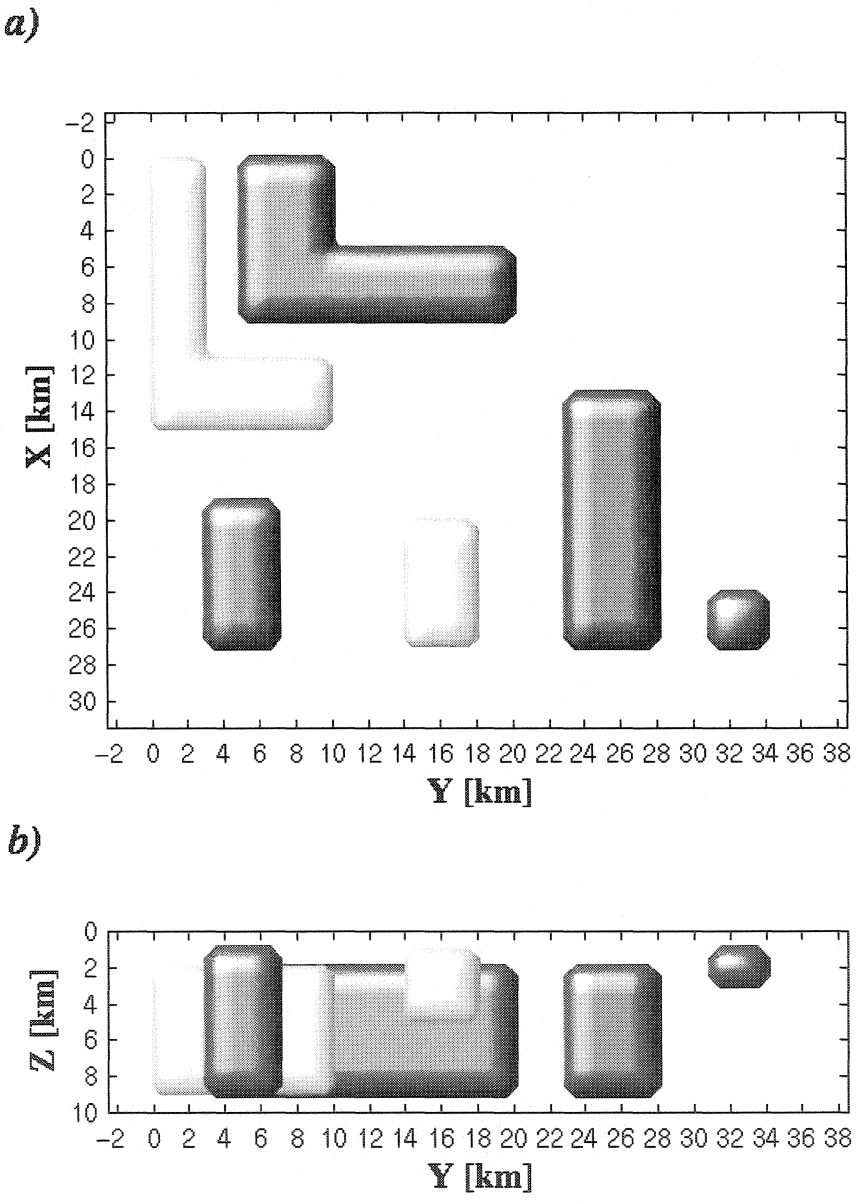

Figure 2.11: Model of multiple bodies. a) plan view. b) vertical section. Lighter and denser blocks have contrast of density of $-0.2\ g.cm^{-3}$ (pale gray) and $+0.18\ g.cm^{-3}$ (dark gray) compared to the background density of $2.82\ g.cm^{-3}$.

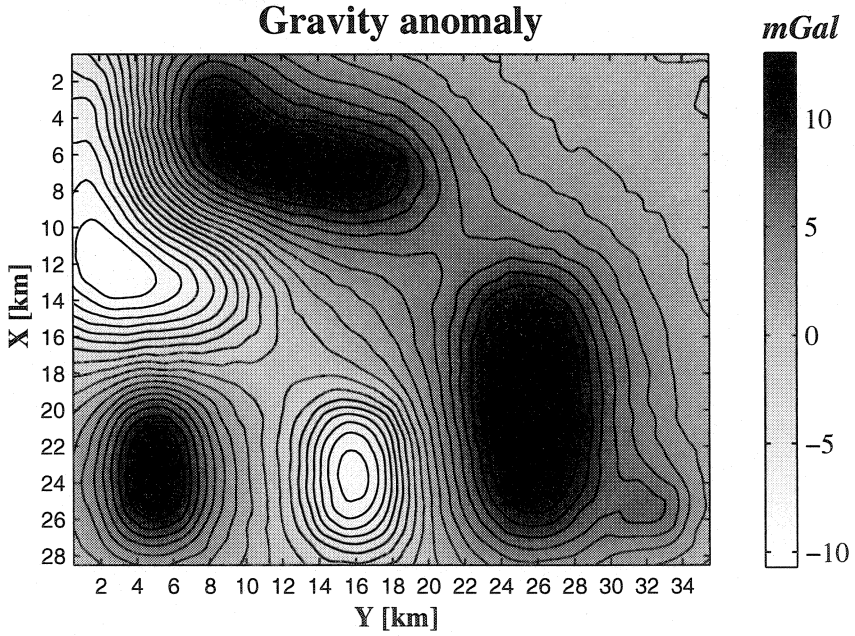

Figure 2.12: Anomaly due to the synthetic model shown in figure 2.11 and contaminated by uncorrelated Gaussian noise.

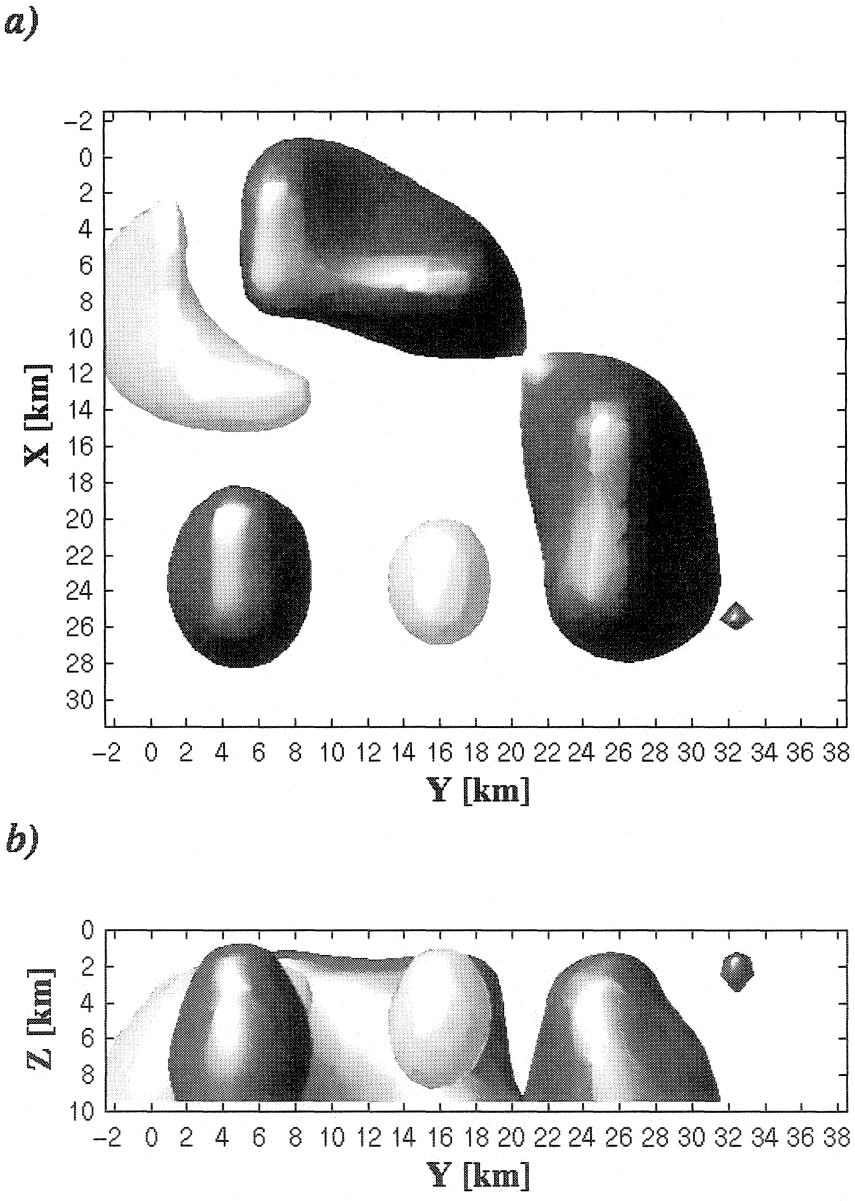

Figure 2.13: Density model obtained from inverting data of figure 2.12 using flatness and minimum volume constraints. $\beta = 0.9$ and a global misfit $\chi^2 = 1089$ are used.

2.3.8 Test on real data

2.3.8.1 Geological context

The data used for testing the inversion code cover the Blake River Group, a subdivision of the Abitibi Greenstone Belt in Quebec (Canada), well-known for the Cu-Zn-Au rich mining camp of Rouyn-Noranda. The Blake River Group is located between the Destor-Porcupine Fault (DPF) to the north and the Larder Lake-Cadillac Fault (LLCF) to the south (figure 2.14). Inside the andesite-basalt matrix (2.85 $g.cm^{-3}$) composed of several volcanic cycles (Péloquin *et al.*, 1990; Gibson et Watkinson, 1990), the region is intruded with syn- or post-volcanic granodiorite-tonalite (2.74 $g.cm^{-3}$) plutons mapped at the surface such as the Flavrian pluton (FP) and the Dufault pluton (DP). Rhyolitic rocks (2.7 $g.cm^{-3}$) alternate with andesitic flows in the volcanic sequence and are mainly mapped along the Larder Lake-Cadillac Fault on about 30 km in the W-E direction and in the eastern part of the Dufault pluton in the NW-SE direction. It is generally at the contact between felsic-rhyolites and mafic andesites that massive sulphide mineralization is found. Some diorite-gabbro (> 3 $g.cm^{-3}$) dykes and sills cut the Blake River Group in a SW-NE direction, more or less parallel to the Hunter Creek and Lake Tarssac faults (HCF and LTF). The volcanoclastic rocks (2.85 $g.cm^{-3}$) are more scattered and found along DPF and LLCF faults. The gravity data used in this paper is extracted from a larger data set. The test zone (28x35 km^2 area) is delimited by a black box in figure 2.14. Black dotted lines indicates cross sections chosen among results of inversion shown in figures 2.16 and 2.17.

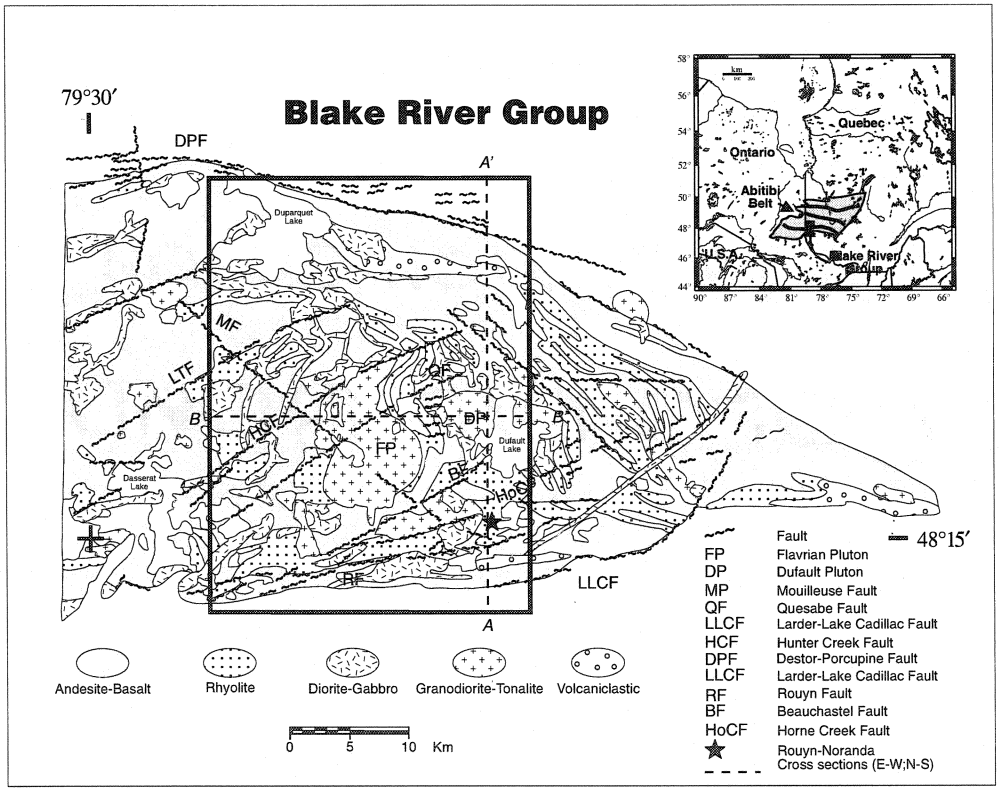

Figure 2.14: Geologic map of the northern part of the Rouyn-Noranda mining camp. Major lithological contacts and faults are shown. The black box indicates the area mapped by gravity data. Black dotted lines indicate cross sections chosen among results of reconstruction shown in figure 2.16 with the observed data set mapped in figure 2.15.

2.3.8.2 Residual Bouguer anomaly

The gravity data collected in the north-west area of Rouyn-Noranda between UTM coordinates [622000, 650000] East and [5340000, 5375000] North have been corrected for topography. It consists of 1056 stations. The Bouguer anomaly according to a 1 km square grid is obtained by kriging gravity data with a Gaussian model. The Residual Bouguer anomaly (figure 2.15) is obtained by subtracting the regional anomaly obtained by upward continuing the Bouguer anomaly at 20 km (Jacobsen, 1987) from the Bouguer anomaly. It reaches a maximum magnitude of about 17 $mGal$. The residual anomaly displays extreme magnitudes in four majors parts. The west section has the greatest amplitude associated to andesite-basalt rocks and a SW-NE strike. The central-south section has the lowest amplitude and coincides with the Powell at [East,North]=[640,5345] km. At north of these anomalies an elongated anomaly between -0.87 and 2.94 mGal correspond to a gabbro-diorite unit appearing on the surface. Another weak magnitude anomaly is located at the central-east section and correspond to the Dufault pluton ([East,North]=[647,5355] km). The Flavrian pluton observable on the geologic map is located at the center. Faults and plutons are positioned schematically to better correlate positive and negative amplitude of the residual anomaly with known geology. The road and the city of Rouyn are exactly located.

2.3.8.3 Inversion result

The residual Bouguer anomaly (figure 2.15) was sampled every 1 km for the inversion (29x36 gravity stations). The subsurface is discretized into cells of 1 km side ; the domain is enlarged in x and y directions with 3 cell-wide walls according to a $q = 5\%$ defined in equation 2.8, resulting in a model subsurface parameteriza-

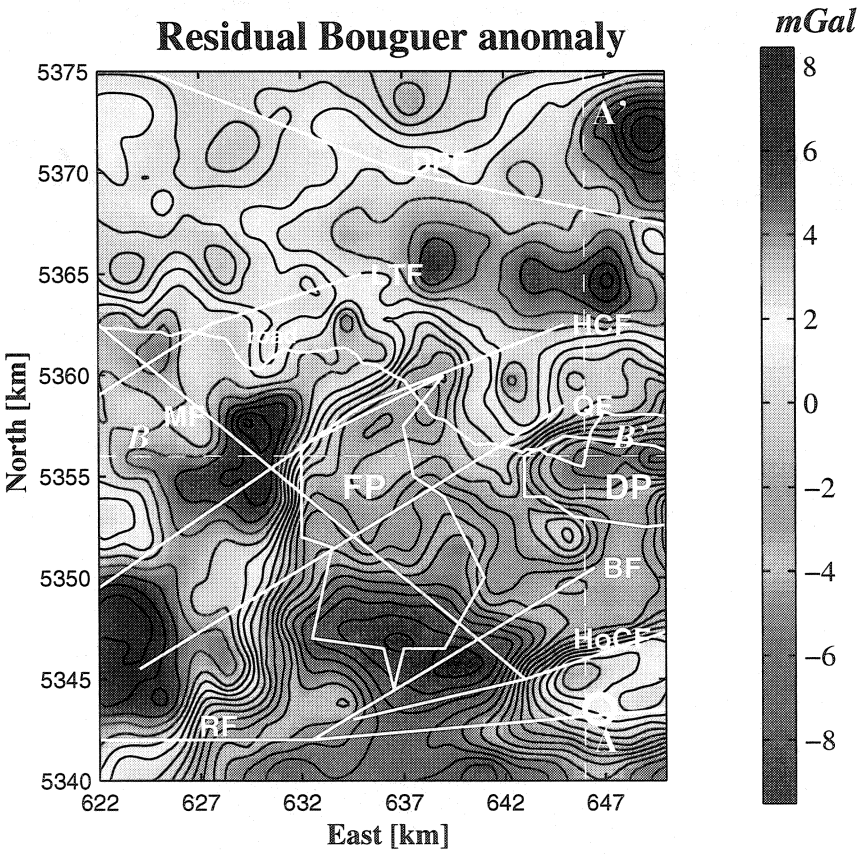

Figure 2.15: Residual Bouguer anomaly over the Blake River Group (Abitibi region, Quebec). White dotted lines indicate cross sections displayed in figure 2.16. Circle = city of Rouyn-Noranda. See figure 2.14 for abbreviations of geologic structures.

tion of 35x42x10 prisms. Inversion is carried out with a priori information about the background density ρ_B of 2.82 $g.cm^{-3}$ (see Bellefleur (1992)). Combination of flatness and minimum volume constraints are appropriate for the mineral exploration which seeks to detect dipping bodies with high contrast of density. A weight Q with $\beta = 1$ and a rms^k_{GL} error $\leq 10^{-2} * rms^0_{GL}$ and rms^k_{CG} error $\leq 10^{-1} * rms^0_{CG}$ are used. Time execution is about 3 hours and amount of memory is 3.5 M-bytes in double precision on an Ultra-1 143 MHz SUN workstation. Figures 2.16 and 2.17 show the result of the 3D inversion of the Blake River Group. Two cross sections located at East=646 km and North=5356 km are visible on figure 2.16. We observe on cross-section A-A' the mafic volcanic complex of Rouyn (CxR) with a density larger than 2.85 $g.cm^{-3}$ and the Dufault Pluton (DP) with a density smaller than 2.74 $g.cm^{-3}$ (see Perron et Calvert (1998) for the choice of density values). The CxR has a vertical extension of about 8 km, whereas the DP seems to stop at 5 km. Bellefleur (1992) and Deschamps *et al.* (1993) estimate a same vertical extension of 6 km for the CxR. Keating (1992, 1993) finds a vertical extension superior to 6 km and mentions that the effect of a two-dimensional inversion compare to a three-dimensional one is to underestimate thicknesses. For this two major bodies, their shapes show a trend in the a E-W direction visible on figure 2.17. The 3D inversion result is in agreement with the major lithological contacts and gives more precision about the volume of plutons and intrusive rocks. Major structures and faults are drawn with black lines on figure 2.17. Correlation can be made with the Lithoprobe seismic reflection profiles 14 and the 3D density distribution to identify the DPF fault visible in figure 2.17 (see Green *et al.* (1990)). High-resolution and regional seismic reflection have been carried out along the Lithoprobe line 21 which is coincident with the road in figure 2.17. Verpaelst *et al.* (1995) find

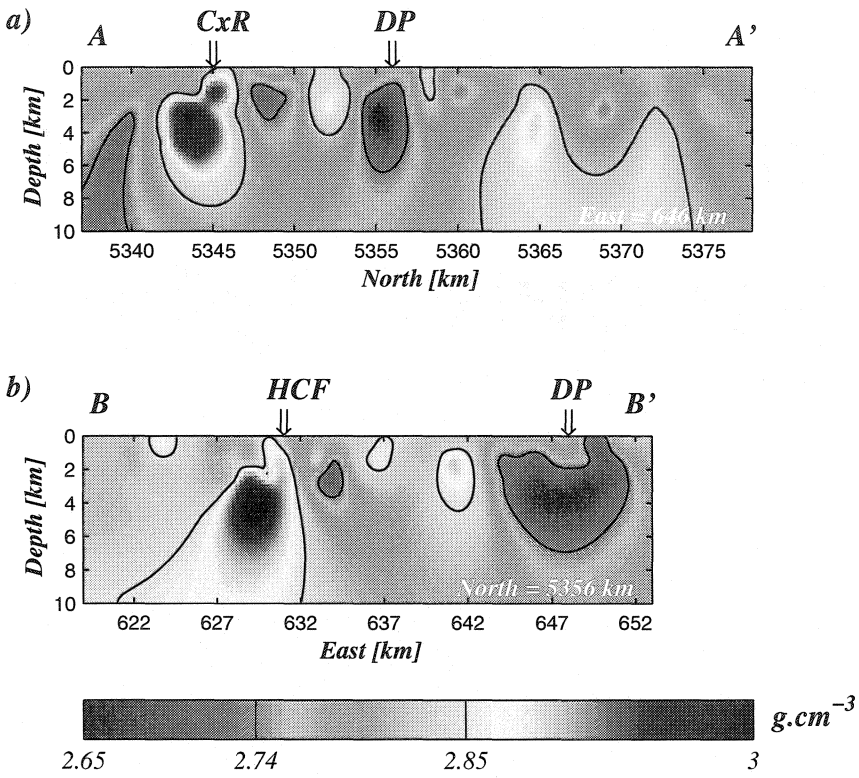

Figure 2.16: Results of 3D inversion of the Blake River Group data using $\beta = 1.0$, flatness operator and minimum volume constraint ($\alpha_V = 0.1$). a) North-South cross section A-A' at position East = 646 km. b) West-East cross section B-B' at position North = 5356 km. DP=Dufault Pluton; CxR = volcanic Complex of Rouyn; HCF=Hunter Creek Fault.

a "northeast-facing dip to the Blake River Group central mines sequence, which has been disrupted by the sub-vertical Hunter Creek fault". Hunter Creek fault is located on cross-section B-B' in figure 2.16b at position East = 630 km.

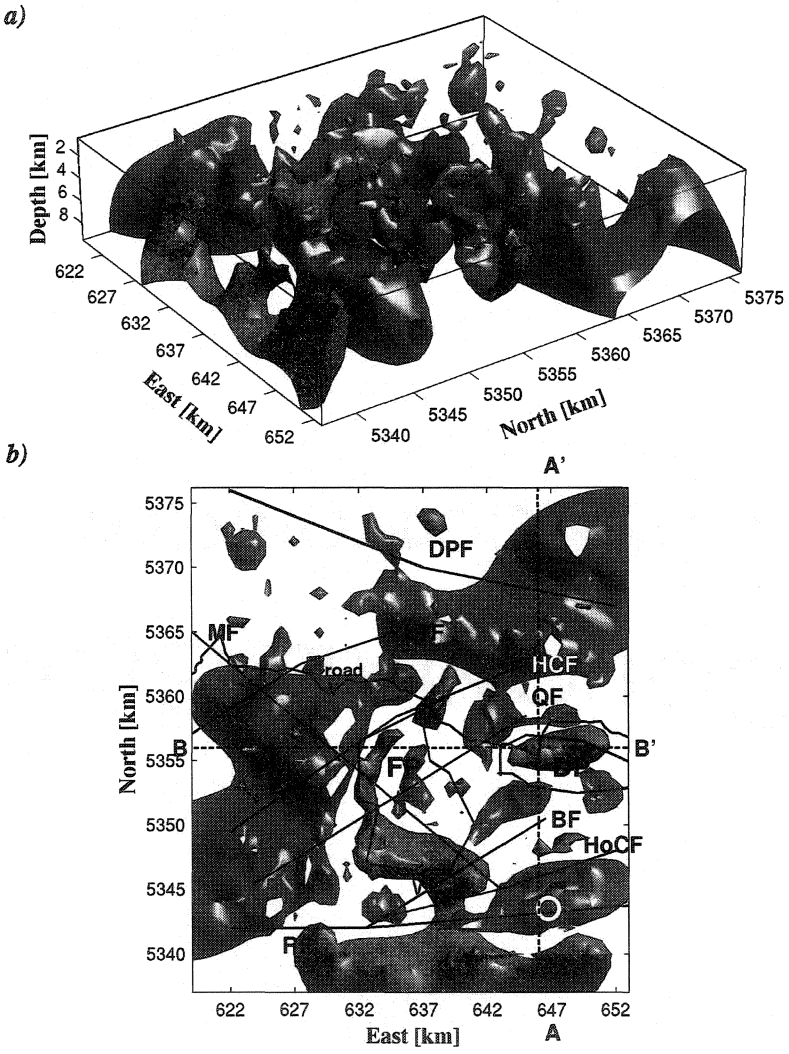

Figure 2.17: Isosurfaces of the 3D inversion results (lighting from the right) are presented in two different views a) looking from the SE with a vertical elevation of 30° and b) above. Pale and dark gray motifs correspond to density lower than 2.74 $g.cm^{-3}$ and density higher than 2.85 $g.cm^{-3}$ respectively. Major faults (DPF,LTF,HCF,MF,QF,BF,HoCF,RF), city of Rouyn (white circle), Flavrian Pluton (FP) and Dufault Pluton (DP) are drawn to help correlation. See figure 2.14 for legend of features.

2.4 Discussion and conclusions

The 3D gravity inversion using the criterion of minimum distance as proposed by Green (1975) and formulate with a Lagrange function yields a flexible code which allows inclusion of flatness, smoothness and minimum volume constraints that can be used if needed. The code allows to investigate different approaches to find an acceptable solution. Different powers for the depth weighting factor have been analyzed to better understand the inverse reconstruction and avoid concentration of the solution at the surface or at depth. In each case β must lie in the range $[0.5, 1]$. We suggest a standard selection of $\beta = 0.8$ for the multi-grid and $\beta = 0.9$ for the others constraints. The multi-grid technique quickly yields a good approximation of the density structure, but it cannot be combined with other constraints. This is due to two factors : (1) inter-grid interpolation already include minimum volume constraint ; (2) flatness constraint needs a sufficient number of cells to be efficient. Good contrast of density can be obtained for each technique but geometry is never exactly recovered. The best combination of constraints appears to be, at least for our study, flatness and minimum volume. By analyzing the kernel, we have found that sensitivity coefficients describe a symmetry with respect to the vertical z axis. This symmetry allows efficient minimization of data storage. A simple analytical relation have been derived from the kernel of spheric cells to assist in the choice of the discretization domain. The code only needs an estimate of the background density. Local constraints can be included by weighting particular cells. Density bounds can also be included to limit density contrast excursions. Weight depending on power of depth for each cell is always recommended.

The basic solution is minimum distance. Then, this method in conjunction

with the multi-grid technique and flatness constraint can improve solution for slowly varying densities often encountered in the oil exploration. Method using the minimum volume constraint (compactness) is particularly suited to high contrast of density like in archaeological or geotechnical investigations for cavity detection. Flatness and minimum volume constraints can be the best suited combination for mineral exploration which seeks to detect a combination of high density contrasts for small bodies and low contrasts for large bodies (background geology). When the number of parameters is large (e.g.> to 100x100x40 cells) the code becomes slow to run. Future work will include adaptive mesh refinement (AMR) in the inversion process to minimize the size of the matrix $\boldsymbol{G}$ and the time to run the forward problem. However, the program needs modest storage memory allowing it to run on a laptop computer. The code is written in C language and is available from the first author.

2.4.1 Acknowledgements

This work was supported by NSERC Strategic Grant STR0181406. We acknowledge Bruno Meurers (Associate Editor of GP in gravity and magnetism) and two anonymous referees for their valuable comments and suggestions.

2.4.2 References

Backus G. and Gilbert J. F., 1967. Numerical Applications of a Formalism for Geophysical Inverse Problems, *Geophysical Journal of the Royal Astronomical Society*, **13**. 247–276.

Banerjee B. and Gupta S.P. D., 1977. Gravitational attraction of a rectangular

parallelepiped, *Geophysics*, **42**(5). 1053–1055.

Barbosa V. C. F. and Silva J. B. C., 1994. Generalized compact gravity inversion, *Geophysics*, **59**(1). 57–68.

Bear G. W., Al-Shukri H. J., and Rudman A. J., 1995. Linear inversion of gravity data for 3-D density distributions, *Geophysics*, **60**(5). 1354–1364.

Bellefleur G., 1992. *Contribution of potential methods to the geological and the deep structure cartography in the Blake River Group*, Master's thesis, Ecole Polytechnique, Montreal, (in French).

Bhattacharyya B. K. and Leu L.-K., 1977. Spectral analysis of gravity and magnetic anomalies due to rectangular prismatic bodies, *Geophysics*, **42**(1). 41–50.

Briggs W., 1987. *A Multigrid Tutorial*, Society for Industrial and Applied Mathematics.

Deschamps F., Chouteau M., and Dion D.-J., 1993. Geological interpretation of aeromagnetic and gravimetric data in the region located at the west part of the Rouyn-Noranda city, in *Études géophysiques récentes de certains secteurs de la ceinture volcanosédimentaire de l'Abitibi*, edited by M. Germain, vol. DV 93-10 of *Ministère des Ressources naturelles. Secteur des mines*, pp. 78–130, (in French).

Djeridane S., 1996. *Two-dimensional gravimetric inversion minimizing subsurface structures; Application to Abitibi and Opatica sub-provinces*, Master's thesis, Ecole Polytechnique, (in French).

Gauvin J., 1995. *Lessons of mathematical programming*, Ecole Polytechnique, Montreal, (in French).

Gibson H. and Watkinson D., 1990. Volcanogenic massive sulphide deposits of the Noranda cauldron and shield volcano, Quebec, in *Northwestern Quebec Polymetallic Belt*, edited by M. Rive, P. Verpaelst, Y. Gagnon, J. Lulin, G. Riverin, and A. Simard, vol. 43.

Golub G. H. and Van Loan C. F., 1996. *Matrix computations*, Johns Hopkins University Press, 3rd edn.

Green A., Milkereit B., Mayrand L., Ludden J., C.Hubert, Jackson S., Sutcliffe R., West G., Verpaelst P., and Simard A., 1990. Deep structure of an Archaean greenstone terrane, *Nature*, **344**. 327–330.

Green W. R., 1975. Inversion of gravity profiles by use of a Backus-Gibert approach, *Geophysics*, **40**(5). 763–772.

Guillen A. and Menichetti V., 1984. Gravity and magnetic inversion with minimization of a specific functional, *Geophysics*, **49**(8). 1354–1360.

Haáz I. B., 1953. Relations between the potential of the attraction of the mass contained in a finite rectangular prism and its first and second derivates (in hungarian), *Geofizikai Kozlemenyek*, **2**(7).

Hackbusch W. and Trottenberg U., 1982. *Multigrid Methods*, Springer-Verlag.

Jackson D., 1979. The use of a priori data to resolve non-uniqueness in linear inversion, *Geophysical Journal of the Royal Astronomical Society*, **57**. 137–157.

Jacobsen B. H., 1987. A case for upward continuation as a standard separation filter for potentiel-field maps, *Geophysics*, **52**(8). 1138–1148.

Keating P., 1993. Interpretation of the gravity anomaly field in the Noranda - Val d'Or region, Abitibi Greenstone Belt, Canadian Shield, *Canadian Journal of*

Earth Science, **29**. 962–971.

Keating P., 1993. Interpretation of the gravity anomaly field in the Noranda - Val d'Or region., in *Études géophysiques récentes de certains secteurs de la ceinture volcanosédimentaire de l'Abitibi*, edited by M. Germain, vol. DV 93-10 of *Ministère des Ressources naturelles. Secteur des mines*, pp. 57–76, (in French).

Last B. J. and Kubik K., 1983. Compact gravity inversion, *Geophysics*, **48**(6). 713–721.

Li X. and Chouteau M., 1998. Three-dimensional gravity modeling in all space, *Surveys in Geophysics*, **19**. 339–368.

Li Y. and Oldenburg D. W., 1996. 3-D inversion of magnetic data, *Geophysics*, **61**(2). 394–408.

Li Y. and Oldenburg D. W., 1998. 3-D inversion of gravity data, *Geophysics*, **63**(1). 109–119.

Lines L. R. and Treitel S., 1983. Tutorial : A review of least squares inversion and its application to geophysical problems, *Geophysical Prospecting*, **32**. 159–186.

Nagy D., 1966. The gravitational attraction of a right rectangular prism, *Geophysics*, **31**(2). 362–371.

Péloquin A., Potvin R., Paradis S., Laflèche M., Verpaelst P., and Gibson H., 1990. The Blake River Group, Rouyn-Noranda area, Québec : a stratigraphic synthesis, in *Northwestern Québec Polymetallic Belt*, edited by M. Rive, P. Verpaelst, Y. Gagnon, J. Lulin, G. Riverin, and A. Simard, vol. 43, Canadian Institute of Mining and Metallurgy.

Perron G. and Calvert A., 1998. Case History : Shallow, high-resolution seismic imaging at the Ansil mining camp in the Abitibi greenstone belt, *Geophysics*, **63**(2). 379–391.

Pilkington M., 1997. 3-D magnetic imaging using conjugate gradients, *Geophysics*, **62**(4). 1132–1142.

Verpaelst P., Peloquin A., Adam E., Barnes A., Ludden J., Dion D.-J., Hubert C., Milkereit B., and Labrie M., 1995. Seismic reflection profiles across the "Mines Series" in the Noranda camp of the Abitibi belt, eastern Canada, *Canadian Journal of Earth Science*, **32**. 167–176.

2.4.3 Appendix : Determination of the cell size to fit the gravity anomaly

There is relationship between the cell size and the wavelength of the computed anomaly. Shortest wavelength observed in the data will come from the shallowest bodies. To analyze the sensitivity of the method with respect to the cell size used in computing the gravity effect, we search the maximum size of a prism located in the top layer to fit the highest frequency (Nyquist frequency) displayed by the anomaly. The Fourier transform $F_g(u,v)$ of the gravity effect due to a prismatic body with a finite vertical extend can be formulated from Bhattacharyya et Leu (1977). If we note $u = 2\pi f_x$, $v = 2\pi f_y$, $s = \sqrt{(u^2+v^2)}$, $h_1 = z'_1 - z_i$, $a = x'_2 - x'_1$, $b = y'_2 - y'_1$ and $c = z'_2 - z'_1$ then $F_g(u,v)$ is

$$F_g(u,v) = 16\pi\gamma\rho \; \frac{sin(\frac{ua}{2})}{u} \; \frac{sin(\frac{vb}{2})}{v} \; \frac{sinh(\frac{sc}{2})}{s} \; e^{-s(h_1+\frac{c}{2})} \; e^{-iu(x'_1+\frac{a}{2})} \; e^{-iv(y'_1+\frac{b}{2})} \quad (2.16)$$

The Nyquist frequency of gravity data in x direction is given by $f_N = \frac{1}{2\delta x}$. If we suppose that $\delta x = 1$ and $a = b = c$ then $u_N = 2\pi f_N = \pi$. We can plot for an observation at the surface (center of top face with $h_1 = 0$) the normalized power spectra $\frac{|F_g(u,v=0)|^2}{|F_g(0,0)|^2}$ in the direction u versus the ratio $n = \frac{a}{\delta x}$ (figure 2.18). The anomaly from the cubic cell will be able to reproduce the highest frequency in the data (Nyquist frequency) if the power at the Nyquist frequency is still large enough. We impose a threshold $\geq 1\%$ of normalized power ($\geq 10\%$ of normalized amplitude) as a minimum bound to fulfil this condition. From figure 2.18, it can be concluded that cells with a size $\frac{a}{\delta x} \leq 1.2$ are needed. In all cases presented in this paper, we use $a = \delta x$. The same reasoning is valid for δy.

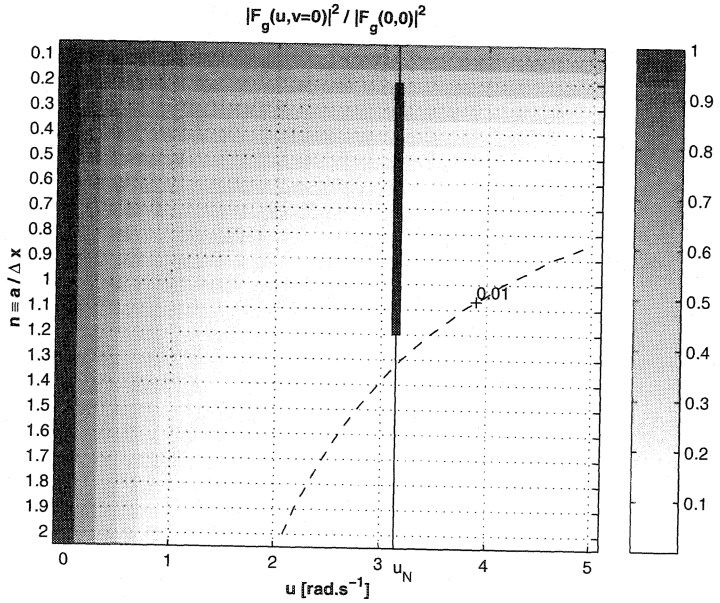

Figure 2.18: Normalized power spectra $\frac{|F_g(u,v=0)|^2}{|F_g(0,0)|^2}$ in the direction u versus the ratio $n = \frac{a}{\delta x}$. Fine line at u_N represents the highest frequency (Nyquist frequency) displayed by the gravity data. Thick line at u_N gives the range of $n = \frac{a}{\delta x}$ for which the highest frequency in the gravity anomaly can be explained by a cell of size a at the surface. Dashed line correspond to 1 % of the normalized power spectra.

2.4.4 Appendix : Multi-grid

Gravity observations are sampled in x and y directions for solving first long anomaly wavelengths and then short wavelengths. We need for this to decompose the observation set in several levels. The first level is the finest composed of all data and the last one is the coarsest. These levels can be run in different manner by designing a cycle (Nested N-cycle, V-cycle, W-cycle, Full Multi-grid FMV-cycle and FMVI-cycle) described in figure 2.19. When the inter-grid transfer of density ρ_j move from a fine grid δ^i to a coarse grid δ^{i+1}, noted $R = I_{\delta^i}^{\delta^{i+1}}$, it is called *restriction* (or injection). A *prolongation* is made by the operator $P = I_{\delta^{i+1}}^{\delta^i}$ for an interpolation from level δ^{i+1} to level δ^i. We use here simple tri-linear interpolation I of ρ_j weighted by $\mathcal{V}_{jj}^{-1}$, defined in section "Formulation" to obtain a better result. Because two successive level grids do not coincide but overlap each other, we need to define a neighborhood around each cell ρ_j during the inter-grid transfer of the density to avoid a density smoothing. Thus, the limits of interpolation at a point $\mathtt{x}$ in the space for prolongation and restriction are defined as $\rho_j^{\delta^{i+1}}(\mathtt{x} - \nu\delta^{\mathtt{i}}) \leq \rho_{\mathtt{j}}^{\delta^{\mathtt{i}}}(\mathtt{x})\ \mathcal{V}_{\mathtt{jj}}^{-1} \leq \rho_{\mathtt{j}}^{\delta^{\mathtt{i}+1}}(\mathtt{x} + \nu\delta^{\mathtt{i}})$ and $\rho_j^{\delta^i}(\mathtt{x} - \nu\delta^{\mathtt{i}+1}) \leq \rho_{\mathtt{j}}^{\delta^{\mathtt{i}+1}}(\mathtt{x})\ \mathcal{V}_{\mathtt{jj}}^{-1} \leq \rho_{\mathtt{j}}^{\delta^{\mathtt{i}}}(\mathtt{x} + \nu\delta^{\mathtt{i}+1})$ respectively (where $\nu = 0.5$ only for prolongation in z direction, otherwise $\nu = 1$). Increments of the grid for each level in x and y directions are calculated as $\delta^i = i\ \delta^1$, and for z direction as $\delta_z^i = \frac{ncz\ \delta_z^1}{t}$ where $t = \{\frac{ncz}{i}\} \geq 1$ is an integer value ($t \in N$). We calculate the Jacobian matrix $\boldsymbol{G}^{\delta^i}$ depending on the increments δ^i in x, y, z directions, and solve the system of equation 2.11 (with $\boldsymbol{A} \equiv \boldsymbol{G}^{\delta^i}$) with the same global *rms* tolerance at each level i.

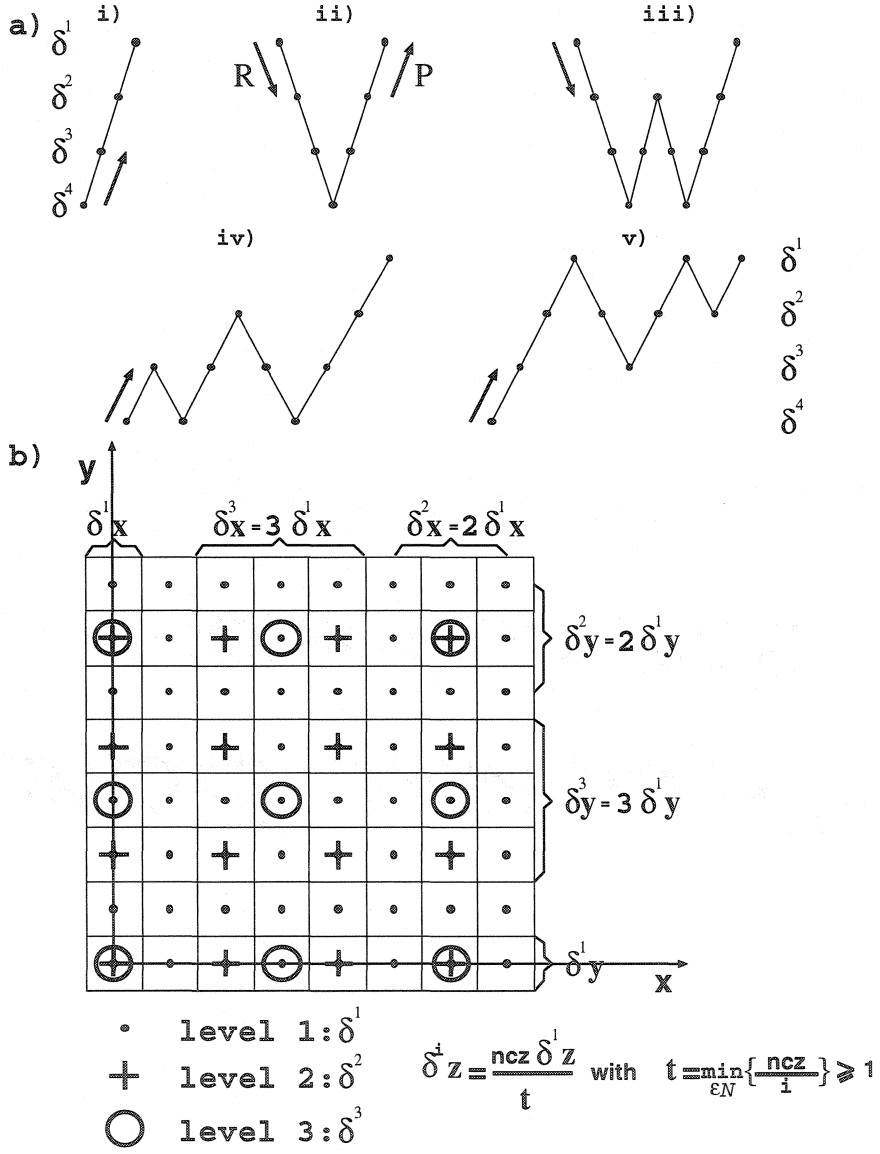

Figure 2.19: a) Types of cycle with restriction ($R = I_{\delta^i}^{\delta^{i+1}}$) and prolongation ($P = I_{\delta^{i+1}}^{\delta^i}$) : i) Nested, ii) V-cycle, iii) W-cycle, iv) FMV-cycle, v) FMVI-cycle. b) Discretization in all directions and sampling of data ($\bullet, +, \bigcirc$) for each level $i = 1, 2, 3$ (δ^i).

Chapitre 3

MODÉLISATION ÉLECTRIQUE

3.1 Introduction

La deuxième méthode géophysique consiste à détecter des gisements miniers à l'aide de mesures de potentiel électrique. Dans ce chapitre, on présente une méthode particulière pour la modélisation du potentiel électrique. Cette méthode a fait l'objet d'un article : "3D modeling and sensitivity in DC resistivity using charge density", dont le texte a été soumis au mois de novembre 2002 et accepté au mois de février 2004 dans la revue Geophysical Prospecting (Boulanger et Chouteau, 2004).

L'interprétation des données électriques quand le milieu est hétérogène est souvent faite en utilisant soit la modélisation par différences finies (FD), soit la modélisation par éléments finis (FE). La méthode par FD est la plus répandue, puisqu'elle est relativement simple à programmer comparée à la méthode des éléments finis. Bien que la méthode par équation intégrale (IE) ait été moins utilisée pour l'interprétation des données de résistivité électrique, beaucoup de

chercheurs ont contribué à son développement. Une des raisons principales pour son utilisation limitée est que les matrices résultantes à résoudre sont grandes et pleines ; c'est pourquoi aucun code 3D n'a été développé pour un milieu hétérogène avec une conductivité arbitraire. Cependant, un des avantages de la formulation par rapport aux méthodes FE et FD est qu'il est possible de calculer le potentiel à n'importe quel point dans l'espace 3D sans être obligé d'interpoler le potentiel calculé aux noeuds de la maille. On modélise donc avec exactitude le potentiel en un point. On présente ici un code qui tient compte de ces derniers avantages et étend la méthode IE au-delà des ses limitations, i.e. un milieu hétérogène 3D avec une conductivité arbitraire. Une méthode de calcul de la densité de charge pour un milieu hétérogène arbitraire 3D est développée. Le volume est discrétisé avec des prismes rectangulaires de différentes tailles dans un système Cartésien. Pour une distribution de conductivité donnée, un système d'équations linéaires est établi. Ce système d'équations linéaires, indépendant de la position de la source, permet le calcul du potentiel et de la densité de courant pour toutes les configurations possibles. Le calcul des densités de charge est validé en utilisant des valeurs analytiques trouvées dans la littérature.

La même approche a été utilisée par Snyder (1976) qui présente un calcul des densités de charge pour un domaine 2D avec une extension infinie. Une variété de fomulations intégrales, pour le calcul du potentiel électrique quand le milieu est constitué d'un prisme dans un milieu homogène ou tabulaire, peut être trouvé dans Schulz (1985); Poirmeur et Vasseur (1988); Hvozdara et Kaikkonen (1998). Spiegel *et al.* (1980) proposent un calcul du potentiel en utilisant la densité de charge pour un domaine 2D avec une topographie. Poursuivant le développement de Hohmann (1975), Beasley et Ward (1986) évaluent le potentiel à n'importe quel

point à partir du calcul du champ électrique dans chaque cellule. Li et Oldenburg (1991) proposent une étude sommaire sur le calcul du potentiel avec les densités de charge.

Dans le but de développer un code d'inversion 3D, il est important de calculer la sensibilité électrique 3D (dérivée première ou Jacobienne) et les dérivées secondes (Hessien). Plusieurs auteurs ont déjà proposé différentes techniques pour évaluer les coefficients de sensibilité. Boerner et West (1989) calculent les dérivées de Frechet basées sur une hypothèse de perturbation autour d'une valeur moyenne de la conductivité. McGillivray et Oldenburg (1990) proposent une étude comparative des cas 1D et 2D en utilisant un configuration pôle-pôle pour calculer la sensibilité. Sasaki (1994) montre un cas 3D avec une configuration dipôle-dipôle et Park et Van (1991) montrent une distribution 3D associée avec une inversion. Une explication théorique peut aussi être trouvée dans l'article de Geselowitz (1971). Récemment, Spitzer (1998*b*) a fait une étude comparative sur les différentes méthodes de calcul de la sensibilité. Dans son article, les coupes de sensibilité sont montrées pour une variété de configurations possibles de sources et de récepteurs dans le cas d'un milieu homogène. Une comparaison est faite pour une configuration pôle-pôle dans le cas d'un milieu stratifié et d'un prisme rectangulaire de conductivité variable dans un milieu hôte homogène. Bing et Greenhalgh (1999) proposent aussi un calcul numérique pour les dérivées secondes dans le cas 2.5D pour différentes configurations de mesures entre forages.

A partir de la méthode IE, une nouvelle formulation pour le calcul de la sensibilité comparable à celle développée par Park et Van (1991) est trouvée. L'avantage est qu'elle requiert seulement le calcul du champ électrique au point source. Les dérivées secondes pour le cas 3D sont évaluées en suivant le même raisonnement

que celui utilisé pour les dérivées premières.

La première partie de l'article présente le développement du système linéaire discret pour le calcul de la densité de charge. La seconde partie de l'article consiste à évaluer les coefficients de sensibilité suivant la méthode de Park et Van (1991) et la nouvelle méthode. La troisième section est consacrée à la compression matricielle pour stocker de larges matrices et pour accélérer les calculs. Une quatrième partie est dévouée au calcul du champ électrique pour permettre une mise à jour rapide des coefficients de sensibilité pendant l'inversion. Les résultats du code sont testés avec les réponses de modèles simples tels que le milieu tabulaire à deux couches et le contact vertical.

3.2 Résumé

Un programme de modélisation de résistivité électrique 3D est développé pour interpréter des données en surface et en forage. Basé sur une équation intégrale, le code calcule les densités de charge causées par les gradients de conductivité à chaque interface de la maille, permettant ainsi l'estimation du potentiel partout sans le besoin d'interpoler celui-ci entre les noeuds. La modélisation génère une matrice énorme constituée des intégrales des fonctions de Green. Cette matrice est stockée en utilisant une méthode de compression pyramidale. Le potentiel est comparé avec des solutions analytiques et des solutions numériques obtenues par un code de modélisation par différences finies pour deux modèles : le cas à deux couches et le contact vertical. La méthode intégrale est plus précise autour du point source et aux limites du domaine pour le calcul du potentiel en utilisant une configuration pôle-pôle. Une technique est proposée pour calculer les matrices de

sensibilité (le Jacobien) et Hessiennes pour les cas 3D. La sensibilité est basée sur la dérivation du potentiel électrique par rapport à un bloc de conductivité en utilisant l'équation intégrale ; elle nécessite de calculer seulement le champ électrique au point source. Une extension directe de cette technique permet de déterminer les dérivées secondes. La technique est comparée avec des solutions analytiques et avec la méthode de calcul de la sensibilité utilisant le produit scalaire des densités de courant calculées aux points source et récepteur. Les résultats sont très précis quand la fonction de Green incluant la source image est utilisée. Le calcul des trois composantes du champ électrique sur les interfaces de la maille est fait simultanément et rapidement en tirant avantage de la compression matricielle.

3.3 3D modeling and sensitivity in DC resistivity using charge density

3.3.1 Abstract

A three-dimensional (3D) electrical resistivity modeling code is developed to interpret surface and subsurface data. Based on the integral equation, it calculates the charge density caused by conductivity gradients at each interface of the mesh allowing the estimation of the potential everywhere without the need to interpolate between nodes. Modeling generates a huge matrix made of Green's functions which is stored by using the method of pyramidal compression. The potential is compared with the analytical and the numerical solutions obtained by finite differences codes for two models : the two-layer case and the vertical contact. The integral method is more accurate around the source point and at the limits of the domain for the potential calculation using a pole-pole array. A technique is proposed to calculate the sensitivity (Jacobian) and Hessian matrices in 3D. The sensitivity is based on the derivative with regards to the block conductivity of the potential computed using integral equation; it only needs to compute the electrical field at the source location. A direct extension of this technique allows the determination of the second derivatives. The technique is compared with the analytical solutions and with the calculation of the sensitivity according to the method using the inner product of the current densities calculated at the source and receiver points. Results are very accurate when the Green's function that includes the source image is used. The calculation of the three components of the electric field on the interfaces of the mesh is made simultaneously and quickly in taking advantage of matrix compression.

Key words : resistivity, 3D, integral equation, charge density, modeling, sensitivity, Jacobian and Hessian matrices, compression

Short title : 3D resistivity modeling using charge density

3.3.2 Introduction

Interpretation of electrical data when the medium is heterogeneous is usually done using either finite differences (FD) modeling (Brewitt-Taylor et Weaver, 1976; Mufti, 1978; Dey et Morrison, 1979*a*,*b*; Scriba, 1981; Mundry, 1984; Wurmstich et Morgan, 1994; Spitzer, 1995; Zhang *et al.*, 1995; Zhao et Yedlin, 1996; Spitzer et Wurmstich, 1999; Wang et Mezzatesta, 2001) or finite elements (FE) modeling (Coggon, 1971; Pridmore *et al.*, 1981; Murai et Kagawa, 1985; Sasaki, 1992, 1994; LaBrecque *et al.*, 1996, 1999; Lesur *et al.*, 1999*a*; Bing et Greenhalgh, 2001). The method by FD is the most widespread, since it is relatively simple to program compared to the FE method. Even though the integral equation (IE) method has been less used for the interpretation of DC resistivity data, many researchers have contributed to its development, Bhattacharya et Patra (1968); Pratt (1972); Raiche (1974); Hohmann (1975); Snyder (1976); Spiegel *et al.* (1980); Ting et Hohmann (1981); Wannamaker *et al.* (1984); Schulz (1985); Beasley et Ward (1986); Poirmeur et Vasseur (1988); Li et Oldenburg (1991); Xiong (1989, 1992*a*,*b*); Hvozdara et Kaikkonen (1998) just to mention a few. One of the main reasons for its limited use is that the resulting matrices to solve are large and full ; a consequence is that the 3D codes are not developed for a heterogeneous medium with arbitrary conductivity. However, one of the main advantages of the formulation compared to the FE and FD methods is that it is possible to calculate the potential at any point in the 3D space without the need of interpolating the potential computed

at the mesh nodes (Spitzer *et al.*, 1999). We present here a code that benefits of the latter advantage and extends the IE method beyond present limitation, i.e. a 3D heterogeneous medium with arbitrary conductivity. A method of calculation of charge densities for an arbitrary 3D heterogeneous medium is developed. The volume is discretized with rectangular prisms of different size in a Cartesian system. For a given distribution of conductivity, a system of linear equations is calculated. This system of linear equations, independent of the source position, enables the calculation of the potential and the current density for all the possible configurations. The calculation of the charge density is validated using analytical values found in the literature.

The same approach has been used by Snyder (1976) who presents a calculation of the charge density for a 2D domain with an infinite extension. Various integral formulations for the calculation of the electric potential when the medium consists of a prism within a homogeneous or tabular medium are found in the articles of Schulz (1985); Poirmeur et Vasseur (1988); Hvozdara et Kaikkonen (1998). Spiegel *et al.* (1980) propose a calculation of the potential using the charge density for a 2D domain with topography. Extending the development of Hohmann (1975), Beasley et Ward (1986) evaluate the potential at any point from the electric field computed in each cell. Li et Oldenburg (1991) propose a summary study on the calculation of the potential with charge density.

In the objective of developing a 3D inversion code, it is also of great importance to calculate the 3D electrical sensitivity (first derivatives or Jacobian) and the second derivatives (Hessian). Several authors have already proposed various techniques to evaluate the sensitivity coefficients. Boerner et West (1989) calculate Frechet derivatives based on the assumption of a disturbance around a value

of average conductivity. McGillivray et Oldenburg (1990) propose a comparative study for the 1D and 2D cases using pole-pole array. Sasaki (1994) shows a 3D case with a dipole-dipole array and Park et Van (1991) a 3D distribution associated with an inversion. A theoretical explanation can also be found in the article of Geselowitz (1971). Recently, Spitzer (1998*b*) made a comparative study on the various methods for the 3D sensitivity calculation. In its article, sections of sensitivity are shown for various possible configurations of sources and receivers in the case of a homogeneous medium. A comparison is made for a pole-pole array for a layered earth and a rectangular prism of variable conductivity located in a homogeneous host medium. Bing et Greenhalgh (1999) also propose a numerical calculation for the second derivatives in 2.5D for different cross-hole measurement configurations.

From the IE method, a new formulation for the calculation of the sensitivity comparable with that developed by Park et Van (1991) is found. The advantage is that it requires only the calculation of the electric field at the point source. Second derivatives in 3D are evaluated following the same reasoning as in the case of the first derivatives.

The first part of the paper presents the development of the discrete linear system for the calculation of the charge density. The second part of the paper consists in evaluating the sensitivity coefficients according to the method of Park et Van (1991) and the new method. The third section deals with matrix compression to store broad matrices and speed up the computations. A fourth part is devoted to the calculation of the electric field to allow the fast update of the sensitivity coefficients during the inversion. The results of the code are tested against responses of simple models such as the tabular medium with two layers and the vertical

contact.

3.3.3 Theory

3.3.3.1 Modeling by the calculation of the charge density

Generally, the calculation of the electric potential $V(\boldsymbol{r}, \boldsymbol{r_s})$, at the point $\boldsymbol{r}$ from a current source I located at the point $\boldsymbol{r_s}$, by the IE method for a domain made up of n bodies having each one a closed surface Γ_i, is given by Snyder (1976); Li et Oldenburg (1991) and is written

$$V(\boldsymbol{r}, \boldsymbol{r_s}) = \frac{I}{4\pi\sigma_s} G(\boldsymbol{r}, \boldsymbol{r_s}) + \frac{1}{4\pi} \sum_{i=1}^{n} \int_{\Gamma_i} \frac{\tau(\boldsymbol{r_i})}{\epsilon_0} G(\boldsymbol{r}, \boldsymbol{r_i})\, ds \tag{3.1}$$

where $\tau(\boldsymbol{r_i})$ and ϵ_0 are the charge density on the surface Γ_i and the permittivity of the vaccum, respectively. $G(\boldsymbol{r}, \boldsymbol{r_s})$ and $G(\boldsymbol{r}, \boldsymbol{r_i})$ are the Green's functions. ds is an elementary surface.

If one cuts out the domain into rectangular prisms in a Cartesian coordinates system, the charge density from equation (3.1) requires to be dissociated for the x, y and z directions. Thus for a prism of conductivity σ_{npq} six charge densities are generated $\tau^{x^-}_{n,p,q} = \tau^x(x_{n-\frac{1}{2}}, y_p, z_q; \boldsymbol{r_s})$, $\tau^{x^+}_{n,p,q} = \tau^x(x_{n+\frac{1}{2}}, y_p, z_q; \boldsymbol{r_s})$, $\tau^{y^-}_{n,p,q} = \tau^y(x_n, y_{p-\frac{1}{2}}, z_q; \boldsymbol{r_s})$, $\tau^{y^+}_{n,p,q} = \tau^y(x_n, y_{p+\frac{1}{2}}, z_q; \boldsymbol{r_s})$, $\tau^{z^-}_{n,p,q} = \tau^z(x_n, y_p, z_{q-\frac{1}{2}}; \boldsymbol{r_s})$ and $\tau^{z^+}_{n,p,q} = \tau^z(x_n, y_p, z_{q+\frac{1}{2}}; \boldsymbol{r_s})$ (see figure 3.1). However, one can sweep the whole domain with only three components $\tau^{x^-}_{n,p,q}$, $\tau^{y^-}_{n,p,q}$ et $\tau^{z^-}_{n,p,q}$, because $\tau^{x^-}_{n,p,q} \equiv \tau^{x^+}_{n-1,p,q}$, $\tau^{y^-}_{n,p,q} \equiv \tau^{y^+}_{n,p-1,q}$ and $\tau^{z^-}_{n,p,q} \equiv \tau^{z^+}_{n,p,q-1}$. The potential is expressed thus by

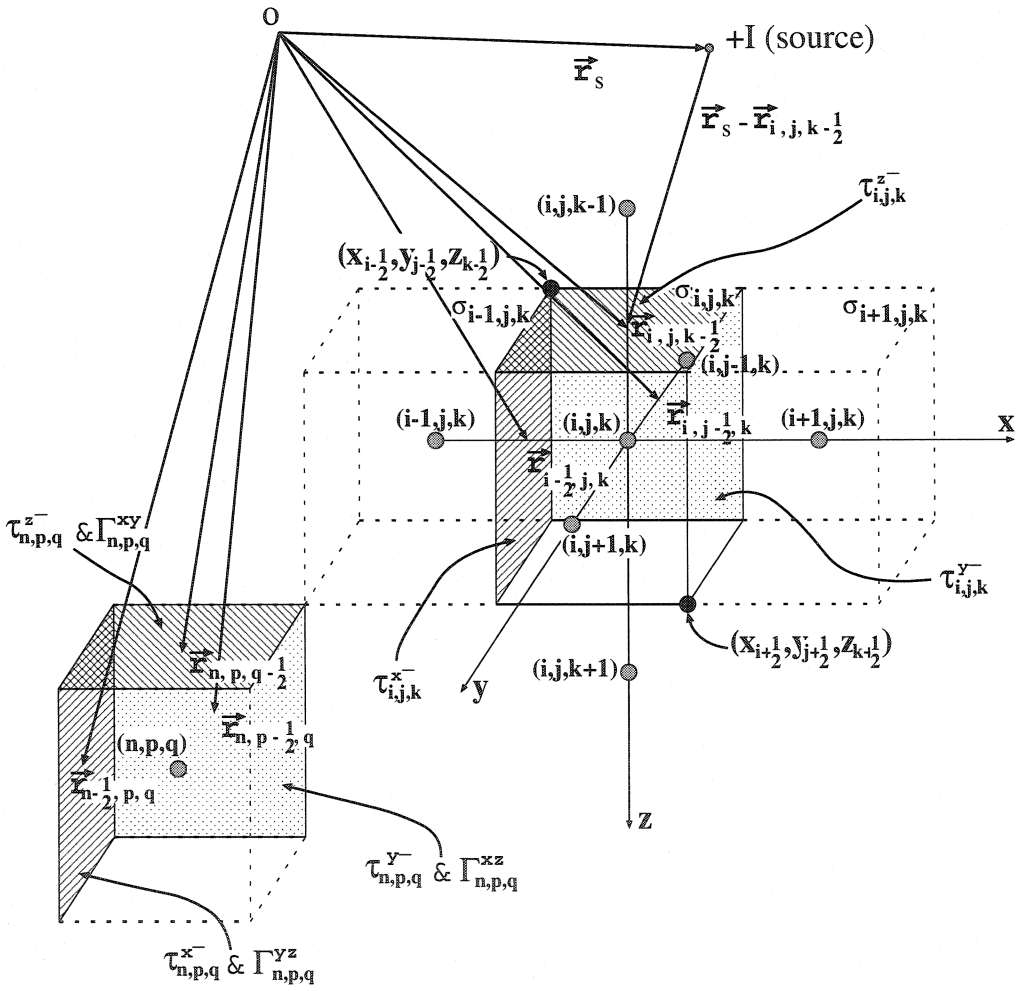

Figure 3.1: Domain discretization with 3D prisms and notation used for the calculation of the charge density.

$$
\begin{aligned}
V(\boldsymbol{r},\boldsymbol{r_s}) =& \frac{I}{4\pi\sigma_s}\, G(\boldsymbol{r},\boldsymbol{r_s}) + \frac{1}{4\pi}\sum_{n=1}^{nx}\sum_{p=1}^{ny}\sum_{q=1}^{nz}\left[\int_{\Gamma^{yz}_{n,p,q}} \frac{\tau^{x^-}_{n,p,q}}{\epsilon_0}\, G(\boldsymbol{r},\boldsymbol{r_{n-\frac{1}{2},p,q}})dy_p dz_q \right. \\
&\left. + \int_{\Gamma^{xz}_{n,p,q}} \frac{\tau^{y^-}_{n,p,q}}{\epsilon_0}\, G(\boldsymbol{r},\boldsymbol{r_{n,p-\frac{1}{2},q}})dx_n dz_q + \int_{\Gamma^{xy}_{n,p,q}} \frac{\tau^{z^-}_{n,p,q}}{\epsilon_0}\, G(\boldsymbol{r},\boldsymbol{r_{n,p,q-\frac{1}{2}}})dx_n dy_p\right] \\
=& \frac{I}{4\pi\sigma_s} G(\boldsymbol{r},\boldsymbol{r_s}) + \frac{1}{4\pi}\sum_{n=1}^{nx}\sum_{p=1}^{ny}\sum_{q=1}^{nz}\left[\frac{\tau^{x^-}_{n,p,q}}{\epsilon_0}\, J(\boldsymbol{r}, x_{n-\frac{1}{2}}) + \frac{\tau^{y^-}_{n,p,q}}{\epsilon_0}\, J(\boldsymbol{r}, y_{p-\frac{1}{2}})\right. \\
&\left. + \frac{\tau^{z^-}_{n,p,q}}{\epsilon_0}\, J(\boldsymbol{r}, z_{q-\frac{1}{2}})\right]
\end{aligned}
\tag{3.2}
$$

where nx, ny, nz are the number of cells according to the x, y and z directions respectively. Notation of the surface integrals $J(\boldsymbol{r}.)$ is given in appendix 3.4.4. The system is valid for the Green's function $G(\boldsymbol{r_i},\boldsymbol{r_j}) = \frac{1}{|\boldsymbol{r_i}-\boldsymbol{r_j}|}$ or $G(\boldsymbol{r_i},\boldsymbol{r_j}) = \frac{1}{|\boldsymbol{r_i}-\boldsymbol{r_j}|} + \frac{1}{|\boldsymbol{r_i}-\boldsymbol{r'_j}|}$ with $|\boldsymbol{r_i}-\boldsymbol{r_j}| = ((x_i-x_j)^2+(y_i-y_j)+(z_i-z_j))^{1/2}$ and $|\boldsymbol{r_i}-\boldsymbol{r'_j}| = ((x_i-x_j)^2+(y_i-y_j)+(z_i+z_j))^{1/2}$. σ_s is the conductivity of the cell where the point source is located. The charge densities are considered constant on each face of the prism. The potential calculation for different configurations is given in appendix 3.4.3. By taking the same convention as Snyder (1976); Li et Oldenburg (1991) with the normal $\boldsymbol{n}$ always directed in the positive direction of the axes, one has $\frac{\tau_{i-1}}{\epsilon_0} = \frac{\sigma_i-\sigma_{i-1}}{\sigma_{i-1}}\boldsymbol{n}\cdot\nabla V_i$ (see figure 3.2). The charge density for the three components $\tau^{x^-}_{i,j,k}$, $\tau^{y^-}_{i,j,k}$ and $\tau^{z^-}_{i,j,k}$, is

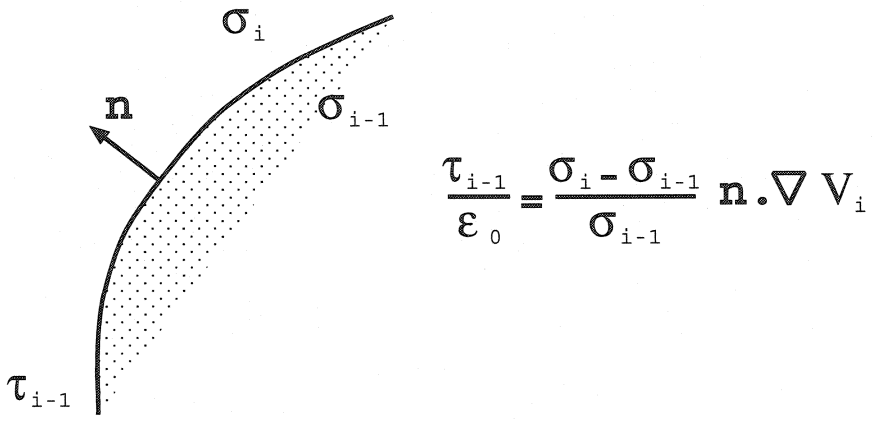

Figure 3.2: Charge density at a conductivity interface.

$$\begin{aligned}
\frac{\tau^{x^-}_{i,j,k}}{\epsilon_0} &= \frac{\sigma_{i,j,k} - \sigma_{i-1,j,k}}{\sigma_{i-1,j,k}}\ \partial_x V_i(\boldsymbol{r_{i-\frac{1}{2},j,k}}, \boldsymbol{r_s}) \\
\frac{\tau^{y^-}_{i,j,k}}{\epsilon_0} &= \frac{\sigma_{i,j,k} - \sigma_{i,j-1,k}}{\sigma_{i,j-1,k}}\ \partial_y V_j(\boldsymbol{r_{i,j-\frac{1}{2},k}}, \boldsymbol{r_s}) \\
\frac{\tau^{z^-}_{i,j,k}}{\epsilon_0} &= \frac{\sigma_{i,j,k} - \sigma_{i,j,k-1}}{\sigma_{i,j,k-1}}\ \partial_z V_k(\boldsymbol{r_{i,j,k-\frac{1}{2}}}, \boldsymbol{r_s})
\end{aligned} \tag{3.3}$$

where $\partial_x V_i$, $\partial_y V_j$ and $\partial_z V_k$ indicate the gradient of the potential in the cell of conductivity $\sigma_{i,j,k}$ for the x, y and z directions respectively. Two cases explaining the charge polarity on several interfaces are presented in figure 3.3, without taking into account the interactions between the various interfaces. For the charge density $\tau^{x^-}_{i,j,k}$ for example, there is a singular point when the indices $n = i$, $p = j$ and $q = k$. Snyder (1976); Li et Oldenburg (1991) showed that the limit of $\int_{\Gamma^{yz}_{n,p,q}} \frac{\tau^{x^-}_{i,j,k}}{\epsilon_0} \partial_x G(\boldsymbol{r_{i-\frac{1}{2},j,k}}, \boldsymbol{r_{n-\frac{1}{2},p,q}}) dy_p dz_q$ when $\Gamma^{yz}_{n,p,q}$ tends towards 0 is $-2\pi \frac{\tau^{x^-}_{i,j,k}}{\epsilon_0}$ (see appendix 3.4.4). Having solved the problem of singularity, one can include the integral on the diagonal of the linear system below. In fact, the integral $J^a_x(\boldsymbol{r_{i-\frac{1}{2},j,k}}, x_{i-\frac{1}{2}})$ is equal to -2π when $G(\boldsymbol{r_i}, \boldsymbol{r_j}) = \frac{1}{|\boldsymbol{r_i} - \boldsymbol{r_j}|}$ and differs from -2π

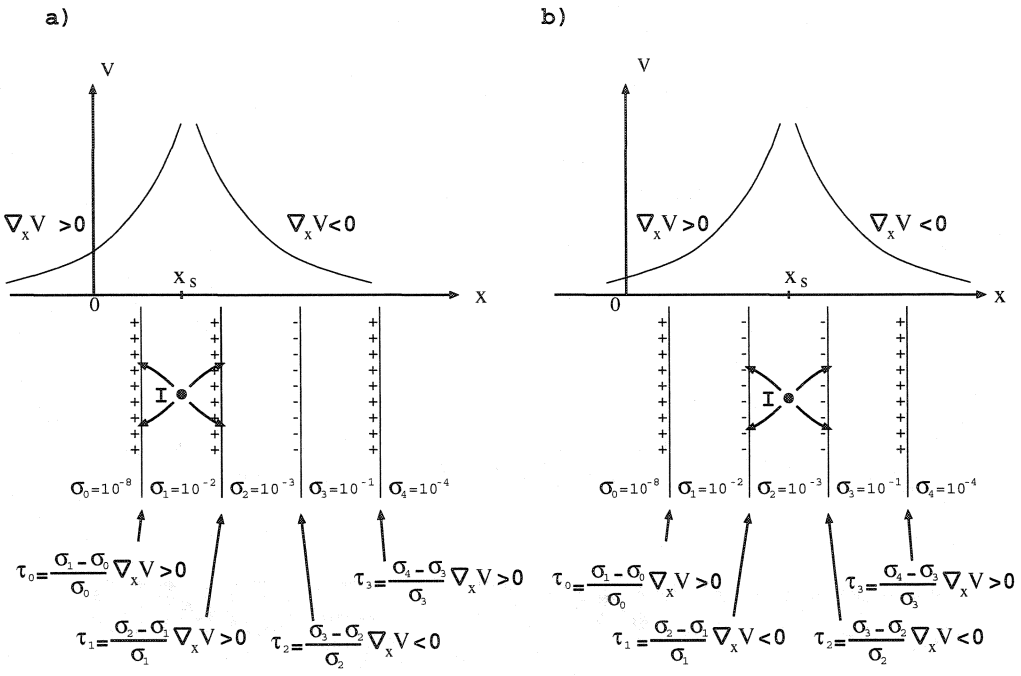

Figure 3.3: Sign of the charge density at the interfaces of a medium made up of parallel vertical slabs. a) the source is located in the medium of conductivity σ_1 and b) the source is located in the medium of conductivity σ_2 ($[\sigma_0, \sigma_1, \sigma_2, \sigma_3, \sigma_4] = [10^{-8}, 10^{-2}, 10^{-3}, 10^{-1}, 10^{-4}]\ S/m$). The electric potential V decreases around the point source I. When the current flows from a conducting medium (C) to a resistive medium(R), charges are positive at the interface (in summary : charge + : $C \rightarrow R$ and charge - : $R \rightarrow C$).

while taking $G(\boldsymbol{r_i}, \boldsymbol{r_j}) = \frac{1}{|r_i - r_j|} + \frac{1}{|r_i - r_j'|}$. Using the notations of appendix 3.4.4 and replacing (3.2) into (3.3), the following system of equations can be set up

$$
\begin{aligned}
&\left[1-\hbar_{i,j,k}^{x^-}[2\pi+J_x^a(\boldsymbol{r_{i-\frac{1}{2},j,k}},x_{i-\frac{1}{2}})]\right]\frac{\tau_{i,j,k}^{x^-}}{\epsilon_0}\\
-\hbar_{i,j,k}^{x^-}&\left[\sum_{n=1,n\neq i}^{nx}\sum_{p=1,p\neq j}^{ny}\sum_{q=1,q\neq k}^{nz}J_x^a(\boldsymbol{r_{i-\frac{1}{2},j,k}},x_{n-\frac{1}{2}})\frac{\tau_{n,p,q}^{x^-}}{\epsilon_0}\right.\\
&+\sum_{n=1}^{nx}\sum_{p=1}^{ny}\sum_{q=1}^{nz}J_x^a(\boldsymbol{r_{i-\frac{1}{2},j,k}},y_{p-\frac{1}{2}})\frac{\tau_{n,p,q}^{y^-}}{\epsilon_0}\\
&\left.+\sum_{n=1}^{nx}\sum_{p=1}^{ny}\sum_{q=1}^{nz}J_x^a(\boldsymbol{r_{i-\frac{1}{2},j,k}},z_{q-\frac{1}{2}})\frac{\tau_{n,p,q}^{z^-}}{\epsilon_0}\right]=\frac{I\hbar_{i,j,k}^{x^-}}{\sigma_s}\partial_x G(\boldsymbol{r_{i-\frac{1}{2},j,k}},\boldsymbol{r_s})\\
&\left[1-\hbar_{i,j,k}^{y^-}[2\pi+J_y^a(\boldsymbol{r_{i,j-\frac{1}{2},k}},y_{j-\frac{1}{2}})]\right]\frac{\tau_{i,j,k}^{y^-}}{\epsilon_0}\\
-\hbar_{i,j,k}^{y^-}&\left[\sum_{n=1}^{nx}\sum_{p=1}^{ny}\sum_{q=1}^{nz}J_y^a(\boldsymbol{r_{i,j-\frac{1}{2},k}},x_{n-\frac{1}{2}})\frac{\tau_{n,p,q}^{x^-}}{\epsilon_0}\right.\\
+\sum_{n=1,n\neq i}^{nx}&\sum_{p=1,p\neq j}^{ny}\sum_{q=1,q\neq k}^{nz}J_y^a(\boldsymbol{r_{i,j-\frac{1}{2},k}},y_{p-\frac{1}{2}})\frac{\tau_{n,p,q}^{y^-}}{\epsilon_0}\\
&\left.+\sum_{n=1}^{nx}\sum_{p=1}^{ny}\sum_{q=1}^{nz}J_y^a(\boldsymbol{r_{i,j-\frac{1}{2},k}},z_{q-\frac{1}{2}})\frac{\tau_{n,p,q}^{z^-}}{\epsilon_0}\right]=\frac{I\hbar_{i,j,k}^{y^-}}{\sigma_s}\partial_y G(\boldsymbol{r_{i,j-\frac{1}{2},k}},\boldsymbol{r_s})\\
&\left[1-\hbar_{i,j,k}^{z^-}(2\pi+J_z^a(\boldsymbol{r_{i,j,k-\frac{1}{2}}},z_{k-\frac{1}{2}})]\right]\frac{\tau_{i,j,k}^{z^-}}{\epsilon_0}\\
-\hbar_{i,j,k}^{z^-}&\left[\sum_{n=1}^{nx}\sum_{p=1}^{ny}\sum_{q=1}^{nz}J_z^a(\boldsymbol{r_{i,j,k-\frac{1}{2}}},x_{n-\frac{1}{2}})\frac{\tau_{n,p,q}^{x^-}}{\epsilon_0}\right.\\
&+\sum_{n=1}^{nx}\sum_{p=1}^{ny}\sum_{q=1}^{nz}J_z^a(\boldsymbol{r_{i,j,k-\frac{1}{2}}},y_{p-\frac{1}{2}})\frac{\tau_{n,p,q}^{y^-}}{\epsilon_0}\\
+\sum_{n=1,n\neq i}^{nx}&\sum_{p=1,p\neq j}^{ny}\sum_{q=1,q\neq k}^{nz}\left.J_z^a(\boldsymbol{r_{i,j,k-\frac{1}{2}}},z_{q-\frac{1}{2}})\frac{\tau_{n,p,q}^{z^-}}{\epsilon_0}\right]=\frac{I\hbar_{i,j,k}^{z^-}}{\sigma_s}\partial_z G(\boldsymbol{r_{i,j,k-\frac{1}{2}}},\boldsymbol{r_s})
\end{aligned}
\tag{3.4}
$$

where $\hbar_{i,j,k}^{x^-}=\frac{1}{2\pi}\frac{\sigma_{i,j,k}-\sigma_{i-1,j,k}}{\sigma_{i,j,k}+\sigma_{i-1,j,k}}$, $\hbar_{i,j,k}^{y^-}=\frac{1}{2\pi}\frac{\sigma_{i,j,k}-\sigma_{i,j-1,k}}{\sigma_{i,j,k}+\sigma_{i,j-1,k}}$ and $\hbar_{i,j,k}^{z^-}=\frac{1}{2\pi}\frac{\sigma_{i,j,k}-\sigma_{i,j,k-1}}{\sigma_{i,j,k}+\sigma_{i,j,k-1}}$ and

indices $i = [1, nx]$, $j = [1, ny]$ et $k = [1, nz]$. A proof is given for the validity of all the integrals when they are calculated outwards, on and inside the boundary of the prism in appendix 3.4.4. For boundary conditions, we have $\tau^{x^-}_{1,j,k} = 0$ and $\hbar^{x^-}_{1,j,k} = 0$ $(\forall\ j, k)$ and $\tau^{y^-}_{i,1,k} = 0$ and $\hbar^{y^-}_{i,1,k} = 0$ $(\forall\ i, k)$.

The equation (3.4) defines a system of linear equations $\boldsymbol{Ax = b}$ which can be broken up into $\boldsymbol{A = I + kD}$ where $\boldsymbol{I}$, $\boldsymbol{k}$ and $\boldsymbol{D}$ are respectively the identity matrix, the diagonal matrix whose elements are the coefficients $\hbar^{x^-}_{i,j,k}$, $\hbar^{y^-}_{i,j,k}$, $\hbar^{z^-}_{i,j,k}$, and the matrix containing the negative values of the surface integrals $J^a_x(\boldsymbol{r}, .)$, $J^a_y(\boldsymbol{r}, .)$ and $J^a_z(\boldsymbol{r}, .)$ except for $\pm 2\pi$. $\boldsymbol{x}$ and $\boldsymbol{b}$ are respectively the charge density $\frac{\tau^{x^-}_{i,j,k}}{\epsilon_0}$, $\frac{\tau^{y^-}_{i,j,k}}{\epsilon_0}$, $\frac{\tau^{z^-}_{i,j,k}}{\epsilon_0}$ and the terms $\frac{I\hbar^{x^-}_{i,j,k}}{\sigma_s}\partial_x G(\boldsymbol{r_{i-\frac{1}{2},j,k}}, \boldsymbol{r_s})$, $\frac{I\hbar^{y^-}_{i,j,k}}{\sigma_s}\partial_y G(\boldsymbol{r_{i,j-\frac{1}{2},k}}, \boldsymbol{r_s})$, $\frac{I\hbar^{z^-}_{i,j,k}}{\sigma_s}\partial_z G(\boldsymbol{r_{i,j,k-\frac{1}{2}}}, \boldsymbol{r_s})$. Since only the source term $\boldsymbol{b}$ changes in the system, we avoid calculating $\boldsymbol{D}$ and thus the integrals $J^a_x(r, .)$, $J^a_y(r, .)$ and $J^a_z(r, .)$ again, for the same conductivity domain. An apparent chargeability described in the article of Seigel (1959) can also be calculated by updating only the matrix $\boldsymbol{k}$ and the vector $\boldsymbol{b}$. As the matrix $\boldsymbol{A}$ is not symmetrical, the system $\boldsymbol{A^T Ax = A^T b}$ is initially solved with a conjugate gradient (Hestenes et Stiefel, 1952; Golub et Van Loan, 1996) to draw advantage from the structure of the matrix $\boldsymbol{A}$ $(dim(\boldsymbol{A}) = (3 * nx * ny * nz)^2)$.

To validate the calculation of the charge density, a two-layer model consisting of a layer thickness $h = 4m$ and conductivity $\sigma_1 = 0.001\ S/m$, and of an infinite medium of conductivity $\sigma_2 = 0.1\ S/m$ is chosen (see figure 3.4). The calculation of the charge density is validated with the following solution developed by Li et Oldenburg (1991)

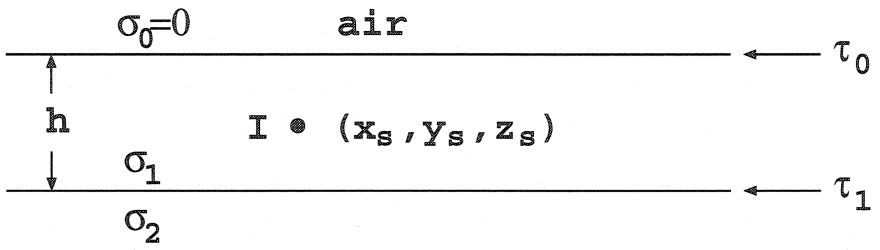

Figure 3.4: Layered model made up of a layer of thickness h and conductivity σ_1, and an infinite medium of conductivity σ_2. Source I is located in the medium of conductivity σ_1.

$$\begin{aligned}
\frac{\tau_0(\eta)}{\epsilon_0} &= \frac{I}{2\pi\sigma_1}\left[\frac{d}{(\eta^2+d^2)^{3/2}} + \sum_{n=1}^{\infty} k_1^n \left(\frac{2nh-d}{(\eta^2+(2nh-d)^2)^{3/2}}\right.\right. \\
&\quad \left.\left. + \frac{2nh+d}{(\eta^2+(2nh+d)^2)^{3/2}}\right)\right] \\
\frac{\tau_1(\eta)}{\epsilon_0} &= \frac{I}{2\pi\sigma_1}\left[k_1\frac{(h-d)}{(\eta^2+(h-d)^2)^{3/2}} + \sum_{n=1}^{\infty} k_1^n \left(\frac{2nh-(h-d)}{(\eta^2+(2nh-(h-d))^2)^{3/2}}\right.\right. \\
&\quad \left.\left. + k_1\frac{2nh+(h-d)}{(\eta^2+(2nh+(h-d))^2)^{3/2}}\right)\right]
\end{aligned} \tag{3.5}$$

with $k_1 = \frac{\sigma_1-\sigma_2}{\sigma_1+\sigma_2}$ and $\eta = ((x-x_s)^2+(y-y_s)^2)^{1/2}$. The numerical and analytical values of charge density at the interfaces of the tabular medium are compared on figure 3.5. The calculated charge density is practically identical. The charge density is positive on the surface and negative at the interface $\sigma_1 - \sigma_2$. When the source is exactly at the surface ($z_s = 0$), the charge density is a Dirac function (see Li et Oldenburg (1991)). The calculation of the charge density with the Green's function $G(\boldsymbol{r_i}, \boldsymbol{r_j}) = \frac{1}{|\boldsymbol{r_i}-\boldsymbol{r_j}|}$ thus causes a numerical problem which should be intercepted to avoid the singularity. However, one will see further in the tests, that the Green's function $G(\boldsymbol{r_i}, \boldsymbol{r_j}) = \frac{1}{|\boldsymbol{r_i}-\boldsymbol{r_j}|} + \frac{1}{|\boldsymbol{r_i}-\boldsymbol{r'_j}|}$ has a more stable behavior for the calculation

of the potential and the sensitivity, since the $\boldsymbol{b}$ term of the system $\boldsymbol{Ax} = \boldsymbol{b}$ is not singular for $\boldsymbol{r_i} = \boldsymbol{r_j}$.

3.3.3.2 Calculation of the sensitivity coefficient

Calculation of the sensitivity by the method of Park et Van (1991)

The sensitivity of the potential at the receiver due to the change of resistivity of a cell is given by the scalar product of the current density $\boldsymbol{j}_s$ of a point source at the transmitter and current density $\boldsymbol{j}_r$ of a fictitious source point at the receiver, integrated on the disturbed volume v.

$$\frac{\partial V}{\partial \rho} = \frac{1}{I} \int_v dv \; \boldsymbol{j}_s \cdot \boldsymbol{j}_r \tag{3.6}$$

From the bilinear equation described by Lanczos (1961), Park et Van (1991) give an unambiguous demonstration of (3.6).

Sensitivity for a homogeneous medium

The current density is evaluated by calculating the gradient of the homogeneous potential $V = \frac{I}{4\pi\sigma_s} G(\boldsymbol{r_{i,j,k}}, \boldsymbol{r_{s_u}})$ at the transmitter and the receiver locations with $G(\boldsymbol{r_{i,j,k}}, \boldsymbol{r_{s_u}}) = \frac{1}{|\boldsymbol{r_{i,j,k}} - \boldsymbol{r_{s_u}}|} + \frac{1}{|\boldsymbol{r_{i,j,k}} - \boldsymbol{r'_{s_u}}|}$. The coordinates of the source s_u, the receiver r_w and the center of the disturbed prism are noted as $(x_{s_u}, y_{s_u}, z_{s_u})$, $(x_{r_w}, y_{r_w}, z_{r_w})$ and (x_i, y_j, z_k) respectively. The indices i, j, k locate the cell according to the x, y and z directions respectively. The indices u and w take values 1 (polar case) and 2 (dipolar case). The equation (3.6) for $\frac{\partial V}{\partial \rho}$ has dimensions $[\frac{1}{A}][\frac{1}{\Omega.M}]^2[\frac{V}{M}]^2[M^3] = [\frac{A}{M}]$. The product of the sensitivity coefficient multiplied by the resistivity gives Volts ($[V] = [A][\Omega]$). By taking the notation "p " for pole and "d " for dipole, the

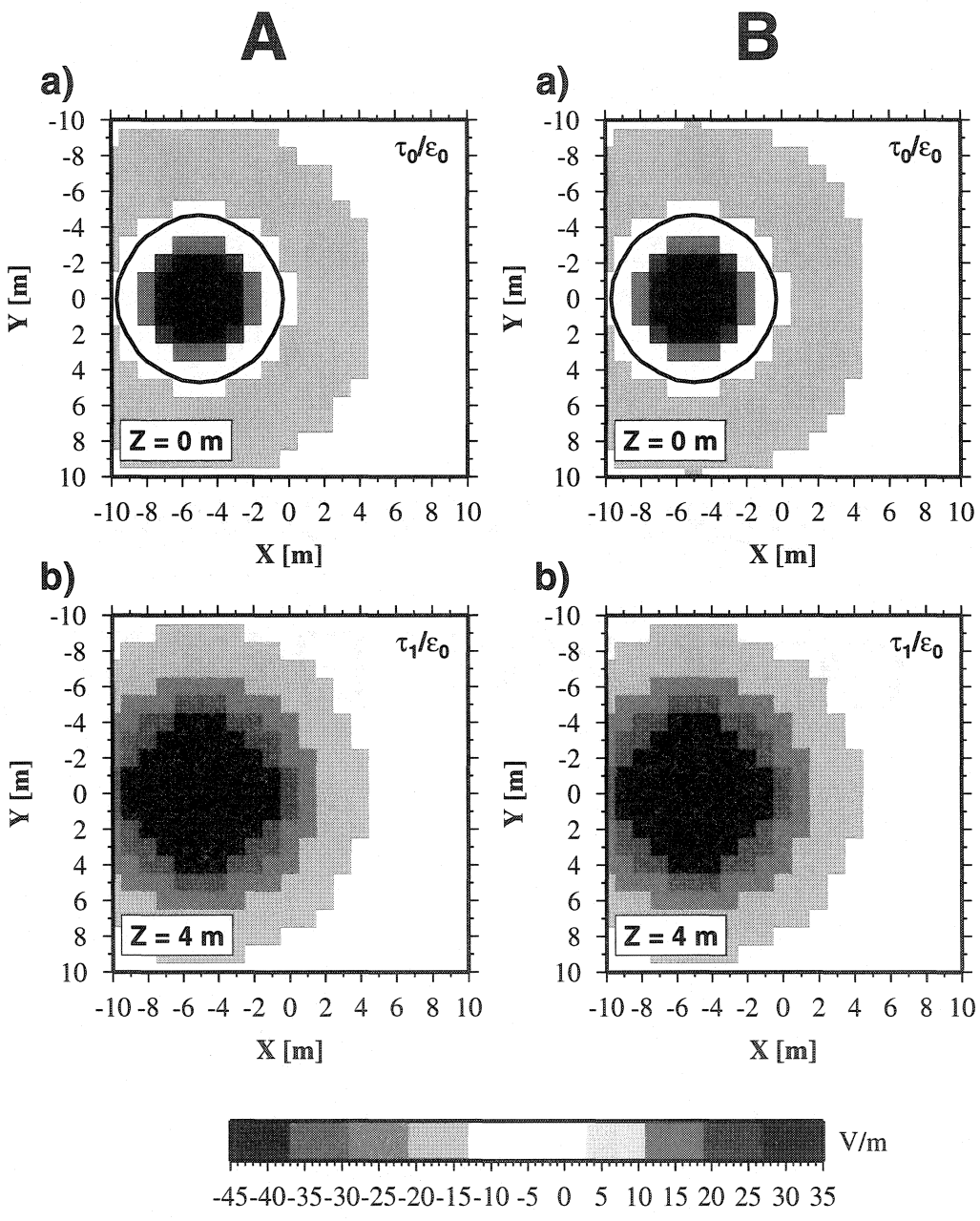

Figure 3.5: Charge density for the two-layer case with the top layer of $4\ m$ thickness and conductivity $0.0001\ S/m$, and a lower half space of $0.1\ S/m$ (see equation 3.5). A) Analytical normalized charge density. B) Numerical normalized charge density. The figures a) and b) correspond to $\frac{\tau_0}{\epsilon_0}$ and $\frac{\tau_1}{\epsilon_0}$. The black contour indicates zero value. The source is located at $(x_s, y_s, z_s) = (-5, 0, 2)\ m$.

coefficients of sensitivity are calculated according to

$$\begin{aligned}
\frac{\partial V_{p-p}}{\partial \rho} &= \frac{1}{I}\int_v dv\ \boldsymbol{j}_{s_1}\cdot\boldsymbol{j}_{r_1} \\
\frac{\partial V_{d-p}}{\partial \rho} &= \frac{1}{I}\int_v dv\ (\boldsymbol{j}_{s_1}-\boldsymbol{j}_{s_2})\cdot\boldsymbol{j}_{r_1} \\
\frac{\partial V_{p-d}}{\partial \rho} &= \frac{1}{I}\int_v dv\ \boldsymbol{j}_{s_1}\cdot(\boldsymbol{j}_{r_1}-\boldsymbol{j}_{r_2}) \\
\frac{\partial V_{d-d}}{\partial \rho} &= \frac{1}{I}\int_v dv\ (\boldsymbol{j}_{s_1}-\boldsymbol{j}_{s_2})\cdot(\boldsymbol{j}_{r_1}-\boldsymbol{j}_{r_2})
\end{aligned} \tag{3.7}$$

The current density is expressed for a homogeneous medium in a cell of coordinates (x_i, y_j, z_k) according to

$$\boldsymbol{j}_{s_u} = \begin{cases} j_{x_{s_u}} &= -\frac{I}{4\pi}\partial_{x_i}\ G(\boldsymbol{r_{i,j,k}}, \boldsymbol{r_{s_u}}) \\ j_{y_{s_u}} &= -\frac{I}{4\pi}\partial_{y_j}\ G(\boldsymbol{r_{i,j,k}}, \boldsymbol{r_{s_u}}) \\ j_{z_{s_u}} &= -\frac{I}{4\pi}\partial_{z_k}\ G(\boldsymbol{r_{i,j,k}}, \boldsymbol{r_{s_u}}) \end{cases} \tag{3.8}$$

For the receiver point, s is replaced by r and u by w obtaining the current density. The explicit result for any array with four electrodes in the case of a homogeneous medium is given in appendix 3.4.5. To obtain $\frac{\partial \rho_a}{\partial \rho}$, it is enough to take into account the geometrical factor K and the value of the current I at the point source, that is to say $\frac{\partial \rho_a}{\partial \rho} = \frac{K}{I_s}\ \frac{\partial V}{\partial \rho}$.

Calculation of the current density using the charge density

The current density calculated in the center of the cell (i, j, k) of conductivity $\sigma_{i,j,k}$ is $\boldsymbol{j_s}(\boldsymbol{r_{i,j,k}}, \boldsymbol{r_s}) = \sigma_{i,j,k}\boldsymbol{E(r_{i,j,k}, r_s)}$. Three components of the electric field $\boldsymbol{E(r_{i,j,k}, r_s)} = -\boldsymbol{\nabla V(r_{i,j,k}, r_s)}$ calculated in the center of the cell (i, j, k) are expressed according to

$$
\begin{aligned}
E_x(\boldsymbol{r_{i,j,k}}, \boldsymbol{r_s}) = &-\frac{1}{4\pi}\Big[\frac{I}{\sigma_s}\partial_x G(\boldsymbol{r_{i,j,k}}, \boldsymbol{r_s}) + \sum_{n=1}^{nx}\sum_{p=1}^{ny}\sum_{q=1}^{nz}\Big[\frac{\tau^{x^-}_{n,p,q}}{\epsilon_0} J^a_x(\boldsymbol{r_{i,j,k}}, x_{n-\frac{1}{2}}) \\
&+ \frac{\tau^{y^-}_{n,p,q}}{\epsilon_0} J^a_x(\boldsymbol{r_{i,j,k}}, y_{p-\frac{1}{2}}) + \frac{\tau^{z^-}_{n,p,q}}{\epsilon_0} J^a_x(\boldsymbol{r_{i,j,k}}, z_{q-\frac{1}{2}})\Big]\Big] \\
E_y(\boldsymbol{r_{i,j,k}}, \boldsymbol{r_s}) = &-\frac{1}{4\pi}\Big[\frac{I}{\sigma_s}\partial_y G(\boldsymbol{r_{i,j,k}}, \boldsymbol{r_s}) + \sum_{n=1}^{nx}\sum_{p=1}^{ny}\sum_{q=1}^{nz}\Big[\frac{\tau^{x^-}_{n,p,q}}{\epsilon_0} J^a_y(\boldsymbol{r_{i,j,k}}, x_{n-\frac{1}{2}}) \\
&+ \frac{\tau^{y^-}_{n,p,q}}{\epsilon_0} J^a_y(\boldsymbol{r_{i,j,k}}, y_{p-\frac{1}{2}}) + \frac{\tau^{z^-}_{n,p,q}}{\epsilon_0} J^a_y(\boldsymbol{r_{i,j,k}}, z_{q-\frac{1}{2}})\Big]\Big] \\
E_z(\boldsymbol{r_{i,j,k}}, \boldsymbol{r_s}) = &-\frac{1}{4\pi}\Big[\frac{I}{\sigma_s}\partial_z G(\boldsymbol{r_{i,j,k}}, \boldsymbol{r_s}) + \sum_{n=1}^{nx}\sum_{p=1}^{ny}\sum_{q=1}^{nz}\Big[\frac{\tau^{x^-}_{n,p,q}}{\epsilon_0} J^a_z(\boldsymbol{r_{i,j,k}}, x_{n-\frac{1}{2}}) \\
&+ \frac{\tau^{y^-}_{n,p,q}}{\epsilon_0} J^a_z(\boldsymbol{r_{i,j,k}}, y_{p-\frac{1}{2}}) + \frac{\tau^{z^-}_{n,p,q}}{\epsilon_0} J^a_z(\boldsymbol{r_{i,j,k}}, z_{q-\frac{1}{2}})\Big]\Big]
\end{aligned}
\tag{3.9}
$$

By multiplying equation (3.9) by conductivity $\sigma_{i,j,k}$, the current density can be broken up into a primary term $j^P_x(\boldsymbol{r_{i,j,k}}, \boldsymbol{r_s})$ and a secondary term $j^S_x(\boldsymbol{r_{i,j,k}}, \boldsymbol{r_s})$. The component $j_x(\boldsymbol{r_{i,j,k}}, \boldsymbol{r_s}) = j^P_x(\boldsymbol{r_{i,j,k}}, \boldsymbol{r_s}) + j^S_x(\boldsymbol{r_{i,j,k}}, \boldsymbol{r_s})$ is written

$$
\begin{aligned}
j_x(\boldsymbol{r_{i,j,k}}, \boldsymbol{r_s}) = &-\frac{I}{4\pi}\partial_x G(\boldsymbol{r_{i,j,k}}, \boldsymbol{r_s}) - \frac{1}{4\pi}\Big[\frac{I(\sigma_{i,j,k} - \sigma_s)}{\sigma_s}\partial_x G(\boldsymbol{r_{i,j,k}}, \boldsymbol{r_s}) + \sigma_{i,j,k}\sum_{n=1}^{nx}\sum_{p=1}^{ny} \\
&\sum_{q=1}^{nz}\Big[\frac{\tau^{x^-}_{n,p,q}}{\epsilon_0} J^a_x(\boldsymbol{r_{i,j,k}}, x_{n-\frac{1}{2}}) + \frac{\tau^{y^-}_{n,p,q}}{\epsilon_0} J^a_x(\boldsymbol{r_{i,j,k}}, y_{p-\frac{1}{2}}) + \frac{\tau^{z^-}_{n,p,q}}{\epsilon_0} J^a_x(\boldsymbol{r_{i,j,k}}, z_{q-\frac{1}{2}})\Big]\Big]
\end{aligned}
\tag{3.10}
$$

The current density $\boldsymbol{j_r}$ for a fictitious source located at the point (x_r, y_r, z_r) (r for receiver) is written in the same manner by replacing s by r. The sensitivity coefficient for a heterogeneous medium at the point (i, j, k) and for a pole-pole array with a transmitting point located in (x_s, y_s, z_s) and a receiving point located in (x_r, y_r, z_r), is written

$$\frac{\partial V(\boldsymbol{r_r}, \boldsymbol{r_s})}{\partial \rho_{i,j,k}} = \frac{1}{I} \int_v dv \, [\boldsymbol{j}^P(\boldsymbol{r_{i,j,k}}, \boldsymbol{r_s}) + \boldsymbol{j}^S(\boldsymbol{r_{i,j,k}}, \boldsymbol{r_s})] \cdot [\boldsymbol{j}^P(\boldsymbol{r_{i,j,k}}, \boldsymbol{r_r}) + \boldsymbol{j}^S(\boldsymbol{r_{i,j,k}}, \boldsymbol{r_r})] \quad (3.11)$$

Calculation of the sensitivity using the IE

To calculate the sensitivity, it is proposed to take the derivative of equation (3.2) with regards to conductivity $\sigma_{i,j,k}$ of the block (i, j, k) located at (x_i, y_j, z_k) for a pole-pole array with a transmitting point located at (x_s, y_s, z_s) and a receiving point located at (x_r, y_r, z_r). To simplify the writing, the elements of surface $dy_p dz_q$, $dx_n dz_q$ and $dx_n dy_p$ are all associated to ds.

$$\begin{aligned}
\frac{\partial V(\boldsymbol{r_r}, \boldsymbol{r_s})}{\partial \sigma_{i,j,k}} = \frac{1}{4\pi} \Bigg[& \int_{\Gamma^{yz}_{i,j,k}} ds \; G(\boldsymbol{r_{i-\frac{1}{2},j,k}}, \boldsymbol{r_r}) \frac{\partial}{\partial \sigma_{i,j,k}} \left[\frac{\tau^{x^-}_{i,j,k}}{\epsilon_0} \right] \\
& + \int_{\Gamma^{yz}_{i,j,k}} ds \; G(\boldsymbol{r_{i+\frac{1}{2},j,k}}, \boldsymbol{r_r}) \frac{\partial}{\partial \sigma_{i,j,k}} \left[\frac{\tau^{x^+}_{i,j,k}}{\epsilon_0} \right] \\
& + \int_{\Gamma^{xz}_{i,j,k}} ds \; G(\boldsymbol{r_{i,j-\frac{1}{2},k}}, \boldsymbol{r_r}) \frac{\partial}{\partial \sigma_{i,j,k}} \left[\frac{\tau^{y^-}_{i,j,k}}{\epsilon_0} \right] \\
& + \int_{\Gamma^{xz}_{i,j,k}} ds \; G(\boldsymbol{r_{i,j+\frac{1}{2},k}}, \boldsymbol{r_r}) \frac{\partial}{\partial \sigma_{i,j,k}} \left[\frac{\tau^{y^+}_{i,j,k}}{\epsilon_0} \right] \\
& + \int_{\Gamma^{xy}_{i,j,k}} ds \; G(\boldsymbol{r_{i,j,k-\frac{1}{2}}}, \boldsymbol{r_r}) \frac{\partial}{\partial \sigma_{i,j,k}} \left[\frac{\tau^{z^-}_{i,j,k}}{\epsilon_0} \right] \\
& + \int_{\Gamma^{xy}_{i,j,k}} ds \; G(\boldsymbol{r_{i,j,k+\frac{1}{2}}}, \boldsymbol{r_r}) \frac{\partial}{\partial \sigma_{i,j,k}} \left[\frac{\tau^{z^+}_{i,j,k}}{\epsilon_0} \right] \Bigg] \\
& - \frac{I}{4\pi\sigma_s^2} G(\boldsymbol{r_s}, \boldsymbol{r_r}) \; \delta(x_i - x_s)\delta(y_j - y_s)\delta(z_k - z_s)
\end{aligned} \quad (3.12)$$

The boundary conditions for the x direction, with the normal $\boldsymbol{n}$ directed out-

wards of the cell (i, j, k) (see figure 3.2), are

$$\begin{aligned} \frac{\tau^{x^-}_{i,j,k}}{\epsilon_0} &= \frac{\sigma_{i-1,j,k} - \sigma_{i,j,k}}{\sigma_{i,j,k}}\, \boldsymbol{n}\cdot\hat{\boldsymbol{x}}\; \partial_x V_{i-1}(\boldsymbol{r}_{\boldsymbol{i-\frac{1}{2},j,k}}, \boldsymbol{r}_{\boldsymbol{s}}) \\ \frac{\tau^{x^+}_{i,j,k}}{\epsilon_0} &= \frac{\sigma_{i+1,j,k} - \sigma_{i,j,k}}{\sigma_{i,j,k}}\, \boldsymbol{n}\cdot\hat{\boldsymbol{x}}\; \partial_x V_{i+1}(\boldsymbol{r}_{\boldsymbol{i+\frac{1}{2},j,k}}, \boldsymbol{r}_{\boldsymbol{s}}) \end{aligned} \tag{3.13}$$

$\hat{\boldsymbol{x}}$ correspond to a unit vector in x direction. From equation (3.13), the partial derivatives with regards to conductivity $\sigma_{i,j,k}$ are calculated. By using the following relations $\sigma_{i-1,j,k}\, \boldsymbol{n}\cdot\hat{\boldsymbol{x}}\; \partial_x V_{i-1}(\boldsymbol{r}_{\boldsymbol{i-\frac{1}{2},j,k}}, \boldsymbol{r}_{\boldsymbol{s}}) = \sigma_{i,j,k}\, \boldsymbol{n}\cdot\hat{\boldsymbol{x}}\; \partial_x V_i(\boldsymbol{r}_{\boldsymbol{i-\frac{1}{2},j,k}}, \boldsymbol{r}_{\boldsymbol{s}})$ and $\sigma_{i+1,j,k}\, \boldsymbol{n}\cdot\hat{\boldsymbol{x}}\; \partial_x V_{i+1}(\boldsymbol{r}_{\boldsymbol{i+\frac{1}{2},j,k}}, \boldsymbol{r}_{\boldsymbol{s}}) = \sigma_{i,j,k}\, \boldsymbol{n}\cdot\hat{\boldsymbol{x}}\; \partial_x V_i(\boldsymbol{r}_{\boldsymbol{i+\frac{1}{2},j,k}}, \boldsymbol{r}_{\boldsymbol{s}})$ and the previously calculated partial derivatives, we write

$$\begin{aligned} \frac{\partial}{\partial\sigma_{i,j,k}}\left[\frac{\tau^{x^-}_{i,j,k}}{\epsilon_0}\right] &= -\frac{1}{\sigma_{i,j,k}}\, \boldsymbol{n}\cdot\hat{\boldsymbol{x}}\; \partial_x V_i(\boldsymbol{r}_{\boldsymbol{i-\frac{1}{2},j,k}}, \boldsymbol{r}_{\boldsymbol{s}}) \\ \frac{\partial}{\partial\sigma_{i,j,k}}\left[\frac{\tau^{x^+}_{i,j,k}}{\epsilon_0}\right] &= -\frac{1}{\sigma_{i,j,k}}\, \boldsymbol{n}\cdot\hat{\boldsymbol{x}}\; \partial_x V_i(\boldsymbol{r}_{\boldsymbol{i+\frac{1}{2},j,k}}, \boldsymbol{r}_{\boldsymbol{s}}) \end{aligned} \tag{3.14}$$

By replacing $ds\, \boldsymbol{n}$ by $\boldsymbol{ds}$ and by introducing equation (3.14) into (3.12), we find

$$\begin{aligned}\frac{\partial V(\boldsymbol{r_r},\boldsymbol{r_s})}{\partial \sigma_{i,j,k}} = \frac{-1}{4\pi\sigma_{i,j,k}}\Bigg[&\int_{\Gamma^{yz}_{i,j,k}} G(\boldsymbol{r_{i-\frac{1}{2},j,k}},\boldsymbol{r_r})\ \partial_x V_i(\boldsymbol{r_{i-\frac{1}{2},j,k}},\boldsymbol{r_s})\ \hat{\boldsymbol{x}}\cdot\boldsymbol{ds} \\ &+\int_{\Gamma^{yz}_{i,j,k}} G(\boldsymbol{r_{i+\frac{1}{2},j,k}},\boldsymbol{r_r})\ \partial_x V_i(\boldsymbol{r_{i+\frac{1}{2},j,k}},\boldsymbol{r_s})\ \hat{\boldsymbol{x}}\cdot\boldsymbol{ds} \\ &+\int_{\Gamma^{xz}_{i,j,k}} G(\boldsymbol{r_{i,j-\frac{1}{2},k}},\boldsymbol{r_r})\ \partial_y V_j(\boldsymbol{r_{i,j-\frac{1}{2},k}},\boldsymbol{r_s})\ \hat{\boldsymbol{y}}\cdot\boldsymbol{ds} \\ &+\int_{\Gamma^{xz}_{i,j,k}} G(\boldsymbol{r_{i,j+\frac{1}{2},k}},\boldsymbol{r_r})\ \partial_y V_j(\boldsymbol{r_{i,j+\frac{1}{2},k}},\boldsymbol{r_s})\ \hat{\boldsymbol{y}}\cdot\boldsymbol{ds} \\ &+\int_{\Gamma^{xy}_{i,j,k}} G(\boldsymbol{r_{i,j,k-\frac{1}{2}}},\boldsymbol{r_r})\ \partial_z V_k(\boldsymbol{r_{i,j,k-\frac{1}{2}}},\boldsymbol{r_s})\ \hat{\boldsymbol{z}}\cdot\boldsymbol{ds} \\ &+\int_{\Gamma^{xy}_{i,j,k}} G(\boldsymbol{r_{i,j,k+\frac{1}{2}}},\boldsymbol{r_r})\ \partial_z V_k(\boldsymbol{r_{i,j,k+\frac{1}{2}}},\boldsymbol{r_s})\ \hat{\boldsymbol{z}}\cdot\boldsymbol{ds}\Bigg] \\ &-\frac{I}{4\pi\sigma_s^2}G(\boldsymbol{r_s},\boldsymbol{r_r})\ \delta(x_i-x_s)\delta(y_j-y_s)\delta(z_k-z_s)\end{aligned} \tag{3.15}$$

Equation (3.15) follows the Green theorem $\int_S U\boldsymbol{\nabla}V\cdot\boldsymbol{ds} = \int_V[U\boldsymbol{\nabla^2}V + \boldsymbol{\nabla}U\cdot\boldsymbol{\nabla}V]dv$ for the term between square bracket. Therefore, it can be written

$$\begin{aligned}\frac{\partial V(\boldsymbol{r_r},\boldsymbol{r_s})}{\partial \sigma_{i,j,k}} = \frac{-1}{4\pi\sigma_{i,j,k}}\int_{V_{i,j,k}} dv[&G(\boldsymbol{r_{i,j,k}},\boldsymbol{r_r})\boldsymbol{\nabla^2}V(\boldsymbol{r_{i,j,k}},\boldsymbol{r_s}) + \boldsymbol{\nabla}G(\boldsymbol{r_{i,j,k}},\boldsymbol{r_r})\cdot \\ &\boldsymbol{\nabla}V(\boldsymbol{r_{i,j,k}},\boldsymbol{r_s})] - \frac{I}{4\pi\sigma_s^2}G(\boldsymbol{r_s},\boldsymbol{r_r})\ \delta(x_i-x_s)\delta(y_j-y_s)\delta(z_k-z_s)\end{aligned} \tag{3.16}$$

The Laplacian of the potential is written $\boldsymbol{\nabla^2}V(\boldsymbol{r_{i,j,k}},\boldsymbol{r_s}) = -\frac{\boldsymbol{\nabla}\sigma_{i,j,k}\cdot\boldsymbol{\nabla}V(\boldsymbol{r_{i,j,k}},\boldsymbol{r_s})}{\sigma_{i,j,k}} - \frac{I\delta(\boldsymbol{r_{i,j,k}}-\boldsymbol{r_s})}{\sigma_{i,j,k}}$. Since a constant conductivity is considered in each cell, the term $\boldsymbol{\nabla}\sigma_{i,j,k}$ is null. The term $-\frac{I\delta(\boldsymbol{r_{i,j,k}}-\boldsymbol{r_s})}{\sigma_{i,j,k}}$ is null everywhere except at the point source $\boldsymbol{r_{i,j,k}} = \boldsymbol{r_s}$. Moreover, the integral $\frac{-1}{4\pi\sigma_{i,j,k}}\int_{V_{i,j,k}} G(\boldsymbol{r_{i,j,k}},\boldsymbol{r_r})\boldsymbol{\nabla^2}V(\boldsymbol{r_{i,j,k}},\boldsymbol{r_s})dv$ at the point source becomes $\frac{I}{4\pi\sigma_s^2}\int_{V_{i,j,k}} G(\boldsymbol{r_{i,j,k}},\boldsymbol{r_r})\delta(\boldsymbol{r_{i,j,k}}-\boldsymbol{r_s})dv = \frac{I}{4\pi\sigma_s^2}G(\boldsymbol{r_s},\boldsymbol{r_r})\ \delta(x_i-x_s)\delta(y_j-y_s)\delta(z_k-$

z_s). By taking into account the relation $\frac{\partial V}{\partial \rho_i} = -\sigma_i^2 \frac{\partial V}{\partial \sigma_i}$, the sensitivity for a pole-pole array is simplified and given by

$$\begin{aligned} \frac{\partial V(\boldsymbol{r_r}, \boldsymbol{r_s})}{\partial \sigma_{i,j,k}} &= \frac{-1}{4\pi \sigma_{i,j,k}} \int_{V_{i,j,k}} \nabla G(\boldsymbol{r_{i,j,k}}, \boldsymbol{r_r}) \cdot \nabla V(\boldsymbol{r_{i,j,k}}, \boldsymbol{r_s}) dv \\ \frac{\partial V(\boldsymbol{r_r}, \boldsymbol{r_s})}{\partial \rho_{i,j,k}} &= \frac{1}{4\pi \rho_{i,j,k}} \int_{V_{i,j,k}} \nabla G(\boldsymbol{r_{i,j,k}}, \boldsymbol{r_r}) \cdot \nabla V(\boldsymbol{r_{i,j,k}}, \boldsymbol{r_s}) dv \end{aligned} \tag{3.17}$$

The sensitivity for a cell (i, j, k) is thus the scalar product of the electric field resulting from the source point r_s and the gradient of the Green's function resulting from the receiving point r_r, calculated at the point $r_{i,j,k}$. This relation differs from the one given by Park et Van (1991) and described in equation (3.6). The relation of Park et Van (1991) requires the calculation of the electric field at the source and at the receiving positions, while the proposed method only needs the calculation of the electric field at the source point, thus dividing by two the computation time. Moreover, the sensitivity calculated according to equation (3.17) is balanced by the conductivity $\sigma_{i,j,k}$ (or the resistivity $\rho_{i,j,k}$) of each cell. Equation (3.17) has units given by $[\frac{\partial V}{\partial \rho}] \equiv [\frac{1}{\Omega.M}][\frac{1}{M^2}][\frac{V}{M}][M^3] = [\frac{A}{M}]$. In the case of a homogeneous medium, it is shown below that the relations (3.6) and (3.17) are identical. Setting $V(\boldsymbol{r_{i,j,k}}, \boldsymbol{r_r}) = \frac{I\rho_{i,j,k}}{4\pi} G(\boldsymbol{r_{i,j,k}}, \boldsymbol{r_r})$, the relation (3.6) can be simplified for a cell (i, j, k),

$$\begin{aligned} \frac{\partial V(\boldsymbol{r_r}, \boldsymbol{r_s})}{\partial \rho_{i,j,k}} &= \frac{1}{I} \int_{V_{i,j,k}} \sigma_{i,j,k} \nabla V(\boldsymbol{r_{i,j,k}}, \boldsymbol{r_r}) \cdot \sigma_{i,j,k} \nabla V(\boldsymbol{r_{i,j,k}}, \boldsymbol{r_s}) dv \\ &= \frac{1}{I} \int_{V_{i,j,k}} \frac{1}{\rho_{i,j,k}^2} \nabla \Big[\frac{I\rho_{i,j,k}}{4\pi} G(\boldsymbol{r_{i,j,k}}, \boldsymbol{r_r}) \Big] \cdot \nabla V(\boldsymbol{r_{i,j,k}}, \boldsymbol{r_s}) dv \\ &= \frac{1}{4\pi \rho_{i,j,k}} \int_{V_{i,j,k}} \nabla G(\boldsymbol{r_{i,j,k}}, \boldsymbol{r_r}) \cdot \nabla V(\boldsymbol{r_{i,j,k}}, \boldsymbol{r_s}) dv \end{aligned} \tag{3.18}$$

If the charge density is considered constant on each interface and is taken out

from the integral in (3.2), another simplified form of the sensitivity can be obtained using the same calculation method,

$$\begin{aligned}\frac{\partial V(\boldsymbol{r_r}, \boldsymbol{r_s})}{\partial \rho_{i,j,k}} = \frac{1}{4\pi\rho_{i,j,k}} \Big[& J(\boldsymbol{r_r}, \boldsymbol{x_{i+\frac{1}{2}}}) \partial_x V_i(\boldsymbol{r_{i+\frac{1}{2},j,k}}, \boldsymbol{r_s}) - J(\boldsymbol{r_r}, \boldsymbol{x_{i-\frac{1}{2}}}) \partial_x V_i(\boldsymbol{r_{i-\frac{1}{2},j,k}}, \boldsymbol{r_s}) \\ & + J(\boldsymbol{r_r}, \boldsymbol{y_{j+\frac{1}{2}}}) \partial_y V_j(\boldsymbol{r_{i,j+\frac{1}{2},k}}, \boldsymbol{r_s}) - J(\boldsymbol{r_r}, \boldsymbol{y_{j-\frac{1}{2}}}) \partial_y V_j(\boldsymbol{r_{i,j-\frac{1}{2},k}}, \boldsymbol{r_s}) \\ & + J(\boldsymbol{r_r}, \boldsymbol{z_{k+\frac{1}{2}}}) \partial_z V_k(\boldsymbol{r_{i,j,k+\frac{1}{2}}}, \boldsymbol{r_s}) - J(\boldsymbol{r_r}, \boldsymbol{z_{k-\frac{1}{2}}}) \partial_z V_k(\boldsymbol{r_{i,j,k-\frac{1}{2}}}, \boldsymbol{r_s}) \Big] \\ & + \frac{I}{4\pi} G(\boldsymbol{r_s}, \boldsymbol{r_r}) \ \delta(x_i - x_s)\delta(y_j - y_s)\delta(z_k - z_s)\end{aligned} \tag{3.19}$$

Figure 3.6 shows the calculation of the sensitivity for a homogeneous medium for a pole-pole array using (3.19). However, it can be seen that the calculation of the sensitivity with (3.19) generates an artifact around the source. The artifact persists on various scales whatever the cell size. This behavior is caused because a constant charge density on the interfaces of each prism is chosen. This approximation is valid far from the point of current injection, but becomes invalid close to the source. The volume of the cell must tend towards zero so that the approximation becomes valid. It is thus not recommended to use this notation for a coarse discretization. Note that this artifact around the source is not present for the sensitivity calculated with (3.17).

Calculation of the second derivatives using the IE

In this section, the calculation of the second derivatives in 3D is proposed for the inverse problem. The minimization of a nonlinear least squares problem can be carried out by the Newton method. It requires to calculate the gradient and

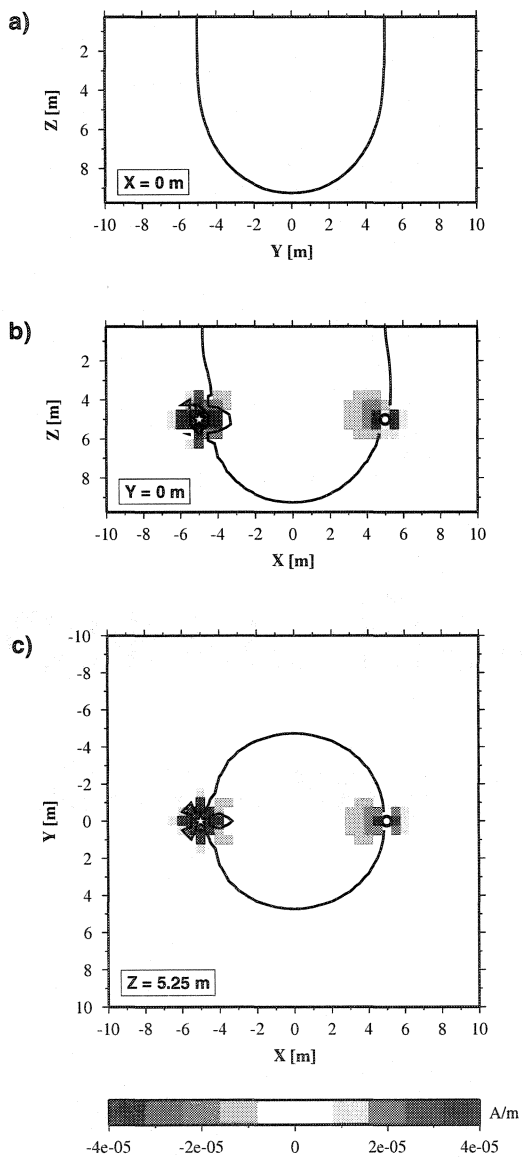

Figure 3.6: Sensitivity for a pole-pole array calculated analytically for a homogeneous medium using equation (3.19). Three sections are represented : a) in X=0 m b) in Y=0 m and c) in Z=5.25 m. The solid black line indicates the null sensitivity. In all the figures, the star and the circle correspond to the source and the receiver, respectively.

the Hessian matrix (Björck, 1996; Nocedal et Wright, 2000). We note $r_i(\boldsymbol{\sigma}) = V_i^{obs} - V_i(\boldsymbol{r_r}, \boldsymbol{r_s})$ the error for the ith observation , where V_i^{obs} and $V_i(\boldsymbol{r_r}, \boldsymbol{r_s})$ are the observed and calculated data respectively ($i = 1, ..., m$). By minimizing the function $\phi(\boldsymbol{\sigma}) = \frac{1}{2}||\boldsymbol{r(\sigma)}||^2$, the gradient $\boldsymbol{\nabla\phi(\sigma)}$ and the Hessian matrix $\boldsymbol{\nabla^2\phi(\sigma)}$ are written

$$\begin{aligned} \boldsymbol{\nabla\phi(\sigma)} &= \boldsymbol{J(\sigma)^T r(\sigma)} \\ \boldsymbol{\nabla^2\phi(\sigma)} &= \boldsymbol{J(\sigma)^T J(\sigma)} + \sum_{i=1}^{m} r_i(\boldsymbol{\sigma}) \boldsymbol{C_i(\sigma)} \end{aligned} \tag{3.20}$$

where $J(\boldsymbol{\sigma})_{ij} = \frac{\partial r_i(\boldsymbol{\sigma})}{\partial \sigma_j}$ and $C_i(\boldsymbol{\sigma})_{jk} = \frac{\partial^2 r_i(\boldsymbol{\sigma})}{\partial \sigma_j \partial \sigma_k}$ are the Frechet and second derivatives of the residual vector $r(\boldsymbol{\sigma})$ respectively. When the problem is linearized, the Hessian is often approximated by the first term like $\boldsymbol{\nabla^2\phi(\sigma)} \approx \boldsymbol{J(\sigma)^T J(\sigma)}$ by neglecting the second term. While taking as a starting point the preceding paragraph and by deriving successively equation (3.12) with regards to conductivities $\sigma_{i,j,k}$, $\sigma_{i-1,j,k}$, $\sigma_{i+1,j,k}$, $\sigma_{i,j-1,k}$, $\sigma_{i,j+1,k}$, $\sigma_{i,j,k-1}$ and $\sigma_{i,j,k+1}$, the coefficients of the second derivative sparse matrix are

$$\begin{aligned} \frac{\partial^2 V(\boldsymbol{r_r}, \boldsymbol{r_s})}{\partial \sigma_{i,j,k}^2} =& \frac{+1}{4\pi\sigma_{i,j,k}^2} \int_{V_{i,j,k}} \boldsymbol{\nabla} G(\boldsymbol{r_{i,j,k}}, \boldsymbol{r_r}) \cdot \boldsymbol{\nabla} V(\boldsymbol{r_{i,j,k}}, \boldsymbol{r_s}) dv \\ &+ \frac{I}{4\pi\sigma_s^3} G(\boldsymbol{r_s}, \boldsymbol{r_r})\ \delta(x_i - x_s)\delta(y_j - y_s)\delta(z_k - z_s) \end{aligned} \tag{3.21}$$

$$\frac{\partial^2 V(\boldsymbol{r_r},\boldsymbol{r_s})}{\partial\sigma_{i-1,j,k}\partial\sigma_{i,j,k}} = \frac{-1}{4\pi\sigma_{i,j,k}\sigma_{i-1,j,k}}\int_{\Gamma^{yz}_{i,j,k}} G(\boldsymbol{r_{i-\frac{1}{2},j,k}},\boldsymbol{r_r})\ \boldsymbol{n}\cdot\boldsymbol{\partial}_x V_i(\boldsymbol{r_{i-\frac{1}{2},j,k}},\boldsymbol{r_s})dy_j dz_k$$
$$\frac{\partial^2 V(\boldsymbol{r_r},\boldsymbol{r_s})}{\partial\sigma_{i+1,j,k}\partial\sigma_{i,j,k}} = \frac{-1}{4\pi\sigma_{i,j,k}\sigma_{i+1,j,k}}\int_{\Gamma^{yz}_{i,j,k}} G(\boldsymbol{r_{i+\frac{1}{2},j,k}},\boldsymbol{r_r})\ \boldsymbol{n}\cdot\boldsymbol{\partial}_x V_i(\boldsymbol{r_{i+\frac{1}{2},j,k}},\boldsymbol{r_s})dy_j dz_k \tag{3.22}$$

$$\frac{\partial^2 V(\boldsymbol{r_r},\boldsymbol{r_s})}{\partial\sigma_{i,j-1,k}\partial\sigma_{i,j,k}} = \frac{-1}{4\pi\sigma_{i,j,k}\sigma_{i,j-1,k}}\int_{\Gamma^{xz}_{i,j,k}} G(\boldsymbol{r_{i,j-\frac{1}{2},k}},\boldsymbol{r_r})\ \boldsymbol{n}\cdot\boldsymbol{\partial}_y V_j(\boldsymbol{r_{i,j-\frac{1}{2},k}},\boldsymbol{r_s})dx_i dz_k$$
$$\frac{\partial^2 V(\boldsymbol{r_r},\boldsymbol{r_s})}{\partial\sigma_{i,j+1,k}\partial\sigma_{i,j,k}} = \frac{-1}{4\pi\sigma_{i,j,k}\sigma_{i,j+1,k}}\int_{\Gamma^{xz}_{i,j,k}} G(\boldsymbol{r_{i,j+\frac{1}{2},k}},\boldsymbol{r_r})\ \boldsymbol{n}\cdot\boldsymbol{\partial}_y V_j(\boldsymbol{r_{i,j+\frac{1}{2},k}},\boldsymbol{r_s})dx_i dz_k \tag{3.23}$$

$$\frac{\partial^2 V(\boldsymbol{r_r},\boldsymbol{r_s})}{\partial\sigma_{i,j,k-1}\partial\sigma_{i,j,k}} = \frac{-1}{4\pi\sigma_{i,j,k}\sigma_{i,j,k-1}}\int_{\Gamma^{xy}_{i,j,k}} G(\boldsymbol{r_{i,j,k-\frac{1}{2}}},\boldsymbol{r_r})\ \boldsymbol{n}\cdot\boldsymbol{\partial}_z V_k(\boldsymbol{r_{i,j,k-\frac{1}{2}}},\boldsymbol{r_s})dx_i dy_j$$
$$\frac{\partial^2 V(\boldsymbol{r_r},\boldsymbol{r_s})}{\partial\sigma_{i,j,k+1}\partial\sigma_{i,j,k}} = \frac{-1}{4\pi\sigma_{i,j,k}\sigma_{i,j,k+1}}\int_{\Gamma^{xy}_{i,j,k}} G(\boldsymbol{r_{i,j,k+\frac{1}{2}}},\boldsymbol{r_r})\ \boldsymbol{n}\cdot\boldsymbol{\partial}_z V_k(\boldsymbol{r_{i,j,k+\frac{1}{2}}},\boldsymbol{r_s})dx_i dy_j \tag{3.24}$$

Similar relations are found when $V(\boldsymbol{r_r},\boldsymbol{r_s})$ is derived with respect to ρ. The cross terms are obtained with the relation $\frac{\partial^2 V}{\partial\rho_i\partial\rho_j} = \sigma_i^2\sigma_j^2\frac{\partial^2 V}{\partial\sigma_i\partial\sigma_j}$. The diagonal term is written $\frac{\partial^2 V(\boldsymbol{r_r},\boldsymbol{r_s})}{\partial\rho^2_{i,j,k}} = \frac{+1}{4\pi\rho^2_{i,j,k}}\int_{V_{i,j,k}}\boldsymbol{\nabla}G(\boldsymbol{r_{i,j,k}},\boldsymbol{r_r})\cdot\boldsymbol{\nabla}V(\boldsymbol{r_{i,j,k}},\boldsymbol{r_s})dv + \frac{I}{4\pi\rho_s}G(\boldsymbol{r_s},\boldsymbol{r_r})\ \delta(x_i - x_s)\delta(y_j - y_s)\delta(z_k - z_s)$ starting from the relation $\frac{\partial^2 V}{\partial\rho_i^2} = 2\sigma_i^3\frac{\partial V}{\partial\sigma_i} + \sigma_i^4\frac{\partial^2 V}{\partial\sigma_i^2}$.

3.3.4 Matrix compression

To make the problem of modeling with IE feasible, the matrix $\boldsymbol{A}$ which allows the calculation of the charge density is compressed. The authors Li et Oldenburg (1997) use wavelets to compress the sensitivity matrix in a magnetic inversion

problem. Portniaguine (1999) selects another method arising from the work of Burt et Adelson (1983) and Losano et Laget (1996) to compress the sensitivity matrix in a gravimetric inversion problem. The second method, named pyramidal compression, is chosen for reasons of fast implementation and conclusive results. A detailed explanation can be obtained from the thesis of Portniaguine (1999). Here we present the method using another form of writing to compress the matrices, and the practical algorithms used in the code of pyramidal compression.

3.3.4.1 Compression and restoration

The compression of a vector column $\boldsymbol{v_1}$ of the level 1 on the level 2 is written $\boldsymbol{v_2} = \boldsymbol{W_1 v_1}$ where $\boldsymbol{W_1}$ is the matrix of compression of level 1. To compress $\boldsymbol{v_1}$ up to the level L, the vectors $\boldsymbol{v_2}$, $\boldsymbol{v_3}$, ..., $\boldsymbol{v_{L-1}}$ are successively compressed by the matrix $\boldsymbol{W_k}$, that is to say $\boldsymbol{v_{k+1}} = \boldsymbol{W_k v_k}$ where $\boldsymbol{W_k}$ is the matrix compression of the level k. It is to be noted that the vector $\boldsymbol{v_k}$ is pre multiplied by $\boldsymbol{W_k}$. The pyramidal compression of a vector column $\boldsymbol{v_1}$ of the level 1 on the level L is written

$$\boldsymbol{v_L} = \boldsymbol{W_{L-1} \ldots W_2 W_1 v_1} \tag{3.25}$$

Property : each matrix $\boldsymbol{W_k}$ is equal to its inverse, that is to say

$$\boldsymbol{W_k} = \boldsymbol{W_k}^{-1} \tag{3.26}$$

The restoration of the vector $\boldsymbol{v_1}$ is written by pre multiplying (3.25) with the matricies $(\boldsymbol{W_{L-1} \ldots W_2 W_1})^{-1}$. By taking into account the preceding property, one thus has

$$\boldsymbol{v_1} = \boldsymbol{W_1 W_2 \ldots W_{L-1} v_L} \tag{3.27}$$

If $\boldsymbol{\mathcal{W}} = \boldsymbol{W_{L-1} \ldots W_2 W_1}$ is the product of all the matrices of compression and $\boldsymbol{\mathcal{W}^{-1}} = \boldsymbol{W_1 W_2 \ldots W_{L-1}}$ is the product of all the matrices of restoration, the product of the matrices of compression by those of restoration is equal to the identity matrix ($\boldsymbol{\mathcal{W}^{-1}\mathcal{W}} = \boldsymbol{I}$). The algorithms of creation, pre and post-multiplication of the compression matrix $\boldsymbol{W_k}$ on a level k are given in appendix 3.4.8.

The final stage consists in taking only the significant elements of the compressed vector $\boldsymbol{v_L}$ and cancelling the others compared to a fixed threshold. The threshold corresponds to a percentage q of the absolute value of the maximum amplitude of the compressed vector $\boldsymbol{v_L}$. The resulting vector $\tilde{\boldsymbol{v}}_{\boldsymbol{L}}$ is sparse by carrying out the *thresholding*

$$\tilde{v}_L(i) = \begin{cases} v_L(i) & , |v_L(i)| \geq q \max(|\boldsymbol{v_L}|) \\ 0 & , |v_L(i)| < q \max(|\boldsymbol{v_L}|) \end{cases}, \quad \forall i \tag{3.28}$$

3.3.4.2 Approaches to compress a linear system

Portniaguine (1999) proposes two solutions to compress a linear system $\boldsymbol{Ax} = \boldsymbol{b}$. The first method consists in *preconditioning* the linear system $\boldsymbol{\mathcal{W}Ax} = \boldsymbol{\mathcal{W}b}$, giving $\tilde{\boldsymbol{A}}\boldsymbol{x} = \tilde{\boldsymbol{b}}$ after the thresholding. The second, named *incomplete factorization* matrix $\boldsymbol{A}$, is written $\boldsymbol{\mathcal{W}^{-1}}\tilde{\boldsymbol{A}} = \boldsymbol{A}$. The system to be solved is $\boldsymbol{\mathcal{W}^{-1}}\tilde{\boldsymbol{A}}\boldsymbol{x} = \boldsymbol{b}$. A third method is proposed. Based on the property $\boldsymbol{\mathcal{W}^{-1}\mathcal{W}} = \boldsymbol{I}$, the matrix identity $\boldsymbol{I}$ is inserted in the linear system between $\boldsymbol{A}$ and $\boldsymbol{x}$. The system is written $(\boldsymbol{A\mathcal{W}^{-1}})(\boldsymbol{\mathcal{W}x}) = \boldsymbol{b}$, giving after thresholding

$$\tilde{A}\tilde{x} = b \tag{3.29}$$

with $\tilde{A} = AW^{-1}$ and $\tilde{x} = Wx$. The solution of the system is obtained by the relation $x = W^{-1}\tilde{x}$. For the first and second methods, $\dim(W) = \dim(\tilde{b})$. For the third method, dimension changes since the vectors line is compressed instead of the vectors column ($\dim(W) = \dim(x)$).

3.3.4.3 Resolution of the system of equations for the integral method

For our system of equations applied to the integral method, the system $\tilde{A}^T\tilde{A}\tilde{x} = \tilde{A}^T b$ is initially solved. Whereas the matrices W and W^{-1} are not stored, the matrix $\tilde{A}$ is stored in a particular way. $\tilde{A}$ is obtained by post-multiplication of A with W^{-1}, that is to say $\tilde{A} = W^{-1} + k\tilde{D}$ where $\tilde{D} = DW^{-1}$. The compressed system is solved with the conjugate gradient method.

$$[(W^{-1})^T + \tilde{D}^T k][W^{-1} + k\tilde{D}]\ \tilde{x} = [(W^{-1})^T + \tilde{D}^T k]b \tag{3.30}$$

It is needed to store the sparse matrix $\tilde{D}$ and to calculate the products of this one and of its transposed by a vector column. The algorithms of storage and product of a sparse matrix by a vector for the *sparse row-wise* format taken from the book of Pissanetzky (1984) are given in appendix 3.4.9. This method requires less memory compared to the standard method consisting in storing two integers and a real for each element of the sparse matrix. The product of the matrix k by a vector column does not cause a problem, since this matrix is diagonal. The products of $(W^{-1})^T$ and W^{-1} by a vector column are carried out according to the codes of compression and restoration described in appendix 3.4.8.

The system $\tilde{\boldsymbol{A}}\tilde{\boldsymbol{x}} = \boldsymbol{b}$ can also be directly solved, where $\tilde{\boldsymbol{A}}$ is nonsymmetrical, with the iterative methods "Quasi Minimal Residual" (Freund et Nachtigal, 1991b,a), "Conjugate Gradient Squared" (Sonneveld, 1989), "Bi-Conjugate Gradient Stabilized" (Van Der Vorst, 1992) and "Bi-Conjugate Gradient Stabilized(l)" (Sleijpen et Fokkema, 1993). A comparison between the different iterative methods is done in Table 3.1. Finally, the resolution of the nonsymmetrical linear system is done by the "Bi-Conjugate Gradient Stabilized(l)" method with l=2. We choose a threshold q=0.001 % to compress the matrix $\boldsymbol{D}$, which requires to store less than 40% of the original matrix.

TAB. 3.1: Comparaison between different solvers for the two-layer model consisting of 11*11*6 cells. The relative tolerance for all solvers is 1e-6. The computer is a Dell Inspiron 8100 PIII 733 MHz. The maximum number of iterations is 500. Time is in seconds. PCG : Preconditioned conjugate gradient. QMR : Quasi Minimal Residual. CGS : Conjugate Gradient Squared. BICGSTAB : Bi-Conjugate Gradient Stabilized. BICGSTAB(l) : Bi-Conjugate Gradient Stabilized(l) with l=2

	$G(\boldsymbol{r_i}, \boldsymbol{r_j}) = \frac{1}{\lvert \boldsymbol{r_i} - \boldsymbol{r_j} \rvert}$			$G(\boldsymbol{r_i}, \boldsymbol{r_j}) = \frac{1}{\lvert \boldsymbol{r_i} - \boldsymbol{r_j} \rvert} + \frac{1}{\lvert \boldsymbol{r_i} - \boldsymbol{r_j'} \rvert}$		
Method	time(s)	iteration	deviation	time(s)	iteration	deviation
PCG	3.26	158	7.58e-7	2.57	155	8.28e-7
QMR	90.21	500	1.07e-1	7.69	42	9.79e-7
CGS	3.26	19	9.08e-7	2.53	15	7.44e-7
BICGSTAB	4.64	20	8.69e-7	3.49	15	5.63e-7
BICGSTAB(l)	1.73	8	4.73e-8	1.73	7	2.65e-8

To prevent obtaining values different from zero where the charge density must be null, an additional constraint to the system $\tilde{\boldsymbol{A}}\tilde{\boldsymbol{x}} = \boldsymbol{b}$ is introduced. The indices of the values of $\mathbf{x}$ which must be null are gathered as a set N. A matrix $\boldsymbol{I_N}$ made up of 1 is generated, in such a way that $\boldsymbol{I_N x} = \mathbf{0}$ only for the $\boldsymbol{x} \in N$. The new compressed system to solve is written, with $\tilde{\boldsymbol{I}}_{\boldsymbol{N}} = \boldsymbol{I_N W}^{-1}$,

$$[\mathcal{W}^{-1} + k\tilde{D} + \tilde{I}_N]\ \tilde{x} = b \tag{3.31}$$

3.3.5 Electric field

First method : charge density

Once the charge density is obtained in the whole space, the three components of the electric field can be calculated on the interfaces of the prisms. If $\tilde{x}$ is the solution of the linear system (3.4) ($[\mathcal{W}^{-1} + k\tilde{D}]\ \tilde{x} = b$), then the secondary electric field E^S is obtained by a multiplication of $\tilde{x}$ by the opposite of the matrix $\tilde{D}$ plus one corrective term $-2\pi Ix$, since the elements of $\tilde{D}$ are $\tilde{D_{ii}} = -[2\pi + J^a_{ii}]$ on the diagonal and $\tilde{D_{ij}} = -J^a_{ij}$ on the off-diagonal. The total field E is given by the sum of the primary field E^P and of the secondary field E^S (E=E^P+E^S), as follows

$$E = -\frac{1}{4\pi}[\frac{I}{\sigma_s}\nabla G + (-\tilde{D}\tilde{x} - 2\pi Ix)] \tag{3.32}$$

The electric field at the center of the cell (i, j, k) is needed; it can be evaluated by interpolating the values of the computed field at the interfaces of the prisms with a cubic spline (Press *et al.*, 1992). A calculation equivalent to that carried out with the equation (3.9) can also be used.

Second method : surface integral

The calculation of the electric field described by Beasley et Ward (1986) for a conducting block located in a homogeneous medium can be generalized when the model consists of several prisms. The x component of the gradient of the potential is written

$$\begin{aligned}\partial_{x_i} V(\boldsymbol{r}_{\boldsymbol{i-\frac{1}{2},j,k}}, \boldsymbol{r}_{\boldsymbol{s}}) =& \frac{I}{4\pi\sigma_s} \partial_{x_i} G(\boldsymbol{r}_{\boldsymbol{i-\frac{1}{2},j,k}}, \boldsymbol{r}_{\boldsymbol{s}}) + \sum_{n=1}^{nx}\sum_{p=1}^{ny}\sum_{q=1}^{nz} \\ & \Big[k^{x^-}_{n,p,q} J^a_x(\boldsymbol{r}_{\boldsymbol{i-\frac{1}{2},j,k}}, x_{n-\frac{1}{2}}) \partial_{x_n} V(\boldsymbol{r}_{\boldsymbol{n-\frac{1}{2},p,q}}, \boldsymbol{r}_{\boldsymbol{s}}) \\ & + k^{y^-}_{n,p,q} J^a_x(\boldsymbol{r}_{\boldsymbol{i-\frac{1}{2},j,k}}, y_{p-\frac{1}{2}}) \partial_{y_n} V(\boldsymbol{r}_{\boldsymbol{n,p-\frac{1}{2},q}}, \boldsymbol{r}_{\boldsymbol{s}}) \\ & + k^{z^-}_{n,p,q} J^a_x(\boldsymbol{r}_{\boldsymbol{i-\frac{1}{2},j,k}}, z_{q-\frac{1}{2}}) \partial_{z_n} V(\boldsymbol{r}_{\boldsymbol{n,p,q-\frac{1}{2}}}, \boldsymbol{r}_{\boldsymbol{s}})\Big]\end{aligned} \tag{3.33}$$

with $k^{x^-}_{n,p,q} = \frac{1}{4\pi}\frac{\sigma_{n,p,q}-\sigma_{n-1,p,q}}{\sigma_{n-1,p,q}}$, $k^{y^-}_{n,p,q} = \frac{1}{4\pi}\frac{\sigma_{n,p,q}-\sigma_{n,p-1,q}}{\sigma_{n,p-1,q}}$ et $k^{z^-}_{n,p,q} = \frac{1}{4\pi}\frac{\sigma_{n,p,q}-\sigma_{n,p,q-1}}{\sigma_{n,p,q-1}}$ and indices $i = [1, nx]$, $j = [1, ny]$ et $k = [1, nz]$. The system of equations is written as $[\boldsymbol{I} + \boldsymbol{Dk}]\boldsymbol{x} = \boldsymbol{b}$ where $\boldsymbol{k}$ is the diagonal matrix of the elements $k^{x^-}_{n,p,q}$, $k^{y^-}_{n,p,q}$ and $k^{z^-}_{n,p,q}$. It is necessary to pre multiply $[\boldsymbol{I} + \boldsymbol{Dk}]$ by $\boldsymbol{\mathcal{W}}$ and to solve the system $\boldsymbol{\mathcal{W}}^{-1}[\boldsymbol{\mathcal{W}} + \tilde{\boldsymbol{D}}\boldsymbol{k}]\boldsymbol{x} = \boldsymbol{b}$ with $\tilde{\boldsymbol{D}} = \boldsymbol{\mathcal{W}}\boldsymbol{\mathcal{D}}$.

3.3.6 Tests

3.3.6.1 Calculation of the electric potential

To validate the calculation of the potential generated by a polar source, the models of the vertical contact and the two-layer subsurface were used. The IE and the FD methods (Spitzer, 1995; Spitzer *et al.*, 1999) were compared with the analytical solution. The code using FD method includes the singularity removal decribed by Lowry *et al.* (1989).

Vertical contact

On figure 3.7, the potential in log_{10} analytically calculated for a vertical contact (10 $\Omega.m$ / 1000 $\Omega.m$) is shown in the three directions. The source is located at $(-5, 0, 0)$ m for the analytical solution and the Green's function $G(\boldsymbol{r_i}, \boldsymbol{r_j}) =$

$\frac{1}{|r_i-r_j|} + \frac{1}{|r_i-r'_j|}$. For the Green's function $G(r_i, r_j) = \frac{1}{|r_i-r_j|}$ the source is located at $(-5, 0, 0.01)$ m to avoid the singularity. The black line delimits the vertical contact. The figures a) and b) correspond to the sections $X = 0$ m and $Y = 0$ m. Figure c) represents the plane $Z = 0.5$ m. The calculations of the potential and of the current density are given in appendix 3.4.7. Figures 3.8, 3.9 and 3.10 display the potential and the relative deviation compared to figure 3.7 for the IE method using the Green's functions $G(r_i, r_j) = \frac{1}{|r_i-r_j|}$, $G(r_i, r_j) = \frac{1}{|r_i-r_j|} + \frac{1}{|r_i-r'_j|}$ and the FD method, respectively. The three methods give satisfactory results. The maximum relative deviation for figures 3.8 and 3.9 are 56% and 16% at the vertical contact, on the source side. Around the source the deviation does not exceed 5%. The maximum relative deviation for figure 3.10 is 100% at the point source, at the contact and in the medium of 1000 $\Omega.m$. The more one moves away from the current source, the more the amplitude of the potential decreases and more likely the relative error is to increase.

The two-layer case

On figure 3.11, the potential in log_{10} analytically calculated for a two-layer subsurface (first layer of 1000 $\Omega.m$ with a thickness of 4 m overlying an infinite homogeneous medium of 10 $\Omega.m$) is shown in the three directions. The source is located at $(-5, 0, 0)$ m. The figures a) and b) correspond to the sections $X = 0$ m and $Y = 0$ m. Figure c) represents the plane $Z = 0.5$ m. The calculations of the potential and the current density are given in appendix 3.4.6. Figures 3.12, 3.13 and 3.14 show the potential and the relative deviation compared to figure 3.11 for the IE method using the Green's functions $G(r_i, r_j) = \frac{1}{|r_i-r_j|}$, $G(r_i, r_j) = \frac{1}{|r_i-r_j|} + \frac{1}{|r_i-r'_j|}$ and the FD method, respectively. The maximum relative deviation for figure 3.12 is

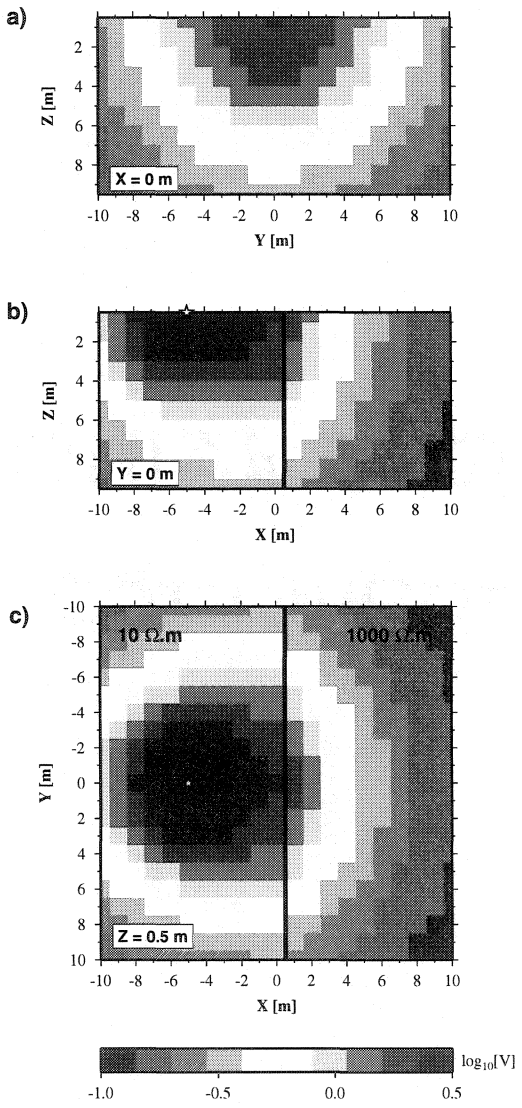

Figure 3.7: Potential ($log_{10}[V]$) for pole-pole array calculated analytically for a vertical contact (medium 1 : 10 $\Omega.m$ and medium 2 : 1000 $\Omega.m$). The source is located at $(-5, 0, 0)$ m. The black line delimits the vertical contact. Figures a) and b) correspond to sections X=0 m and Y=0 m. Figure c) displays the plan Z=0.5 m.

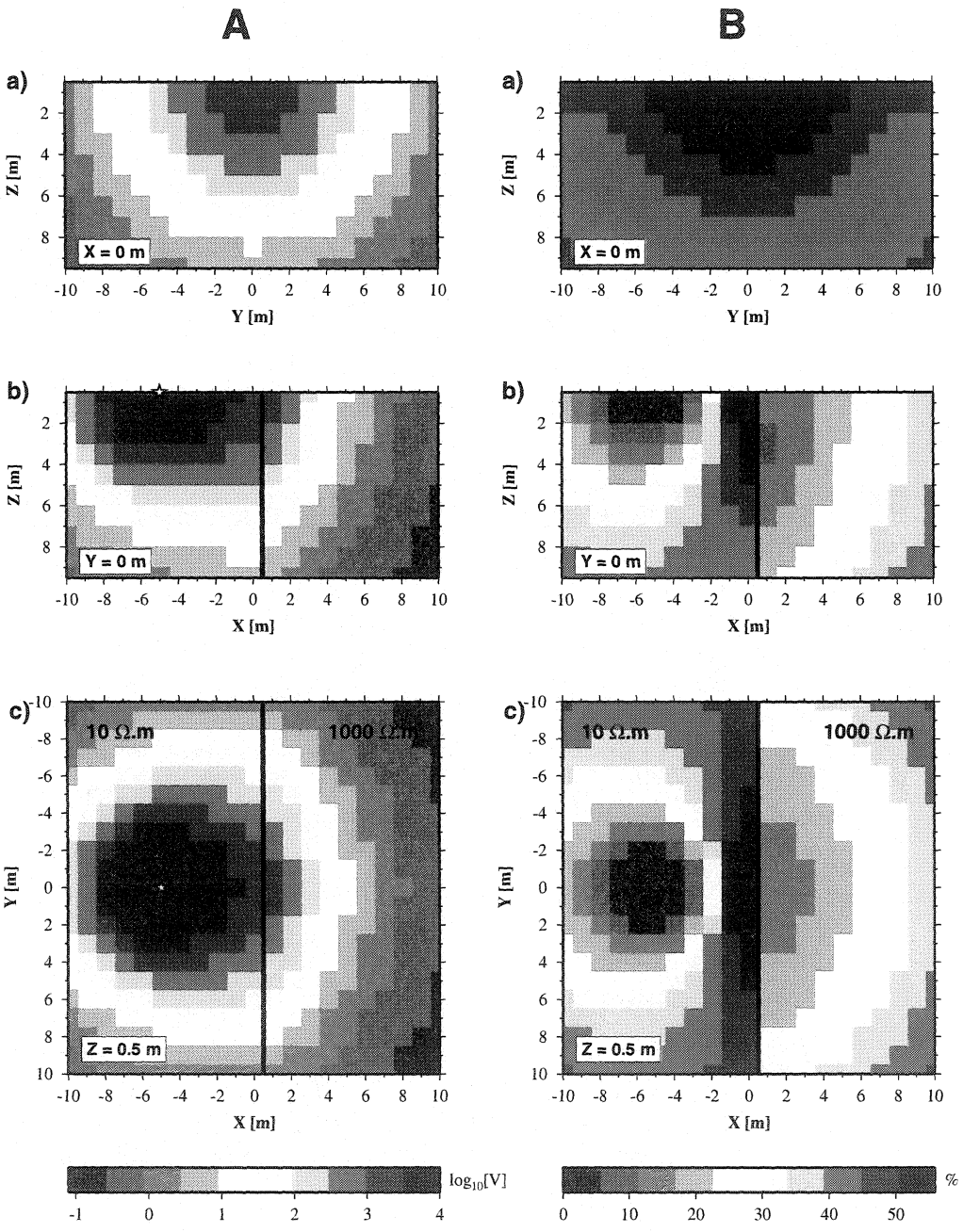

Figure 3.8: A) Potential for a pole-pole array calculated numerically by the IE method for a vertical contact. The Green function used is $G(\boldsymbol{r_i}, \boldsymbol{r_j}) = \frac{1}{|\boldsymbol{r_i} - \boldsymbol{r_j}|}$. B) Relative deviation expressed as a percentage between figure 3.8A and figure 3.7. The maximum deviation is 56%.

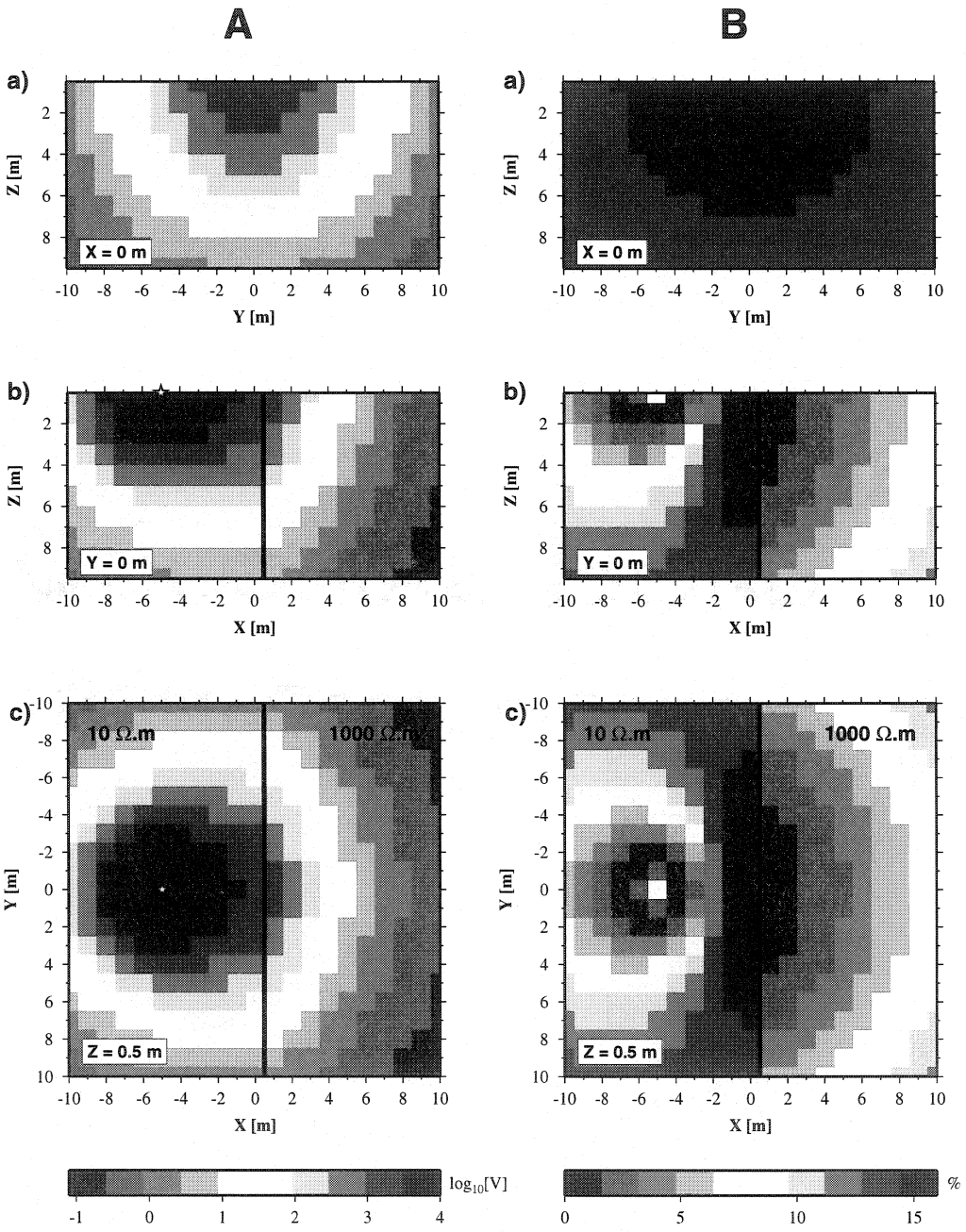

Figure 3.9: A) Potential for a pole-pole array calculated numerically by the IE method for a vertical contact. The Green function used is $G(\boldsymbol{r_i}, \boldsymbol{r_j}) = \frac{1}{|r_i - r_j|} + \frac{1}{|r_i - r'_j|}$. B) Relative deviation expressed as a percentage between figure 3.9A and figure 3.7. The maximum deviation is 16%.

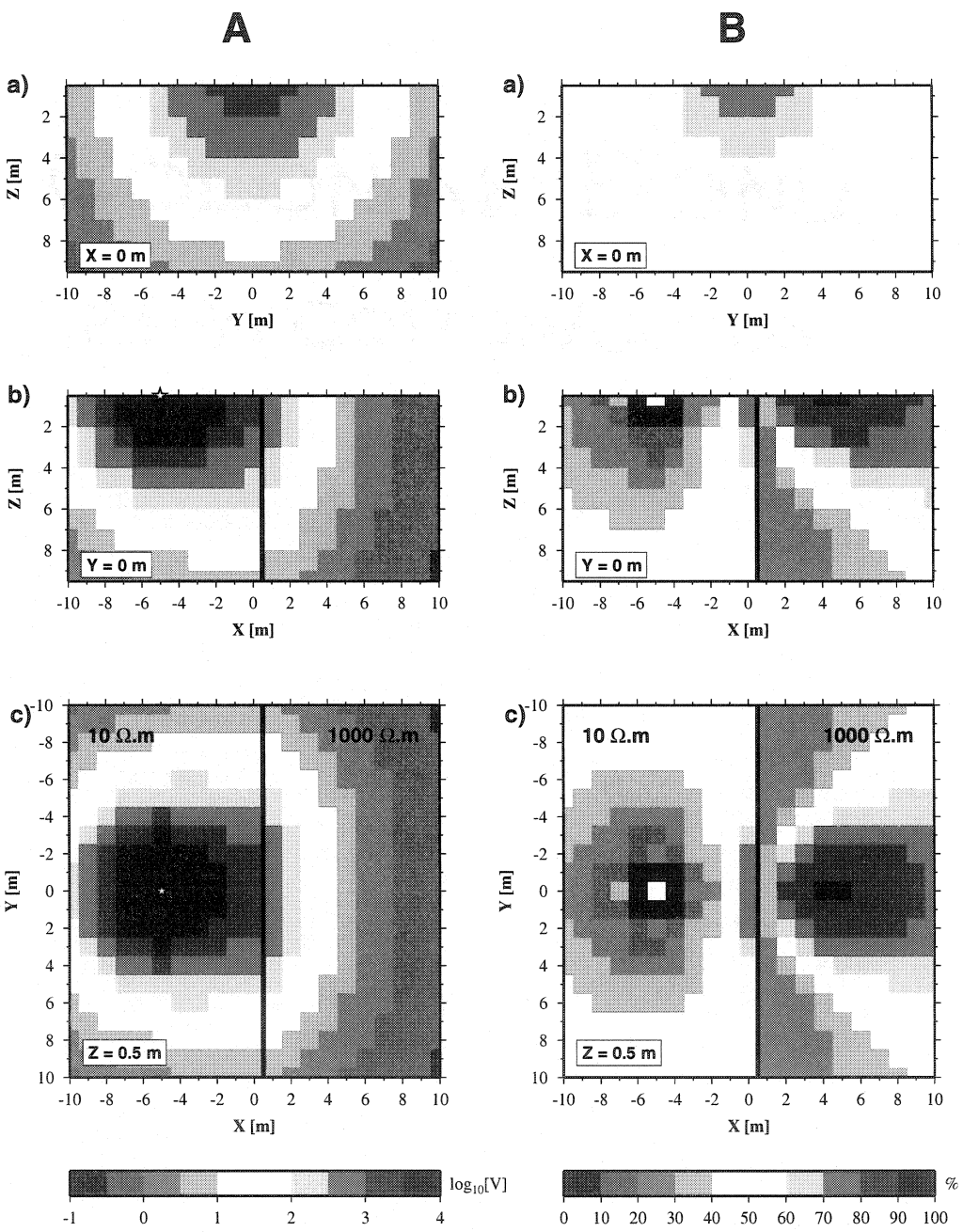

Figure 3.10: A) Potential for a pole-pole array calculated numerically by the FD method for a vertical contact. B) Relative deviation expressed as a percentage between figure 3.10A and figure 3.7. The maximum deviation is 100%.

80% uniformly distributed around the source in the 1000 $\Omega.m$ layer. The maximum relative deviation for figure 3.13 is 27% and is in the 10 $\Omega.m$ medium under the source. Around the source the deviation does not exceed 2.5%. The maximum relative deviation for figure 3.14 is 40% at the source point and radially symmetric about the source.

3.3.6.2 Calculation of the sensitivity

In the following figures, the transmitting current is positive. The sources and the receivers are represented by a star and a circle, respectively. The calculation of the sensitivity for a homogeneous medium using a dipole-dipole array is given in appendix 3.4.5.

Pole-pole, dipole-pole and dipole-dipole arrays for a homogeneous medium

Figure 3.15 shows the sensitivity calculated analytically for various arrays (pole-pole, dipole-pole and dipole-dipole) for electrodes at the ground surface and at depth. The solid black line indicates the null sensitivity associated with the polarity change. It is noticed that sensitivity increases near the transmitting and receiving positions. One can see in figure 3.15 a) that the negative sensitivity includes the area located between the electrodes and extends to the surface (it is a circle on the surface). On figure 3.15 b), when the electrodes are superimposed, the zone of negative sensitivity forms a closed spherical surface. With the dipole-pole array, frequently used in electric prospecting, the sensitivity is assymmetrical (figures 3.15 c, d and e). The sensitivities for various arrays of dipoles/poles are shown in figures 3.15 f, g and h.

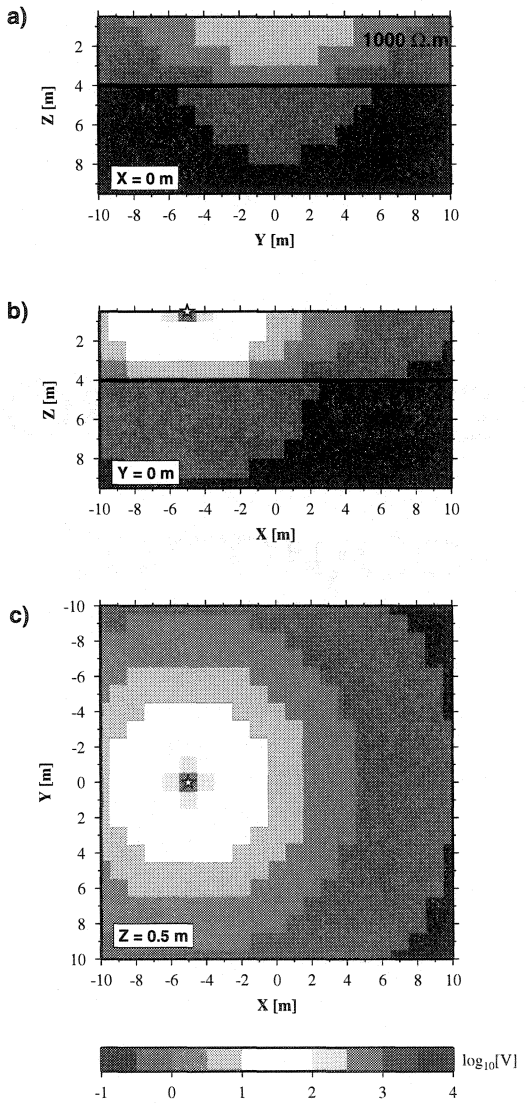

Figure 3.11: Potential ($log_{10}[V]$) for a pole-pole array calculated analytically for the two-layer case (first layer of $1000\ \Omega.m$ with $4\ m$ thickness and an infinite homogeneous medium of $10\ \Omega.m$). The source is located in $(-5, 0, 0)$ m. Figures a) and b) correspond to sections X=0 m and Y=0 m. Figure c) displays the plan Z=0.5 m.

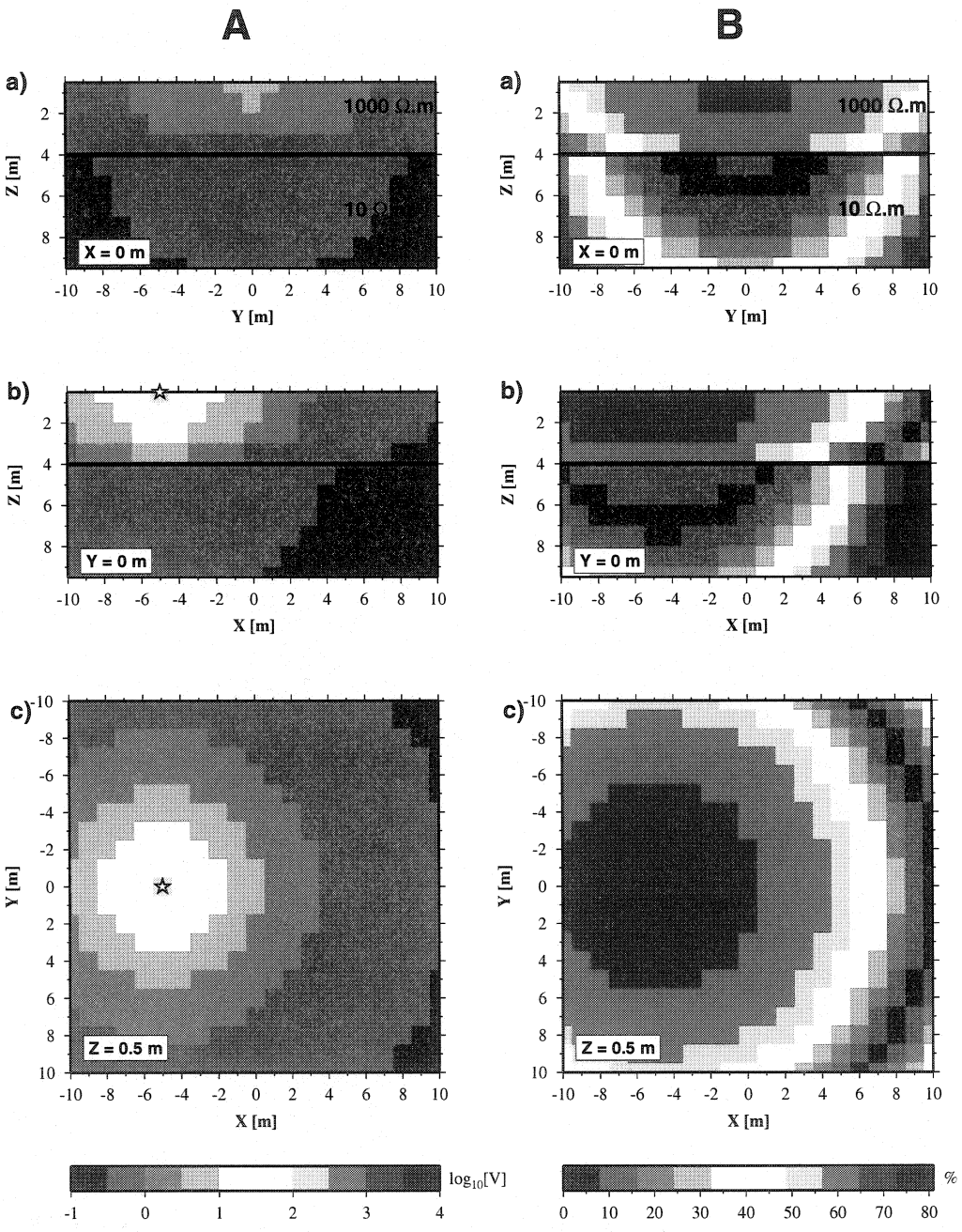

Figure 3.12: A) Potential for a pole-pole array calculated numerically by the IE method (equation (3.9)) from the two-layer model. The Green function used is $G(\boldsymbol{r_i}, \boldsymbol{r_j}) = \frac{1}{|\boldsymbol{r_i} - \boldsymbol{r_j}|}$. B) Relative deviation expressed as a percentage between figure 3.12A and figure 3.11. The maximum deviation is 80%.

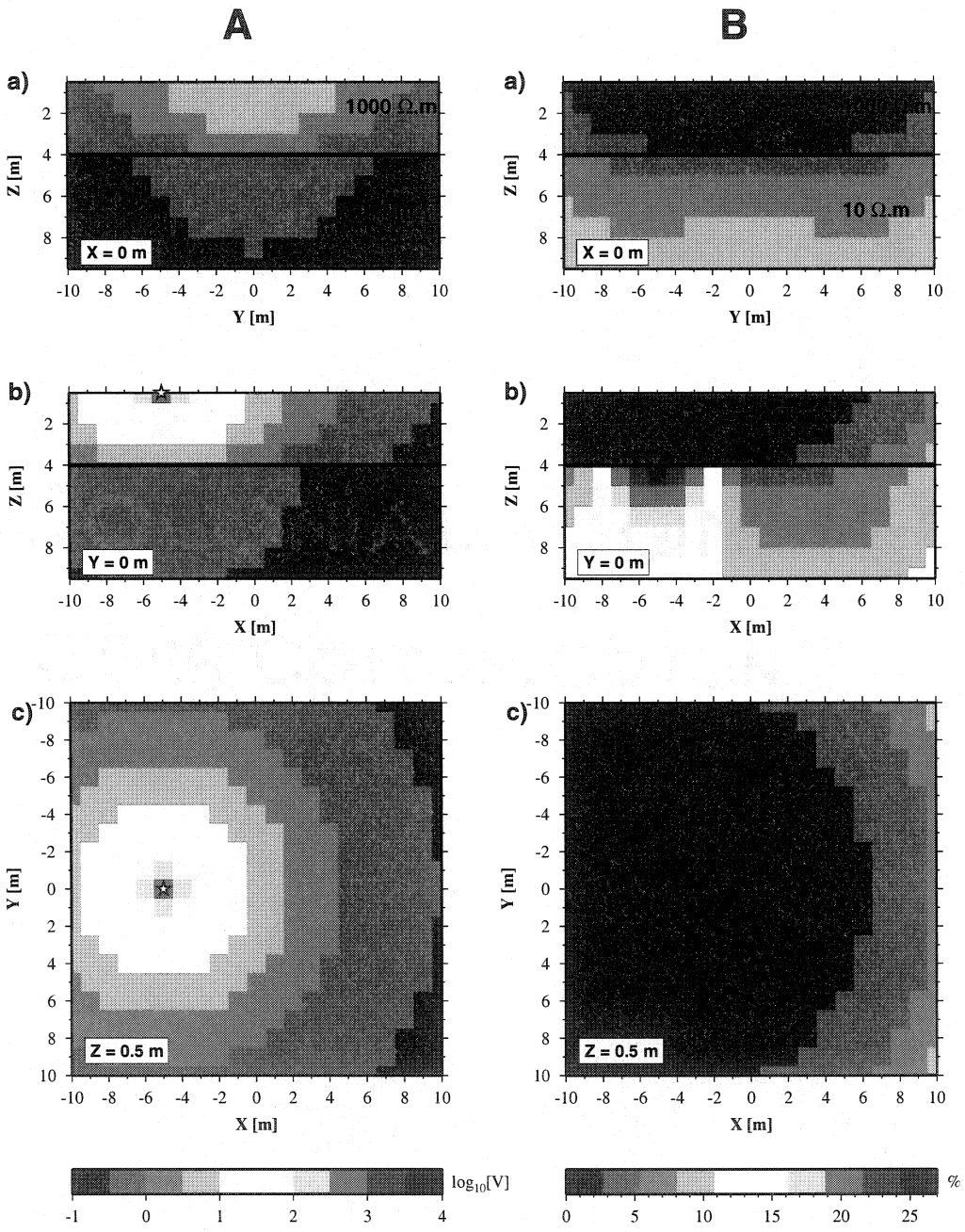

Figure 3.13: A) Potential calculated numerically by the IE method for the two-layer model for a pole-pole array. The Green function used is $G(\boldsymbol{r_i}, \boldsymbol{r_j}) = \frac{1}{|\boldsymbol{r_i} - \boldsymbol{r_j}|} + \frac{1}{|\boldsymbol{r_i} - \boldsymbol{r'_j}|}$. B) Relative deviation expressed as a percentage between figure 3.13A and figure 3.11. The maximum deviation is 27%.

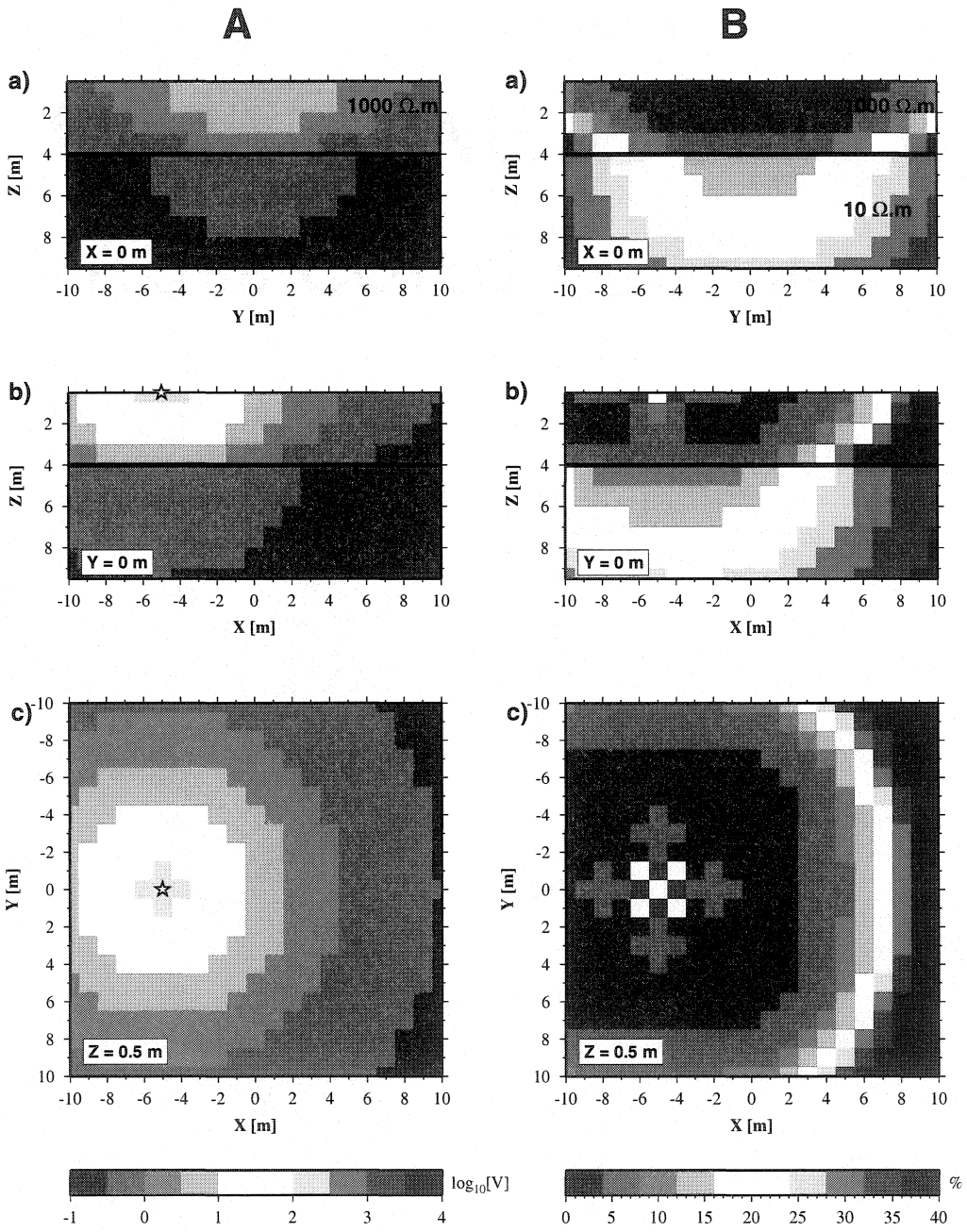

Figure 3.14: A) Potential for a pole-pole array calculated numerically by FD method for the two-layer model. B) Relative deviation expressed as a percentage between figure 3.14A and figure 3.11. The maximum deviation is 40%.

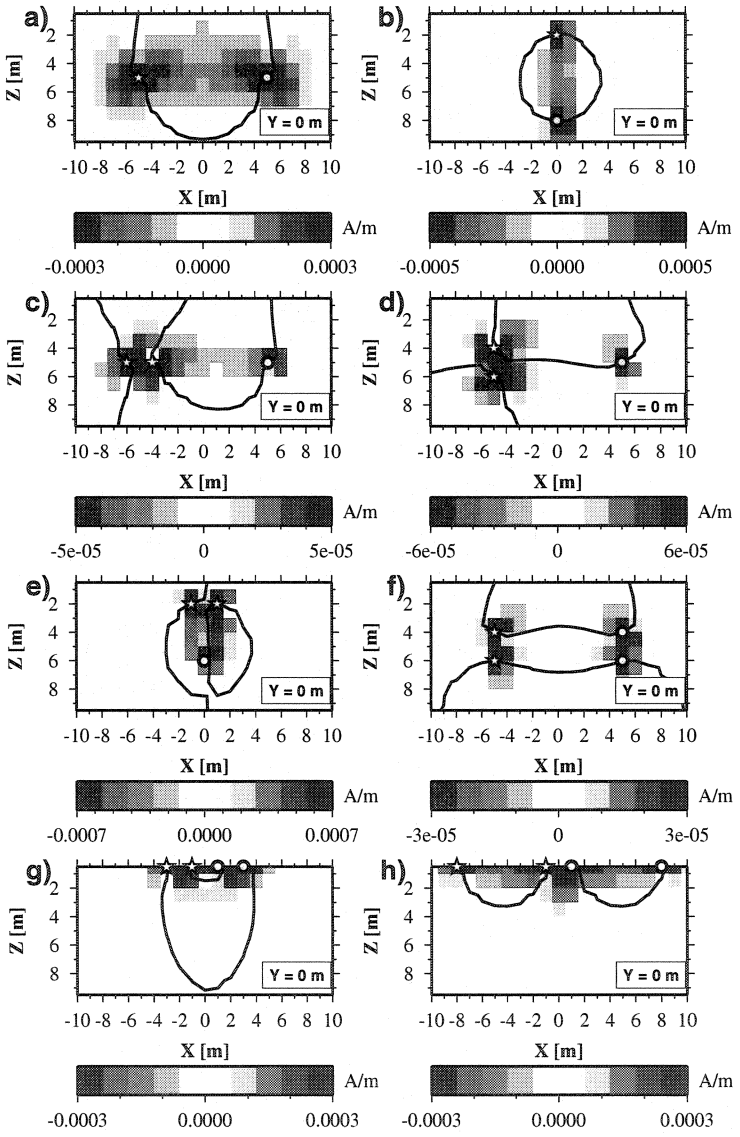

Figure 3.15: Sensitivity for a homogeneous medium calculated according to equation (3.6) for various arrays along section Y=0m. a) pole-pole. b) pole-pole. c) dipole-pole. d) dipole-pole. e) dipole-pole. f) dipole-dipole. g) dipole-dipole. h) dipole-dipole. The fine black line indicates the value of null sensitivity. The star and the circle correspond to the source and the receiver, respectively.

Pole-pole array for a vertical contact

We use the case of the vertical contact located at $X = 0\ m$, of resistivity $10\ \Omega.m$ for $x < 0\ m$ and $1000\ \Omega.m$ for $x > 0\ m$ to validate and compare the methods of sensitivity calculation. The calculations of the current densities and of the electric field are given in appendix 3.4.7. Sensitivity calculated analytically and numerically by IE method are shown in figure 3.16. The sensitivity is calculated numerically using equations (3.4), (3.6) and (3.9) for the Green's functions $G(\boldsymbol{r_i}, \boldsymbol{r_j}) = \frac{1}{|\boldsymbol{r_i}-\boldsymbol{r_j}|}$ and $G(\boldsymbol{r_i}, \boldsymbol{r_j}) = \frac{1}{|\boldsymbol{r_i}-\boldsymbol{r_j}|} + \frac{1}{|\boldsymbol{r_i}-\boldsymbol{r'_j}|}$. It can be seen on these figures that the amplitude and the line of null sensitivity are similar. On figure 3.17, the sensitivities $\frac{\partial V}{\partial \rho}$ calculated analytically and numerically using equations (3.4), (3.9) and (3.17) are shown. By comparing figures 3.16 and 3.17, the role played by the current density resulting from the receiving point in the equation (3.6) can be observed. It generates a zone of negative sensitivity being propagated at infinity and parallel to the vertical contact.

Pole-pole array for the two-layer case

The case of two layers is one of the most used examples in the literature. Roy et Apparao (1971) proposed an analytical calculation of the potential in the form of series. The calculation of the current densities is given in appendix 3.4.6. Figure 3.18 shows the sensitivity calculated analytically and numerically by the IE method using equations (3.4), (3.6) and (3.9) for a 4 m thick first layer of $1000\ \Omega.m$ and a homogeneous medium of $10\ \Omega.m$. The dissociation of the zone of negative sensitivity at the interface between the two layers can be observed. The line of sensitivity is almost equivalent on the three figures. The amplitude of the sensitivity for the IE method using the Green's function $G(\boldsymbol{r_i}, \boldsymbol{r_j}) = \frac{1}{|\boldsymbol{r_i}-\boldsymbol{r_j}|}$ is

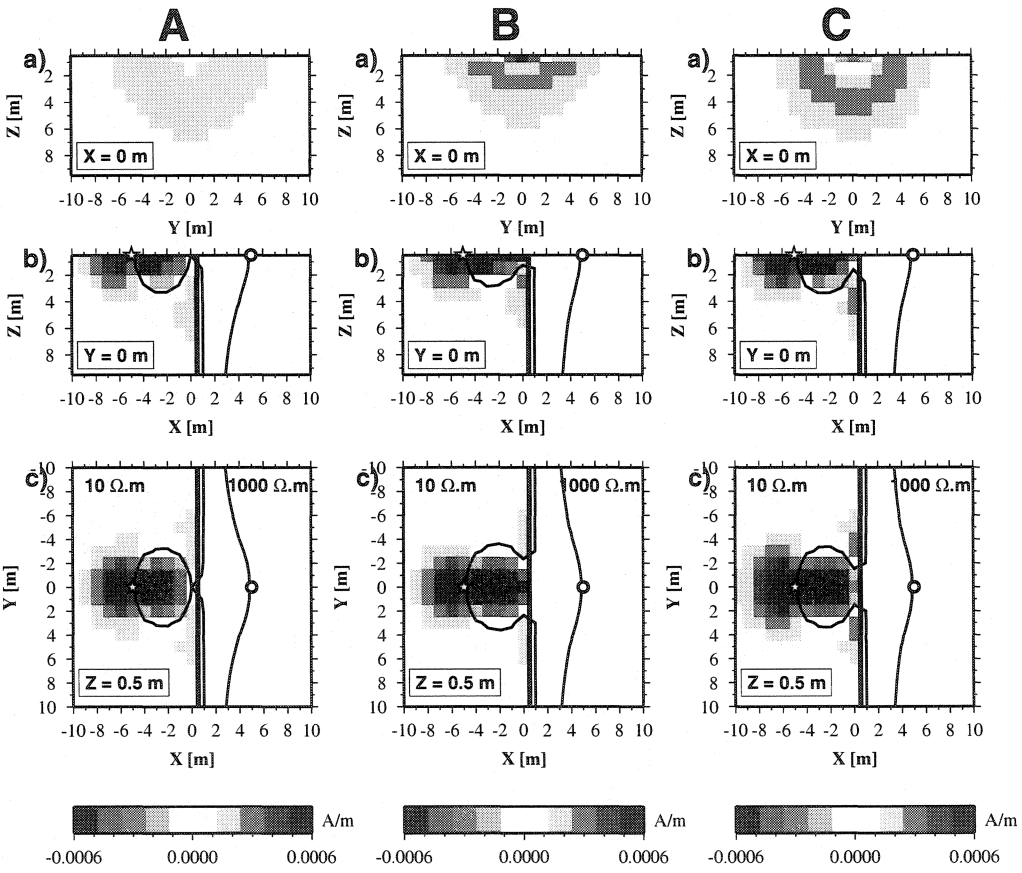

Figure 3.16: Sensitivity for a pole-pole array for a vertical contact (medium 1 : 10 $\Omega.m$ and medium 2 : 1000 $\Omega.m$). A) Analytical sensitivity. B) Sensitivity by IE method with the Green function $G(\boldsymbol{r}_i, \boldsymbol{r}_j) = \frac{1}{|r_i - r_j|}$. C) Sensitivity by IE method with the Green function $G(\boldsymbol{r}_i, \boldsymbol{r}_j) = \frac{1}{|r_i - r_j|} + \frac{1}{|r_i - r'_j|}$. Figures a) and b) correspond to sections X=0 m and Y=0 m. Figure c) displays the plan Z=0.5 m. The thick black line represents the contact. The finer black line delineates the value of zero sensitivity.

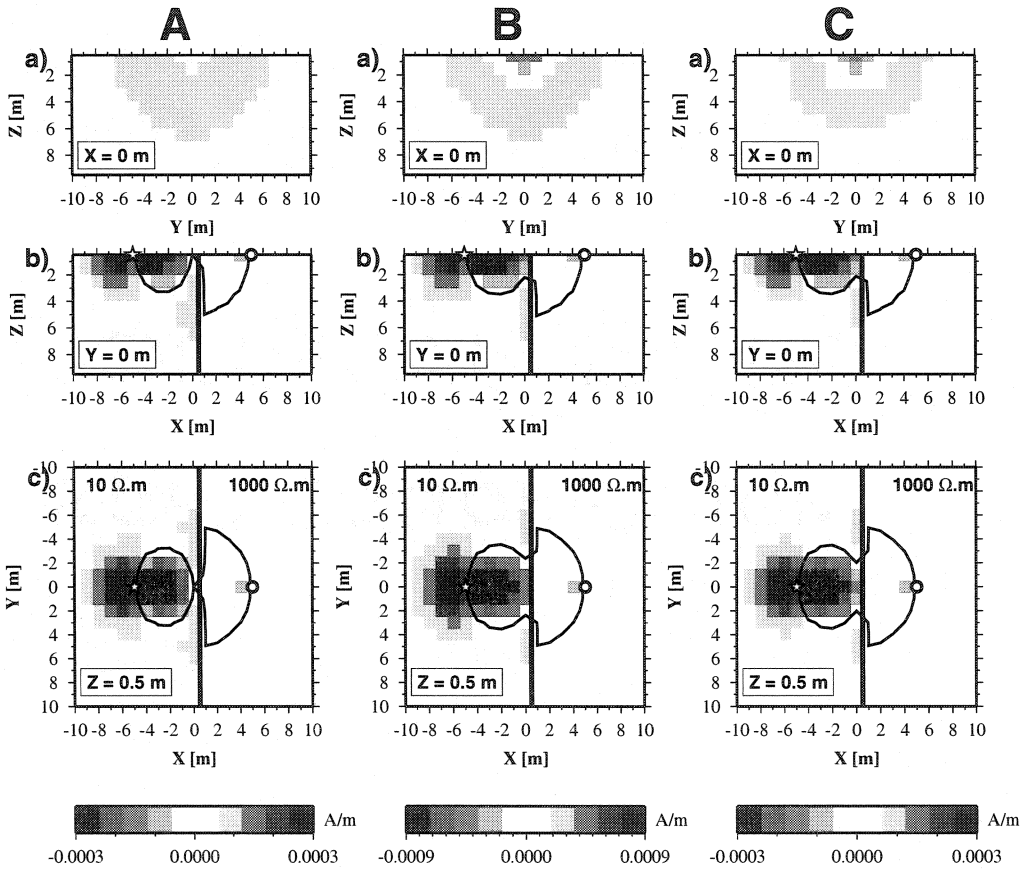

Figure 3.17: Sensitivity $\frac{\partial V}{\partial \rho}$ for a pole-pole array for a vertical contact (medium 1 : $10\ \Omega.m$ and medium 2 : $1000\ \Omega.m$) calculated using equation (3.17). A) Analytical sensitivity. B) Sensitivity by IE method with the Green function $G(\boldsymbol{r_i}, \boldsymbol{r_j}) = \frac{1}{|r_i - r_j|}$. C) Sensitivity by IE method with the Green function $G(\boldsymbol{r_i}, \boldsymbol{r_j}) = \frac{1}{|r_i - r_j|} + \frac{1}{|r_i - r'_j|}$. Figures a) and b) correspond to sections X=0 m and Y=0 m. Figure c) displays the plan Z=0.5 m. The thick black line represents the contact. The finer black line delineates the value of zero sensitivity.

higher because the source is exactly on the surface causing a lesser evaluation of the charge density.

On figure 3.19, the sensitivities $\frac{\partial V}{\partial \rho}$ calculated analytically and numerically by the IE method using equations (3.4), (3.9) and (3.17) are shown. It can be seen that the zone of negative sensitivity is also dissociated and assymmetrical compared to figure 3.18. The amplitude of the sensitivity is this time stronger near the current source.

3.4 Discussion and conclusions

A code for 3D electrical modeling, formulated using the IE developed by Snyder (1976), allows the calculation of the potential everywhere in the space without interpolation between the nodes. The calculation of the charge density is obtained by solving a linear system ($[\boldsymbol{I} + \boldsymbol{kD}]\ \boldsymbol{x} = \boldsymbol{b}$). For various configurations and different model of conductivity, only the vectors $\boldsymbol{k}$ and $\boldsymbol{b}$ need to be changed. The calculation of the charge density is validated for the layered earth, whose solution was developed by Li et Oldenburg (1991). The charge densities are of the same order of magnitude and of the same sign.

The potential obtained by the IE method is compared with the analytical and numerical solutions obtained by FD method, for a tabular medium and a vertical contact. The two numerical methods offer satisfying results. However, the IE method remains of better accuracy around the point source and in the periphery of the domain.

To store the linear system, the matrix D is compressed in CRS format with the method of pyramidal compression. For a threshold of q=0.001%, less than 40% of

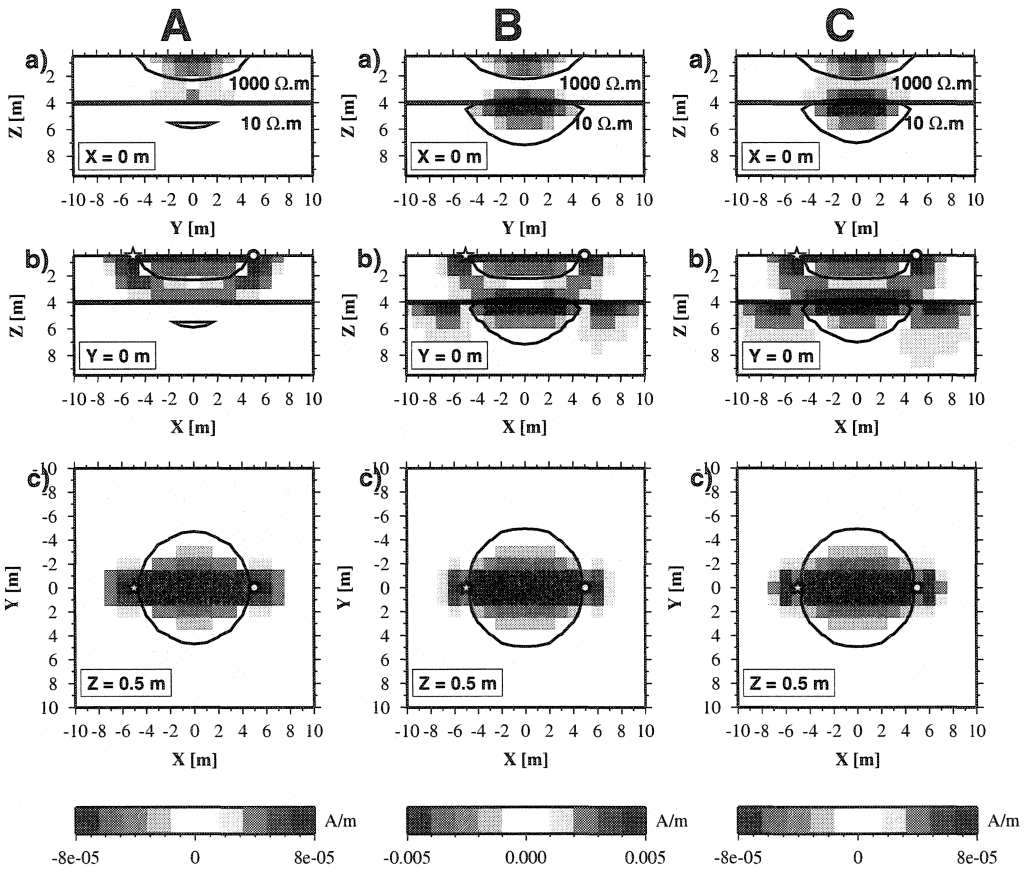

Figure 3.18: Sensitivity $\frac{\partial V}{\partial \rho}$ for a pole-pole array for the two-layer model calculated using equation (3.6). A) Analytical sensitivity. B) Sensitivity by integral method with the Green function $G(\boldsymbol{r}_i, \boldsymbol{r}_j) = \frac{1}{|r_i - r_j|}$. C) Sensitivity by integral method with the Green function $G(\boldsymbol{r}_i, \boldsymbol{r}_j) = \frac{1}{|r_i - r_j|} + \frac{1}{|r_i - r'_j|}$. Figures a) and b) correspond to sections X=0 m and Y=0 m. Figure c) displays the plan Z=0.5 m. The thick black line represents the interface between the two medium. The finer black line delineates the value of zero sensitivity.

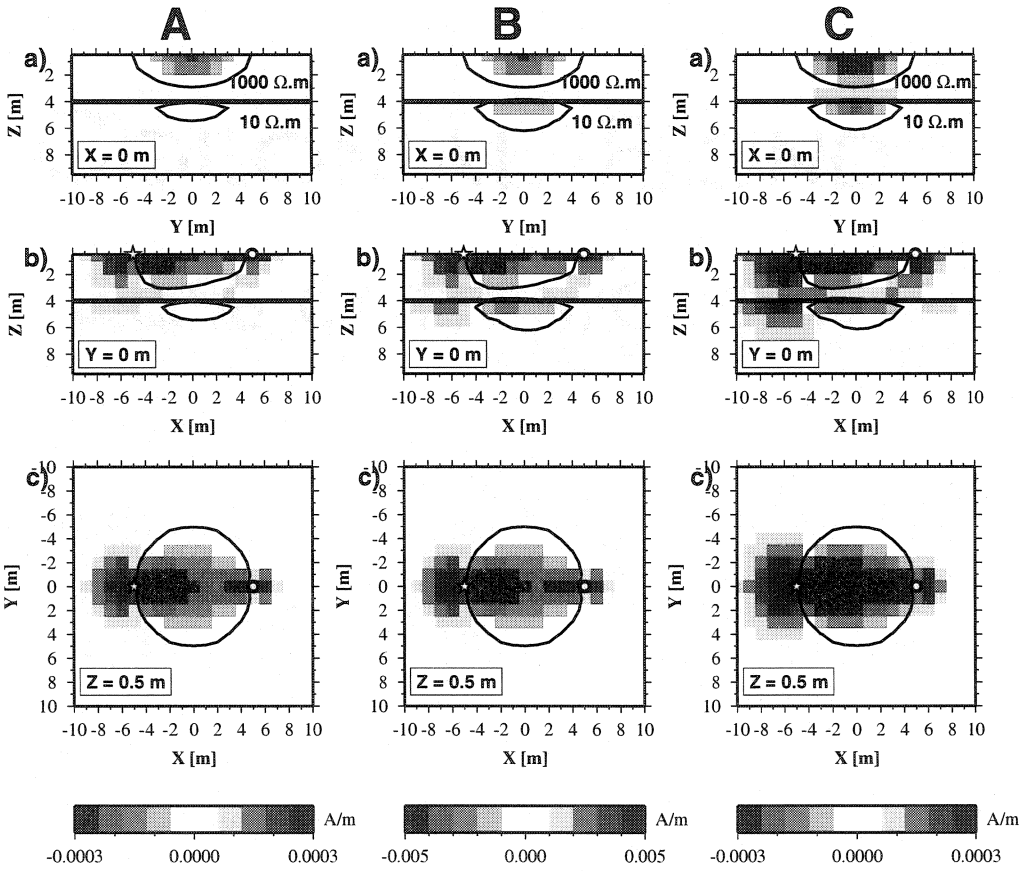

Figure 3.19: Sensitivity $\frac{\partial V}{\partial \rho}$ for a pole-pole array for the two-layered model calculated from equation (3.17). A) Analytical sensitivity. B) Sensitivity by IE method with the Green function $G(\boldsymbol{r_i}, \boldsymbol{r_j}) = \frac{1}{|r_i - r_j|}$. C) Sensitivity by IE method with the Green function $G(\boldsymbol{r_i}, \boldsymbol{r_j}) = \frac{1}{|r_i - r_j|} + \frac{1}{|r_i - r'_j|}$. Figures a) and b) correspond to sections X=0 m and Y=0 m. Figure c) displays the plan Z=0.5 m. The thick black line represents the interface between the two medium. The finer black line delineates the value of zero sensitivity.

the original matrix is stored. The resolution of the nonsymmetrical linear system is done by the "Bi-Conjugate Gradient Stabilized(l)" method with l=2.

The calculation of the sensitivity based on the IE method requires twice less calculation than that proposed by Park et Van (1991) which need two forward modeling runs to calculate the current density at the source and receiver points. For a layered earth and a vertical contact, the distribution and the amplitudes of analytically and numerically calculated sensitivities are shown. It can be noted that the sensitivity calculated with the Green's function $G(\boldsymbol{r}_i, \boldsymbol{r}_j) = \frac{1}{|\boldsymbol{r}_i - \boldsymbol{r}_j|} + \frac{1}{|\boldsymbol{r}_i - \boldsymbol{r}'_j|}$ offers a better result.

The calculation of the electric field component at a given point is obtained by the summation of all the charge densities multiplied by a surface integral. This method is satisfactory when the domain is not too large. A second method consists in taking advantage of the compressed matrix $\boldsymbol{D}$ to quickly and simultaneously calculate the three components of the electric field on the interfaces of the prisms. The three components are interpolated with a cubic spline to yield the estimates at the center of the prisms.

3.4.1 Acknowledgements

The authors thank Klaus Spitzer for his kind permission to use his 3D DC FD modeling code. The authors also thank Oleg Portniaguine to have provided them with an example and explanations on pyramidal compression and Antoine Saucier from Ecole Polytechnique for his helpful suggestions. Thanks to Mayana Kissiova for editing the manuscript. We acknowledge the anonymous referees for their valuable comments and suggestions. This work was supported by the Natural Science and Engineering Research Council of Canada (NSERC) Grant RGPIN 848

and by the Centre de Recherche en Calcul Appliqué (CERCA).

3.4.2 References

Beasley, C. W. and Ward, S. H. (1986). Three-dimensional mise-à-la-masse modeling applied to mapping fracture zones. *Geophysics*, 51(1) :98–113.

Bhattacharya, P. K. and Patra, H. P. (1968). *Direct current geoelectric sounding. Principles and interpretations*, volume 9 of *Methods in Geochemistry and Geophysics*. Elsevier Publishing Company.

Bing, Z. and Greenhalgh, S. A. (1999). Explicit expressions and numerical calculations for Frechet and second derivatives in 2.5D Helmholtz equation inversion. *Geophysical Prospecting*, 47(3) :443–468.

Bing, Z. and Greenhalgh, S. A. (2001). Finite element three-dimensional direct current resistivity modelling : accuracy and efficiency considerations. *Geophysical Journal International*, 145(3) :679–688.

Björck, A. (1996). *Numerical methods for least squares problems*. SIAM Publications.

Boerner, D. E. and West, G. F. (1989). Frechet derivatives and single scattering theory. *Geophysical Journal International*, 98 :385–390.

Brewitt-Taylor, C. R. and Weaver, J. T. (1976). On the finite difference solution of two-dimensional induction problems. *Geophysical Journal of the Royal Astronomical Society*, 47 :375–396.

Burt, P. J. and Adelson, E. H. (1983). The Laplacian pyramid as a compact image code. *IEEE Transactions on Communications*, COM-31 :337–345.

Coggon, J. H. (1971). Electromagnetic and electrical modeling by finite element method. *Geophysics*, 36(1) :132–155.

Dey, A. and Morrison, H. F. (1979a). Resistivity modeling for arbitrarily shaped three-dimensional structures. *Geophysics*, 44(4) :753–780.

Dey, A. and Morrison, H. F. (1979b). Resistivity modelling for arbitrarily shaped two-dimensional structures. *Geophysical Prospecting*, 27 :106–136.

Freund, R. and Nachtigal, N. (1991a). An implementation of the QMR method based on coupled two-term recurrences. *SIAM Journal on Scientific and Statistical Computation*, 15 :313–337.

Freund, R. and Nachtigal, N. (1991b). QMR : A quasi-minimal residual method for non-Hermitian linear systems. *Numerical Mathematics*, 60 :315–339.

Geselowitz, D. B. (1971). An application of electrocardiographic lead theory to impedance plethysmography. *IEEE Trans. Bio-Medical Engineering*, BME-18(1) :38–41.

Golub, G. H. and Van Loan, C. F. (1996). *Matrix computations*. Johns Hopkins University Press, 3 edition.

Hestenes, M. and Stiefel, E. (1952). Methods of conjugate gradients for solving linear systems. *Journal of Research of the National Bureau of Standards*, 49(6) :409–436.

Hohmann, G. W. (1975). Three-dimensional induced polarization and electromagnetic modeling. *Geophysics*, 40(2) :309–324.

Hvozdara, M. and Kaikkonen, P. (1998). An integral equations solution of the forward D.C. geoelectric problem for a 3-D body of inhomogeneous conductivity buried in a halfspace. *Journal of Applied Geophysics*, 39 :95–107.

LaBrecque, D. J., G.Morelli, Daily, W., Ramirez, A., and Lundegard, P. (1999). *Occam's Inversion of 3-D Electrical Resistivity Tomography*, pages 575–590. SEG, M. Oristaglio and B. Spies.

LaBrecque, D. J., Miletto, M., Daily, W., Ramirez, A., and Owen, E. (1996). The effects of noise on Occam's inversion of resistivity tomography data. *Geophysics*, 61(2) :538–548.

Lanczos, C. (1961). *Linear differential operators.* Van Nostrand (Dover,1997).

Lesur, V., Cuer, M., and Straub, A. (1999). 2-D and 3-D interpretation of electrical tomography measurements, Part 1 : The forward problem. *Geophysics*, 64(2) :386–395.

Li, Y. and Oldenburg, D. W. (1991). Aspects of charge accumulation in DC resistivity experiments. *Geophysical Prospecting*, 39 :803–826.

Li, Y. and Oldenburg, D. (1997). Fast inversion of large scale magnetic data using wavelets. *Expanded Abstracts, SEG*, vol. I :490–493. Dallas.

Losano, V. and Laget, B. (1996). Fractional pyramids for color image segmentation. In *Proceeding of the IEEE Southwest symposium on image analysis and interpretation, April 8-9, San Antonio, Texas*, pages 13–17.

Lowry, T., Allen, M. B., and Shive, P. N. (1989). Singularity removal : A refinement of resistivity modeling techniques. *Geophysics*, 54(6) :766–774.

McGillivray, P. and Oldenburg, D. W. (1990). Methods for calculating Frechet derivates and sensitivities for the non-linear inverse problem : a comparative study. *Geophysical Prospecting*, 38 :499–524.

Mufti, I. (1978). A practical approach to finite-difference resistivity modeling :. *Geophysics*, 43 :930–942.

Mundry, E. (1984). Geoelectrical model calculations for two-dimensional resistivity distributions. *Geophysical Prospecting*, 32 :124–131.

Murai, T. and Kagawa, Y. (1985). Electrical impedance computed tomography based on finite element model. *IEEE Transactions on Biomedical Engineering*, BME-32(3).

Nocedal, J. and Wright, S. J. (2000). *Numerical Optimization.* Springer.

Park, S. K. and Van, G. P. (1991). Inversion of pole-pole data for 3-D resistivity structure beneath arrays of electrodes. *Geophysics*, 56(7) :951–960.

Pissanetzky, S. (1984). *Sparse Matrix Technology.* Academic Press.

Poirmeur, C. and Vasseur, G. (1988). Three-dimensional modeling of a hole-to-hole electrical method : Application to the interpretation of a field survey. *Geophysics*, 53(3) :402–414.

Portniaguine, O. (1999). *Image focusing and data compression in the solution of geophysical inverse problems.* PhD thesis, University of Utah, Dept. of Geology and Geophysics.

Pratt, D. A. (1972). The surface integral approach to the solution of the 3D resistivity problem. *Bulletin of the Australian Society for Exploration Geophysics*, 3 :33–50.

Press, W. H., Teukolsky, S. A., Vetterling, W. T., and Flannery, B. P. (1992). *Numerical Recipes in C : The Art of Scientific Computing.* Cambridge University Press, 2nd edition.

Pridmore, D. F., Hohmann, G. W., Ward, S. H., and Sill, W. R. (1981). An investigation of finite-element modeling for electrical and electromagnetic data in three dimensions. *Geophysics*, 46 :1009–1024.

Raiche, A. P. (1974). An integral equation approach to three-dimensional modelling. *Geophysical Journal of the Royal Astronomical Society*, 36 :363–376.

Roy, A. and Apparao, A. (1971). Depth of investigation in direct current methods. *Geophysics*, 36(5) :943–959.

Sasaki, Y. (1992). Resolution of resistivity tomography inferred from numerical simulation. *Geophysical Prospecting*, 40 :453–463.

Sasaki, Y. (1994). 3-D resistivity inversion using the finite-element method. *Geophysics*, 59(11) :1839–1848.

Schulz, R. (1985). The method of integral equation in direct current resistivity method and its accuracy. *Journal of Geophysics*, 56 :192–200.

Scriba, H. (1981). Computation of the electric potential in three-dimensional structures. *Geophysical Prospecting*, 29 :790–802.

Seigel, H. O. (1959). Mathematical formulation and type curves for induced polarization. *Geophysics*, 24(3) :547–565.

Sleijpen, G. and Fokkema, D. (1993). BICGSTAB(l) for linear equations involving unsymmetric matrices with complex spectrum. *Electronic Transactions on Numerical Analysis*, 1 :11–32.

Snyder, D. D. (1976). A method for modeling the resistivity and IP response of two-dimensional bodies. *Geophysics*, 41 :997–1015.

Sonneveld, P. (1989). CGS, a fast Lanczos-type solver for nonsymmetric linear systems. *SIAM Journal on Scientific and Statistical Computation*, 10 :36–52.

Spiegel, R. J., Sturdivant, V. R., and Owen, T. E. (1980). Modeling resistivity anomalies from localized voids under irregular terrain. *Geophysics*, 45(7) :1164–1183.

Spitzer, K. (1995). A 3-D finite-difference algorithm for dc resistivity modelling using conjugate gradient methods. *Geophysical Journal International*, 123 :903–914.

Spitzer, K. (1998). The three-dimensional DC sensitivity for surface and subsurface sources. *Geophysical Journal International*, 134 :736–746.

Spitzer, K., Chouteau, M., and Boulanger, O. (1999). Grid-independent electrode positioning for 3D DC resistivity and IP forward modelling. In *Symposium 3DEM2, Salt Lake City, Utah*, pages 189–192.

Spitzer, K. and Wurmstich, B. (1999). Speed and accuracy in 3-D resistivity modeling. In Oristaglio, M., Pies, B., and Cooper, M. R., editors, *Three-Dimensional Electromagnetics*, number 7 in Geophysical Developments. Society of Exploration Geophysicists.

Telford, W. M., Geldart, L. P., and Sheriff, R. E. (1990). *Applied geophysics.* Cambridge University Press, 2 edition.

Ting, S. and Hohmann, G. (1981). Integral equation modeling of three-dimensional magnetotelluric response. *Geophysics*, 46 :182–197.

Van Der Vorst, H. (1992). Bi-CGSTAB : A fast and smoothly converging variant of Bi-CG for the solution of nonsymmetric linear systems. *SIAM Journal on Scientific and Statistical Computation*, 13 :631–644.

Wang, T. and Mezzatesta, A. (2001). 3D DC resistivity modeling using the sweeping-seed conjugate gradient method. *Geophysics*, 66(2) :441–447.

Wannamaker, P., Hohmann, G., and SanFilipo, W. (1984). Electromagnetic modeling of three-dimensional bodies in layered earths using integral equations. *Geophysics*, 49 :60–74.

Wurmstich, B. and Morgan, F. D. (1994). Modeling of streaming potential responses caused by oil well pumping. *Geophysics*, 59(1) :46–56.

Xiong, Z. (1989). Short note : Electromagnetic fields of electric dipoles embedded in a stratified anisotropic earth. *Geophysics*, 54 :1643–1646.

Xiong, Z. (1992a). Electromagnetic modeling of 3-D structures by the method of system iteration using integral equations. *Geophysics*, 57 :1556–1561.

Xiong, Z. (1992b). Short note : Symmetry properties of the scattering matrix in 3-D electromagnetic modeling using the integral equation method. *Geophysics*, 57 :1199–1202.

Zhang, J., Mackie, R. L., and Madden, T. R. (1995). Three-dimensional resistivity forward modeling and inversion using conjugate gradients. *Geophysics*, 60(5) :1313–1325.

Zhao, S. and Yedlin, M. J. (1996). Some refinements on the finite-difference method for 3-D resistivity modeling. *Geophysics*, 61(5) :1301–1307.

Zhdanov, M. S. and Keller, G. V. (1994). *The geoelectrical methods in geophysical exploration*, volume 31 of *Methods in geochemistry and geophysics*. Elsevier.

3.4.3 Appendix : Potential Calculation with charge density

For a dipole-dipole array the sources and receivers are located at the points A and B, and M and N, respectively. I_{AB} is the current in Ampere between electrodes A and B. σ_A is the conductivity of the cell where the source point A is located. σ_B is the conductivity of the cell where the source point B is located. The potential V_{AM}, V_{AN}, V_{BM}, V_{BN} between the different electrodes combinations is given by

$$
\begin{aligned}
V_{AM} =& \frac{I_{AB}}{4\pi\sigma_A} G(\boldsymbol{r_M}, \boldsymbol{r_A}) + \frac{1}{4\pi} \sum_{n=1}^{nx} \sum_{p=1}^{ny} \sum_{q=1}^{nz} \left[\frac{\tau^{x^-}_{n,p,q}(\boldsymbol{r_A})}{\epsilon_0} J(\boldsymbol{r_M}, x_{n-\frac{1}{2}}) + \frac{\tau^{y^-}_{n,p,q}(\boldsymbol{r_A})}{\epsilon_0} \right. \\
& \left. J(\boldsymbol{r_M}, y_{p-\frac{1}{2}}) + \frac{\tau^{z^-}_{n,p,q}(\boldsymbol{r_A})}{\epsilon_0} J(\boldsymbol{r_M}, z_{q-\frac{1}{2}}) \right] \\
V_{AN} =& \frac{I_{AB}}{4\pi\sigma_A} G(\boldsymbol{r_N}, \boldsymbol{r_A}) + \frac{1}{4\pi} \sum_{n=1}^{nx} \sum_{p=1}^{ny} \sum_{q=1}^{nz} \left[\frac{\tau^{x^-}_{n,p,q}(\boldsymbol{r_A})}{\epsilon_0} J(\boldsymbol{r_N}, x_{n-\frac{1}{2}}) + \frac{\tau^{y^-}_{n,p,q}(\boldsymbol{r_A})}{\epsilon_0} \right. \\
& \left. J(\boldsymbol{r_N}, y_{p-\frac{1}{2}}) + \frac{\tau^{z^-}_{n,p,q}(\boldsymbol{r_A})}{\epsilon_0} J(\boldsymbol{r_N}, z_{q-\frac{1}{2}}) \right] \\
V_{BM} =& \frac{I_{AB}}{4\pi\sigma_B} G(\boldsymbol{r_M}, \boldsymbol{r_B}) + \frac{1}{4\pi} \sum_{n=1}^{nx} \sum_{p=1}^{ny} \sum_{q=1}^{nz} \left[\frac{\tau^{x^-}_{n,p,q}(\boldsymbol{r_B})}{\epsilon_0} J(\boldsymbol{r_M}, x_{n-\frac{1}{2}}) + \frac{\tau^{y^-}_{n,p,q}(\boldsymbol{r_B})}{\epsilon_0} \right. \\
& \left. J(\boldsymbol{r_M}, y_{p-\frac{1}{2}}) + \frac{\tau^{z^-}_{n,p,q}(\boldsymbol{r_B})}{\epsilon_0} J(\boldsymbol{r_M}, z_{q-\frac{1}{2}}) \right] \\
V_{BN} =& \frac{I_{AB}}{4\pi\sigma_B} G(\boldsymbol{r_N}, \boldsymbol{r_B}) + \frac{1}{4\pi} \sum_{n=1}^{nx} \sum_{p=1}^{ny} \sum_{q=1}^{nz} \left[\frac{\tau^{x^-}_{n,p,q}(\boldsymbol{r_B})}{\epsilon_0} J(\boldsymbol{r_N}, x_{n-\frac{1}{2}}) + \frac{\tau^{y^-}_{n,p,q}(\boldsymbol{r_B})}{\epsilon_0} \right. \\
& \left. J(\boldsymbol{r_N}, y_{p-\frac{1}{2}}) + \frac{\tau^{z^-}_{n,p,q}(\boldsymbol{r_B})}{\epsilon_0} J(\boldsymbol{r_N}, z_{q-\frac{1}{2}}) \right]
\end{aligned}
$$

The potential ΔV calculated for any array for four electrodes is $\Delta V = (V_{AM} - V_{AN}) - (V_{BM} - V_{BN})$.

3.4.4 Appendix : Surface integrals for Green function and its gradients

The Green function $G(\boldsymbol{r_i}, \boldsymbol{r_j})$ is written with $|\boldsymbol{r_i} - \boldsymbol{r_j}| = [(x_i - x_j)^2 + (y_i - y_j)^2 + (z_i - z_j)^2]^{1/2}$ and $|\boldsymbol{r_i} - \boldsymbol{r'_j}| = [(x_i - x_j)^2 + (y_i - y_j)^2 + (z_i + z_j)^2]^{1/2}$

$$G(\boldsymbol{r_i}, \boldsymbol{r_j}) = \frac{1}{|\boldsymbol{r_i} - \boldsymbol{r_j}|} + \frac{1}{|\boldsymbol{r_i} - \boldsymbol{r'_j}|}$$

In the case where $G(\boldsymbol{r_i}, \boldsymbol{r_j}) = \frac{1}{|\boldsymbol{r_i} - \boldsymbol{r_j}|}$, the terms associated with the vector $|r_i - r'_j|$ in the integrals $J^a(\boldsymbol{r_i}, .)$ and $J(\boldsymbol{r_i}, .)$ are neglected.

The various integrals depending on the minimum (m) and maximum (M) boundaries are :

$$\begin{aligned}
J^a_x(\boldsymbol{r_i}, x_j) &= \int_{z_m}^{z_M} \int_{y_m}^{y_M} \partial_{x_i} G(\boldsymbol{r_i}, \boldsymbol{r_j})\, dy_j dz_j \\
&= \left| \left| -atan\Big(\frac{bc}{a\ |\boldsymbol{r_i} - \boldsymbol{r_j}|}\Big) + atan\Big(\frac{bd}{a\ |\boldsymbol{r_i} - \boldsymbol{r'_j}|}\Big) \right|_{y_m}^{y_M} \right|_{z_m}^{z_M} \\
J^a_y(\boldsymbol{r_i}, y_j) &= \int_{x_m}^{x_M} \int_{z_m}^{z_M} \partial_{y_i} G(\boldsymbol{r_i}, \boldsymbol{r_j})\, dz_j dx_j \\
&= \left| \left| -atan\Big(\frac{ca}{b\ |\boldsymbol{r_i} - \boldsymbol{r_j}|}\Big) + atan\Big(\frac{da}{b\ |\boldsymbol{r_i} - \boldsymbol{r'_j}|}\Big) \right|_{z_m}^{z_M} \right|_{x_m}^{x_M} \\
J^a_z(\boldsymbol{r_i}, z_j) &= \int_{y_m}^{y_M} \int_{x_m}^{x_M} \partial_{z_i} G(\boldsymbol{r_i}, \boldsymbol{r_j})\, dx_j dy_j \\
&= \left| \left| -atan\Big(\frac{ab}{c\ |\boldsymbol{r_i} - \boldsymbol{r_j}|}\Big) - atan\Big(\frac{ab}{d\ |\boldsymbol{r_i} - \boldsymbol{r'_j}|}\Big) \right|_{x_m}^{x_M} \right|_{y_m}^{y_M}
\end{aligned}$$

$$J_x^a(\boldsymbol{r_i}, y_j) = \int_{z_m}^{z_M} \int_{x_m}^{x_M} \partial_{x_i} G(\boldsymbol{r_i}, \boldsymbol{r_j})\ dx_j dz_j$$
$$= \left| \left| ln(c + |\boldsymbol{r_i} - \boldsymbol{r_j}|) - ln(d + |\boldsymbol{r_i} - \boldsymbol{r'_j}|) \right|_{x_m}^{x_M} \right|_{z_m}^{z_M}$$

$$J_y^a(\boldsymbol{r_i}, z_j) = \int_{x_m}^{x_M} \int_{y_m}^{y_M} \partial_{y_i} G(\boldsymbol{r_i}, \boldsymbol{r_j})\ dy_j dx_j$$
$$= \left| \left| ln(a + |\boldsymbol{r_i} - \boldsymbol{r_j}|) + ln(a + |\boldsymbol{r_i} - \boldsymbol{r'_j}|) \right|_{y_m}^{y_M} \right|_{x_m}^{x_M}$$

$$J_z^a(\boldsymbol{r_i}, x_j) = \int_{y_m}^{y_M} \int_{z_m}^{z_M} \partial_{z_i} G(\boldsymbol{r_i}, \boldsymbol{r_j})\ dz_j dy_j$$
$$= \left| \left| ln(b + |\boldsymbol{r_i} - \boldsymbol{r_j}|) - ln(b + |\boldsymbol{r_i} - \boldsymbol{r'_j}|) \right|_{z_m}^{z_M} \right|_{y_m}^{y_M}$$

$$J_x^a(\boldsymbol{r_i}, z_j) = \int_{y_m}^{y_M} \int_{x_m}^{x_M} \partial_{x_i} G(\boldsymbol{r_i}, \boldsymbol{r_j})\ dx_j dy_j$$
$$= \left| \left| ln(b + |\boldsymbol{r_i} - \boldsymbol{r_j}|) + ln(b + |\boldsymbol{r_i} - \boldsymbol{r'_j}|) \right|_{x_m}^{x_M} \right|_{y_m}^{y_M}$$

$$J_y^a(\boldsymbol{r_i}, x_j) = \int_{z_m}^{z_M} \int_{y_m}^{y_M} \partial_{y_i} G(\boldsymbol{r_i}, \boldsymbol{r_j})\ dy_j dz_j$$
$$= \left| \left| ln(c + |\boldsymbol{r_i} - \boldsymbol{r_j}|) - ln(d + |\boldsymbol{r_i} - \boldsymbol{r'_j}|) \right|_{y_m}^{y_M} \right|_{z_m}^{z_M}$$

$$J_z^a(\boldsymbol{r_i}, y_j) = \int_{x_m}^{x_M} \int_{z_m}^{z_M} \partial_{z_i} G(\boldsymbol{r_i}, \boldsymbol{r_j})\ dz_j dx_j$$
$$= \left| \left| ln(a + |\boldsymbol{r_i} - \boldsymbol{r_j}|) - ln(a + |\boldsymbol{r_i} - \boldsymbol{r'_j}|) \right|_{z_m}^{z_M} \right|_{x_m}^{x_M}$$

$$
\begin{aligned}
J(\boldsymbol{r_i}, z_j) &= \int_{x_m}^{x_M} \int_{y_m}^{y_M} G(\boldsymbol{r_i}, \boldsymbol{r_j})\, dy_j dx_j \\
&= \Bigg| -c\ atan\Big(\frac{ab}{c|\boldsymbol{r_i} - \boldsymbol{r_j}|}\Big) - d\ atan\Big(\frac{ab}{d|\boldsymbol{r_i} - \boldsymbol{r'_j}|}\Big) \\
&+ b\ ln(a + |\boldsymbol{r_i} - \boldsymbol{r_j}|) + a\ ln(b + |\boldsymbol{r_i} - \boldsymbol{r_j}|) \\
&+ b\ ln(a + |\boldsymbol{r_i} - \boldsymbol{r'_j}|) + a\ ln(b + |\boldsymbol{r_i} - \boldsymbol{r'_j}|)\Big|_{y_m}^{y_M}\Bigg|_{x_m}^{x_M}
\end{aligned}
$$

$$
\begin{aligned}
J(\boldsymbol{r_i}, x_j) &= \int_{y_m}^{y_M} \int_{z_m}^{z_M} G(\boldsymbol{r_i}, \boldsymbol{r_j})\, dz_j dy_j \\
&= \Bigg| -a\ atan\Big(\frac{bc}{a|\boldsymbol{r_i} - \boldsymbol{r_j}|}\Big) + a\ atan\Big(\frac{bd}{a|\boldsymbol{r_i} - \boldsymbol{r'_j}|}\Big) \\
&+ c\ ln(b + |\boldsymbol{r_i} - \boldsymbol{r_j}|) + b\ ln(c + |\boldsymbol{r_i} - \boldsymbol{r_j}|) \\
&- d\ ln(b + |\boldsymbol{r_i} - \boldsymbol{r'_j}|) - b\ ln(d + |\boldsymbol{r_i} - \boldsymbol{r'_j}|)\Big|_{z_m}^{z_M}\Bigg|_{y_m}^{y_M}
\end{aligned}
$$

$$
\begin{aligned}
J(\boldsymbol{r_i}, y_j) &= \int_{z_m}^{z_M} \int_{x_m}^{x_M} G(\boldsymbol{r_i}, \boldsymbol{r_j})\, dx_j dz_j \\
&= \Bigg| -b\ atan\Big(\frac{ca}{b|\boldsymbol{r_i} - \boldsymbol{r_j}|}\Big) + b\ atan\Big(\frac{da}{b|\boldsymbol{r_i} - \boldsymbol{r'_j}|}\Big) \\
&+ a\ ln(c + |\boldsymbol{r_i} - \boldsymbol{r_j}|) + c\ ln(a + |\boldsymbol{r_i} - \boldsymbol{r_j}|) \\
&- a\ ln(d + |\boldsymbol{r_i} - \boldsymbol{r'_j}|) - d\ ln(a + |\boldsymbol{r_i} - \boldsymbol{r'_j}|)\Big|_{x_m}^{x_M}\Bigg|_{z_m}^{z_M}
\end{aligned}
$$

with $a = x_i - x_j$, $b = y_i - y_j$, $c = z_i - z_j$ et $d = z_i + z_j$.

Singular points can be observed for the preceding integrals when the point (x, y, z) approaches the origin. Singularities are resolved analytically.

Singularity 1

Considering the integral

$$J(\boldsymbol{r}, z) = \int_{-a}^{a} \int_{-a}^{a} \frac{dxdy}{(x^2 + y^2 + z^2)^{1/2}}$$

For $z = 0$,

$$J(\boldsymbol{r}, 0) = \int_{-a}^{a} \int_{-a}^{a} \frac{dxdy}{(x^2 + y^2)^{1/2}}$$

The change of variables $x = a\ \tilde{x}$ and $y = a\ \tilde{y}$ leads to

$$\begin{aligned} J(\boldsymbol{r}, 0) &= a \int_{-1}^{+1} \int_{-1}^{+1} \frac{d\tilde{x}d\tilde{y}}{(\tilde{x}^2 + \tilde{y}^2)^{1/2}} \\ &= 4a \int_{0}^{+1} \int_{0}^{+1} \frac{d\tilde{x}d\tilde{y}}{(\tilde{x}^2 + \tilde{y}^2)^{1/2}} \end{aligned}$$

because the integral is an even function of $\tilde{x}$ and $\tilde{y}$. If we use polar coordinates ($\tilde{x} = r\ cos(\theta)$ and $\tilde{y} = r\ sin(\theta)$) and if we integrate over a disc instead of a square, then we get the approximation

$$J(\boldsymbol{r}, 0) \simeq \int_{0}^{\delta} \int_{0}^{2\pi} \frac{r\ dr\ d\theta}{r} = 2\pi\delta$$

Assuming that the surface of the disc is equal to the surface of the square ($\pi\delta^2 = 4a^2$), we get

$$J(\boldsymbol{r}, 0) \simeq 4\sqrt{\pi}a \equiv 7.0898\ a$$

$J(\boldsymbol{r}, 0)$ can be calculated exactly. Indeed,

$$
\begin{aligned}
J(\boldsymbol{r},0) &= 4a \int_0^{+1}\int_0^{+1} \frac{d\tilde{x}\ d\tilde{y}}{(\tilde{x}^2+\tilde{y}^2)^{1/2}} \\
&= 4a \int_{\theta=0}^{\theta=\pi/2}\int_{r=0}^{r=r(\theta)} \frac{r\ dr\ d\theta}{r} \\
&= 4a \int_{\theta=0}^{\theta=\pi/2} d\theta \int_{r=0}^{r=r(\theta)} dr \\
&= 4a \int_{\theta=0}^{\theta=\pi/2} r(\theta) d\theta
\end{aligned}
$$

The integration is made in two stages on the square domain for $(x,y) \in [0,1]$x$[0,1]$. If $0 \leq \theta \leq \frac{\pi}{4}$ then $r(\theta) = \frac{1}{cos(\theta)}$. If $\frac{\pi}{4} \leq \theta \leq \frac{\pi}{2}$ then $r(\theta) = \frac{1}{cos(\frac{\pi}{2}-\theta)} = \frac{1}{sin(\theta)}$. Hence

$$
J(\boldsymbol{r},0) = 4a\Big[\int_{\theta=0}^{\theta=\pi/4} \frac{d\theta}{cos(\theta)} + \int_{\theta=\pi/4}^{\theta=\pi/2} \frac{d\theta}{sin(\theta)}\Big]
$$

which yields

$$
J(\boldsymbol{r},0) = 4a\Big[asinh(1) + ln(cotan(\frac{\pi}{8}))\Big] \ \simeq 7.05099\ a
$$

Singularity 2

We consider

$$
J_x^a(\boldsymbol{r},x) = \int_{-a}^{+a}\int_{-a}^{+a} \frac{x\ dy\ dz}{(x^2+y^2+z^2)^{3/2}}
$$

where $a > 0$. We want to calculate $\lim_{x\to 0} J_x^a(\boldsymbol{r},x)$. The change of variables $y = x\ \tilde{y}$ and $z = x\ \tilde{z}$ leads to

$$
J_x^a(\boldsymbol{r},x) = sgn(x) \int_{-\frac{a}{x}}^{+\frac{a}{x}}\int_{-\frac{a}{x}}^{+\frac{a}{x}} \frac{d\tilde{y}\ d\tilde{z}}{(1+\tilde{y}^2+\tilde{z}^2)^{3/2}}
$$

where $sgn(x) = \frac{x^3}{|x|^3}$ denotes the sign of x. If $x > 0$, we have

$$\lim_{x \to 0^+} J_x^a(\boldsymbol{r}, x) = sgn(x) \int_{-\infty}^{+\infty} \int_{-\infty}^{+\infty} \frac{d\tilde{y}\ d\tilde{z}}{(1 + \tilde{y}^2 + \tilde{z}^2)^{3/2}}$$

Using polar coordinates ($\tilde{y} = r\ cos(\theta)$ and $\tilde{z} = r\ sin(\theta)$), we have

$$\begin{aligned} J_x^a(\boldsymbol{r}, 0^+) &= \int_0^{+\infty} \int_0^{2\pi} \frac{r dr d\theta}{(1 + r^2)^{3/2}} \\ &= 2\pi \left| \frac{-1}{\sqrt{1 + r^2}} \right|_0^{+\infty} \\ &= 2\pi \end{aligned}$$

Similarly, we get $J_x^a(\boldsymbol{r}, 0^-) = -2\pi$. It follows that $\lim_{x \to 0} J_x^a(\boldsymbol{r}, x)$ does not exist since

$$\begin{cases} J_x^a(\boldsymbol{r}, 0^+) = +2\pi \\ J_x^a(\boldsymbol{r}, 0^-) = -2\pi \end{cases} \tag{3.34}$$

The result is the same for $\frac{1}{|\boldsymbol{r_i} - \boldsymbol{r_j}|}$ and $\frac{1}{|\boldsymbol{r_i} - \boldsymbol{r'_j}|}$. It follows that if $G(\boldsymbol{r_i}, \boldsymbol{r_j}) = \frac{1}{|\boldsymbol{r_i} - \boldsymbol{r_j}|} + \frac{1}{|\boldsymbol{r_i} - \boldsymbol{r'_j}|}$, then

$$\begin{cases} J_x^a(\boldsymbol{r}, 0^+) = +4\pi \\ J_x^a(\boldsymbol{r}, 0^-) = -4\pi \end{cases} \tag{3.35}$$

The results (3.34) and (3.35) reflect the discontinuity of the electric field when crossing an electrically charged interface at the junction of two adjacents cells.

Singularity 3

Considering the integral

$$J_x^a(\boldsymbol{r}, y) = \int_{-a}^{+a} \int_{-a}^{+a} \frac{x \; dx \; dz}{(x^2 + y^2 + z^2)^{3/2}} \; ,$$

we want to calculate $\lim_{y \to 0} J_x^a(\boldsymbol{r}, y)$. We have

$$\begin{aligned} J_x^a(\boldsymbol{r}, y) &= \int_{-a}^{+a} x \; dx \int_{-a}^{+a} \frac{dz}{(x^2 + y^2 + z^2)^{3/2}} \\ &= \int_{-a}^{+a} x \; f(x^2 + y^2) \; dx \end{aligned}$$

The function $xf(x^2 + y^2)$, seen as a function of x, is odd, therefore

$$\forall y \in R, J_x^a(\boldsymbol{r}, y) = 0$$

3.4.5 Appendix : Sensitivity coefficient for a homogeneous medium

$$
\begin{aligned}
\frac{\partial V_{d-d}}{\partial \rho} = \int_v dv \; \frac{I}{16\pi^2} \times \\
\Bigg[\Bigg[\Bigg(&\frac{[K_{s_1,r_1} + (z_k - z_{s_1})(z_k - z_{r_1})]}{|\boldsymbol{r_{i,j,k}} - \boldsymbol{r_{s_1}}|^3 \, |\boldsymbol{r_{i,j,k}} - \boldsymbol{r_{r_1}}|^3} + \frac{[K_{s_1,r_1} + (z_k + z_{s_1})(z_k - z_{r_1})]}{|\boldsymbol{r_{i,j,k}} - \boldsymbol{r'_{s_1}}|^3 \, |\boldsymbol{r_{i,j,k}} - \boldsymbol{r_{r_1}}|^3} \\
+ &\frac{[K_{s_1,r_1} + (z_k - z_{s_1})(z_k + z_{r_1})]}{|\boldsymbol{r_{i,j,k}} - \boldsymbol{r_{s_1}}|^3 \, |\boldsymbol{r_{i,j,k}} - \boldsymbol{r'_{r_1}}|^3} + \frac{[K_{s_1,r_1} + (z_k + z_{s_1})(z_k + z_{r_1})]}{|\boldsymbol{r_{i,j,k}} - \boldsymbol{r'_{s_1}}|^3 \, |\boldsymbol{r_{i,j,k}} - \boldsymbol{r'_{r_1}}|^3}\Bigg) \\
-\Bigg(&\frac{[K_{s_2,r_1} + (z_k - z_{s_2})(z_k - z_{r_1})]}{|\boldsymbol{r_{i,j,k}} - \boldsymbol{r_{s_2}}|^3 \, |\boldsymbol{r_{i,j,k}} - \boldsymbol{r_{r_1}}|^3} + \frac{[K_{s_2,r_1} + (z_k + z_{s_2})(z_k - z_{r_1})]}{|\boldsymbol{r_{i,j,k}} - \boldsymbol{r'_{s_2}}|^3 \, |\boldsymbol{r_{i,j,k}} - \boldsymbol{r_{r_1}}|^3} \\
+ &\frac{[K_{s_2,r_1} + (z_k - z_{s_2})(z_k + z_{r_1})]}{|\boldsymbol{r_{i,j,k}} - \boldsymbol{r_{s_2}}|^3 \, |\boldsymbol{r_{i,j,k}} - \boldsymbol{r'_{r_1}}|^3} + \frac{[K_{s_2,r_1} + (z_k + z_{s_2})(z_k + z_{r_1})]}{|\boldsymbol{r_{i,j,k}} - \boldsymbol{r'_{s_2}}|^3 \, |\boldsymbol{r_{i,j,k}} - \boldsymbol{r'_{r_1}}|^3}\Bigg)\Bigg] \\
-\Bigg[\Bigg(&\frac{[K_{s_1,r_2} + (z_k - z_{s_1})(z_k - z_{r_2})]}{|\boldsymbol{r_{i,j,k}} - \boldsymbol{r_{s_1}}|^3 \, |\boldsymbol{r_{i,j,k}} - \boldsymbol{r_{r_2}}|^3} + \frac{[K_{s_1,r_2} + (z_k + z_{s_1})(z_k - z_{r_2})]}{|\boldsymbol{r_{i,j,k}} - \boldsymbol{r'_{s_1}}|^3 \, |\boldsymbol{r_{i,j,k}} - \boldsymbol{r_{r_2}}|^3} \\
+ &\frac{[K_{s_1,r_2} + (z_k - z_{s_1})(z_k + z_{r_2})]}{|\boldsymbol{r_{i,j,k}} - \boldsymbol{r_{s_1}}|^3 \, |\boldsymbol{r_{i,j,k}} - \boldsymbol{r'_{r_2}}|^3} + \frac{[K_{s_1,r_2} + (z_k + z_{s_1})(z_k + z_{r_2})]}{|\boldsymbol{r_{i,j,k}} - \boldsymbol{r'_{s_1}}|^3 \, |\boldsymbol{r_{i,j,k}} - \boldsymbol{r'_{r_2}}|^3}\Bigg) \\
-\Bigg(&\frac{[K_{s_2,r_2} + (z_k - z_{s_2})(z_k - z_{r_2})]}{|\boldsymbol{r_{i,j,k}} - \boldsymbol{r_{s_2}}|^3 \, |\boldsymbol{r_{i,j,k}} - \boldsymbol{r_{r_2}}|^3} + \frac{[K_{s_2,r_2} + (z_k + z_{s_2})(z_k - z_{r_2})]}{|\boldsymbol{r_{i,j,k}} - \boldsymbol{r'_{s_2}}|^3 \, |\boldsymbol{r_{i,j,k}} - \boldsymbol{r_{r_2}}|^3} \\
+ &\frac{[K_{s_2,r_2} + (z_k - z_{s_2})(z_k + z_{r_2})]}{|\boldsymbol{r_{i,j,k}} - \boldsymbol{r_{s_2}}|^3 \, |\boldsymbol{r_{i,j,k}} - \boldsymbol{r'_{r_2}}|^3} + \frac{[K_{s_2,r_2} + (z_k + z_{s_2})(z_k + z_{r_2})]}{|\boldsymbol{r_{i,j,k}} - \boldsymbol{r'_{s_2}}|^3 \, |\boldsymbol{r_{i,j,k}} - \boldsymbol{r'_{r_2}}|^3}\Bigg)\Bigg]\Bigg]
\end{aligned}
$$

where $K_{s_u,r_w} = (x_i - x_{s_u})(x_i - x_{r_w}) + (y_j - y_{s_w})(y_j - y_{r_w})$, $|\boldsymbol{r_{i,j,k}} - \boldsymbol{r_{s_u}}| = ((x_i - x_{s_u})^2 + (y_j - y_{s_u})^2 + (z_k - z_{s_u})^2)^{1/2}$, $|\boldsymbol{r_{i,j,k}} - \boldsymbol{r'_{s_u}}| = ((x_i - x_{s_u})^2 + (y_j - y_{s_u})^2 + (z_k + z_{s_u})^2)^{1/2}$, $|\boldsymbol{r_{i,j,k}} - \boldsymbol{r_{r_w}}| = ((x_i - x_{r_w})^2 + (y_j - y_{r_w})^2 + (z_k - z_{r_w})^2)^{1/2}$ and $|\boldsymbol{r_{i,j,k}} - \boldsymbol{r'_{r_w}}| = ((x_i - x_{r_w})^2 + (y_j - y_{r_w})^2 + (z_k + z_{r_w})^2)^{1/2}$. The indices u and w take values 1 (polar case) and 2 (dipolar case).

3.4.6 Appendix : Sensitivity for the two-layer model

The formulation of the analytical potential for a two-layer model is given in Bhattacharya et Patra (1968); Zhdanov et Keller (1994) and in Roy et Apparao (1971). The layered medium consists of a layer with a thickness h and a resistivity ρ_1 overlying an infinite half space of resistivity ρ_2. The reflexion coefficient is $k = \frac{\rho_2-\rho_1}{\rho_2+\rho_1}$ ($\frac{\rho_2}{\rho_1} = \frac{1+k}{1-k}$). For a source +I located on the surface at $(x_s, y_s, 0)$, the potential $V_{1,s}$ and $V_{2,s}$ for any point (x, yz) are given below, while posing $|\boldsymbol{r} - \boldsymbol{r_s}| = [(x - x_s)^2 + (y - y_s)^2 + z^2]^{1/2}$, $|\boldsymbol{r} - \boldsymbol{r'_s}| = [(x - x_s)^2 + (y - y_s)^2 + (z + 2nh)^2]^{1/2}$ and $|\boldsymbol{r} - \boldsymbol{r''_s}| = [(x - x_s)^2 + (y - y_s)^2 + (z - 2nh)^2]^{1/2}$.

$$V_{1,s} = \frac{\rho_1 I}{2\pi}\Big[\frac{1}{|\boldsymbol{r} - \boldsymbol{r_s}|} + \sum_{n=1}^{\infty}\frac{k^n}{|\boldsymbol{r} - \boldsymbol{r'_s}|} + \sum_{n=1}^{\infty}\frac{k^n}{|\boldsymbol{r} - \boldsymbol{r''_s}|}\Big]$$

for $0 \leq z \leq h$, and

$$V_{2,s} = \frac{\rho_2 I(1-k)}{2\pi}\Big[\frac{1}{|\boldsymbol{r} - \boldsymbol{r_s}|} + \sum_{n=1}^{\infty}\frac{k^n}{|\boldsymbol{r} - \boldsymbol{r'_s}|}\Big]$$

for $z \geq h$. The current density due to a source located at the point $(x_s, y_s, 0)$ is expressed for medium 1 ($\boldsymbol{j}_{1,s} = \sigma_1 \boldsymbol{E}_{1,s}$) and medium 2 ($\boldsymbol{j}_{2,s} = \sigma_2 \boldsymbol{E}_{2,s}$) as

$$\boldsymbol{j}_{1,s} = \begin{cases} j_{1,x_s} &= \frac{I}{2\pi}\Big[\frac{(x-x_s)}{|\boldsymbol{r}-\boldsymbol{r_s}|^3} + \sum_{n=1}^{\infty}\frac{(x-x_s)k^n}{|\boldsymbol{r}-\boldsymbol{r'_s}|^3} + \sum_{n=1}^{\infty}\frac{(x-x_s)k^n}{|\boldsymbol{r}-\boldsymbol{r''_s}|^3}\Big] \\ j_{1,y_s} &= \frac{I}{2\pi}\Big[\frac{(y-y_s)}{|\boldsymbol{r}-\boldsymbol{r_s}|^3} + \sum_{n=1}^{\infty}\frac{(y-y_s)k^n}{|\boldsymbol{r}-\boldsymbol{r'_s}|^3} + \sum_{n=1}^{\infty}\frac{(y-y_s)k^n}{|\boldsymbol{r}-\boldsymbol{r''_s}|^3}\Big] \\ j_{1,z_s} &= \frac{I}{2\pi}\Big[\frac{z}{|\boldsymbol{r}-\boldsymbol{r_s}|^3} + \sum_{n=1}^{\infty}\frac{(z+2nh)k^n}{|\boldsymbol{r}-\boldsymbol{r'_s}|^3} + \sum_{n=1}^{\infty}\frac{(z-2nh)k^n}{|\boldsymbol{r}-\boldsymbol{r''_s}|^3}\Big] \end{cases}$$

for $0 \leq z \leq h$, and

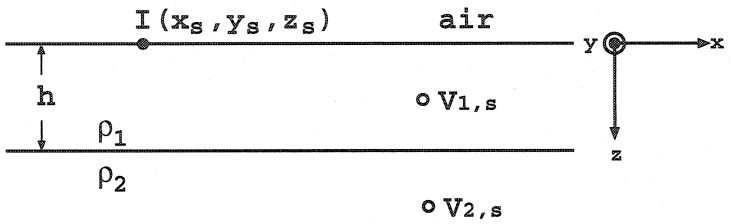

Figure 3.20: Two-layer model made up of a top layer with thickness h and resistivity ρ_1 overlying a half space of infinite resistivity ρ_2. The current is transmitted at the location $I(x_s, y_s, z_s)$ and the potential is observed at points $V_{1,s}$ and $V_{2,s}$.

$$\boldsymbol{j}_{2,s} = \begin{cases} j_{2,x_s} &= \frac{I(1-k)}{2\pi}\left[\frac{(x-x_s)}{|\boldsymbol{r}-\boldsymbol{r_s}|^3} + \sum_{n=1}^{\infty}\frac{(x-x_s)k^n}{|\boldsymbol{r}-\boldsymbol{r'_s}|^3}\right] \\ j_{2,y_s} &= \frac{I(1-k)}{2\pi}\left[\frac{(y-y_s)}{|\boldsymbol{r}-\boldsymbol{r_s}|^3} + \sum_{n=1}^{\infty}\frac{(y-y_s)k^n}{|\boldsymbol{r}-\boldsymbol{r'_s}|^3}\right] \\ j_{2,z_s} &= \frac{I(1-k)}{2\pi}\left[\frac{z}{|\boldsymbol{r}-\boldsymbol{r_s}|^3} + \sum_{n=1}^{\infty}\frac{(z+2nh)k^n}{|\boldsymbol{r}-\boldsymbol{r'_s}|^3}\right] \end{cases}$$

for $z \geq h$. For a fictitious source located at the point (x_r, y_r, z_r), s is replaced by r.

3.4.7 Appendix : Sensitivity for a vertical contact

The solution of the potential for a vertical contact is given by the authors Telford *et al.* (1990); Zhdanov et Keller (1994). The two quarter-spaces have a resistivity of ρ_1 and ρ_2. d is the distance between the source and the vertical contact. Writing $k_s = \frac{\rho_2 - \rho_1}{\rho_2 + \rho_1}$, $|\boldsymbol{r} - \boldsymbol{r_s}| = [(x - x_s)^2 + (y - y_s)^2 + z^2]^{1/2}$ and $|\boldsymbol{r} - \boldsymbol{r'_s}| = [(2d + x_s - x)^2 + (y - y_s)^2 + z^2]^{1/2}$. d is the distance between the point source and the vertical contact. For a source located in medium 1 and 2, the potentials are written

$$V_{1,s} = \frac{\rho_1 I}{2\pi}\left[\frac{1}{|\boldsymbol{r} - \boldsymbol{r_s}|} + \frac{k_s}{|\boldsymbol{r} - \boldsymbol{r'_s}|}\right]$$

and

$$V_{2,s} = \frac{\rho_2 I(1 - k_s)}{2\pi}\frac{1}{|\boldsymbol{r} - \boldsymbol{r_s}|}$$

The current density due to a source located at (x_s, y_s, z_s) is expressed by

$$\boldsymbol{j}_{1,s} = \begin{cases} j_{1,x_s} &= \frac{I}{2\pi}\left[\frac{(x-x_s)}{|\boldsymbol{r}-\boldsymbol{r_s}|^3} - \frac{k_s(2d+x_s-x)}{|\boldsymbol{r}-\boldsymbol{r'_s}|^3}\right] \\ j_{1,y_s} &= \frac{I}{2\pi}\left[\frac{(y-y_s)}{|\boldsymbol{r}-\boldsymbol{r_s}|^3} + \frac{k_s(y-y_s)}{|\boldsymbol{r}-\boldsymbol{r'_s}|^3}\right] \\ j_{1,z_s} &= \frac{I}{2\pi}\left[\frac{(z-z_s)}{|\boldsymbol{r}-\boldsymbol{r_s}|^3} + \frac{k_s(z-z_s)}{|\boldsymbol{r}-\boldsymbol{r'_s}|^3}\right] \end{cases}$$

and

$$\boldsymbol{j}_{2,s} = \begin{cases} j_{2,x_s} &= \frac{I(1-k_s)}{2\pi}\frac{(x-x_s)}{|\boldsymbol{r}-\boldsymbol{r_s}|^3} \\ j_{2,y_s} &= \frac{I(1-k_s)}{2\pi}\frac{(y-y_s)}{|\boldsymbol{r}-\boldsymbol{r_s}|^3} \\ j_{2,z_s} &= \frac{I(1-k_s)}{2\pi}\frac{(z-z_s)}{|\boldsymbol{r}-\boldsymbol{r_s}|^3} \end{cases}$$

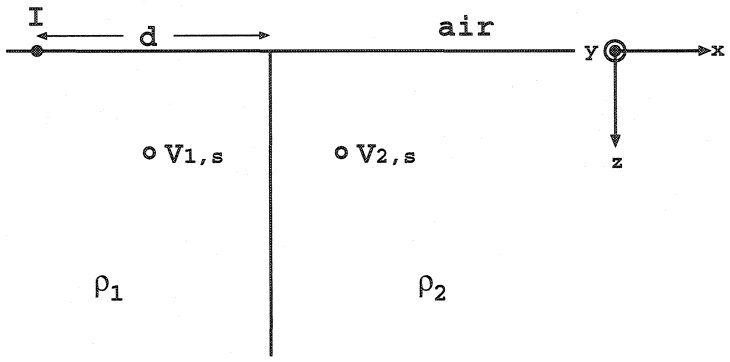

Figure 3.21: The vertical contact model with resistivities of ρ_1 and ρ_2. The current is transmitted at the location $I(x_s, y_s, z_s)$ and the potential is observed at points $V_{1,s}$ and $V_{2,s}$.

For a fictitious source located in medium 2 at the point (x_r, y_r, z_r), we replace s by r and k_r by $-k_s$.

3.4.8 Appendix : Algorithms of pyramidal compression

Algorithms 1 and 2 generate the matrix of compression $\boldsymbol{W_k}$ and $\boldsymbol{W_k^T}$ on the level k, respectively. Algorithm 3 calculates the product $\boldsymbol{Wx}$ on the level k. Algorithm 4 calculates the product $\boldsymbol{xW}$ and $\boldsymbol{W^Tx}$ on the level k. The level k is determined by the relation $k = floor\left[\frac{log(n-1)}{log(2)}\right]$ with $n = length(x_{in})$.

Algorithm 1 Matrix of compression $W(x_{in}, k)$ on the level k

$n = length(x_{in})$
$\delta = 2^{k-1}$
for $i = 1 : n$ **do**
  $W(i, i) = 1$
end for
for $i = 1 + \delta : 2\delta : n - \delta$ **do**
  $W(i, i - \delta) = 0.5$
  $W(i, i) = -1$
  $W(i, i + \delta) = 0.5$
end for

Algorithm 2 Matrix of compression transposed $W^T(x_{in}, k)$ on the level k

$n = length(x_{in})$
$\delta = 2^{k-1}$
for $i = 1 : n$ **do**
  $W(i, i) = 1$
end for
for $i = 1 + \delta : 2\delta : n - \delta$ **do**
  $W(i - \delta, i) = 0.5$
  $W(i, i) = -1$
  $W(i + \delta, i) = 0.5$
end for

Algorithm 3 Pre multiplication $x_{out} = Wx(x_{in}, k)$ on the level k

$x_{out} = x_{in}$
$n = length(x_{in})$
$\delta = 2^{k-1}$
$w_1 = -1$
$w_2 = 0.5$
for $i = 1 + \delta : 2\delta : n - \delta$ **do**
  $x_{out}(i) = w_2 * x_{in}(i - \delta) + w_1 * x_{in}(i) + w_2 * x_{in}(i + \delta)$
end for

Algorithm 4 Post multiplication $x_{out} = xW(x_{in}, k)$ et Pre multiplication transposed $x_{out} = W^T x(x_{in}, k)$ on the level k

$x_{out} = x_{in}$
$n = length(x_{in})$
$\delta = 2^{k-1}$
$w_1 = -1$
$w_2 = 0.5$
for $i = 1 + \delta : 2\delta : n - \delta$ **do**
  $x_{out}(i - \delta) = x_{out}(i - \delta) + x_{in}(i) * w_2;$
  $x_{out}(i) = x_{in}(i) * w_1;$
  $x_{out}(i + \delta) = x_{out}(i + \delta) + x_{in}(i) * w_2;$
end for

3.4.9 Appendix : Storage and products of sparse matrices

Storage of the sparse matrices by the *sparse row-wise* format is based after the book of Pissanetzky (1984). Algorithm 5 allows the storage of the sparse matrix $\boldsymbol{A}$ in the vectors val (element A_{ij}), colind (index of the column) and rowptr (index of the line). The reader will refer to the cited book for more explanations. Algorithm 6 calculates the product of the matrix $\boldsymbol{A}$ by a vector $\boldsymbol{x}$. Algorithm 7 calculates the product of the transposed matrix $\boldsymbol{A}^T$ by a vector $\boldsymbol{x}$. Algorithm 8 calculates the diagonal of the product $\boldsymbol{A}^T\boldsymbol{A}$ for preconditioning the conjugate gradient when solving for the system $\boldsymbol{A}^T\boldsymbol{A}\boldsymbol{x} = \boldsymbol{A}^T\boldsymbol{b}$.

Algorithm 5 Storage of the sparse matrix $\boldsymbol{A}$: $storage(A)$

```
rowptr = zeros(1, size(A,1) + 1)
val = []
colind = []
rowptr(1) = 1
nnz = 1
for i = 1 : size(A,1) do
  for j = 1 : size(A,2) do
    if ((A(i,j) ≠ 0)) then
      val(nnz) = A(i,j)
      colind(nnz) = j
      nnz = nnz + 1
    end if
  end for
  rowptr(i + 1) = nnz
end for
```

Algorithm 6 Product of the sparse matrix $\boldsymbol{A}$ by the vector $\boldsymbol{x}$ $(\boldsymbol{y} = \boldsymbol{A}\boldsymbol{x})$: $y = spAx(val, colind, rowptr, nnz, x, y)$

```
for i = 1 : length(y) do
  temp = 0
  for j = rowptr(i) : rowptr(i + 1) − 1 do
    temp = temp + val(j) * x(colind(j))
  end for
  y(i) = temp
end for
```

Algorithm 7 Product of the transposed sparse matrix A^T by the vector x ($y = A^T x$) : $y = spAtx(val, colind, rowptr, nnz, x, y)$

```
for i = 1 : length(y) do
  y(i) = 0
end for
for j = 1 : length(x) do
  if (rowptr(j + 1) − 1 ≥ rowptr(j)) then
    for i = rowptr(j) : rowptr(j + 1) − 1 do
      y(colind(i)) = y(colind(i)) + val(i) ∗ x(j)
    end for
  end if
end for
```

Algorithm 8 Diagonal of the product $A^T A$: $y = diagspAtA(val, colind, rowptr, y)$

```
for i = 1 : size(A, 1) do
  for j = rowptr(i) : rowptr(i + 1) − 1 do
    y(colind(j)) = y(colind(j)) + val(j)^2
  end for
end for
```

Chapitre 4

INVERSION ÉLECTRIQUE

4.1 Introduction

Ce chapitre met en place la deuxième méthode d'interprétation géophysique pour la recherche de gisements miniers. Il est le prolongement du chapitre précédent, puisqu'après avoir mis en place un code de modélisation électrique 3D, il est naturel de formuler une méthode d'inversion électrique. Cette méthode a fait l'objet d'une publication dont le titre est :"3D geostatistical electrical tomographic imaging : principles and application for mining targets". L'article a été soumis au mois de février 2004 à la revue Geophysics (Boulanger *et al.*, 2004).

Le but de l'inversion électrique est de reconstruire une distribution 3D de résistivité à partir des mesures de potentiel électrique en utilisant différentes configurations de sources et de récepteurs. En tomographie de résistivité électrique, le courant est injecté par un pôle ou un dipôle situé en surface et/ou en forage. Le potentiel électrique est mesuré le long des forages ou à la surface du sol avec un pôle ou un dipôle en mode tomographique. La configuration pôle-pôle est utilisée

dans cet article. Le but est de cartographier la distribution de résistivité dans une région balayée par la méthode. Plusieurs méthodes ont été publiées dans les 25 dernières années pour inverser un ensemble de données de résistivité. Parmi celles-ci on a : la méthode des moindres carrés, la méthode des moindres carrés amortie, la méthode des moindres carrés amortie pondérée, la méthode du maximum *a posteriori*, la rétro projection, la méthode SIRT, la méthode du recuit simulé et la méthode des algorithmes génétiques. Toutes ces méthodes peuvent être appliquées à des données prises en surface et en forage.

Plusieurs auteurs ont testé la régularisation de Thikonov avec la dérivée première ou seconde pour retrouver une solution. Cette méthode requiert la définition d'un paramètre de régularisation, le multiplicateur de Lagrange, qui équilibre la norme du modèle et l'erreur sur les données. Deux méthodes sont utilisées en ce moment pour trouver ce multiplicateur : i) la méthode empirique "L-curve" qui est rapide mais pas toujours efficace ; ii) la validation croisée généralisée (GCV) qui est mieux établie pour les systèmes surdéterminés, mais coûteuse en temps calcul sous la forme classique. Une variante de la méthode GCV classique, la validation croisée généralisée stochastique, est plus rapide. Ces méthodes fonctionnent bien quand les données sont bien distribuées tout autour de la cible avec plus de données que de paramètres. Pour des systèmes sous déterminés ces méthodes sont encore en développement. Ce type de régularisation échoue lorsque les données sont 2D pour des corps tabulaires ou connectés. Après plusieurs tests avec la formulation de Thikonov, on a conclu qu'il était nécessaire de fixer les paramètres le long des forages quand les données tomographiques sont prises en configuration pôle-pôle entre deux forages. C'est le cas pour nos deux sites tests de la mine de Casa Berardi et du dépôt de Mc Connell. Une autre limitation importante de la méthode de la

régularisation de Thikonov est qu'il n'est pas possible d'incorporer une anisotropie dans la formulation pour retrouver des corps allongés. Pour cette raison, on a sélectionné une méthode stochastique qui tient compte des corrélations entre les paramètres par le biais d'une matrice de covariance pleine. Cette méthode n'est pas largement utilisée dans la communauté scientifique, parce qu'il est nécessaire d'évaluer un plateau, un effet pépite et une portée pour le modèle de covariance le long des directions principales. De plus la matrice est pleine et énorme.

L'information géologique à partir de la surface et des forages est souvent disponible et peut être utilisée pour définir un modèle géologique 3D en utilisant un système d'information géographique (GIS). Il est alors possible d'imposer des gradients de résistivité entre les différentes unités lithologiques. Plusieurs auteurs ont déjà utilisé des contraintes de gradient pour améliorer les performances du krigeage.

On propose d'inclure ici toute l'information a priori dans la fonction objective. Les exemples d'information disponible sont : les résistivités connues le long des forages ou ailleurs ; les mesures de résistivité in situ ; les gradients de résistivité électrique ; et les limites globales sur les paramètres de résistivité. La matrice de covariance est déterminée à partir des données observées et guidée par l'information géologique pour la zone d'investigation. On montre l'équivalence formelle entre la méthode du maximum a posteriori et le cokrigeage dans le cas non linéaire.

L'article est divisé en trois parties principales. La première partie de l'article présente la notation et la théorie, et les méthodes utilisées pour l'estimation de la résistivité électrique. On fait une revue rapide de la méthode du maximum a posteriori et du cokrigeage, et on prouve l'équivalence formelle dans le cas Gaussien. La méthode pour déterminer le modèle de covariance est présentée. La deuxième

partie de l'article consiste à tester la méthode d'imagerie en utilisant différentes contraintes avec des données synthétiques. La troisième partie présente l'application de la méthode pour les données de la mine d'or de Casa Berardi et du dépôt de nickel de Mc Connell.

4.2 Résumé

On présente une méthode de tomographie de résistivité électrique robuste basée sur une approche géostatistique non linéaire avec de nouvelles contraintes. Cette méthode estime un modèle de covariance analytique pour les paramètres de résistivité à partir des données de potentiel. Les paramètres de résistivité sont obtenus en cokrigeant les données de potentiel électrique mesuré, les paramètres fixés le long des forages et les gradients de résistivité connus dans le sous-sol. La modélisation est faite en utilisant une méthode intégrale. Le code est testé sur plusieurs modèles synthétiques pour démontrer la validité de notre approche. Les données sont collectées en configuration pôle-pôle dans un plan incluant les forages émetteur et récepteur. De forts contrastes de résistivité simulant des cas réels rencontrés dans l'industrie minière sont retrouvés en utilisant cette méthode. Pour les applications réelles, l'ajustement de la matrice de covariance est aidé par l'information géologique disponible et les cas d'études menés sur les sites. On teste le code sur deux cas réels : la mine d'or de Casa Berardi (Québec, Canada) et le dépot de Mc Connell (Ontario, Canada). Les géométries majeures et les résistivités sont en accord avec l'information géologique et les études préliminaires effectuées sur les sites.

4.3 3D geostatistical electrical tomographic imaging : principles and application for mining targets

4.3.1 Abstract

We present a robust electrical resistivity tomography method based on a non-linear geostatistical approach with new constraints. This method estimates an analytical covariance model for the resistivity parameters from the potential data. The resistivity parameters are obtained by cokriging the measured electrical potential data, the fixed resistivity parameters along the boreholes and the known resistivity gradients in the subsurface. Forward modelling is done using an integral equation method. We test the code on various synthetic models to demonstrate the validity of our approach. The data here is collected in the pole-pole array in a plane including the transmitter and receiver boreholes. High resistivity contrasts simulating real cases encountered in the mining industry are recovered using this method. In real applications, the adjustment of the covariance matrix is aided by available geological information and the case histories on the sites. We test the code on two real cases : the Casa Berardi gold mine (Quebec, Canada) and the Mc Connell deposit (Ontario,Canada). Major geometry and resistivities agree with the available geological information and previously reported case histories on the sites.

Key words : resistivity, cokriging, covariance estimation, fixed parameters, gradient constraint, 3D, Casa Berardi, Mc Connell

Short title : 3D electrical cokriging

4.3.2 Introduction

The goal of resistivity inversion is to reconstruct the 3D resistivity distribution from electrical potential measurements using various source-receiver configurations. In electrical resistivity tomography, current is injected by a pole or a dipole located at the surface and/or in boreholes. The electrical potential is measured along the boreholes or at the ground surface with a pole or a dipole in tomographic mode. The pole-pole configuration is used in this article. The goal is to map the resistivity distribution in the region scanned by the method. Numerous methods have been published in the past 25 years to invert a set of resistivity data. These are : *the least squares method* (Dines et Lytle, 1981; Daily et Owen, 1991), *the damped least squares method* (Inman, 1975; Petrick *et al.*, 1977; Pelton *et al.*, 1978; Petrick *et al.*, 1981; Tong et Yang, 1990; Olayinka et Yaramanci, 2000), *the weighted damped least squares method* (Lytle *et al.*, 1980; Smith et Vozoff, 1984; Daniels et Dyck, 1984; Yorkey *et al.*, 1987; Daily et Owen, 1991; Li et Oldenburg, 1992; Kallman et Berryman, 1992; Meju, 1992; Ramirez *et al.*, 1993; Ellis et Oldenburg, 1994; Narayan *et al.*, 1994; Sasaki, 1994; Loke et Barker, 1996*a*; LaBrecque *et al.*, 1996; Borcea *et al.*, 1996; Shi *et al.*, 1997; Cohen-Bacrie *et al.*, 1997; Vauhkonen *et al.*, 1998; Lesur *et al.*, 1999*b*; Bing et Greenhalgh, 2000; Ramirez et Daily, 2001), *the maximum a posteriori estimation method* (Pous *et al.*, 1987; Park et Van, 1991; Zhang *et al.*, 1995; Maillol *et al.*, 1999), *the back-projection* (Wexler *et al.*, 1985; Noel et Xu, 1991; Shima, 1992; Santosa et Vogelius, 1990), *the SIRT method* (Dines et Lytle, 1979, 1981; Brunner *et al.*, 1999), *the simulated annealing* (Sen *et al.*, 1993; Chunduru *et al.*, 1996) and *the genetic algorithm* (Chunduru *et al.*, 1995). All these methods can be applied to surface and borehole acquired data.

Many authors have tested the Thikonov regularization method with the first

or second derivative to recover a solution. This method requires defining a regularization parameter, the Lagrange multiplier, which balances the model norm and the data error. Two methods are used at the present time to find the optimum trade-off : i) the empirical L-curve method which is fast (Hansen, 1992), but not always efficient (Vogel, 1996) ; ii) generalized cross validation (GCV) which is more established for over-determined systems, but is expensive in CPU time when implemented in the classical form (Golub *et al.*, 1979; Whaba, 1990; Fortier *et al.*, 1993; Marcotte, 1995). A variant of classical GCV, stochastic GCV, is faster (Hutchinson, 1990; Williams et Burrage, 1995; Golub et von Matt, 1997; Sidje et Williams, 1996). These methods work well when the data are distributed in 3D space around the target with more data than parameters. For under-determined systems these methods are still in development. This type of regularization fails for 2D distribution of data where the body is tabular or connected between boreholes. After numerous tests with the Thikonov formulation, we conclude that it is necessary to fix parameters along the boreholes when the tomographic data is acquired in pole-pole configuration between two holes, which is the case for our real test sites, the Casa Berardi mine and the Mc Connell deposit. Another important limitation of Thikonov regularization is that it is not possible to incorporate anisotropy in the formulation to recover elongated bodies. For this reason, one will rather select a stochastic method which accounts for large scale correlations between the parameters by means of a full covariance matrix. This method is not widely used in the geophysical scientific community, because it is necessary to evaluate the sill, the nugget effect and the range of the covariance model along the principal directions. Moreover the covariance matrix is full and huge.

Geological information from the surface and from boreholes is commonly avai-

lable and can be used to define a 3D geological model using a geographical information system (GIS). It is then possible to impose resistivity gradients between the different lithological units. Severals authors have already used the gradient constraints to improve kriging performance (Chiles et Delfiner, 1999; Brochu et Marcotte, 2003).

We propose here to include all available a priori information in the objective function. Examples of available information are : known values of resistivity along boreholes or elsewhere ; measurements of in-situ resistivities ; electrical resistivity gradients ; and global limits on the resistivity parameters. The covariance matrix is determined from the observed data and guided by the available geological model for the area under investigation. We show the formal equivalence between the maximum a posteriori estimation method and cokriging in the non-linear case.

The paper is divided in three main parts. The first part of the paper presents the notation and the theory and methods used for estimation of the electrical resistivity. We review briefly the maximum a posteriori and the cokriging methods and prove their formal equivalence in the Gaussian case. The method for determining the covariance model parameters is also presented. The second part of the paper consists of testing the imaging method using different constraints with synthetic data. The third part presents the application of the method on survey data at the Casa Berardi gold mine and the Mc Connell nickel deposit.

4.3.3 Formulation

4.3.3.1 Maximum a posteriori estimation method (MAP)

The MAP estimation method stems from the theory of probability and assumes Gaussian probability density functions $\boldsymbol{f}$. Using the Bayes theorem ($\boldsymbol{f}_{\rho|d} = \frac{\boldsymbol{f}_{d|\rho}\ \boldsymbol{f}_{\rho}}{\boldsymbol{f}_{d}}$), the MAP estimation consists of maximizing the conditional probability density $\boldsymbol{f}_{\rho|d}$ for the model $\boldsymbol{\rho}$, given the data $\boldsymbol{d}$ ($\hat{\boldsymbol{\rho}}_{\boldsymbol{MAP}} = arg\ max_{\rho}\{\boldsymbol{f}_{\rho|d}\}$) or minimizing the negative of the exponential argument of $\boldsymbol{f}_{\rho|d} \propto exp\{-\phi(\boldsymbol{\rho})\}$ ($\hat{\boldsymbol{\rho}}_{\boldsymbol{MAP}} = arg\ min_{\rho}\{\phi(\boldsymbol{\rho})\}$). The argument $\phi(\boldsymbol{\rho}) = \phi_{\rho}(\boldsymbol{\rho}) + \phi_{d}(\boldsymbol{\rho})$, where $\phi_{\rho}(\boldsymbol{\rho}) = [\boldsymbol{\rho} - \boldsymbol{\rho_0}]^T \boldsymbol{C}^{-1}_{\boldsymbol{\rho_0\rho_0}} [\boldsymbol{\rho} - \boldsymbol{\rho_0}]$ is the norm of the parameters corresponding to the unconditional probability density for the model $\boldsymbol{f}_{\rho}$, and $\phi_{d}(\boldsymbol{\rho}) = [\boldsymbol{d} - \boldsymbol{a}(\boldsymbol{\rho})]^T \boldsymbol{C_0}^{-1} [\boldsymbol{d} - \boldsymbol{a}(\boldsymbol{\rho})]$ is the quadratic error between the observed and calculated data corresponding to the conditional probability density $\boldsymbol{f}_{\boldsymbol{d|\rho}}$ for the data $\boldsymbol{d}$, given $\boldsymbol{\rho}$. The unconditional probability density $\boldsymbol{f}_{\boldsymbol{d}}$ for the data $\boldsymbol{d}$ is a multiplicative constant. The maximum likelihood method (ML) and the least squares method (LS) correspond to $\hat{\boldsymbol{\rho}}_{\boldsymbol{ML}} = arg\ min_{\rho}\{\phi_{d}(\boldsymbol{\rho})\}$ and $\hat{\boldsymbol{\rho}}_{\boldsymbol{LS}} = arg\ min_{\rho}\{\phi_{d}(\boldsymbol{\rho})\}$ with $\boldsymbol{C_0} = \boldsymbol{I}$, respectively. $\hat{\boldsymbol{\rho}}_{\boldsymbol{ML}}$ and $\hat{\boldsymbol{\rho}}_{\boldsymbol{LS}}$ correspond to the case where only the data estimate the solution. Thus when the number of data is small, the estimation can be sensitive to error. The estimated solution $\hat{\boldsymbol{\rho}}_{\boldsymbol{MAP}}$ is more stable because *a priori* information included in $\phi_{\rho}(\boldsymbol{\rho})$ counteract the effect of the error in the data. A $\hat{\boldsymbol{\rho}}_{\boldsymbol{MAP}}$ solution is given in Tarantola et Valette (1982).

For the MAP estimation method we use a model composed of M cells and N data including N_P measurements of electrical potential, N_F fixed resistivity cells and N_G imposed gradients. Matrices and vectors are defined as :

- $\boldsymbol{C}_{\boldsymbol{\rho_0\rho_0}}$ is the positive-definite covariance matrix of the M parameters $\boldsymbol{\rho}$ with the dimension $dim(\boldsymbol{C}_{\boldsymbol{\rho_0\rho_0}}) = M^2$

• $\boldsymbol{C_{d_0 d_0}}$, $\boldsymbol{C_{d_F d_F}}$ and $\boldsymbol{C_{d_g d_g}}$ are the positive semi-definite diagonal variance matrices of the error on the measured data $\boldsymbol{d_0}$ ($(C_{d_0 d_0})_{ii}$ is a constant adjusted in (4.6)), on the fixed parameters $\boldsymbol{\rho_F}$ (e.g. $(C_{d_F d_F})_{ii} = 1$ $(\Omega.m)^2$) and on the gradients $\boldsymbol{g}$ (e.g. $(C_{d_g d_g})_{ii} = 0.1$), respectively. $\boldsymbol{C_0}$ combines the three diagonal matrices $\boldsymbol{C_{d_0 d_0}}$, $\boldsymbol{C_{d_F d_F}}$ and $\boldsymbol{C_{d_g d_g}}$.

• $\boldsymbol{d}^T = [\boldsymbol{d_0}^T, \boldsymbol{\rho_F}^T, \boldsymbol{g}^T]$ where $\boldsymbol{d}$ is a vector consisting of the N observed data $\boldsymbol{d_0}$, the N_F fixed resistivities $\boldsymbol{\rho_F}$ of certain cells and the $N_G = N_{G_x} + N_{G_y} + N_{G_z}$ known gradients $\boldsymbol{g^T} = [\boldsymbol{g_x^T g_y^T g_z^T}]$ between two adjacent cells in the x, y and z directions.

• $\boldsymbol{a(\rho)}^T = [\boldsymbol{V(\rho)}^T (\boldsymbol{F\rho})^T (\boldsymbol{H\rho})^T]$ is the non-linear forward modelling operator consisting of $\boldsymbol{V(\rho)}$ for the electrical modelling, $\boldsymbol{F\rho}$ for the fixed parameters and $\boldsymbol{H\rho}$ for the gradients in the x, y and z directions ($\boldsymbol{H^T} = [\boldsymbol{H_x^T H_y^T H_z^T}]$)

• $\boldsymbol{J(\rho)}^T \equiv \frac{\partial \boldsymbol{a(\rho)}}{\partial \boldsymbol{\rho}}^T \equiv [\frac{\partial \boldsymbol{V(\rho)}}{\partial \boldsymbol{\rho}}^T \boldsymbol{F^T H^T}]$ is the Jacobian matrix consisting of the first derivatives with respect to $\boldsymbol{\rho}$ of $\boldsymbol{V(\rho)}$, $\boldsymbol{F\rho}$ and $\boldsymbol{H\rho}$, respectively. All the coefficients of $\boldsymbol{F}$ have the value 1 when the cell is fixed and 0 elsewhere. All the coefficients of $\boldsymbol{H}$ have the value -1 and 1 where the gradient is known between two cells and 0 elsewhere. Matrix dimensions are $dim(\frac{\partial \boldsymbol{V(\rho)}}{\partial \boldsymbol{\rho}}) = N\text{x}M$, $dim(F) = N_F\text{x}M$, and $dim(H) = N_G\text{x}M$.

• positivity of $\boldsymbol{\rho}$ is imposed during the inversion by cutting out resistivities beyond the global limits $[\rho_{min}, \rho_{max}]$.

Tarantola et Valette (1982) proposed a formulation of stochastic inversion for a nonlinear problem by generalizing the solution of a linear problem (Franklin, 1970; Jordan et Franklin, 1971). By noting $\boldsymbol{J_k} \equiv \boldsymbol{J(\rho_k)}$, the MAP solution is iteratively

obtained using the relation :

$$\rho_{k+1} = \rho_0 + C_{\rho_0\rho_0}\ J_k^T\ [J_k\ C_{\rho_0\rho_0} J_k^T + C_0]^{-1}[d - a(\rho_k) + J_k(\rho_k - \rho_0)] \qquad (4.1)$$

The solution of (4.1) is obtained by preconditioned conjugate gradient least squares PCCGLS (see appendix 4.4.3). The *a posteriori* covariance matrix for the estimated parameters is written as :

$$C_{\hat{\rho}\hat{\rho}} = C_{\rho_0\rho_0} - C_{\rho_0\rho_0}\ J_k^T\ [J_k\ C_{\rho_0\rho_0} J_k^T + C_0]^{-1}\ J_k\ C_{\rho_0\rho_0} \qquad (4.2)$$

4.3.3.2 Estimation of the parameter covariance matrix

For solving equations (4.1) and (4.2) and, later (4.8), (4.11) and (4.12) the parameter covariance matrix needs to be estimated. The parameter covariance model must be estimated from the available potential data. By linearizing the forward model we have, at iteration k, the first order approximation :

$$V(\rho_k) = V(\rho_0) + J_k\ \delta\rho_k + R(\rho_0, \delta\rho_k) \qquad (4.3)$$

with $\delta\rho_k = \rho_k - \rho_0$, $J_k = J(\rho_k) \equiv \frac{\partial V(\rho_k)}{\partial \rho}$ and $d \equiv d_0$ and where $R(\rho_0, \delta\rho_k)$ is a residual term expected to be small.

The error e between the noise-free data $V(\rho_k)$ and the mesured data d_0 is given by

$$d_0 = V(\rho_k) + e \qquad (4.4)$$

e includes the contribution of the residual terms $R(\rho_0, \delta\rho_k)$. Two assumptions are made. First the error has zero mean, i.e. $E[e] = 0$, and are not correlated,

i.e. $cov(e_i, e_j) = 0$ for $i \neq j$. Second, there is no correlation between the modelled data and the error such that $cov(\boldsymbol{V(\rho_k)}, \boldsymbol{e}) = 0$. Expressing $\boldsymbol{\delta d^k} = \boldsymbol{d_0} - \boldsymbol{V(\rho_0)} = \boldsymbol{d_0} - \boldsymbol{V(\rho_k)} + \boldsymbol{J_k}\ \boldsymbol{\delta\rho_k}$, we have a linear first order relation between $\boldsymbol{\delta d^k}$ and $\boldsymbol{\delta\rho_k}$

$$\boldsymbol{\delta d^k} = \boldsymbol{J_k}\ \boldsymbol{\delta\rho_k} + \boldsymbol{e} \tag{4.5}$$

The search of the solution is done around a mean value of the resistivity $\boldsymbol{\rho_0}$ at iteration $k = 0$, such as that the mathematical expectation of $\boldsymbol{\delta d^0}$ is null. Taking $\boldsymbol{\rho_0}$ as the apparent resistivity $\boldsymbol{\rho_a}$, we often obtain $E[\boldsymbol{\delta d^0}] = E[\boldsymbol{J_0}\ \boldsymbol{\delta\rho_0} + \boldsymbol{e}] = 0$. If $E[\boldsymbol{\delta d^0}] \neq 0$, then we can calculate $\bar{\delta\rho}_0 = \frac{1}{N}\sum_{i=1}^{N}\left(\frac{^{(\nu)}\delta d_i^0}{\sum_{j=1}^{M} J_{0_{ij}}}\right)$ and $\bar{\boldsymbol{\delta d^0}} = \boldsymbol{J_0}\bar{\boldsymbol{\delta\rho_0}}$. Then we update $^{(\nu+1)}\boldsymbol{\delta d^0} = {}^{(\nu)}\boldsymbol{\delta d^0} + \bar{\boldsymbol{\delta d^0}}$ and $^{(\nu+1)}\boldsymbol{\rho_0} = {}^{(\nu)}\boldsymbol{\rho_0} + \bar{\boldsymbol{\delta\rho_0}}$. Others methods can be used to estimate the mean value $\boldsymbol{\rho_0}$.

Writing $E[(\boldsymbol{\delta d^k})\ (\boldsymbol{\delta d^k})^T] = E[(\boldsymbol{J_k}\ \boldsymbol{\delta\rho_k} + \boldsymbol{e})(\boldsymbol{J_k}\ \boldsymbol{\delta\rho_k} + \boldsymbol{e})^T]$ with $E[\boldsymbol{\delta\rho_k}\ \boldsymbol{e}^T] = E[\boldsymbol{\delta\rho_k}^T\ \boldsymbol{e}] = 0$, we obtain a relation between the covariance matrix of the mesured data $\boldsymbol{C_{dd}^k} = E[(\boldsymbol{\delta d^k})\ (\boldsymbol{\delta d^k})^T]$, the covariance matrix of the parameters $\boldsymbol{C_{\rho_0\rho_0}^k} = E[\boldsymbol{\delta\rho_k}\ \boldsymbol{\delta\rho_k}^T]$ and the covariance matrix of the error $\boldsymbol{C_{d_0d_0}} = E[\boldsymbol{e}\ \boldsymbol{e}^T]$ corresponding to the nugget effect of the mesured data, then :

$$\boldsymbol{C_{dd}^k} = \boldsymbol{J_k}\ \boldsymbol{C_{\rho_0\rho_0}^k}\ \boldsymbol{J_k}^T + \boldsymbol{C_{d_0d_0}} \tag{4.6}$$

Note that this matrix is not diagonal and not singular. In addition, we take $\boldsymbol{C_{\rho_0\rho_0}^0} \equiv \boldsymbol{C_{\rho_0\rho_0}}$ as a constant matrix for all iterations, because its evaluation is done before starting the inversion scheme. The covariance matrix $\boldsymbol{C_{\rho_0\rho_0}}$ is calculated from an admissible model (spherical, exponential, Gaussian) with a null or quasi-null correlation at infinity (Deutsch et Journel, 1998). The evaluation of the three ranges a_x, a_y, a_z along the principal directions (after a suitable rotation of

the coordinate system), the sill and the nugget effect ($\boldsymbol{C_{d_0 d_0}}$) of the measured data is done by comparing the theoretical covariance $\boldsymbol{C_{dd}^0 = J_0\ C_{\rho_0 \rho_0}\ J_0{}^T + C_{d_0 d_0}}$ and experimental covariance $\boldsymbol{C_{dd}^{exp}} = (\boldsymbol{\delta d^0})\ (\boldsymbol{\delta d^0})^T$ matrices (Asli *et al.*, 2000). The adjustment between the two matrices is done manually with the following steps :

i) calculate the matrices $\boldsymbol{C_{dd}^0}$ and $\boldsymbol{C_{dd}^{exp}}$;

ii) transform both matrices into vectors $\boldsymbol{v^{th}}$ and $\boldsymbol{v^{exp}}$;

iii) sort $\boldsymbol{v^{th}}$ in decreasing order and apply the same ordering to $\boldsymbol{v^{exp}}$;

iv) bin the vectors $\boldsymbol{v^{th}}$ and $\boldsymbol{v^{exp}}$in N_{lag} lags and compute the mean for each lag with the relations $\bar{v}^{th}[j] = \frac{N_{lag}}{N_P^2} \sum_{i=1+(j-1)*\frac{N_P^2}{N_{lag}}}^{i=j*\frac{N_P^2}{N_{lag}}} v^{th}[i]$ for $j = 1, N_{lag}$ and $\bar{v}^{exp}[j] = \frac{N_{lag}}{N_P^2} \sum_{i=1+(j-1)*\frac{N_P^2}{N_{lag}}}^{i=j*\frac{N_P^2}{N_{lag}}} v^{exp}[i]$ for $j = 1, N_{lag}$;

v) Minimize the error for each lag with the relation $err[j] = \bar{v}^{th}[j] - \bar{v}^{exp}[j]$. We present $\boldsymbol{\bar{v}^{th}}$ and $\boldsymbol{\bar{v}^{exp}}$ as a function of the lag index j for $N_{lag} = 100$.

As the electrical inverse method is non linear, the adjustment between $\boldsymbol{C_{dd}^{exp}}$ and $\boldsymbol{C_{dd}^0}$ is not always well resolved. It is important to well adjust the beginning of the curve $\boldsymbol{C_{dd}^0}$ and $\boldsymbol{C_{dd}^{exp}}$, because the correlation between cells is maximum for small lags. The nugget effect helps to stabilize the cokriging system and smooths the solution when the data are noisy. It is useful to use the geological knowledge of the investigated site to improve the adjustment of the parameters or to fix some parameters *a priori*. The search for the background resistivity $\boldsymbol{\rho_0}$ can be delicate when the body is not intersected by the holes. In this case the user must find a curve $\boldsymbol{C_{dd}^0}$ with a decreasing behavior for the small lags.

4.3.3.3 Cokriging

The cokriging estimator consists of a linear combination of the observed data : $\delta\hat{\rho}_{k+1} = {\Lambda_k}^T\ \delta d^k$ where $dim(\Lambda_k) = N\text{x}M$. The weights ${\Lambda_k}^T$ are determined so as to minimize the estimation variance $L(\hat{\rho}_{k+1};\Lambda) = E[(\rho_{k+1} - \hat{\rho}_{k+1})(\rho_{k+1} - \hat{\rho}_{k+1})^T] = E[\delta\rho_{k+1}\ \delta\rho_{k+1}^T] - E[\delta\rho_{k+1}\ \delta\hat{\rho}_{k+1}^T] - E[\delta\hat{\rho}_{k+1}\ \delta\rho_{k+1}^T] + E[\delta\hat{\rho}_{k+1}\ \delta\hat{\rho}_{k+1}^T]$. The optimal weights are obtained upon differentiation of $L(\rho_{k+1};\Lambda_k)$ with respect to Λ_k :

$$L(\hat{\rho}_{k+1};\Lambda_k) = C_{\rho_0\rho_0} - C^k_{\rho_0 d}\ \Lambda_k - {\Lambda_k}^T C^k_{d\rho_0} + {\Lambda_k}^T\ C^k_{dd}\ \Lambda_k \tag{4.7}$$

with $\rho_{k+1} = \rho_0 + \delta\rho_{k+1}$ the true resistivities and $\hat{\rho}_{k+1} = \rho_0 + \delta\hat{\rho}_{k+1}$ the estimated resistivities. ρ_{k+1} and δd^k are principal and secondary variable, respectively. With the cross covariance $C^k_{d\rho_0} = J_k\ C_{\rho_0\rho_0}$, $J_k = J(\rho_k) \equiv \frac{\partial V(\rho_k)}{\partial \rho}$ and $d \equiv d_0$, the minimization of $L(\hat{\rho}_{k+1};\Lambda_k)$, that is setting $\frac{\partial L(\hat{\rho}_{k+1};\Lambda_k)}{\partial {\Lambda_k}^T} = 0$, yields the solution of the simple cokriging at iteration $k+1$ (Journel et Huijbregts, 1978; Chiles et Delfiner, 1999)

$$\begin{aligned} C^k_{dd}\ \Lambda_k &= C^k_{d\rho_0} \\ \delta\hat{\rho}_{k+1} &= {\Lambda_k}^T\ \delta d^k \end{aligned} \tag{4.8}$$

As long as the matrix C^k_{dd} is non-singular, the number of data can be significantly less than the number of parameters without affecting stability of cokriging estimates. New measurements provide additional information which may modify our original estimate. In the event that the matrix $J_k\ C^k_{\rho_0\rho_0}\ {J_k}^T$ is singular, a numerically stable solution is guaranteed when $C_{d_0d_0} > 0$. This condition should usually be met in practice as $C_{d_0d_0}$ includes both measurement error and the effect of neglected higher order terms in the linear approximation (4.3). If $C_{d_0d_0} = 0$, then $J_k\ C^k_{\rho_0\rho_0}\ {J_k}^T$ must be non-singular (Luenberger, 1969). Combining equation

(4.6) and (4.8), we obtain :

$$\hat{\rho}_{k+1} = \rho_0 + C_{\rho_0\rho_0}\ {J_k}^T\ [J_k C_{\rho_0\rho_0} {J_k}^T + C_{d_0d_0}]^{-1}\ [d_0 - V(\rho_k) + J_k(\rho_k - \rho_0)] \quad (4.9)$$

Equation (4.9) corresponds to dual cokriging and is identical to (4.1) when $d \equiv d_0$. The cokriging variance of the estimated parameters $\hat{\rho}$ is identical to (4.2) and is written $L(\hat{\rho}_{k+1}; \Lambda_k) = C_{\hat{\rho}\hat{\rho}} = C_{\rho_0\rho_0} - {\Lambda_k}^T C^k_{d\rho_0}$. Although the maximum a posteriori estimation method and the cokriging method are equivalent, the first one requires specifying a Gaussian distribution for every variable whereas the second one does not.

Including constraints is straightforward. For the fixed parameters, we have for each considered block $\delta\rho_F = \rho_F - F\rho_0$. For the discreet gradient $\delta g = g - H\ \rho_0$. The estimation variance $L(\hat{\rho}_{k+1}; \Lambda_k, \alpha_k, \beta_k)$ is minimized with respect to the weights Λ_k, α_k and β_k where :

$$\begin{aligned} L(\hat{\rho}_{k+1}; \Lambda_k, \alpha_k, \beta_k) = C_{\rho_0\rho_0} &- C^k_{\rho_0 d}\ \Lambda_k - C_{\rho_0\rho_F}\ \alpha_k - C_{\rho_0 g}\ \beta_k \\ &- {\Lambda_k}^T C^k_{d\rho_0} - {\alpha_k}^T C_{\rho_F\rho_0} - {\beta_k}^T C_{g\rho_0} \\ &+ {\Lambda_k}^T\ C^k_{dd}\ \Lambda_k + {\Lambda_k}^T\ C^k_{d\rho_F}\ \alpha_k + {\Lambda_k}^T\ C^k_{dg}\ \beta_k \\ &+ {\alpha_k}^T\ C^k_{\rho_F d}\ \Lambda_k + {\alpha_k}^T\ C_{\rho_F\rho_F}\ \alpha_k + {\alpha_k}^T\ C_{\rho_F g}\ \beta_k \\ &+ {\beta_k}^T\ C^k_{gd}\ \Lambda_k + {\beta_k}^T\ C_{g\rho_F}\ \alpha_k + {\beta_k}^T\ C_{gg}\ \beta_k \end{aligned} \quad (4.10)$$

The simple cokriging solution at iteration $k+1$ is given by :

$$\begin{bmatrix} C^k_{dd} & C^k_{d\rho_F} & C^k_{dg} \\ C^k_{\rho_F d} & C_{\rho_F\rho_F} & C_{\rho_F g} \\ C^k_{gd} & C_{g\rho_F} & C_{gg} \end{bmatrix} \begin{bmatrix} \Lambda_k \\ \alpha_k \\ \beta_k \end{bmatrix} = \begin{bmatrix} C^k_{d\rho_0} \\ C_{\rho_F\rho_0} \\ C_{g\rho_0} \end{bmatrix} \tag{4.11}$$

$$\delta\hat{\rho}_{k+1} = {\Lambda_k}^T\, \delta d^k + {\alpha_k}^T\, \delta\rho_F + {\beta_k}^T\, \delta g$$

with $\hat{\rho}_{k+1} = \rho_0 + \delta\hat{\rho}_{k+1}$. The cokriging variance of the estimated parameters is written as $L(\hat{\rho}_{k+1}; \Lambda_k, \alpha_k, \beta_k) = C_{\rho_0\rho_0} - {\Lambda_k}^T C^k_{d\rho_0} - {\alpha_k}^T C_{\rho_F\rho_0} - {\beta_k}^T C_{g\rho_0}$.

The covariance matrices for equation (4.11) are given by :

- $C_{\rho_F\rho_0} = F\, C_{\rho_0\rho_0}$ are the N_F lines of the matrix $C_{\rho_0\rho_0}$
- $C^k_{d\rho_F} = C^k_{d\rho_0}\, F^T$ are the N_F columns of the matrix $C^k_{d\rho_0} = J_k\, C_{\rho_0\rho_0}$ (we have $C^k_{\rho_F d} = {C^k_{d\rho_F}}^T$)
- $C_{\rho_F\rho_F} = F\, C_{\rho_0\rho_0}\, F^T + C_{d_F d_F}$ is the N_F x N_F matrix extracted from the matrix $C_{\rho_0\rho_0}$. $C_{d_F d_F}$ is the variance matrix of the error on the fixed parameters ρ_F
- $C_{g\rho_0} = H\, C_{\rho_0\rho_0}$ are the N_G differences between two lines of the matrix $C_{\rho_0\rho_0}$ where a gradient is known
- $C_{g\rho_F} = H\, C_{\rho_0\rho_0}\, F^T$ is the N_G x N_F matrix extracted from the matrix $C_{\rho_0\rho_0}$ (we have $C_{g\rho_F} = {C_{\rho_F g}}^T$)
- $C^k_{gd} = H\, C_{\rho_0\rho_0}\, {J_k}^T$ is the N_G x N matrix extracted from the matrix $C_{\rho_0\rho_0} J_k$ (we have $C^k_{gd} = {C^k_{dg}}^T$)
- $C_{gg} = H\, C_{\rho_0\rho_0}\, H^T + C_{d_g d_g}$ is the N_G x N_G matrix extracted from the matrix $C_{\rho_0\rho_0}$. $C_{d_g d_g}$ is the variance matrix of the error on the gradients g

Solution (4.11), obtained by preconditioned conjugate gradient least squares PCCGLS (see appendix 4.4.3) or a LU decomposition, can be written in dual

cokriging form as

$$\hat{\rho}_{k+1} = \rho_0 + \begin{bmatrix} {C^k_{d\rho_0}}^T & {C_{\rho_F\rho_0}}^T & {C_{g\rho_0}}^T \end{bmatrix} \begin{bmatrix} C^k_{dd} & C^k_{d\rho_F} & C^k_{dg} \\ C^k_{\rho_F d} & C_{\rho_F\rho_F} & C_{\rho_F g} \\ C^k_{gd} & C_{g\rho_F} & C_{gg} \end{bmatrix}^{-1} \begin{bmatrix} \delta d^k \\ \delta\rho_F \\ \delta g \end{bmatrix} \quad (4.12)$$

We note that Equations (4.1) and (4.12) are identical.

4.3.3.4 Optimal step

For the optimal step we have evaluated two methods :

Backtracking method : When the solution is obtained by PCCGLS, we have $\hat{\rho}_{k+1} = \rho_0 + \delta\hat{\rho}_{k+1}$. We deduce the increment $\delta\hat{\rho}_{k+1}$ at the iteration $k+1$. However, selecting the increment $\delta\hat{\rho}_{k+1}$ does not necessarily improve the objective function $\phi_d(\hat{\rho}_{k+1})$. A linear search is done by weighting the increment, then $\hat{\rho}_{k+1} = \rho_0 + \lambda\ \delta\hat{\rho}_{k+1}$. The function $\phi_d(\hat{\rho}_{k+1})$ is calculated for $\hat{\rho}_{k+1}$ by reducing the coefficient λ, initially equal to 1, by a factor $\alpha \in [2, 10]$ until $\lambda \in [10^{-6}, 10^{-2}]$ or until the solution is satisfactory (Dennis et Schnabel, 1996; Nocedal et Wright, 2000).

Golden section method : Another method to choose λ is the golden section method (Culioli, 1994; Bertsekas, 1995) which leads to a better estimation of λ at an increased cost in computation time. This method cuts the interval [0,1] for the values of λ in several intervals and calculates the function $\phi_d(\hat{\rho}_{k+1})$ in each interval. Research of the optimum step λ continues in the interval where the function $\phi_d(\hat{\rho}_{k+1})$ is minimum by subdividing this one until the number of maximum subdivision is reached (see appendix 4.4.4).

For the two methods, the cokriging variance of the estimated parameters is updated as $L'(\hat{\rho}_{k+1}; \Lambda_k, \alpha_k, \beta_k) = C_{\rho_0\rho_0} + (2\lambda - \lambda^2)\ [L(\hat{\rho}_{k+1}; \Lambda_k, \alpha_k, \beta_k) - C_{\rho_0\rho_0}]$.

After a few tests the *Golden section method* was observed to be more efficient and was selected for the inversion scheme.

4.3.3.5 Convergence criterion

Different criteria are selected to stop the inversion process :

i) when the functional $\phi(\boldsymbol{\rho})$ reaches a sill or diverges ;

ii) after a maximum number of iterations ;

iii) if the parameter model $\boldsymbol{\rho_{k+1}}$ is stationary (Gill *et al.*, 1981) by using the relation :

$$\frac{||\boldsymbol{\rho_{k+1}} - \boldsymbol{\rho_k}||}{max(||\boldsymbol{\rho_{k+1}}||, ||\boldsymbol{\rho_k}||)} < tolerance \tag{4.13}$$

where $||\cdot||$ denotes the Euclidian norm.

4.3.3.6 Forward modelling and sensitivity matrix

The forward modelling of the electrical potential is done by an integral equation using charge density (Boulanger et Chouteau, 2004). The calculation of the sensitivity matrix $\frac{\partial \boldsymbol{V(\rho)}}{\partial \boldsymbol{\rho}}$ is estimated with

$$\frac{\partial V(\boldsymbol{r_r}, \boldsymbol{r_s})}{\partial \rho_{i,j,k}} = \frac{1}{4\pi\rho_{i,j,k}} \int_{V_{i,j,k}} \nabla G(\boldsymbol{r_{i,j,k}}, \boldsymbol{r_r}) \cdot \nabla V(\boldsymbol{r_{i,j,k}}, \boldsymbol{r_s}) dv \tag{4.14}$$

where $G(\boldsymbol{r_{i,j,k}}, \boldsymbol{r_r})$ is the Green function given by $G(\boldsymbol{r_{i,j,k}}, \boldsymbol{r_r}) = \frac{1}{|\boldsymbol{r_{i,j,k}} - \boldsymbol{r_r}|} + \frac{1}{|\boldsymbol{r_{i,j,k}} - \boldsymbol{r'_r}|}$ with $|\boldsymbol{r_{i,j,k}} - \boldsymbol{r_r}| = ((x_i - x_r)^2 + (y_j - y_r)^2 + (z_k - z_r)^2)^{1/2}$ and $|\boldsymbol{r_{i,j,k}} - \boldsymbol{r'_r}| = ((x_i - x_r)^2 + (y_j - y_r)^2 + (z_k + z_r)^2)^{1/2}$. $\boldsymbol{r_r}$, $\boldsymbol{r_s}$ and $\boldsymbol{r_{i,j,k}}$ are the distances of the source, the receiver and the cell (i, j, k) from the origin of the cartesian coordinate system. $\boldsymbol{r'_r}$ is the mirror image of the point $\boldsymbol{r_r}$ across the ground-air interface. The sensitivity for a cell (i, j, k) is thus the scalar product of the electric field resulting

from the source point r_s and the gradient of the Green function resulting from the receiving point r_r, calculated at the point $r_{i,j,k}$. The method requires only the calculation of the electric field at the source point.

4.3.4 Modelled data

For all tests with the synthetic data the subsurface is divided into 12 x 12 x 11 = 1584 cubic cells with 20 m sides. The noise-free data are calculated in pole-pole configuration with 20 transmitters and 20 receivers in tomographic mode. The synthetic model and the cokriging result are presented in cross sections at the coordinates $X = 0\ m$, $Y = 0\ m$ and $Z = 70\ m$ (for the conducting prism model) or $Z = 90\ m$ (for the conducting prism body intersected by two holes model and the two conducting prisms models).

4.3.4.1 The conducting prism

The inversion program is tested with a conducting prism of resistivity 10 $\Omega.m$ hosted in a background of 1000 $\Omega.m$ (see Figure 4.1). The initial model resistivity for the cokriging corresponds to the average apparent resistivity of 1054 $\Omega.m$. Figure 4.2 shows the cokriging result after 2 iterations, when no parameters are fixed along the boreholes. The body is correctly located with a spreading between the two boreholes caused by the 2D nature of the measured data. This configuration has good resolution only in the vertical direction. The high sensitivity along the boreholes also contribute in generating low resistivities and artifacts at the transmitter and receiver positions. The resistivity of the conducting prism approaches 400 $\Omega.m$ instead of 10 $\Omega.m$. Figure 4.3 shows the cokriging result after 2 iterations when resistivity values of 1000 $\Omega.m$ are fixed for cells along the boreholes. The

body is correctly located and better resolved with the same resistivity estimate. Figure 4.4 shows the cokriging result after 2 iterations when resistivity values of 1000 $\Omega.m$ are fixed for cells along the boreholes and the known gradients are fixed around the body. The body is well located and well resolved with the correct resistivity of 10 $\Omega.m$. Figure 4.5 shows the adjustment of the covariance matrix $\boldsymbol{C}^{\boldsymbol{0}}_{\boldsymbol{dd}}$ obtained from the modelled data. We used $a_x = 80m$, $a_y = 80m$, $a_z = 80m$, $sill = 5 * 10^5\ (\Omega.m)^2$, $azimuth = 0°$, $dip = 0°$ and $plunge = 0°$ with a spherical model for the parameters of the covariance matrix $\boldsymbol{C_{\rho_0\rho_0}}$ and $\boldsymbol{C_{d_0d_0}} = 6*10^{-2}\ Volt^2$. The background resistivity is chosen to be $\boldsymbol{\rho_0} = 1150\ \Omega.m$ to fit the covariance model. The fit between the theoretical and the experimental covariances is well resolved at small lags. In this example the adjustment of the covariance was not always easy because the high sensitivity along the holes influences the theoretical covariance $\boldsymbol{C}^{\boldsymbol{0}}_{\boldsymbol{dd}}$. Instead of decreasing the experimental covariance curve can oscillate for small lags and decrease for large lags. Increasing or decreasing $\boldsymbol{\rho_0}$ suppresses the oscillations. Figure 4.5 shows that in some cases it is necessary to use a priori information from geological data and borehole resistivity data, if available, to best estimate the parameters of the covariance matrix $\boldsymbol{C_{\rho_0\rho_0}}$ or to fix some parameter *a priori*.

4.3.4.2 Conducting prism intersected by two holes

A conducting body of resistivity 10 $\Omega.m$ is hosted in a homogeneous medium of 1000 $\Omega.m$ (see Figure 4.6). The initial model resistivity for the cokriging corresponds to the average apparent resistivity of 1103 $\Omega.m$. Figure 4.7 shows the cokriging result after 2 iterations when resistivity values of 1000 $\Omega.m$ and 10 $\Omega.m$ are fixed along the boreholes. The geometry of the body and the conductivity are

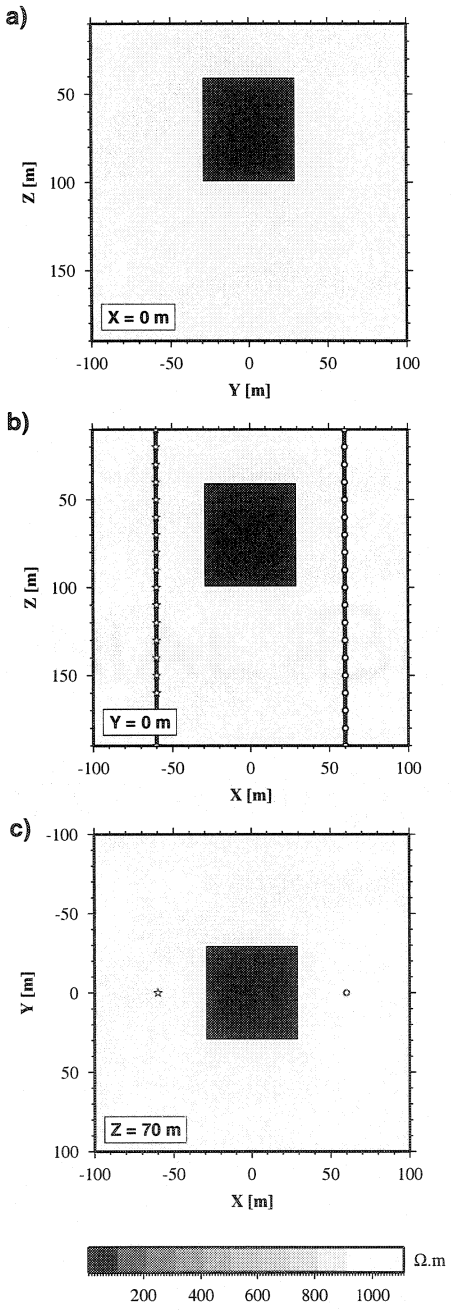

Figure 4.1: Model composed of a conducting prism of 10 $\Omega.m$ hosted in a background of 1000 $\Omega.m$. Transmitter and receiver are presented by a star and a circle, respectively.

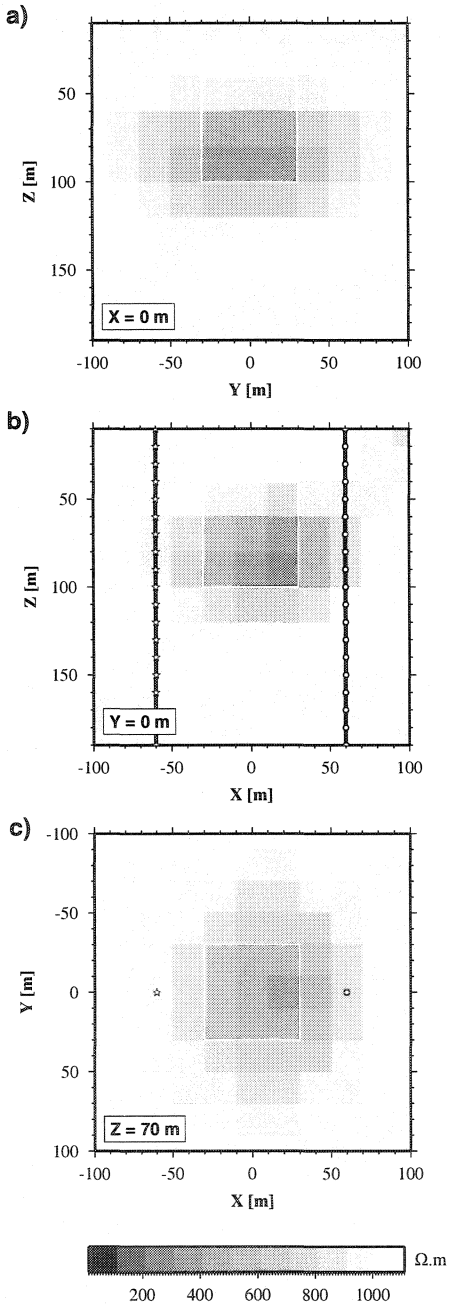

Figure 4.2: Cokriging result without constraints on the model presented at the figure 4.1 after 2 iterations.

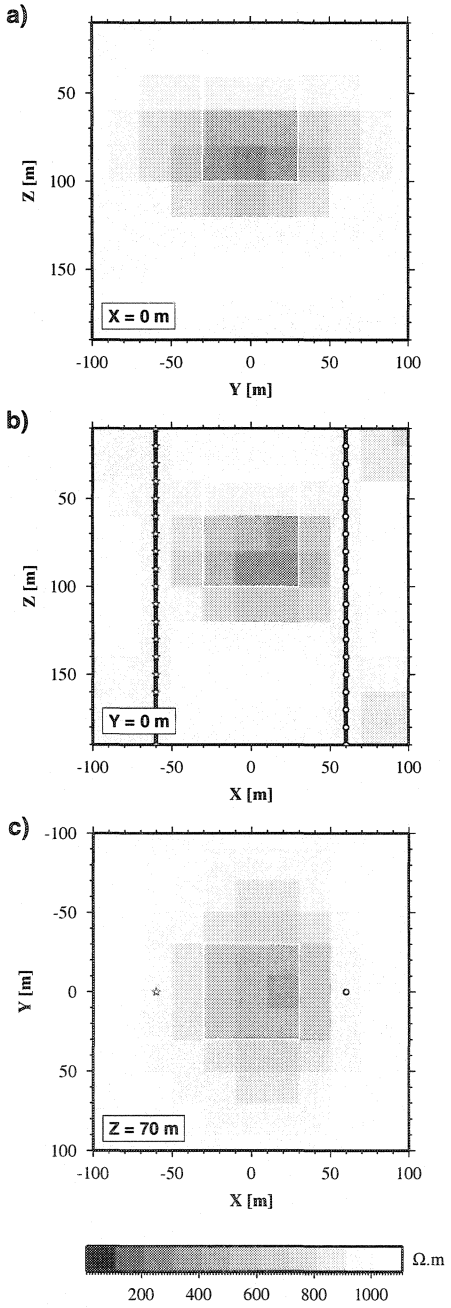

Figure 4.3: Cokriging result with fixed resistivity along the boreholes of the model presented at the figure 4.1 after 2 iterations.

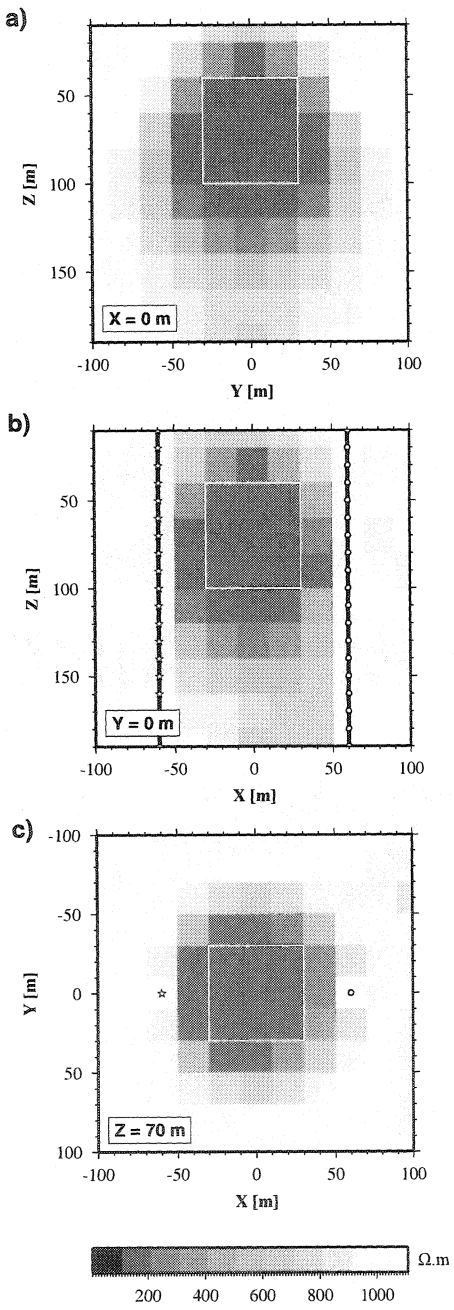

Figure 4.4: Cokriging result with fixed resistivity along the boreholes and fixed gradients around the conducting body of the model presented at the figure 4.1 after 2 iterations.

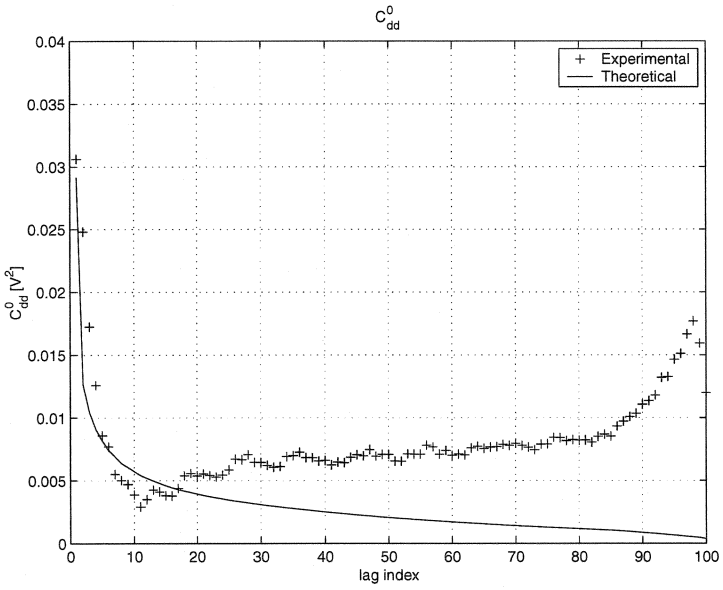

Figure 4.5: Fit of the covariance matrix $\boldsymbol{C^0_{dd}}$ from the synthetic data of the model presented at the figure 4.1. Spherical covariance model parameters $\boldsymbol{C_{\rho_0\rho_0}}$: $a_x = 80m$, $a_y = 80m$, $a_z = 80m$, $sill = 5 * 10^5\ (\Omega.m)^2$, $azimuth = 0°$, $dip = 0°$ and $plunge = 0°$. $\boldsymbol{C_{d_0d_0}} = 6 * 10^{-2}\ Volt^2$. $\boldsymbol{\rho_0} = 1150\ \Omega.m$.

well resolved.

Figure 4.8 shows the cokriging result after 2 iterations when resistivity values of 1000 $\Omega.m$ and 10 $\Omega.m$ are fixed along the boreholes and the known gradients are fixed around the body. The body is correctly located and identified with a resistivity of 10 $\Omega.m$. Figure 4.9 shows the fit of the model covariance matrix $\boldsymbol{C_{dd}^0}$. The experimental covariance $\boldsymbol{C_{dd}^{exp}}$ oscillates around $\boldsymbol{C_{dd}^0}$ and presents a nugget effect except at the first lag. We used $a_x = 300m$, $a_y = 80m$, $a_z = 80m$, $sill = 10^5\ (\Omega.m)^2$, $azimuth = 0°$, $dip = 0°$ and $plunge = 0°$ in a spherical model for the covariance matrix $\boldsymbol{C_{\rho_0\rho_0}}$ and $\boldsymbol{C_{d_0d_0}} = 5\ Volt^2$. The background resistivity was chosen as $\boldsymbol{\rho_0} = 1103\ \Omega.m$ to fit the covariance model.

4.3.4.3 Two conducting prisms

Another simple case consists of two conducting prisms of resistivity 10 $\Omega.m$ intersected by the boreholes in a host medium of 1000 $\Omega.m$ (see Figure 4.10). The initial model resistivity for the cokriging corresponds to the average apparent resistivity of 702 $\Omega.m$. Figure 4.11 shows the cokriging result after 2 iterations when resistivities of 1000 $\Omega.m$ and 10 $\Omega.m$ are fixed along the boreholes. The geometry of the two bodies and the conductivity are well resolved. Figure 4.12 shows the cokriging result after 2 iterations when resistivities of 1000 $\Omega.m$ and 10 $\Omega.m$ are fixed along the boreholes and the gradients are fixed around the body. The body is correctly identified and best identified with a resistivity of 10 $\Omega.m$. Figure 4.13 shows the fit of the model covariance matrix $\boldsymbol{C_{dd}^0}$. As in the previous case, the experimental covariance $\boldsymbol{C_{dd}^{exp}}$ oscillates around $\boldsymbol{C_{dd}^0}$ and presents a nugget effect except at the first lag. We used $a_x = 80m$, $a_y = 80m$, $a_z = 80m$, $sill = 13 * 10^5\ (\Omega.m)^2$, $azimuth = 0°$, $dip = 0°$ and $plunge = 0°$ in a spherical model for

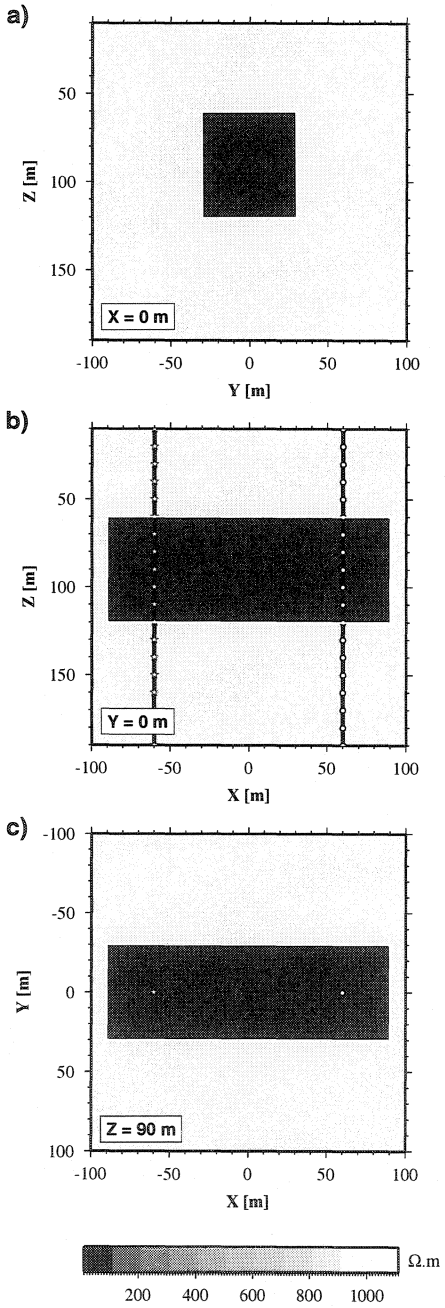

Figure 4.6: Model composed of a conducting prism of $10\ \Omega.m$ intersected by two holes and hosted in a background of $1000\ \Omega.m$.

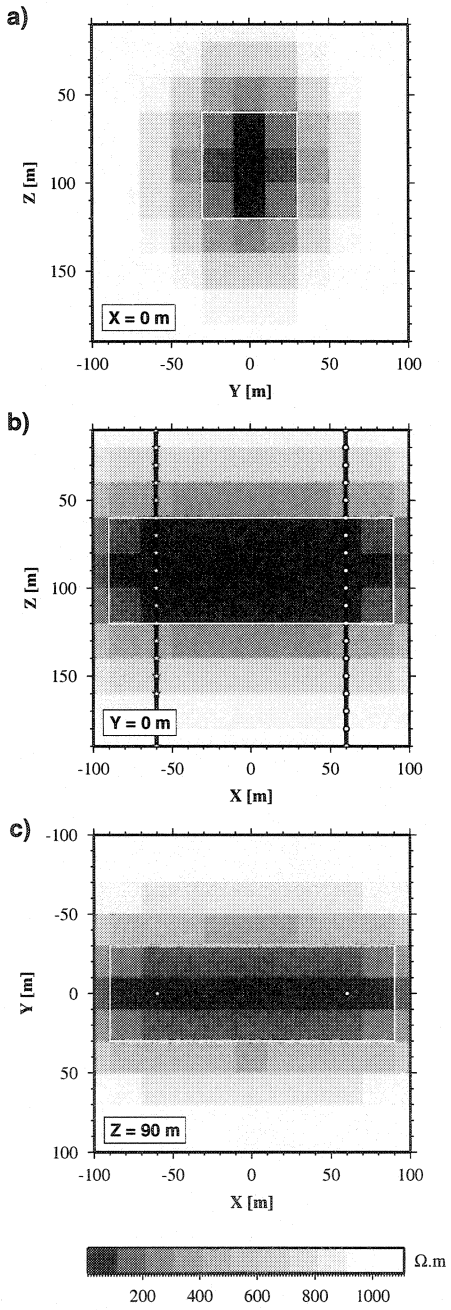

Figure 4.7: Cokriging result with fixed resistivity along the boreholes of the model presented at the figure 4.6 after 2 iterations.

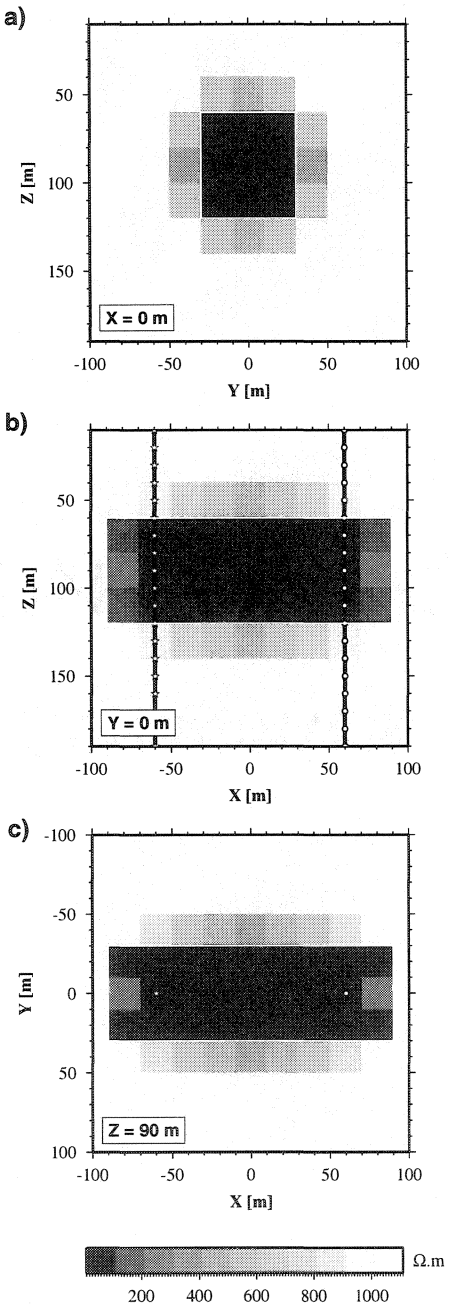

Figure 4.8: Cokriging result with fixed resistivity along the boreholes and fixed gradients around the conducting body of the model presented at the figure 4.6 after 2 iterations.

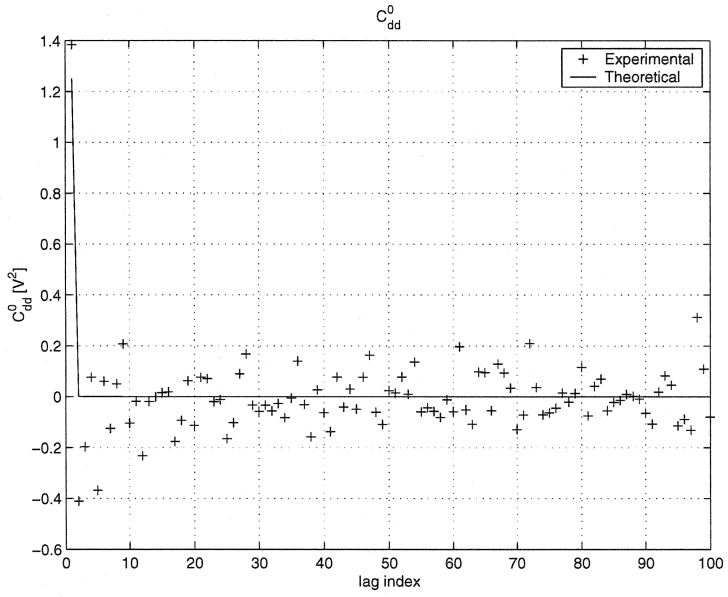

Figure 4.9: Fit of the covariance matrix $\boldsymbol{C^0_{dd}}$ from the synthetic data of the model presented in Figure 4.6. Spherical covariance model parameters $\boldsymbol{C_{\rho_0\rho_0}}$: $a_x = 300m$, $a_y = 80m$, $a_z = 80m$, $sill = 10^5\ (\Omega.m)^2$, $azimuth = 0°$, $dip = 0°$ and $plunge = 0°$. $\boldsymbol{C_{d_0d_0}} = 5\ Volt^2$. $\boldsymbol{\rho_0} = 1103\ \Omega.m$.

the covariance matrix $C_{\rho_0\rho_0}$ and $C_{d_0d_0} = 2\ Volt^2$. The background resistivity was chosen to be $\rho_0 = 702\ \Omega.m$ to fit the covariance model.

4.3.5 Application to survey data

4.3.5.1 Casa Berardi mine

Geological context and geometry of the boreholes

The Casa Berardi gold mine is located within the Abitibi Greenstone Belt in the north-western part of Quebec. The region consists of metavolcanic and metasedimentary rocks. Gold mineralization consists of quartz-dolomite-pyrite-arsenopyrite veins hosted in shear zones, quartz-vein stockworks within silicified host rocks, and disseminated sulfides within fractured host rocks. These different mineralized systems develop in volcanoplastic-pyroclastic units near contacts with sedimentary rocks (Pilote *et al.*, 1990; Spitzer et Chouteau, 2003).

For the interpretation of electrical resistivity at the Casa Berardi mine we used a priori geological information inferred from drilling and the geophysical interpretation of Spitzer et Chouteau (1997, 2003) who used successive forward 3D modelling. Figure 4.14 shows the major simplified lithological characteristics of the site. The auriferous zone is intersected by the two boreholes BH 79652 and BH 79651. Tuffs are found to the south of the auriferous zone and metasediments are encountered to the north. The overburden consists of glacial deposits. Its thickness is approximatively 20-30 m.

The azimuth of the two boreholes is N0°. The holes dip at about 45° (see Figure 4.14). Electrical potential was measured in pole-pole configuration with 17 transmitters in hole BH 79652 and 24 receivers in hole BH 79651. Figure 4.15

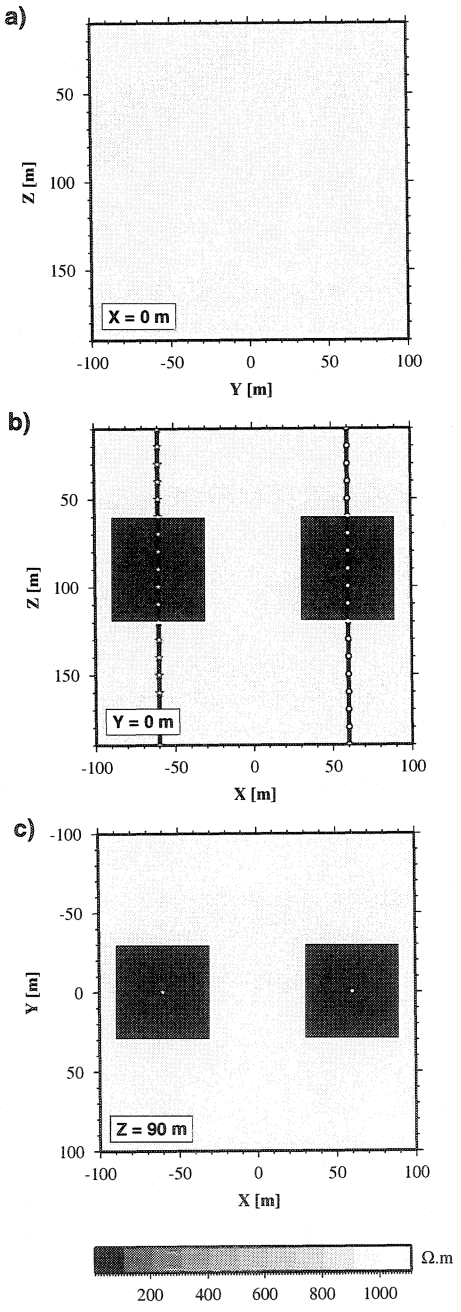

Figure 4.10: Model composed of two conducting prisms of 10 $\Omega.m$ hosted in a background of 1000 $\Omega.m$.

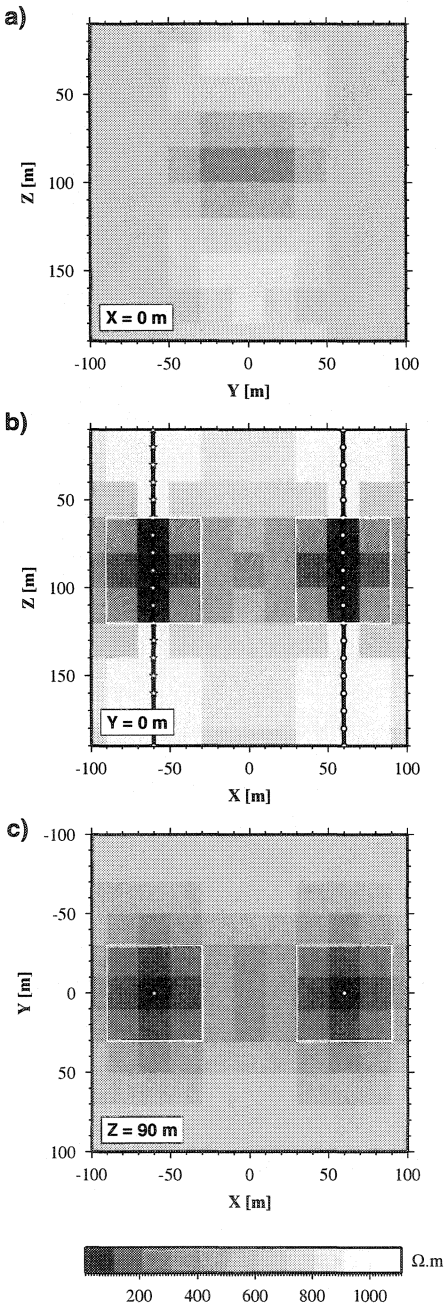

Figure 4.11: Cokriging result with fixed resistivity along the boreholes of the model presented at the figure 4.10 after 2 iterations.

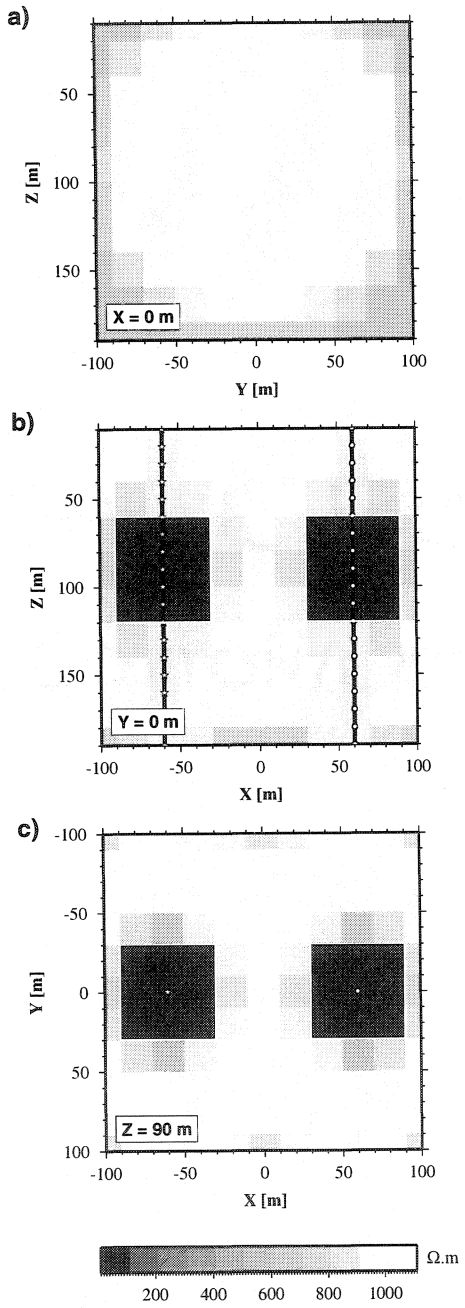

Figure 4.12: Cokriging result with fixed resistivity along the boreholes and fixed gradients around the conducting body of the model presented at the figure 4.10 after 2 iterations.

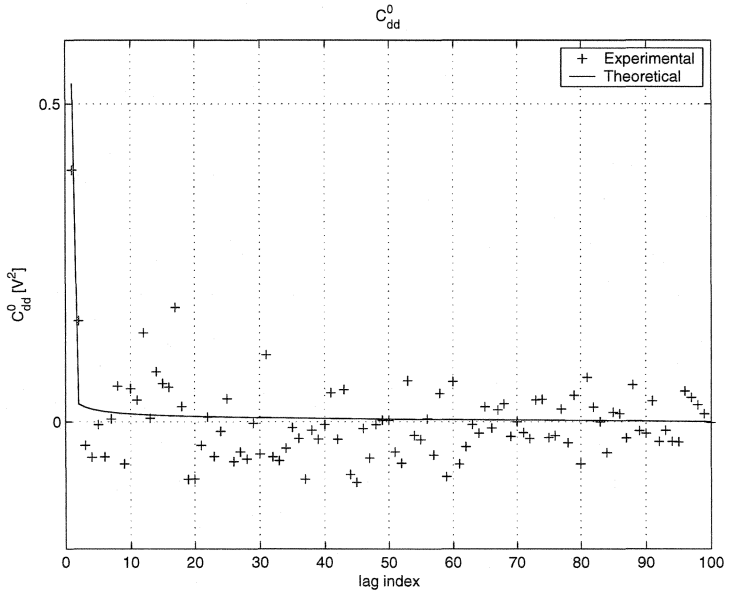

Figure 4.13: Fit of the covariance matrix C^{*0}_{dd} from the synthetic data of the model presented in Figure 4.10. Spherical covariance model parameters $C_{\rho_0\rho_0}$: $a_x = 80m$, $a_y = 80m$, $a_z = 80m$, $sill = 13 * 10^5\ (\Omega.m)^2$, $azimuth = 0°$, $dip = 0°$ and $plunge = 0°$. $C_{d_0d_0} = 2\ Volt^2$. $\rho_0 = 702\ \Omega.m$

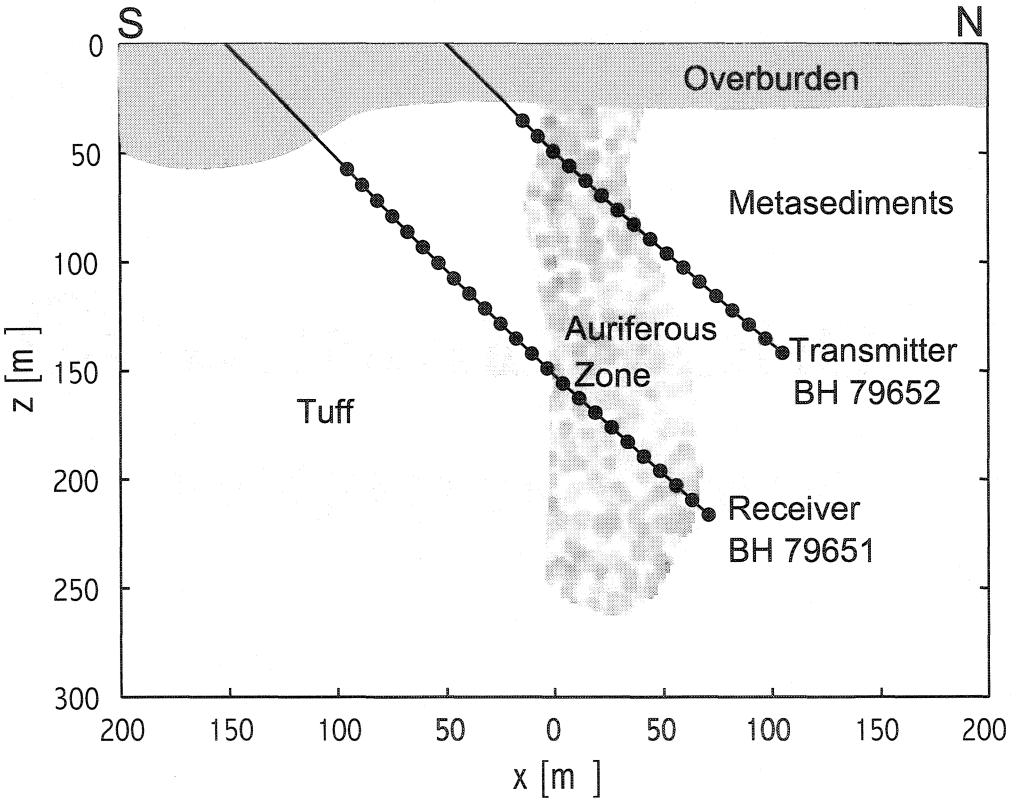

Figure 4.14: Geometry and geology at Casa Berardi.

shows measured apparent resistivity plots. The main feature is the huge increase in apparent resistivity (10000 $\Omega.m$) for deep transmitter/receiver positions.

Cokriging result

Geological information and the electrical forward modelling done by Spitzer et Chouteau (2003) indicate that the tuffs are conductive and the metasediments are highly resistive. The ore body is moderately resistive and the overburden is conductive. In Figure 4.16a we present the sensitivity distribution displayed in

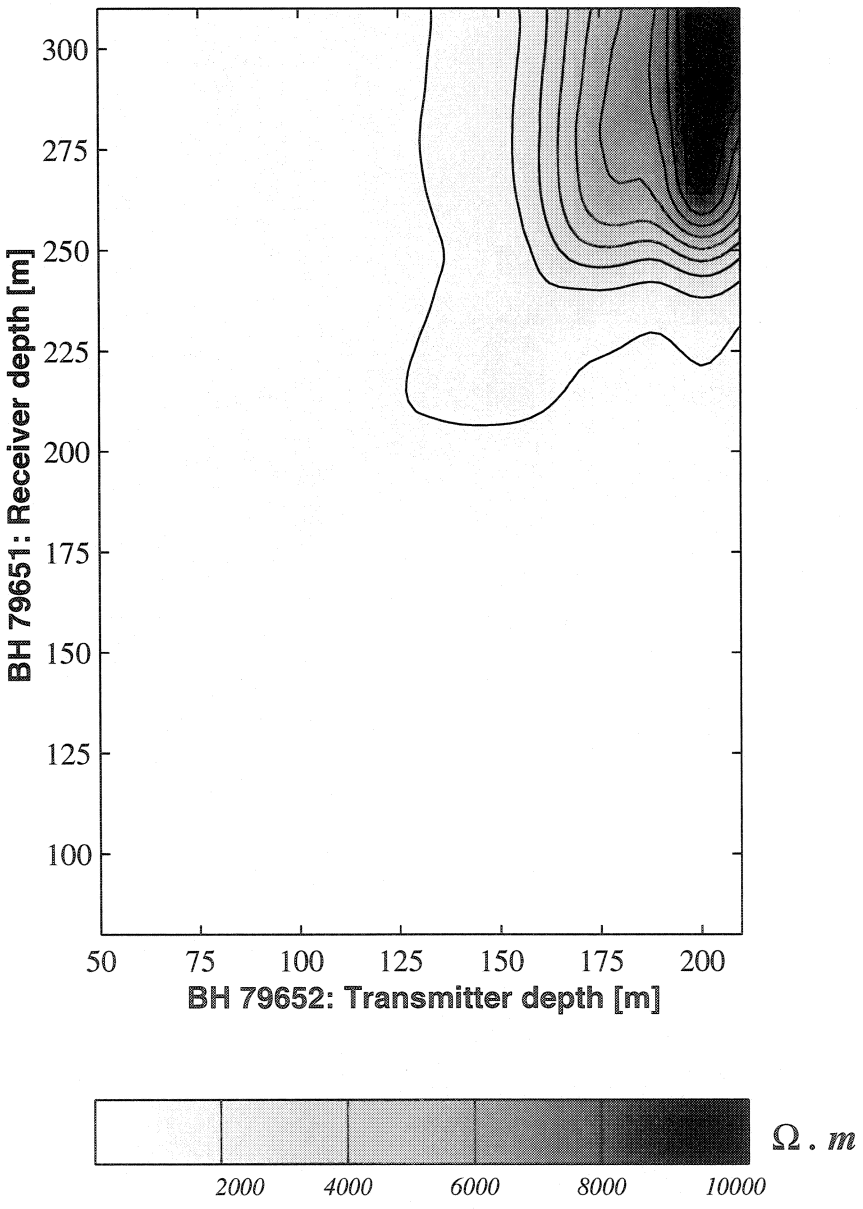

Figure 4.15: Apparent resistivity from potential measurements between the transmitters hole BH 79651 and the receiver hole BH 79652.

terms of the logarithmic cumulative sensitivity for all source-receiver positions ($\Phi_j = \sum_{i=1}^{i=N_P} |(\frac{\partial \boldsymbol{V(\rho)}}{\partial \boldsymbol{\rho_0}})_{ij}|; j = 1, M$). The figure indicates that low sensitivity regions are not important in physical and geological interpretations. In Figure 4.16b, we present the result of the cokriging for the section at $Y = -1m$. For the inversion we use 29x16x21 cubic cells having 15 m sides. The resistivities are constrained to be within the interval [0,40000] $\Omega.m$. Figure 4.17 shows the adjustment of the matrix covariance $\boldsymbol{C^0_{dd}}$ for the data presented in Figure 4.15. We use $a_x = 150m$, $a_y = 400m$, $a_z = 140m$, $sill = 7 * 10^7$ $(\Omega.m)^2$, $azimuth = 0°$, $dip = 0°$ and $plunge = 0°$ in a spherical model for the parameters of the covariance matrix $\boldsymbol{C_{\rho_0\rho_0}}$ and $\boldsymbol{C_{d_0d_0}} = 5\ Volt^2$. The background resistivity is chosen to be $\boldsymbol{\rho_0} = 1300\ \Omega.m$ to fit the covariance model. Fixed parameters are used along the boreholes with resistivity values inspired by the forward model of Spitzer et Chouteau (2003). Major lithological characteristics agree with the results of Spitzer et Chouteau (2003). Metasediments have a very high resistivity of 40000 $\Omega.m$ and tuffs are conductive.

4.3.5.2 Mc Connell deposit

Geological context and geometry of the boreholes

Surveys were done at the Mc Connell nickel deposit near Sudbury (Ontario, Canada) to assess the potential of the borehole electrical method in delineating massive sulphides. The McConnell deposit is a small tabular body steeply dipping to the south with a lateral extension of 150 m. It is intersected by three boreholes BH 78929, BH 78930 and BH 80578 (see Figure 4.18). Metavolcanics are found to the south and norites are encountered to the north. The overburden thickness is approximatively 20 m. The three boreholes have an azimuth of 0° N and dip

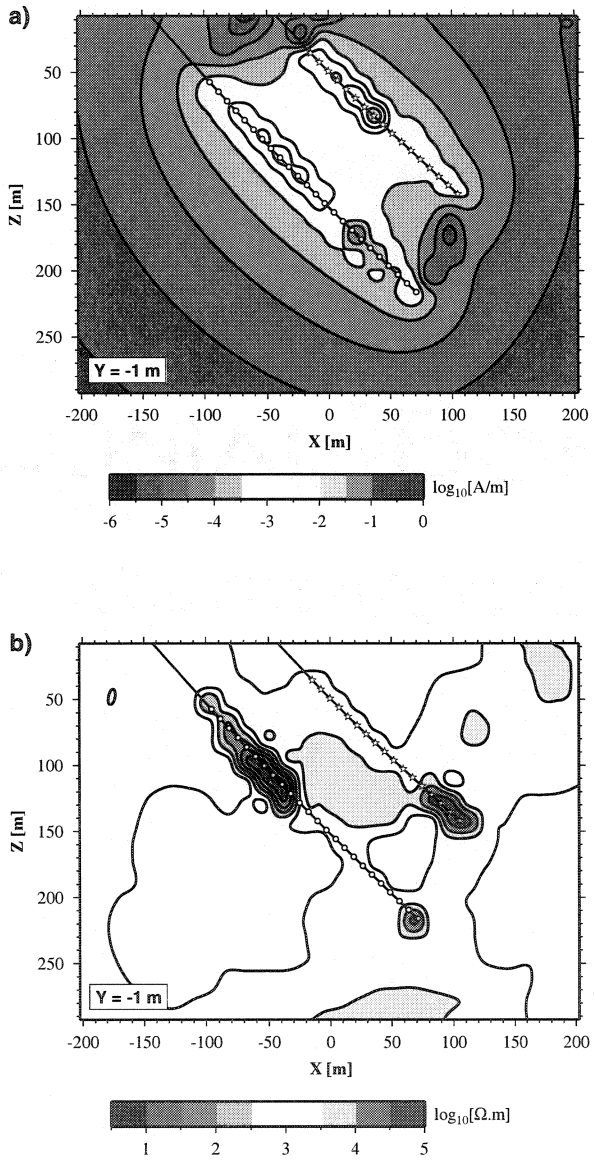

Figure 4.16: a) vertical section of the sensitivity distribution displayed in terms of the logarithmic cumulative sensitivity Φ_j for all the source-receiver positions. b) cokriging result from the Casa Berardi data shown at the figure 4.15 after 1 iteration with resistivity values constrained to be in the interval [0,41000] $\Omega.m$. Resistive features at the bottom and close to the surface are caused by low sensitivities.

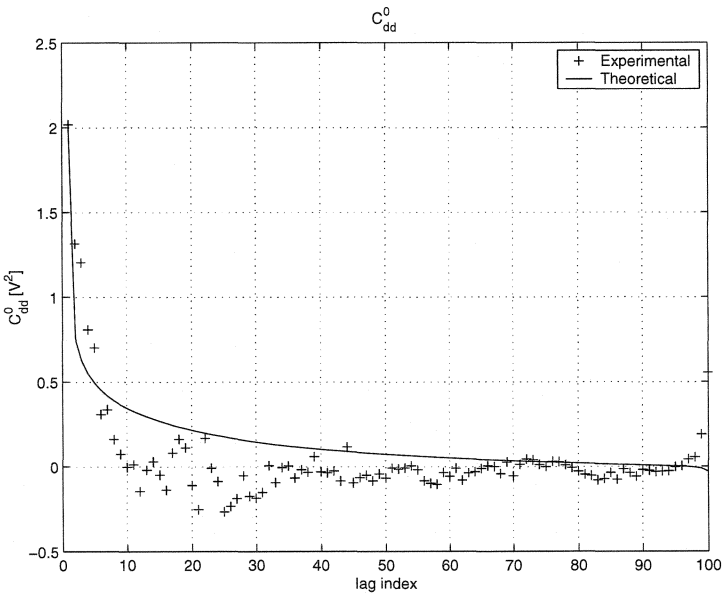

Figure 4.17: Fit of the covariance matrix C^0_{dd} from the Casa Berardi data shown in Figure 4.15. Spherical covariance model parameters $C_{\rho_0\rho_0}$: $a_x = 150m$, $a_y = 400m$, $a_z = 140m$, $sill = 7 * 10^7\ (\Omega.m)^2$, $azimuth = 0°$, $dip = 0°$ and $plunge = 0°$. $C_{d_0d_0} = 5\ Volt^2$. $\rho_0 = 1300\ \Omega.m$.

48° to 80° N. Electrical potential was measured in pole-pole configuration with 13 transmitters in hole BH 78929 and 14 receivers in hole BH 78930 for the first data set (Figure 4.19) and with 14 transmitters in hole BH 78930 and 32 receivers in hole BH 80578 for the second data set (Figure 4.20). Resistivity logging is available for the three holes (Killeen *et al.*, 1996) and is used to fix the parameters along the boreholes.

Cokriging result

Figure 4.21a presents the result of the cokriging for the section at Y=0 m. For the inversion we use 21x10x35 cubic cells having 10 m sides. The resistivities are constrained to be in the interval [0,30000] $\Omega.m$. In Figure 4.21b we present the sensitivity distribution displayed in terms of the logarithmic cumulative sensitivity for all the source-receiver positions ($\Phi_j = \sum_{i=1}^{i=N_P} |(\frac{\partial V(\rho)}{\partial \rho_0})_{ij}|; j = 1, M$). Figure 4.22 shows the adjustment of the matrix covariance $\boldsymbol{C}_{\boldsymbol{dd}}^{\boldsymbol{0}}$ for the data presented in Figures 4.19 and 4.20. We used $a_x = 150m$, $a_y = 60m$, $a_z = 500m$, $sill = 10^6\ (\Omega.m)^2$, $azimuth = -90°$, $dip = 17°$ and $plunge = 0°$ in a spherical model for the covariance matrix $\boldsymbol{C}_{\boldsymbol{\rho_0\rho_0}}$ and $\boldsymbol{C}_{\boldsymbol{d_0d_0}} = 0.5\ Volt^2$. The background resistivity is chosen to be $\boldsymbol{\rho_0} = 1200\ \Omega.m$ to fit the covariance model. These covariance parameters are constrained using geological information available on the Mc Connell deposit (Killeen *et al.*, 1996). Fixed parameters are used along the boreholes. Major lithological characteristics agree with the geological model. The massive sulfide is well located with respect to the proposed geological model. This conducting body is not completely connected between the three holes as shown in Figure 4.18. Around the x-interval [0,80]m and z-interval [110,170] m, a highly conductive body corresponds to a low sensitivity region and is an artifact.

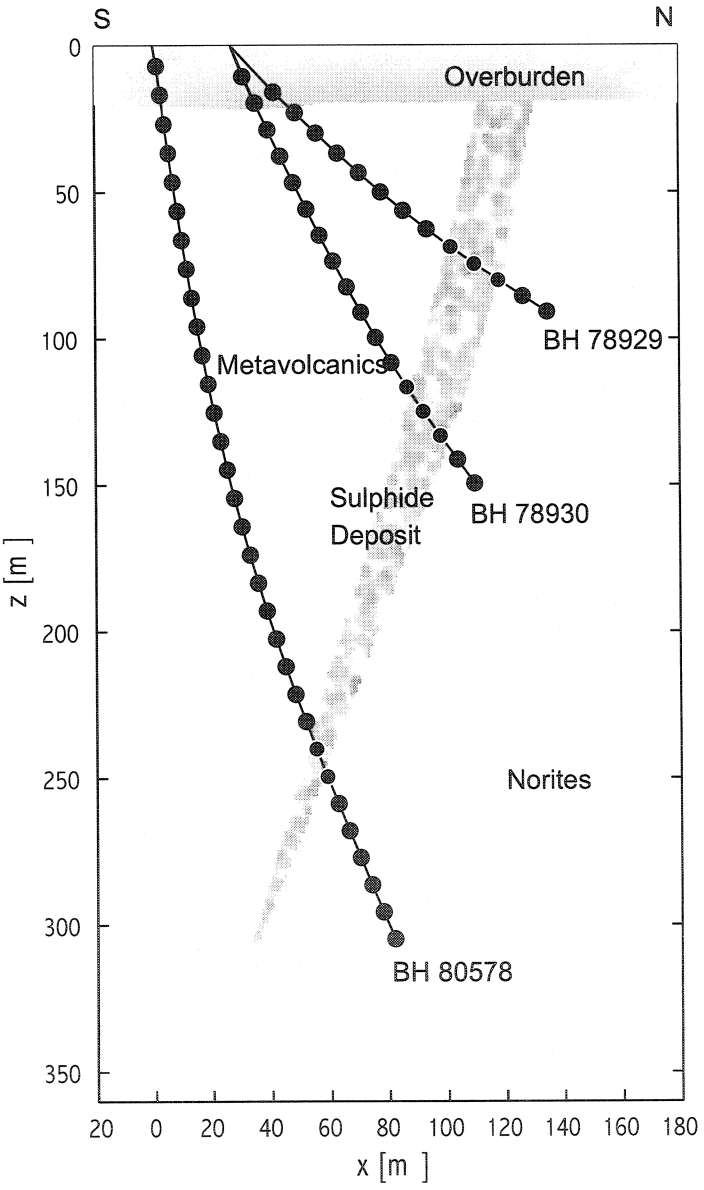

Figure 4.18: Geometry and geology at Mc Connell.

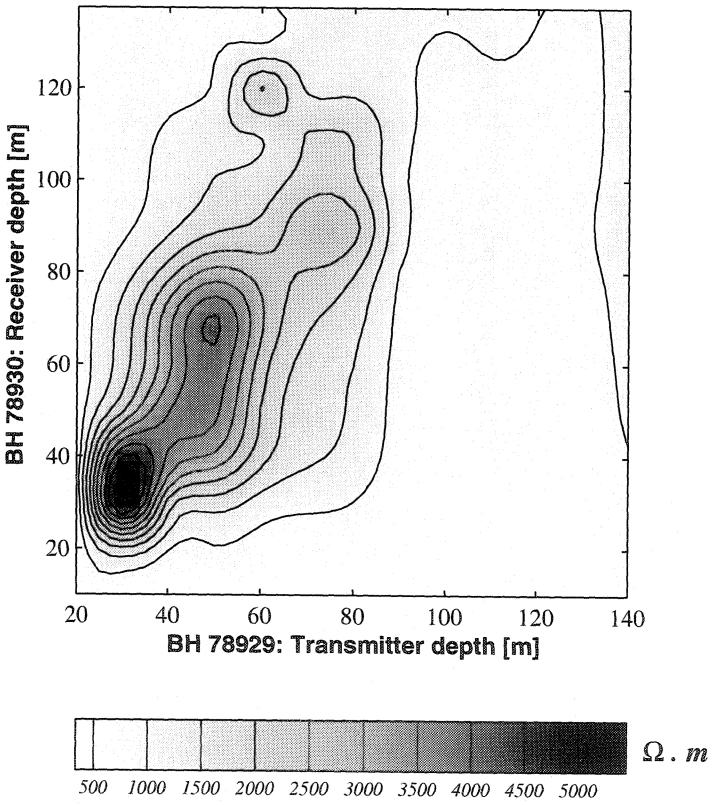

Figure 4.19: Apparent resistivity from potential measurements between the transmitters hole BH 78929 and the receiver hole BH 78930.

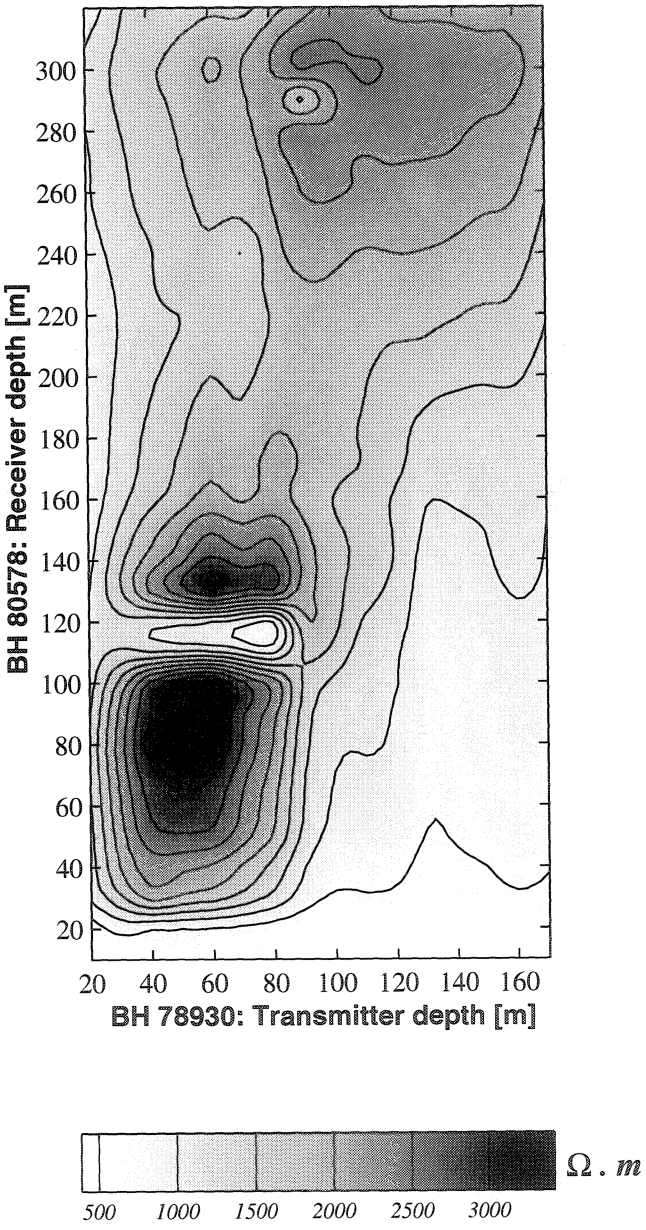

Figure 4.20: Apparent resistivity from potential measurements between the transmitters hole BH 78930 and the receiver hole BH 80578.

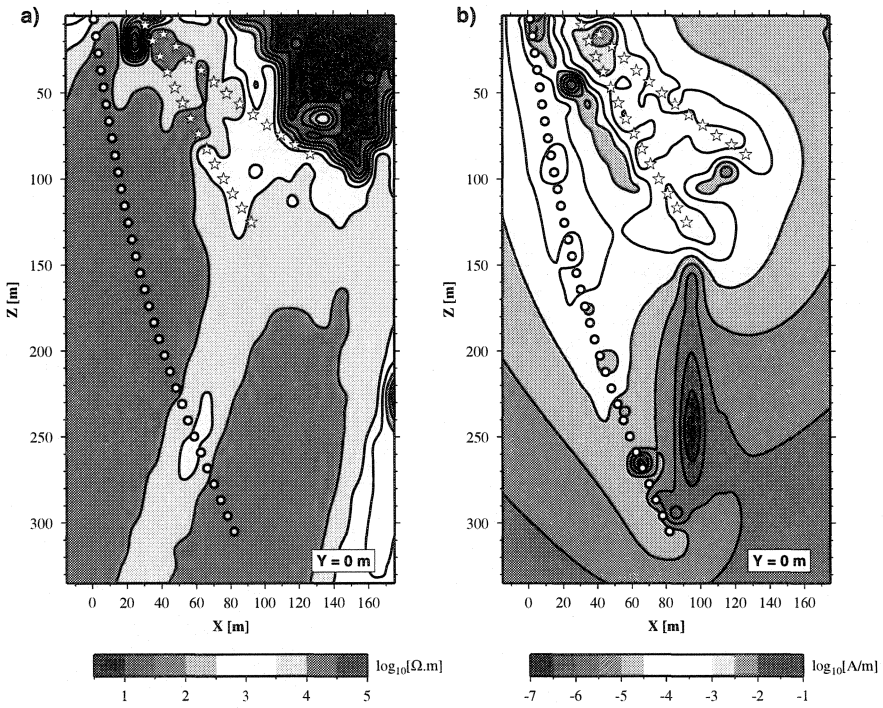

Figure 4.21: a) cokriging result from the Mc Connell data shown at the figures 4.19 and 4.20 after 1 iteration with resistivity values constrained to be in the interval [0,30000] $\Omega.m$. b) vertical section of the sensitivity distribution displayed in terms of the logarithmic cumulative sensitivity Φ_j for all the source-receiver positions. Conductive features close to the surface are caused by low sensitivities.

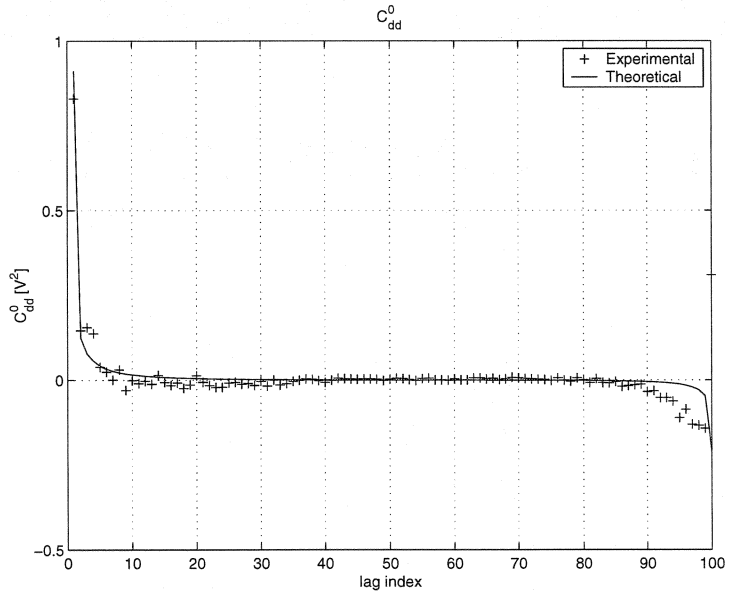

Figure 4.22: Fit of the covariance matrix C^0_{dd} from the Mc Connell data shown in Figures 4.19 and 4.20. Spherical covariance model parameters $C_{\rho_0\rho_0}$: $a_x = 150m$, $a_y = 60m$, $a_z = 500m$, $sill = 10^6\ (\Omega.m)^2$, $azimuth = -90°$, $dip = 17°$ and $plunge = 0°$. $C_{d_0d_0} = 0.5\ Volt^2$. $\rho_0 = 1200\ \Omega.m$.

4.4 Discussion and conclusions

We propose estimating the electrical resistivity using a geostatistical formulation which takes into account the correlations between the parameters (cell resistivities) by means of a full covariance matrix. Obtaining a good fit between the theoretical and experimental covariances is sometimes challenging. Nevertheless, it is possible to obtain at least crude estimates of the sill and the ranges along principal geological directions. It is also possible to validate prior estimates deduced from geological knowledge. Note that cokriging results are relatively robust to moderate misspecification of the covariance function. The sill controls the magnitude of the difference between cokriging estimates without modifying the general picture. On the other hand, the ranges influence the smoothness of the interpolation. However, we verified that increasing or decreasing the range of the covariance function by a factor as large as 50 % had only small impact on the image produced. The geological interpretation that could be drawn from the inversion did not change significantly.

The cokriging solution can be solved in primal form which gives access to the estimation variance or in the dual form using the preconditionned conjugate gradient (PCCGLS) or LU decomposition. PCCGLS and LU are two stable numerical methods.

The program is tested on synthetic data and the solution generally converges rapidly. When the body is not intersected the solution is less well defined due to high sensitivity along the holes and low sensitivity between them. Many authors used *ad hoc* weights to desensitize the cells along the holes without providing a physical justification. In our case the sill in the model covariance compensates for

the low sensitivity between the holes and finds bodies of high resistivity contrast. However the high sensitivity close to the transmitters and the receivers can pose problems when modelling the theoretical covariance. When the bodies are connected between the holes or located along the holes the solution is more precise and better results are obtained with high resistivity contrasts. The incorporation of the resistivity gradients in the three directions improves considerably the solution. The use of gradient constraints is new in electrical tomographic imaging and can be useful in the mining industry if 3D geological model can be built with a GIS. Gradient constraints can also be applied in other fields such as in geotechnical problems where there is better geometrical knowledge on the sites.

A method is said to be ill-posed if a small perturbation in the data corresponds to an arbitrarily large perturbation in the solution. In real applications, noise in the data contributes to larger nugget effects which, in turn, contribute to making the data covariance matrix nonsingular. Cokriging is then stable (well-posed) and a smooth solution is obtained. In two case studies, the Casa Berardi gold mine and the Mc Connell deposits, cokriging succeeds in delineating mining targets when the resistivity along the holes is fixed as a measured data. The solutions agree well with the known geology. Although all the results presented are in 2D tomographic mode, the code is designed for the 3D case with electrical potential data located arbitrary at the surface and along the boreholes.

4.4.1 Acknowledgements

The author would like to thank Mustapha Asli, Erwan Gloaguen and Bernard Giroux from Ecole Polytechnique of Montreal for their helpful suggestions. Thanks to Maria Annecchione for editing the manuscript. This work was supported by the

Natural Science and Engineering Research Council of Canada (NSERC) Grant RGPIN 848.

4.4.2 References

Asli, M., Marcotte, D., and Chouteau, M. (2000). Direct inversion of gravity data by cokriging. In *6th Annual Geostatistical Meeting, Cape Town, Afrique du Sud.*

Bertsekas, D. P. (1995). *Nonlinear programming.* Athena Scientific.

Bing, Z. and Greenhalgh, S. A. (2000). Cross-hole resistivity tomography using different electrode configurations. *Geophysical Prospecting*, 48(5) :887–912.

Björck, A. (1996). *Numerical methods for least squares problems.* SIAM Publications.

Borcea, L., Berryman, J. G., and Papanicolaou, G. C. (1996). High contrast impedance tomography. *Inverse Problems*, 12 :835–856.

Boulanger, O. and Chouteau, M. (2002). 3D modeling and sensitivity in DC resistivity using charge density. *submitted to Geophysical Prospecting.*

Brochu, Y. and Marcotte, D. (2003). A simple approach to account for radial flow and boundary conditions when kriging head fields for confined aquifers. *Mathematical Geology*, 35 :111–139.

Brunner, I., Friedel, S., Jacobs, F., and Danckwardt, E. (1999). Investigation of a Tertiary maar structure using three-dimensional resistivity imaging. *Geophysical Journal International*, 136(3) :771–780.

Chiles and Delfiner (1999). *Geostatistics, Modeling spatial uncertainty.* Wiley series on probability and statistics.

Chunduru, R. K., Sen, M. K., and Stofa, P. L. (1996). 2-D resistivity inversion using spline parametrization and simulated annealing. *Geophysics*, 61(1) :151–161.

Chunduru, R. K., Sen, M. K., Stoffa, P. L., and Nagendra, R. (1995). Non-linear inversion of resistivity profiling data for some regular geometrical bodies. *Geophysical Prospecting*, 43 :979–1003.

Cohen-Bacrie, C., Goussard, Y., and Guardo, R. (1997). Regularized reconstruction in electrical impedance tomography using a variance uniformization constraint. *IEEE Transactions on Medical Imaging*, 16(5) :562–571.

Culioli, J.-C. (1994). *Introduction à l'optimisation.* Ellipses.

Daily, W. and Owen, E. (1991). Cross-borehole resistivity tomography. *Geophysics*, 56(8) :1228–1235.

Daniels, J. J. and Dyck, A. V. (1984). Borehole resistivity and electromagnetic methods applied to mineral exploration. *IEEE Transactions on Geoscience and Remote Sensing*, GE-22(1) :80–87.

Dennis, J. E. and Schnabel, R. B. (1996). *Numerical methods for unconstrained optimization and nonlinear equations.* Society for Industrial and Applied Mathematics.

Deutsch, C. V. and Journel, A. G. (1998). *GSLIB : Geostatistical Software Library and User's Guide.* Oxford University Press, 2 edition.

Dines, K. A. and Lytle, J. (1979). Computerized geophysical tomography. *Proceedings of the IEEE*, 67(7) :1065–1073.

Dines, K. A. and Lytle, R. J. (1981). Analysis of electrical conductivity imaging. *Geophysics*, 46(7) :1025–1036.

Ellis, R. G. and Oldenburg, D. W. (1994). The pole-pole 3-D DC-resistivity inverse problem : a conjugate-gradient approach. *Geophysical Journal International*, 119 :187–194.

Fortier, N., Demoment, G., and Goussard, Y. (1993). GCV and ML method of determining parameters in image restoration by regularization : fast computation in the spatial domain and experimental comparison. *Journal of Visual Communication and Image Representation*, 4(2) :157–170.

Franklin, J. N. (1970). Well-posed stochastic extensions of ill-posed linear problems. *J. Math. Anal. Appl.*, 31 :682–716.

Gill, P. E., Murray, W., and Wright, M. H. (1981). *Practical optimization.* Academic Press.

Golub, G. H., Heath, M., and Wahba, G. (1979). Generalized cross-validation as a method for choosing a good ridge parameter. *Technometrics*, 21(2) :215–223.

Golub, G. H. and von Matt, U. (1997). Generalized cross-validation for large scale problems. *Journal of Computational and Graphical Statistics*, 6(1) :1–34.

Hansen, P. (1992). The L-curve and its use in the numerical treatment of inverse problems. In *Computational inverse problems in electrocardiology, P. Johnston, Advances in Computational Bioengineering, WIT Press, Southampton*, volume 4, pages 119–142.

Hestenes, M. R. (1975). Pseudoinverses and conjugate gradients. *Communications of ACM*, 18 :40–43.

Hutchinson, M. F. (1990). A stochastic estimator of the trace of the influence matrix for laplacian smoothing splines. *Communications in Statistics, Simulation and Computation*, 19 :433–450.

Inman, J. R. (1975). Resistivity inversion with ridge regression. *Geophysics*, 40(5) :798–817.

Jordan, T. H. and Franklin, J. N. (1971). Optimal solutions to a linear inverse problem in geophysics. *Proceeding of the National Academy of Sciences*, 68(2) :291–293.

Journel, A. G. and Huijbregts, C. J. (1978). *Mining Geostatistics.*

Kallman, J. S. and Berryman, J. G. (1992). Weighted least-squares criteria for electrical impedance tomography. *IEEE Trans. Med. Imaging*, 11 :284–292.

Killeen, P., Mwenifumbo, J., and Elliot, J. (1996). Mineral deposit signature by borehole geophysics : data from the borehole geophysical test at Mc Connell nickel deposit (Garson Offset). *Geological Survey of Canada*, Open file 2811.

LaBrecque, D. J., Miletto, M., Daily, W., Ramirez, A., and Owen, E. (1996). The effects of noise on Occam's inversion of resistivity tomography data. *Geophysics*, 61(2) :538–548.

Lesur, V., Cuer, M., and Straub, A. (1999). 2-D and 3-D interpretation of electrical tomography measurements, Part 2 : The inverse problem. *Geophysics*, 64(2) :396–402.

Li, Y. and Oldenburg, D. W. (1992). Approximate inverse mappings in DC resistivity problems. *Geophysical Journal International*, 109 :343–362.

Loke, M. H. and Barker, R. D. (1996). Practical techniques for 3D resistivity surveys and data inversion. *Geophysical Prospecting*, 44 :499–523.

Luenberger, D. (1969). *Optimization by vector space methods.* New York Wiley.

Lytle, R. J., Okada, J. T., and Concepcion, C. (1980). The potential field around subsurface electrically excited conductors. *IEEE Transactions on Geoscience*

and Remote Sensing, GE-18(3) :240–243.

Maillol, J. M., Seguin, M.-K., Gupta, O. P., Akhauri, H. M., and Sen, N. (1999). Electrical resistivity tomography survey for delineating uncharted mine galleries in West Bengal, india. *Geophysical Prospecting*, 47(2) :103–116.

Marcotte, D. (1995). Generalized cross-validation for covariance model selection. *Mathematical Geology*, 27 :659–672.

Meju, M. A. (1992). An effective ridge regression procedure for resistivity data inversion. *Computer and Geosciences*, 18(2/3) :99–118.

Narayan, S., Dusseault, M. B., and Nobes, D. C. (1994). Inversion techniques applied to resistivity inverse problems. *Inverse Problems*, 10(3) :669–696.

Nocedal, J. and Wright, S. J. (2000). *Numerical Optimization.* Springer.

Noel, M. and Xu, B. (1991). Archaeological investigation by electrical resistivity tomography : a preliminary study. *Geophysical Journal International*, 107 :95–102.

Olayinka, A. I. and Yaramanci, U. (2000). Use of block inversion in the 2-D interpretation of apparent resistivity data and its comparison with smooth inversion. *Journal of Applied Geophysics*, 45 :63–81.

Park, S. K. and Van, G. P. (1991). Inversion of pole-pole data for 3-D resistivity structure beneath arrays of electrodes. *Geophysics*, 56(7) :951–960.

Pelton, W. H., Rijo, L., and Swift, M. (1978). Inversion of two-dimensional resistivity and induced-polarization. *Geophysics*, 43(4) :788–803.

Petrick, W. R., Pelton, W. H., and Ward, S. H. (1977). Ridge regression inversion applied to crustal resistivity sounding data from south africa. *Geophysics*, 42 :995–1005.

Petrick, W. R., Sill, W. R., and Ward, S. H. (1981). Three-dimensional resistivity inversion using alpha centers. *Geophysics*, 46(8) :1148–1162.

Pilote, P., Guha, J., Daigneault, R., Robert, F., Cloutier, J.-Y., and Golightly, J. P. (1990). The structural evolution the Casa-Berardi township, Québec. In Rive, M., Verpaelst, P., Gagnon, Y., Lulin, J., Riverin, G., and Simard, A., editors, *Northwestern Québec Polymetallic Belt*, volume 43. Canadian Institute of Mining and Metallurgy.

Pous, J., Marcuello, A., and Queralt, P. (1987). Resistivity inversion with a priori information. *Geophysical Prospecting*, 35 :590–603.

Press, W. H., Teukolsky, S. A., Vetterling, W. T., and Flannery, B. P. (1992). *Numerical Recipes in C : The Art of Scientific Computing.* Cambridge University Press, 2nd edition.

Ramirez, A. and Daily, W. (2001). Electrical imaging at the large block test - Yucca Mountain, Nevada. *Journal of Applied Geophysics*, 46 :85–100.

Ramirez, A., Daily, W., LaBrecque, D., Owen, E., and Chesnut, D. (1993). Monitoring an underground steam injection process using electrical resistance tomography. *Water Resources Research*, 29(1) :73–87.

Santosa, F. and Vogelius, M. (1990). A backprojection algorithm for electrical impedance imaging. *SIAM Journal of Applied Mathematics*, 50(1) :216–243.

Sasaki, Y. (1994). 3-D resistivity inversion using the finite-element method. *Geophysics*, 59(11) :1839–1848.

Sen, M. K., Bahattacharya, B. B., and Stoffa, P. L. (1993). Nonlinear inversion of resistivity sounding data. *Geophysics*, 58(4) :496–507.

Shi, W., Morgan, F. D., and Wharton, A. E. (1997). Application of electrical

resistivity tomography to image harrison caves in barbados, west. In *67th Ann. Internat. Mtg : Society of Exploration Geophysics*, pages 350–353.

Shima, H. (1992). 2-D and 3-D resistivity image reconstruction using crosshole data. *Geophysics*, 57(10) :1270–1281.

Sidje, R. B. and Williams, A. B. (1996). Fast generalized cross validation. In *International Linear Algebra, Year : Linear Algebra in Optimization CERFACS, Albi-Toulouse, France.*

Smith, N. C. and Vozoff, K. (1984). Two-dimensional DC resistivity inversion for dipole-dipole data. *IEEE Transactions on Geoscience and Remote Sensing*, GE-22(1) :21–28.

Spitzer, K. and Chouteau, M. (1997). Crosshole resistivity and IP experiment at Casa Berardi gold mine : interpretation using a newly developed 3D forward modeling code. In *SEG Expanded Abstracts.*

Spitzer, K. and Chouteau, M. (2003). Cas history : A dc resistivity and ip borehole survey at Casa Berardi gold mine in northwestern quebec. *Geophysics*, 68 :453–463.

Tarantola, A. and Valette, B. (1982). Generalized nonlinear inverse problems solved using the least squares criterion. *Reviews of Geophysics and Space Physics*, 20(2) :219–232.

Tong, L.-T. and Yang, C.-H. (1990). Incorporation of topography into two-dimensional resistivity inversion. *Geophysics*, 55(3) :354–361.

Vauhkonen, M., Vadasz, D., Karjalainen, P., Somersalo, E., and Kaipio, J. (1998). Tikhonov regularization and prior information in electrical impedance tomography. *IEEE Transactions on Medical Imaging*, 17(2) :285–293.

Vogel, C. R. (1996). Non-convergence of the L-curve regularization parameter selection method. *Inverse Problems*, 12 :535–547.

Wexler, A., Fry, B., and Neuman, M. R. (1985). Impedance-computed tomography algorithm and system. *Applied Optics*, 24(23) :3985–3992.

Whaba, G. (1990). *Spline models for observational data.* SIAM.

Williams, A. and Burrage, K. (1995). Surface fitting using gcv smoothing splines on supercomputers. *Supercomputing 1995, Association for Computing Machinery, Inc. (ACM).*, pages 871–885.

Yorkey, T., Webster, J. G., and Tompkins, W. (1987). Comparing reconstruction algorithms for electrical impedance tomography. *IEEE Transactions on Biomedical Engineering*, BME-34(11).

Zhang, J., Mackie, R. L., and Madden, T. R. (1995). Three-dimensional resistivity forward modeling and inversion using conjugate gradients. *Geophysics*, 60(5) :1313–1325.

4.4.3 Appendix : Preconditioned conjugate gradient least squares (PCCGLS)

The solution of a linear system $Ax = b$ by the conjugate gradient least squares method is equivalent to a pseudo inverse solution (Hestenes, 1975). Preconditioning can increase the convergence (Björck, 1996), in this article we choose the preconditioning matrix S as $S = diag(A)$. Before preconditioning, the matrix A is scaled with the diagonal matrix $A_d = diag(A)$. The scaled system is written $A_s\ x_s = b_s$ with $A_s = A_d^{-1/2} A A_d^{-1/2}$, $x = A_d^{-1/2} x_s$ and $b_s = A_d^{-1/2} b$.

Algorithm 9 PCCGLS : Preconditioned conjugate gradient least squares (Hestenes, 1975; Björck, 1996). Resolution of the linear system $Ax = b$.

$x \neq 0$
$r = b - Ax$
$d = s = S^{-T}(A^T r)$
$\delta_{new} = s^T s$
for $i = 1, 2, 3, \ldots$ **do**
  $t = S^{-1} d$
  $q = A\ t$
  $\alpha = \frac{\delta_{new}}{q^T q}$
  $x = x + \alpha\ t$
  $r = r - \alpha\ q$
  $s = S^{-T}(A^T r)$
  $\delta_{old} = \delta_{new}$
  $\delta_{new} = s^T s$
  $\beta = \frac{\delta_{new}}{\delta_{old}}$
  $d = s + \beta\ d$
  if $\frac{||s||}{||b||} < \epsilon$ **then**
    break
  end if
end for

4.4.4 Appendix : Golden section method

Algorithm 10 Golden section method (function val=goldensection(a,b,n))

```
gamma = 1/((1 + sqrt(5))/2)
x1 = a
x4 = b
x2 = x4 − gamma ∗ (x4 − x1)
x3 = x1 + gamma ∗ (x4 − x1)
f1 = f(x1)
f2 = f(x2)
f3 = f(x3)
f4 = f(x4)
for k = (n − 1) : −1 : 2 do
  if (f1 < f2) & (f2 < f3) & (f3 < f4) then
    x4 = x2
    f4 = f2
    x2 = x4 − gamma ∗ (x4 − x1)
    f2 = f(x2)
    x3 = x1 + gamma ∗ (x4 − x1)
    f3 = f(x3)
  else if (f1 > f2) & (f2 < f3) & (f3 < f4) then
    x4 = x3
    f4 = f3
    x3 = x2
    f3 = f2
    x2 = x4 − gamma ∗ (x4 − x1)
    f2 = f(x2)
  else if (f1 > f2) & (f2 > f3) & (f3 < f4) then
    x1 = x2
    f1 = f2
    x2 = x3
    f2 = f3
    x3 = x1 + gamma ∗ (x4 − x1)
    f3 = f(x3)
  else if (f1 > f2) & (f2 > f3) & (f3 > f4) then
    x1 = x3
    f1 = f3
    x2 = x4 − gamma ∗ (x4 − x1)
    f2 = f(x2)
    x3 = x1 + gamma ∗ (x4 − x1)
    f3 = f(x3)
  end if
end for
val = 0.5 ∗ (x1 + x4)
```

The golden section search the minimum of the function f between the interval $[a, b]$ in n iterations (Culioli, 1994). The minimum of the function $f(val)$ is found for the value $val \in [a, b]$. If the function f is time consuming we can evaluate $f(x)$ at the positions $x = \{a, a + \epsilon, a + \frac{(b-a)}{3}, a + \frac{2*(b-a)}{3}, b - \epsilon, b\}$ with $\epsilon \simeq 0.01$ to interpolate it by a spline function $s(x)$ (Press *et al.*, 1992). We use now $s(x)$ in the

algorithm 10 instead of $f(x)$ to find the minimum of $s(x)$.

Chapitre 5

DISCUSSION GÉNÉRALE ET SYNTHÈSE DE L'ÉTUDE

Dans le cadre de cette thèse deux types d'imageries ont été développées pour l'exploration minérale, l'une en gravimétrie et l'autre en résistivité électrique. Nous avons mis en place plusieurs codes permettant de modéliser et d'inverser le champ gravimétrique et le potentiel électrique. Ces deux méthodes d'imagerie permettent de localiser des cibles potentielles pour l'industrie minérale. Cette synthèse présente les conclusions attachées aux méthodes développées dans cette thèse, à savoir les avantages et les inconvénients concernant : (1) la modélisation et l'inversion gravimétrique ; (2) la modélisation électrique et ; (3) l'inversion électrique.

5.1 Modélisation et inversion gravimétrique

L'inversion gravimétrique 3D utilisant le critère de distance minimum comme proposé par Green (1975) et formulée avec une fonction de Lagrange fournit un

code flexible qui permet d'inclure les contraintes de minimum de courbure, de rugosité et de volume minimum. Les conclusions suivantes ont été dégagées :

- Le code nous permet d'investiguer différentes approches pour trouver une solution acceptable.
- Différentes puissances du facteur de pondération en fonction de la profondeur ont été analysées pour mieux comprendre le résultat d'une inversion et d'éviter de concentrer la solution à la surface ou en profondeur. Dans chaque cas β doit se trouver dans l'intervalle $[0.5, 1]$. On suggère une sélection standard de $\beta = 0.8$ pour le multi grille et $\beta = 0.9$ pour les autres contraintes.
- La technique du multi grille fournit rapidement une bonne approximation de la structure de la densité, mais elle ne peut être combinée avec d'autres contraintes ; Deux facteurs interviennent : (i) le transfert inter grille inclut déjà la contrainte de volume minimum ; (ii) la contrainte de courbure minimum a besoin d'un nombre suffisant de cellules pour être efficace.
- Un bon contraste de densité peut être obtenu pour chaque méthode, mais la géométrie n'est jamais entièrement restituée.
- La meilleure combinaison de contraintes semble être, du moins pour notre étude, la courbure minimum couplée avec le volume minimum.
- En analysant le noyau, nous avons trouvé que les coefficients de sensibilité décrivent une symétrie par rapport à l'axe z. Cette symétrie nous permet de minimiser la taille de la matrice de sensibilité.
- Une simple relation analytique est formulée à partir du noyau d'une sphère pour nous assister dans la définition du domaine discrétisé.
- Le code nécessite seulement un estimé de la densité du milieu encaissant.
- Des contraintes locales peuvent être inclues en fixant certaines cellules.

- Des bornes de densité peuvent aussi s'ajouter pour limiter les contrastes de densité.
- Une pondération, fonction de la profondeur de chaque cellule, est toujours recommandée.
- La solution par défaut est la distance minimum. Cette méthode, en conjonction avec la technique de multi grille et la courbure minimum, peut améliorer la solution pour les densités variant graduellement d'un point à un autre, souvent présentes en exploration pétrolière.
- La méthode utilisant la contrainte de volume minimum (compacité) est particulièrement adaptée pour les forts contrastes de densité, comme c'est le cas dans les investigations archéologiques et géotechniques pour la détection de cavités ou pour les sites de sulfures massifs.
- Les contraintes de minimum de courbure et de volume minimum peuvent être la meilleure combinaison pour l'exploration minérale qui tente de détecter une combinaison de forts contrastes de densité pour des petits corps et de faibles contrastes de densité pour les grands corps (géologie du milieu encaissant).

5.2 Modélisation électrique

Un code de modélisation électrique formulé à partir de la méthode intégrale permet le calcul du potentiel partout dans l'espace sans le besoin d'interpoler celui-ci entre les noeuds. Le calcul de la densité de charge est obtenu en résolvant un système linéaire. Pour une variété de configurations et différents modèles de conductivité, la mise à jour du système linéaire est rapide. Le calcul des densités de charge est validé avec un modèle tabulaire à deux couches. Les conclusions

suivantes ont été dégagées :

- Le potentiel obtenu par la méthode intégrale est comparé avec des solutions analytiques et des solutions numériques obtenues par différences finies pour un milieu tabulaire et un contact vertical. Les deux méthodes numériques offrent des résultats satisfaisants. Cependant, la méthode intégrale reste la plus précise autour du point source et en périphérie du domaine.
- Pour stocker le système linéaire, la taille de la matrice est réduite avec une méthode de compression pyramidale. Un seuil fixe est donné pour compresser la matrice originale.
- La résolution du système linéaire non symétrique est faite avec la méthode du gradient biconjugué stabilisé (l) avec l=2. Cette méthode semble pour l'instant être la plus performante.
- Le calcul de la sensibilité basé sur la formulation intégrale requiert deux fois moins de calculs, que celle basée sur l'équation adjointe qui nécessite de calculer deux modélisations directes pour évaluer les densités de courant aux points source et récepteur.
- On montre la distribution et les amplitudes des sensibilités calculées pour un modèle tabulaire et un contact vertical. On peut remarquer les différences entre les deux méthodes de calcul de la sensibilité en examinant la ligne de sensibilité nulle.
- La sensibilité calculée avec la fonction de Green $G(\boldsymbol{r}_i, \boldsymbol{r}_j) = \frac{1}{|r_i - r_j|} + \frac{1}{|r_i - r'_j|}$ offre de meilleurs résultats.
- Le calcul des composantes du champ électrique en un point donné est obtenu par la sommation de toutes les densités de charge multipliées par une intégrale de surface. Cette méthode est satisfaisante lorsque le domaine n'est pas trop

large.

- Une deuxième méthode de calcul du champ électrique consiste à tirer avantage du système linéaire compressé pour obtenir rapidement et simultanément les trois composantes du champ électrique aux interfaces des prismes. Les trois composantes sont interpolées avec une méthode de spline cubique pour produire un estimé du champ électrique au centre des prismes.

5.3 Inversion électrique

On propose d'estimer la distribution des résistivités électriques en utilisant une formulation géostatistique qui tient compte des corrélations entre les paramètres (résistivité des cellules) par le biais d'une matrice de covariance pleine. Les conclusions suivantes ont été dégagées :

- Obtenir un bon ajustement entre les covariances théoriques et expérimentales peut parfois être difficile. Cependant il est possible d'obtenir un estimé du plateau et des portées le long des directions principales géologiques. Il est aussi possible de valider un modèle a priori déduit des connaissances géologiques.
- On note que les résultats sont relativement robustes pour une légère imperfection du modèle de covariance. Le plateau contrôle les contrastes de résistivité cokrigés, par rapport à une valeur moyenne, sans modifier l'allure générale. Par contre, les portées influencent le lissage de l'interpolation.
- On a vérifié qu'augmenter ou décroître la portée de la fonction de covariance par un facteur aussi large que 50% a un faible impact sur l'image produite. L'interprétation géologique qui peut être déduite à partir d'une inversion ne change pas significativement.

- La solution du cokrigeage peut être résolue sous la forme primale, donnant accès à la variance de krigeage, ou sous la forme duale.
- Le programme est testé sur des données synthétiques et la solution converge généralement rapidement.
- Quand le corps n'est pas intersecté par un forage la solution est moins bien définie à cause de la forte sensibilité le long des forages et de la faible sensibilité entre ceux-çi.
- Le modèle de covariance compense pour les faibles sensibilités entre les forages et peut trouver des milieux présentant de forts contrastes de résistivité.
- La forte sensibilité le long des forages peut poser des problèmes pour modéliser la matrice de covariance théorique.
- Quand les corps sont connectés entre les forages la solution est plus précise et de meilleurs résultats sont obtenus avec de forts contrastes.
- L'incorporation des gradients de résistivité dans les trois directions améliore considérablement la solution. L'utilisation des gradients comme contrainte est nouvelle en tomographie électrique et peut être utile dans l'industrie minière si un modèle géologique peut être construit avec un système d'information géographique (GIS).
- Une méthode d'inversion est dite mal posée si à une petite perturbation dans les données correspond à une large perturbation dans la solution. Dans les applications réelles, le bruit dans les données contribue à un effet pépite qui lui-même contribue à rendre la matrice de covariance non singulière. Le cokrigeage est donc stable (bien posé) et une solution lisse est obtenue.
- Bien que tous les résultats présentés soient en 2D, le code est construit pour des cas 3D avec des données localisées arbitrairement à la surface et le long

des forages.

Chapitre 6

CONCLUSION ET PERSPECTIVES

Les travaux présentés dans cette thèse avaient pour objectif l'élaboration de deux méthodes d'inversion géophysique pour l'interprétation des gisements miniers : la gravimétrie et la résistivité électrique. Pour atteindre les objectifs fixés, il a fallu mettre en place deux codes de modélisation directe. Pour la gravimétrie la tâche fut simplifiée puisqu'une solution analytique existe déjà et peut être obtenue rapidement par des logiciels de calcul symbolique. Pour la partie électrique, un effort plus considérable a été déployé, puisqu'on est parti d'une simple formulation intégrale générale pour des variables continues, pour ensuite adopter une approche discrète. Après la modélisation directe, l'interprétation automatique des données géophysiques a été faite en programmant deux méthodes d'inversion. Le travail effectué dans le cadre de cette thèse a permis de développer des outils originaux tels que :

En gravimétrie

- La modélisation et l'inversion gravimétrique avec un effort de minimisation de l'espace mémoire équivalent au nombre de paramètres ;
- La recherche automatique d'une zone tampon autour du domaine d'inversion pour éviter les effets de bord ;
- La combinaison de plusieurs contraintes dans l'inversion pour stabiliser la solution ;
- L'étude de la sensibilité en gravimétrie.

En électrique

- L'utilisation de la méthode intégrale pour modéliser un milieu de résistivité hétérogène arbitraire ;
- Le calcul théorique des dérivées premières et secondes de la réponse par rapport à la variation de résistivité pour un domaine 3D ;
- L'utilisation d'une méthode géostatistique non linéaire pour interpréter les données de potentiel électrique ;
- L'évaluation des paramètres de la fonction de covariance à partir des données observées de potentiel électrique.

A travers cette thèse nous avons montré l'utilité et la faisabilité des méthodes d'inversion pour aider l'exploration de gisements. Bien entendu ces travaux ne constituent qu'une vision du problème d'interprétation des données gravimétriques et électriques. Plusieurs idées nous viennent à l'esprit pour améliorer les codes développés.

Notamment, le code d'inversion gravimétrique peut être adapté pour interpréter des données prises sur un terrain comportant une forte topographie. Il suffit de

calculer une densité apparente en tenant compte de la topographie. Cette densité apparente, calculée pour des points situés sur la topographie, permet de calculer une anomalie à une altitude constante pour exploiter le programme actuel. Les cellules se trouvant dans l'air peuvent être fixées à zéro pendant toute l'inversion. Il serait aussi intéressant d'adopter une approche stochastique pour l'inversion gravimétrique en cherchant les paramètres de la fonction de covariance à partir des données observées. On peut aussi introduire une recherche automatique du Lagrangien dans le processus d'inversion gravimétrique avec la méthode de validation croisée généralisée stochastique. On pourrait développer une autre méthode de modélisation basée sur des grilles multiples imbriquées les unes dans les autres (Nested Adaptative Mesh Refinement en anglais) pour accélérer la modélisation directe de l'anomalie gravimétrique.

Pour la partie électrique il faut commencer par améliorer le temps calcul dans la méthode intégrale en compressant davantage les matrices avec les transformées en ondelettes. Cette amélioration permettrait de discrétiser plus finement les domaines d'inversion et d'envisager d'autres méthodes d'optimisation. L'autre facteur à améliorer est le temps calcul pour générer la matrice servant à calculer les densités de charges surfaciques. Bien que le code de modélisation a été construit pour tous les types de configurations électriques sans limitation sur la position des sources et des récepteurs, il a surtout été utilisé pour des configurations pôle-pôle. Il serait souhaitable de le tester pour d'autres configurations.

Bibliographie

ACAR, R. et VOGEL, C. R. (1994). Analysis of bounded variation penalty methods for ill-posed problems. *Inverse Problems*, *10*, 1217–1229.

APPARAO, A., RAO, T. G., SASTRY, R. et SARMA, V. S. (1992). Depth of investigation of buried conductive targets with different electrode arrays in resistivity prospecting. *Geophysical Prospecting*, *40*, 749–760.

ASLI, M., MARCOTTE, D. et CHOUTEAU, M. (2000). Direct inversion of gravity data by cokriging. Dans *6th Annual Geostatistical Meeting, Cape Town, Afrique du Sud.*

AVRIEL, M. (1976). Nonlinear programming. Prentice-Hall.

BACKUS, G. et GILBERT, J. F. (1967). Numerical Applications of a Formalism for Geophysical Inverse Problems. *Geophysical Journal of the Royal Astronomical Society*, *13*, 247–276.

BANERJEE, B. et S.P., D. G. (1977). Gravitational attraction of a rectangular parallelepiped. *Geophysics*, *42*, 1053–1055.

BARBOSA, V. C. F. et SILVA, J. B. C. (1994). Generalized compact gravity inversion. *Geophysics*, *59*, 57–68.

BARKER, R. (1992). A simple algorithm for electrical imaging of the subsurface. *First Break*, *10*, 53–62.

BARKER, R. D. (1979). Signal contribution sections and their use in resistivity studies. *Geophysical Journal of the Royal Astronomical Society*, *59*, 123–129.

BARNETT, C. T. (1976). Theoretical modeling of the magnetic and gravitational fields of an arbitrarily shaped three-dimensional body. *Geophysics*, *41*, 1353–1364.

BAZARAA, M. S. (1979). Nonlinear programming : theory and algorithms. John Wiley and Sons.

BEAR, G. W., AL-SHUKRI, H. J. et RUDMAN, A. J. (1995). Linear inversion of gravity data for 3-D density distributions. *Geophysics*, *60*, 1354–1364.

BEASLEY, C. W. et WARD, S. H. (1986). Three-dimensional mise-à-la-masse modeling applied to mapping fracture zones. *Geophysics*, *51*, 98–113.

BELLEFLEUR, G. (1992). Contribution of potential methods to the geological and the deep structure cartography in the Blake River Group, Abitibi. Mémoire de maitrise, Ecole Polytechnique, Montreal, (in French).

BERRYMAN, J. G. et KOHN, R. V. (1990). Variational constraints for electrical impedance tomography. *Phys. Rev. Lett.*, *65*, 325–328.

BERTETE-AGUIRRE, H., CHERKAEVA, E. et ORISTAGLIO, M. L. (1998). Nonsmooth gravity problem. Dans *68th Ann. Internat. Mtg : SEG*, 490–493.

BERTSEKAS, D. P. (1982). Constrained optimization and lagrange multiplier methods. Academic Press.

BERTSEKAS, D. P. (1995). Nonlinear programming. Athena Scientific.

BHATTACHARYA, P. K. et PATRA, H. P. (1968). Direct current geoelectric sounding. Principles and interpretations, volume 9 of *Methods in Geochemistry and Geophysics*. Elsevier Publishing Company.

BHATTACHARYYA, B. K. et LEU, L.-K. (1977). Spectral analysis of gravity and magnetic anomalies due to rectangular prismatic bodies. *Geophysics*, *42*, 41–50.

BING, Z. et GREENHALGH, S. A. (1999). Explicit expressions and numerical calculations for Frechet and second derivatives in 2.5D Helmholtz equation inversion. *Geophysical Prospecting*, *47*, 443–468.

BING, Z. et GREENHALGH, S. A. (2000). Cross-hole resistivity tomography using different electrode configurations. *Geophysical Prospecting*, *48*, 887–912.

BING, Z. et GREENHALGH, S. A. (2001). Finite element three-dimensional direct current resistivity modelling : accuracy and efficiency considerations. *Geophysical Journal International*, *145*, 679–688.

BJÖRCK, A. (1996). Numerical methods for least squares problems. SIAM Publications.

BOERNER, D. E. et WEST, G. F. (1989). Frechet derivatives and single scattering theory. *Geophysical Journal International*, *98*, 385–390.

BORCEA, L., BERRYMAN, J. G. et PAPANICOLAOU, G. C. (1996). High contrast impedance tomography. *Inverse Problems*, *12*, 835–856.

BOSCHETTI, F., DENTITH, M. et LIST, R. (1997). Inversion of potential field data by genetic algorithms. *Geophysical Prospecting*, *45*, 461–478.

BOULANGER, O. et CHOUTEAU, M. (2001). Constraints in 3D gravity inversion. *Geophysical Prospecting, 49*, 265–280.

BOULANGER, O. et CHOUTEAU, M. (2004). 3D modeling and sensitivity in DC resistivity using charge density. *accepted to Geophysical Prospecting.*

BOULANGER, O., CHOUTEAU, M. et MARCOTTE, D. (2004). 3D geostatistical electrical tomographic imaging : principles and application for mining targets. *submitted to Geophysics.*

BREWITT-TAYLOR, C. R. et WEAVER, J. T. (1976). On the finite difference solution of two-dimensional induction problems. *Geophysical Journal of the Royal Astronomical Society, 47*, 375–396.

BRIGGS, W. (1987). A Multigrid Tutorial. Society for Industrial and Applied Mathematics.

BROCHU, Y. et MARCOTTE, D. (2003). A simple approach to account for radial flow and boundary conditions when kriging head fields for confined aquifers. *Mathematical Geology, 35*, 111–139.

BRUNNER, I., FRIEDEL, S., JACOBS, F. et DANCKWARDT, E. (1999). Investigation of a Tertiary maar structure using three-dimensional resistivity imaging. *Geophysical Journal International, 136*, 771–780.

BUDAK, B. M., SAMARSKII, A. A. et TIKHONOV, A. N. (1964). A collection of problems on mathematical physics. Ed. New York Macmillan (new Ed. Dover).

BURT, P. J. et ADELSON, E. H. (1983). The Laplacian pyramid as a compact image code. *IEEE Transactions on Communications, COM-31*, 337–345.

CADY, J. W. (1980). Calculation of gravity and magnetic anomalies of finite-length right polygonal prisms. *Geophysics*, *45*, 1507–1512.

CAMACHO, A. G., MONTESINOS, F. G. et VIEIRA, R. (1997). A three-dimensional gravity inversion applied to São Miguel Island (Azores). *Journal of Geophysical Research*, *102*, 7717–7730.

CHAVE, A. (1984). The frechet derivates of electromagnetic induction. *Journal of Geophysical Research*, *89*, 3373–3380.

CHILES et DELFINER (1999). Geostatistics, Modeling spatial uncertainty. Wiley series on probability and statistics.

CHUNDURU, R. K., SEN, M. K. et STOFA, P. L. (1996). 2-D resistivity inversion using spline parametrization and simulated annealing. *Geophysics*, *61*, 151–161.

CHUNDURU, R. K., SEN, M. K., STOFFA, P. L. et NAGENDRA, R. (1995). Non-linear inversion of resistivity profiling data for some regular geometrical bodies. *Geophysical Prospecting*, *43*, 979–1003.

COGGON, J. H. (1971). Electromagnetic and electrical modeling by finite element method. *Geophysics*, *36*, 132–155.

COHEN-BACRIE, C., GOUSSARD, Y. et GUARDO, R. (1997). Regularized reconstruction in electrical impedance tomography using a variance uniformization constraint. *IEEE Transactions on Medical Imaging*, *16*, 562–571.

CONSTABLE, S. C., PARKER, R. L. et CONSTABLE, C. G. (1987). Occam's inversion : A practical algorithm for generating smooth models from electromagnetic sounding data. *Geophysics*, *52*, 289–300.

COOK, K. L. et VAN NOSTRAND, R. (1954). Interpretation of resistivity data over filled sinks. *Geophysics*, *14*, 761–770.

COSENTINO, P., LUZIO, D., MARTORANA, R., D'ONOFRIO, L., MARCHISIO, M. et RANIERI, G. (1998). Tomographic pseudo-inversion of pole-pole and pole-dipole resistivity profiles. Dans *SAGEEP, Chicago, Illinois.*

CULIOLI, J.-C. (1994). Introduction à l'optimisation. Ellipses.

DABAS, M., TABBAGH, A. et TABBAGH, J. (1994). 3-D inversion in subsurface electrical surveying-I. Theory. *Geophysical Journal International*, *119*, 975–990.

DAILY, W. et OWEN, E. (1991). Cross-borehole resistivity tomography. *Geophysics*, *56*, 1228–1235.

DANIELS, J. J. (1977). Three-dimensional resistivity and induced-polarization modeling using buried electrodes. *Geophysics*, *42*, 1006–1019.

DANIELS, J. J. et DYCK, A. V. (1984). Borehole resistivity and electromagnetic methods applied to mineral exploration. *IEEE Transactions on Geoscience and Remote Sensing*, *GE-22*, 80–87.

GROOT-HEDLIN, C. D. et CONSTABLE, S. (1990). Occam's inversion to generate smooth two-dimensional models from magnetotelluric data. *Geophysics*, *55*, 1613–1624.

DEMOMENT, G., IDIER, J., GIOVANNELLI, J.-F. et MOHAMMAD-DJAFARI, A. (2001). Problèmes inverses en traitement du signal et de l'image. Technical report, Supélec, Laboratoire des signaux et systèmes, UMR 8506

(CNRS/Supélec/UPS), Supélec, Plateau de Moulon, 91192 Gif-sur-Yvette Cedex, France.

DENNIS, J. E. et SCHNABEL, R. B. (1996). Numerical methods for unconstrained optimization and nonlinear equations. Society for Industrial and Applied Mathematics.

DESCHAMPS, F., CHOUTEAU, M. et DION, D.-J. (1993). Geological interpretation of aeromagnetic and gravimetric data in the region located at the west part of the Rouyn-Noranda city. Dans *Études géophysiques récentes de certains secteurs de la ceinture volcanosédimentaire de l'Abitibi*, Édité par D.-J. Dion, volume DV 93-10 of *Ministère des Ressources naturelles. Secteur des mines*, 78–130, (in French).

DEUTSCH, C. V. et JOURNEL, A. G. (1998). GSLIB : Geostatistical Software Library and User's Guide. Oxford University Press, 2nd edition.

DEY, A. et MORRISON, H. F. (1979*a*). Resistivity modeling for arbitrarily shaped three-dimensional structures. *Geophysics*, *44*, 753–780.

DEY, A. et MORRISON, H. F. (1979*b*). Resistivity modelling for arbitrarily shaped two-dimensional structures. *Geophysical Prospecting*, *27*, 106–136.

DIETER, K., PATERSON, N. R. et GRANT, F. S. (1969). IP and resistivity type curves for three-dimensional bodies. *Geophysics*, *34*, 615–632.

DINES, K. A. et LYTLE, J. (1979). Computerized geophysical tomography. *Proceedings of the IEEE*, *67*, 1065–1073.

DINES, K. A. et LYTLE, R. J. (1981). Analysis of electrical conductivity imaging. *Geophysics*, *46*, 1025–1036.

DJERIDANE, S. (1996). Two-dimensional gravimetric inversion minimizing subsurface structures ; Application to Abitibi and Opatica sub-provinces. Mémoire de maitrise, Ecole Polytechnique, (in French).

DOBECKI, T. L. (1980). Borehole resistivity curves near spherical masses. *Geophysics*, *45*, 1513–1522.

DOBSON, D. C. et SANTOSA, F. (1994). An image-enhancement technique for electrical impedance tomography. *Inverse Problems*, *10*, 317–314.

EDWARDS, L. S. (1977). A modified pseudosection for resistivity and IP. *Geophysics*, *42*, 1020–1036.

ELLIS, R. G. et OLDENBURG, D. W. (1994). The pole-pole 3-D DC-resistivity inverse problem : a conjugate-gradient approach. *Geophysical Journal International*, *119*, 187–194.

EVJEN, H. M. (1938). Depth factors and resolving power of electrical measurements. *Geophysics*, *3*, 78–95.

FORTIER, N., DEMOMENT, G. et GOUSSARD, Y. (1993). GCV and ML method of determining parameters in image restoration by regularization : fast computation in the spatial domain and experimental comparison. *Journal of Visual Communication and Image Representation*, *4*, 157–170.

FRANKLIN, J. N. (1970). Well-posed stochastic extensions of ill-posed linear problems. *J. Math. Anal. Appl.*, *31*, 682–716.

FREUND, R. et NACHTIGAL, N. (1991*a*). An implementation of the QMR method based on coupled two-term recurrences. *SIAM Journal on Scientific and Statistical Computation*, *15*, 313–337.

FREUND, R. et NACHTIGAL, N. (1991*b*). QMR : A quasi-minimal residual method for non-Hermitian linear systems. *Numerical Mathematics*, *60*, 315–339.

GARCIA-ABDESLEM, J. (1995). Inversion of the power spectrum from gravity anomalies of prismatic bodies. *Geophysics*, *60*, 1698–1703.

GAUVIN, J. (1995*a*). Leçons de programmation mathématique. Ed. de l'Ecole Polytechnique de Montréal.

GAUVIN, J. (1995*b*). Lessons of mathematical programming. Ecole Polytechnique, Montreal, (in French).

GESELOWITZ, D. B. (1971). An application of electrocardiographic lead theory to impedance plethysmography. *IEEE Trans. Bio-Medical Engineering*, *BME-18*, 38–41.

GIBSON, H. et WATKINSON, D. (1990). Volcanogenic massive sulphide deposits of the Noranda cauldron and shield volcano, Quebec. Dans *Northwestern Quebec Polymetallic Belt*, Édité par M. Rive, P. Verpaelst, Y. Gagnon, J. Lulin, G. Riverin et A. Simard, volume 43, Canadian Institute of Mining and Metallurgy, 119–132.

GILL, P. E., MURRAY, W. et WRIGHT, M. H. (1981). Practical optimization. Academic Press.

GLOAGUEN, E., MARCOTTE, D., CHOUTEAU, M. et PERROUD, H. (2004). Borehole radar velocity imaging using slowness covariance estimation and co-kring. *submitted to Journal of Applied Geophysics.*

GOLUB, G. H., HEATH, M. et WAHBA, G. (1979). Generalized cross-validation as a method for choosing a good ridge parameter. *Technometrics*, *21*, 215–223.

GOLUB, G. H. et LOAN, C. F. V. (1996). Matrix computations. Johns Hopkins University Press, 3rd edition.

GOLUB, G. H. et MATT, U. V. (1997). Generalized cross-validation for large scale problems. *Journal of Computational and Graphical Statistics*, *6*, 1–34.

GÖTZE, H.-J. et LAHMEYER, B. (1988). Application of three-dimensional interactive modeling in gravity and magnetics. *Geophysics*, *53*, 1096–1108.

GREEN, A., MILKEREIT, B., MAYRAND, L., LUDDEN, J., C.HUBERT, JACKSON, S., SUTCLIFFE, R., WEST, G., VERPAELST, P. et SIMARD, A. (1990). Deep structure of an Archaean greenstone terrane. *Nature*, *344*, 327–330.

GREEN, W. R. (1975). Inversion of gravity profiles by use of a Backus-Gilbert approach. *Geophysics*, *40*, 763–772.

GUILLEN, A. et MENICHETTI, V. (1984). Gravity and magnetic inversion with minimization of a specific functional. *Geophysics*, *49*, 1354–1360.

HAÁZ, I. B. (1953). Relations between the potential of the attraction of the mass contained in a finite rectangular prism and its first and second derivatives (in Hungarian). *Geofizikai Kozlemenyek*, *2*.

HACKBUSCH, W. et TROTTENBERG, U. (1982). Multigrid Methods. Springer-Verlag.

HANSEN, P. (1992). The L-curve and its use in the numerical treatment of inverse problems. Dans *Computational inverse problems in electrocardiology, P. Johnston, Advances in Computational Bioengineering, WIT Press, Southampton*, volume 4, 119–142.

HESTENES, M. et STIEFEL, E. (1952). Methods of conjugate gradients for solving linear systems. *Journal of Research of the National Bureau of Standards, 49*, 409–436.

HESTENES, M. R. (1975). Pseudoinverses and conjugate gradients. *Communications of ACM, 18*, 40–43.

HOHMANN, G. W. (1975). Three-dimensional induced polarization and electromagnetic modeling. *Geophysics, 40*, 309–324.

HOLSTEIN, H. et KETTERIDGE, B. (1996). Gravimetric analysis of uniform polyhedra. *Geophysics, 61*, 357–364.

HUTCHINSON, M. F. (1990). A stochastic estimator of the trace of the influence matrix for Laplacian smoothing splines. *Communications in Statistics, Simulation and Computation, 19*, 433–450.

HVOZDARA, M. (1994). The boundary integral calculation of the D.C. geoelectric field due to a point current source on the surface of 2-layered Earth with a 3-D outcroping perturbing body. *Contr. Geophys. Inst. Slov. Acad. Sci., 25.*

HVOZDARA, M. et KAIKKONEN, P. (1998). An integral equations solution of the forward D.C. geoelectric problem for a 3-D body of inhomogeneous conductivity buried in a halfspace. *Journal of Applied Geophysics*, *39*, 95–107.

INMAN, J. R. (1975). Resistivity inversion with ridge regression. *Geophysics*, *40*, 798–817.

INMAN, J. R., RYU, J. et WARD, S. H. (1973). Resistivity inversion. *Geophysics*, *38*, 1088–1108.

JACKSON, D. (1979). The use of a priori data to resolve non-uniqueness in linear inversion. *Geophysical Journal of the Royal Astronomical Society*, *57*, 137–157.

JACKSON, D. D. (1972). Interpretation of inacurate, insufficient and inconsistent data. *Geophysical Journal of the Royal Astronomical Society*, *28*, 97–109.

JACKSON, P. D., EARL, S. et G, J. R. (2001). 3D resistivity inversion using 2D measurements of electric field. *Geophysical Prospecting*, *49*, 26–39.

JACOBSEN, B. H. (1987). A case for upward continuation as a standard separation filter for potentiel-field maps. *Geophysics*, *52*, 1138–1148.

JORDAN, T. H. et FRANKLIN, J. N. (1971). Optimal solutions to a linear inverse problem in geophysics. *Proceeding of the National Academy of Sciences*, *68*, 291–293.

JOURNEL, A. G. et HUIJBREGTS, C. J. (1978). Mining Geostatistics. Academic Press.

KALLMAN, J. S. et BERRYMAN, J. G. (1992). Weighted least-squares criteria for electrical impedance tomography. *IEEE Trans. Med. Imaging*, *11*, 284–292.

KEATING, P. (1992). Interpretation of the gravity anomaly field in the Noranda - Val d'Or region, Abitibi Greenstone Belt, Canadian Shield. *Canadian Journal of Earth Science, 29*, 962–971.

KEATING, P. (1993). Interpretation of the gravity anomaly field in the Noranda - Val d'Or region. Dans *Études géophysiques récentes de certains secteurs de la ceinture volcanosédimentaire de l'Abitibi*, Édité par M. Germain, volume DV 93-10 of *Ministère des Ressources naturelles. Secteur des mines*, 57–76, (in French).

KELLER, G. V. et FRISCHKNECHT, F. C. (1966). Electrical methods in geophysical prospecting, volume 10 of *International series of monographs in Electromagnetic waves*. Pergamon Press.

KENNETT, B. L. et SAMBRIDGE, M. (1998). Inversion for multiple parameter classes. *Geophysical Journal International, 135*, 304–306.

KILLEEN, P., MWENIFUMBO, J. et ELLIOT, J. (1996). Mineral deposit signature by borehole geophysics : data from the borehole geophysical test at Mc Connell nickel deposit (Garson Offset). *Geological Survey of Canada, Open file 2811.*

KISHIMOTO, M., SAKASAI, K. et ARA, K. (1996). Solution of electromagnetic inverse problem using combinational method of Hopfield neural network and genetic algorithm. *Journal of Applied Physics, 79*, 1–7.

KWOK, Y.-K. (1989). Conjugate complex variables method for the computation of gravity anomalies. *Geophysics, 54*, 1629–1637.

LABRECQUE, D. J., G.MORELLI, DAILY, W., RAMIREZ, A. et LUNDEGARD, P. (1999). Occam's Inversion of 3-D Electrical Resistivity Tomography. SEG, M. Oristaglio and B. Spies, 575–590.

LABRECQUE, D. J., MILETTO, M., DAILY, W., RAMIREZ, A. et OWEN, E. (1996). The effects of noise on Occam's inversion of resistivity tomography data. *Geophysics*, *61*, 538–548.

LABRECQUE, D. J. et WARD, S. H. (1990). Two-dimensional cross-borehole resistivity model fitting. SEG, Geotechnical and environmental geophysics, volume III,S. H. Ward.

LANCZOS, C. (1961). Linear differential operators. Van Nostrand (Dover,1997).

LARGE, D. B. (1971). Electrical potential near a spherical body in a conducting half-space. *Geophysics*, *36*, 763–767.

LAST, B. J. et KUBIK, K. (1983). Compact gravity inversion. *Geophysics*, *48*, 713–721.

LEE, T. (1975). An integral equation and its solution for some two- and three-dimensional problems in resistivity and induced polarization. *Geophysical Journal of the Royal Astronomical Society*, *42*, 81–95.

LEE, T.-C. et BIEHLER, S. (1991). Inversion modeling of gravity with prismatic mass bodies. *Geophysics*, *56*, 1365–1376.

LEHMANN, H. (1995). Potentiel representation by independent configurations on a multi-electrode array. *Geophysical Journal International*, *120*, 331–338.

LESUR, V., CUER, M. et STRAUB, A. (1999*a*). 2-D and 3-D interpretation of electrical tomography measurements, Part 1 : The forward problem. *Geophysics*, *64*, 386–395.

LESUR, V., CUER, M. et STRAUB, A. (1999*b*). 2-D and 3-D interpretation of electrical tomography measurements, Part 2 : The inverse problem. *Geophysics*, *64*, 396–402.

LI, X. et CHOUTEAU, M. (1998). Three-dimensional gravity modeling in all space. *Surveys in Geophysics*, *19*, 339–368.

LI, Y. et OLDENBURG, D. (1997). Fast inversion of large scale magnetic data using wavelets. *Expanded Abstracts, SEG, vol. I*, 490–493, Dallas.

LI, Y. et OLDENBURG, D. W. (1991). Aspects of charge accumulation in DC resistivity experiments. *Geophysical Prospecting*, *39*, 803–826.

LI, Y. et OLDENBURG, D. W. (1992). Approximate inverse mappings in DC resistivity problems. *Geophysical Journal International*, *109*, 343–362.

LI, Y. et OLDENBURG, D. W. (1996). 3-D inversion of magnetic data. *Geophysics*, *61*, 394–408.

LI, Y. et OLDENBURG, D. W. (1998). 3-D inversion of gravity data. *Geophysics*, *63*, 109–119.

LINES, L. R. et TREITEL, S. (1984). Tutorial : A review of least squares inversion and its application to geophysical problems. *Geophysical Prospecting*, *32*, 159–186.

LIU, Q. (1994). Nonlinear inversion of electrode-type resistivity measurements. *IEEE Transactions on Geoscience and Remote Sensing*, *32*, 499–507.

LOKE, M. H. et BARKER, R. D. (1995). Least-squares deconvolution of apparent resistivity pseudosections. *Geophysics*, *60*, 1682–1690.

LOKE, M. H. et BARKER, R. D. (1996*a*). Practical techniques for 3D resistivity surveys and data inversion. *Geophysical Prospecting*, *44*, 499–523.

LOKE, M. H. et BARKER, R. D. (1996*b*). Rapid least-squares inversion of apparent resistivity pseudosections by a quasi-Newton method. *Geophysical Prospecting*, *44*, 131–152.

LOSANO, V. et LAGET, B. (1996). Fractional pyramids for color image segmentation. Dans *Proceeding of the IEEE Southwest symposium on image analysis and interpretation, April 8-9, San Antonio, Texas*, 13–17.

LOWRY, T., ALLEN, M. B. et SHIVE, L. N. (1989). Singularity removal : A refinement of resistivity modeling techniques. *Geophysics*, *54*, 766–774.

LUENBERGER, D. (1969). Optimization by vector space methods. New York Wiley.

LUENBERGER, D. G. (1973). Introduction to linear and nonlinear programming. Addison-Wesley Pub. Co.

LYTLE, R. J. (1982). Resistivity and induced-polarization probing in the vicinity of a spherical anomaly. *IEEE Transactions on Geoscience and Remote Sensing*, *GE-20*, 493–499.

LYTLE, R. J. et HANSON, J. M. (1983). Electrode configuration influence on resistivity measurements about a spherical anomaly. *Geophysics*, *48*, 1113–1119.

LYTLE, R. J., OKADA, J. T. et CONCEPCION, C. (1980). The potential field around subsurface electrically excited conductors. *IEEE Transactions on Geoscience and Remote Sensing*, *GE-18*, 240–243.

MACKIE, R. L., BENNETT, B. R. et MADDEN, T. R. (1988). Long-period magnetotelluric measurements near the central California coast : a land-locked view of the conductivity structure under the Pacific Ocean. *Geophysical Journal*, *95*, 181–194.

MAILLOL, J. M., SEGUIN, M.-K., GUPTA, O. P., AKHAURI, H. M. et SEN, N. (1999). Electrical resistivity tomography survey for delineating uncharted mine galleries in West Bengal, India. *Geophysical Prospecting*, *47*, 103–116.

MARCOTTE, D. (1995). Generalized cross-validation for covariance model selection. *Mathematical Geology*, *27*, 659–672.

MARQUARDT, D. W. (1970). Generalized inverses, ridge regression, biased linear estimation, and nonlinear estimation. *Technometrics*, *12*, 591–612.

McGILLIVRAY, P. et OLDENBURG, D. W. (1990). Methods for calculating Frechet derivates and sensitivities for the non-linear inverse problem : a comparative study. *Geophysical Prospecting*, *38*, 499–524.

McGILLIVRAY, P. R. (1992). Forward modeling of DC resistivity and MMR data. Ph.d. dissertation, University of British Colombia.

McGILLIVRAY, P. R., OLDENBURG, D. W., ELLIS, R. G. et HABASHY, T. M. (1994). Calculation of sensitivities for the frequency-domain electromagnetic problem. *Geophysical Journal International*, *116*, 1–4.

MEJU, M. A. (1992). An effective ridge regression procedure for resistivity data inversion. *Computer and Geosciences*, *18*, 99–118.

MEJU, M. A. (1994). Geophysical data analysis : understanding inverse problem. Theory and practice, volume 6. Society of Exploration Geophysicists.

MENKE, W. (1984). Geophysical data analysis : discrete inverse theory. Academic Press.

MERKEL, R. H. (1971). Resistivity analysis for plane-layer half-space models with buried current sources. *Geophysical Prospecting*, *19*, 626–639.

MERKEL, R. H. et ALEXANDER, S. S. (1971). Resistivity analysis for models of a sphere in a half-space with buried current sources. *Geophysical Prospecting*, *19*, 640–651.

MOONEY, H. M., ORELLANA, E., PICKETT, H. et TORNHEIM, L. (1966). A resistivity computation method for earth models. *Geophysics*, *31*, 192–203.

MOTTL, J. et MOTTLOVÁ, L. (1972). Solution of the inverse gravimetric problem with the aid of integer linear programming. *Geoexploration*, *10*, 53–62.

MUFTI, I. (1978). A practical approach to finite-difference resistivity modeling :. *Geophysics*, *43*, 930–942.

MUFTI, I. R. (1973). Rapid determination of cube's gravity field. *Geophysical Prospecting*, *21*, 724–735.

MUNDRY, E. (1984). Geoelectrical model calculations for two-dimensional resistivity distributions. *Geophysical Prospecting*, *32*, 124–131.

MURAI, T. et KAGAWA, Y. (1985). Electrical impedance computed tomography based on finite element model. *IEEE Transactions on Biomedical Engineering*, *BME-32*.

MUSKAT, M. et EVINGER, H. H. (1941). Current penetration in direct current prospecting. *Geophysics*, *6*, 397–427.

NABIGHIAN, M. N. (1966). The application of finite forward differences in the resistivity computations over a layered earth. *G*, *31*, 971–980.

NABIGHIAN, M. N. et ELLIOT, C. L. (1976). Negative induced-polarization effects from layered media. *Geophysics*, *41*, 1236–1255.

NAGY, D. (1966). The gravitational attraction of a right rectangular prism. *Geophysics*, *31*, 362–371.

NARAYAN, S. (1992). Vertical resolution of two-dimensional dipole-dipole resistivity inversion. Dans *62nd Ann. Internat. Mtg SEG*, 431–434.

NARAYAN, S., DUSSEAULT, M. B. et NOBES, D. C. (1994). Inversion techniques applied to resistivity inverse problems. *Inverse Problems*, *10*, 669–696.

NOCEDAL, J. et WRIGHT, S. J. (2000). Numerical Optimization. Springer.

NOEL, M. et XU, B. (1991). Archaeological investigation by electrical resistivity tomography : a preliminary study. *Geophysical Journal International*, *107*, 95–102.

OKABE, M. (1979). Analytical expressions for gravity anomalies due to homogeneous polyhedral bodies and translations into magnetic anomalies. *Geophysics*, *44*, 730–741.

OLAYINKA, A. I. et YARAMANCI, U. (2000). Use of block inversion in the 2-D interpretation of apparent resistivity data and its comparison with smooth inversion. *Journal of Applied Geophysics*, *45*, 63–81.

OLDENBURG, D. W. et LI, Y. (1994). Subspace linear inverse method. *Inverse Problems*, *10*, 915–935.

OLDENBURG, D. W., McGILLIVRAY, P. R. et ELLIS, R. G. (1993). Generalized subspace methods for large-scale inverse problems. *Geophysical Journal International*, *114*, 12–20.

ONODERA, S. (1963). Numerical analysis of relative resistivity for a horizontally layered earth. *Geophysics*, *28*, 222–231.

ORISTAGLIO, M. L. et WORTHINGTON, M. H. (1980). Inversion of surface and borehole electromagnetic data for two-dimensional electrical conductivity models. *Geophysical Prospecting*, *28*, 633–657.

PARK, S. K. et VAN, G. P. (1991). Inversion of pole-pole data for 3-D resistivity structure beneath arrays of electrodes. *Geophysics*, *56*, 951–960.

PARKER, R. L. (1994). Geophysical inverse theory. Princeton University Press.

PAUL, M. K. (1974). The gravity effect of a homogeneous polyhedron for three-dimensional interpretation. *Pure and Applied Geophysics*, *112*, 553–561.

PÉLOQUIN, A., POTVIN, R., PARADIS, S., LAFLÈCHE, M., VERPAELST, P. et GIBSON, H. (1990). The Blake River Group, Rouyn-Noranda area, Québec : a stratigraphic synthesis. Dans *Northwestern Québec Polymetallic Belt*, Édité par M. Rive, P. Verpaelst, Y. Gagnon, J. Lulin, G. Riverin et A. Simard, volume 43, Canadian Institute of Mining and Metallurgy, 107–118.

PELTON, W. H., RIJO, L. et SWIFT, M. (1978). Inversion of two-dimensional resistivity and induced-polarization. *Geophysics*, *43*, 788–803.

PERRON, G. et CALVERT, A. (1998). Case History : Shallow, high-resolution seismic imaging at the Ansil mining camp in the Abitibi greenstone belt. *Geophysics*, *63*, 379–391.

PETRICK, W. R., PELTON, W. H. et WARD, S. H. (1977). Ridge regression inversion applied to crustal resistivity sounding data from south Africa. *Geophysics*, *42*, 995–1005.

PETRICK, W. R., SILL, W. R. et WARD, S. H. (1981). Three-dimensional resistivity inversion using alpha centers. *Geophysics*, *46*, 1148–1162.

PILKINGTON, M. (1997). 3-D magnetic imaging using conjugate gradients. *Geophysics*, *62*, 1132–1142.

PILOTE, P., GUHA, J., DAIGNEAULT, R., ROBERT, F., CLOUTIER, J.-Y. et GOLIGHTLY, J. P. (1990). The structural evolution the Casa-Berardi township, Québec. Dans *Northwestern Québec Polymetallic Belt*, Édité par M. Rive, P. Verpaelst, Y. Gagnon, J. Lulin, G. Riverin et A. Simard, volume 43, Canadian Institute of Mining and Metallurgy.

PISSANETZKY, S. (1984). Sparse Matrix Technology. Academic Press.

PLOUFF, D. (1966). Digital terrain corrections based on geographic coordinates. *Geophysics*, *31*, 1208.

PLOUFF, D. (1976). Gravity and magnetic field of polygonal prisms and application to magnetic terrain corrections. *Geophysics*, *41*, 727–741.

POHÁNKA, V. (1988). Optimum expression for computation of the gravity field of a homogeneous polyhedral body. *Geophysical Prospecting*, *36*, 733–751.

POIRMEUR, C. et VASSEUR, G. (1988). Three-dimensional modeling of a hole-to-hole electrical method : Application to the interpretation of a field survey. *Geophysics*, *53*, 402–414.

PORTNIAGUINE, O. (1999). Image focusing and data compression in the solution of geophysical inverse problems. Thèse de Doctorat, University of Utah, Dept. of Geology and Geophysics.

PORTNIAGUINE, O. et ZHDANOV, M. S. (1999). Focusing geophysical inversion images. *Geophysics*, *64*, 874–887.

POUS, J., MARCUELLO, A. et QUERALT, P. (1987). Resistivity inversion with a priori information. *Geophysical Prospecting*, *35*, 590–603.

PRATT, D. A. (1972). The surface integral approach to the solution of the 3D resistivity problem. *Bulletin of the Australian Society for Exploration Geophysics*, *3*, 33–50.

PRESS, W. H., TEUKOLSKY, S. A., VETTERLING, W. T. et FLANNERY, B. P. (1992). Numerical Recipes in C : The Art of Scientific Computing. Cambridge University Press, 2nd edition.

PRIDMORE, D. F., HOHMANN, G. W., WARD, S. H. et SILL, W. R. (1981). An investigation of finite-element modeling for electrical and electromagnetic data in three dimensions. *Geophysics*, *46*, 1009–1024.

RAICHE, A. P. (1974). An integral equation approach to three-dimensional modelling. *Geophysical Journal of the Royal Astronomical Society*, *36*, 363–376.

RAMIREZ, A. et DAILY, W. (2001). Electrical imaging at the large block test - Yucca Mountain, Nevada. *Journal of Applied Geophysics*, *46*, 85–100.

RAMIREZ, A., DAILY, W., LABRECQUE, D., OWEN, E. et CHESNUT, D. (1993). Monitoring an underground steam injection process using electrical resistance tomography. *Water Resources Research*, *29*, 73–87.

RENE, R. M. (1986). Gravity inversion using open, reject, and "shape-of-anomaly" fill criteria. *Geophysics*, *51*, 988–994.

ROMAN, I. (1959). An image analysis of multiple-layer resistivity problems. *Geophysics*, *24*, 485–509.

ROMAN, I. (1963). The kernel function in the surface potential for a horizontally stratified earth. *Geophysics*, *28*, 232–240.

ROY, A. et APPARAO, A. (1971). Depth of investigation in direct current methods. *Geophysics*, *36*, 943–959.

SAFON, C., VASSEUR, G. et CUER, M. (1978). Some applications of linear programming to the inverse gravity problem. *Geophysics*, 1215–1230.

SANTOSA, F. et VOGELIUS, M. (1990). A backprojection algorithm for electrical impedance imaging. *SIAM Journal of Applied Mathematics*, *50*, 216–243.

SASAKI, Y. (1989). Two-dimensional joint inversion of magnetotelluric and dipole-dipole resistivity data. *Geophysics*, *54*, 254–262.

SASAKI, Y. (1992). Resolution of resistivity tomography inferred from numerical simulation. *Geophysical Prospecting*, *40*, 453–463.

SASAKI, Y. (1994). 3-D resistivity inversion using the finite-element method. *Geophysics*, *59*, 1839–1848.

SCALES, J. A. (1987). Tomographic inversion via the conjugate gradient method. *Geophysics*, *52*, 179–185.

SCHULZ, R. (1985). The method of integral equation in direct current resistivity method and its accuracy. *Journal of Geophysics*, *56*, 192–200.

SCRIBA, H. (1981). Computation of the electric potential in three-dimensional structures. *Geophysical Prospecting*, *29*, 790–802.

SEIGEL, H. O. (1959). Mathematical formulation and type curves for induced polarization. *Geophysics*, *24*, 547–565.

SEN, M. K., BAHATTACHARYA, B. B. et STOFFA, P. L. (1993). Nonlinear inversion of resistivity sounding data. *Geophysics*, *58*, 496–507.

SHARMA, P. V. (1966). Rapid computation of magnetic anomalies and demagnetization effects caused by bodies of arbitrary shaped. *Pure and Applied Geophysics*, *64*, 89–109.

SHEWCHUK, J. R. (1994). An introduction to the conjuguate gradient method without the agonizing pain. *(ftp ://warp.cs.cmu.edu)*.

SHI, W., MORGAN, F. D. et WHARTON, A. E. (1997). Application of electrical resistivity tomography to image Harrison Caves in Barbados, west. Dans *67th Ann. Internat. Mtg : Society of Exploration Geophysics*, 350–353.

SHIMA, H. (1990). Two-dimensional automatic resistivity inversion technique using alpha centers. *Geophysics*, *55*, 682–694.

SHIMA, H. (1992). 2-D and 3-D resistivity image reconstruction using crosshole data. *Geophysics*, *57*, 1270–1281.

SIDJE, R. B. et WILLIAMS, A. B. (1996). Fast generalized cross validation. Dans *International Linear Algebra, Year : Linear Algebra in Optimization CERFACS, Albi-Toulouse, France.*

SKILLING, J. et BRYAN, R. K. (1984). Maximum entropy image reconstruction, general algorithm. *Monthly Notices of the Royal Astronomical Society*, *211*, 111–124.

SLEIJPEN, G. et FOKKEMA, D. (1993). BICGSTAB(l) for linear equations involving unsymmetric matrices with complex spectrum. *Electronic Transactions on Numerical Analysis*, *1*, 11–32.

SMITH, N. C. et VOZOFF, K. (1984). Two-dimensional DC resistivity inversion for dipole-dipole data. *IEEE Transactions on Geoscience and Remote Sensing, GE-22*, 21–28.

SNYDER, D. D. (1976). A method for modeling the resistivity and IP response of two-dimensional bodies. *Geophysics, 41*, 997–1015.

SNYDER, D. D. et MERKEL, R. M. (1973). Analytical models for the interpretation of electrical surveys using buried current electrodes. *Geophysics, 38*, 513–529.

SONNEVELD, P. (1989). CGS, a fast Lanczos-type solver for nonsymmetric linear systems. *SIAM Journal on Scientific and Statistical Computation, 10*, 36–52.

SOROKIN, L. V. (1951). Gravimetry and gravimetrical prospecting. State Technology Publishing, Moscow.

SPIEGEL, R. J., STURDIVANT, V. R. et OWEN, T. E. (1980). Modeling resistivity anomalies from localized voids under irregular terrain. *Geophysics, 45*, 1164–1183.

SPIES, B. R. et HABASHY, T. M. (1995). Sensitivity analysis of crosswell electromagnetics. *Geophysics, 60*, 834–845.

SPITZER, K. (1995). A 3-D finite-difference algorithm for DC resistivity modelling using conjugate gradient methods. *Geophysical Journal International, 123*, 903–914.

SPITZER, K. (1998*a*). Development of three-dimensional finite difference resis-

tivity, sensitivity and IP forward modeling techniques and their application to surface and borehole surveys. Habilitation thesis, Univ. of Leipzig.

SPITZER, K. (1998*b*). The three-dimensional DC sensitivity for surface and subsurface sources. *Geophysical Journal International, 134*, 736–746.

SPITZER, K. et CHOUTEAU, M. (1997). Crosshole resistivity and IP experiment at Casa Berardi gold mine : interpretation using a newly developed 3D forward modeling code. Dans *SEG Expanded Abstracts.*

SPITZER, K. et CHOUTEAU, M. (2003). Cas History : A dc resistivity and IP borehole survey at Casa Berardi gold mine in northwestern Quebec. *Geophysics, 68*, 453–463.

SPITZER, K., CHOUTEAU, M. et BOULANGER, O. (1999). Grid-independent Electrode Positioning for 3D DC Resistivity and IP Forward Modelling. Dans *Symposium 3DEM2, Salt Lake City, Utah*, 189–192.

SPITZER, K. et WURMSTICH, B. (1999). Speed and accuracy in 3-D resistivity modeling. Dans *Three-Dimensional Electromagnetics*, Édité par M. Oristaglio, B. Pies et M. R. Cooper, number 7 Dans Geophysical Developments, Society of Exploration Geophysicists.

STEFANESCU, S. (1970). Nouvelles applications de la theorie des milieux alpha harmoniques a la prospection electrique en courant continu. *Geophysical Prospecting, 18*, 786–799.

STEFANESCU, S. et STEFANESCU, D. (1974). Mathematical models of conduc-

ting ore bodies for direct current electrical prospecting. *Geophysical Prospecting*, *22*, 246–260.

STRAKHOV, V. N., LAPINA, M. I. et YEFIMOV, A. B. (1986). A solution to forward problems in gravity and magnetism with new analytical expressions for the field elements of standard approximating bodies. *Izvestiya, Earth Physics*, *22*, 471–482.

STRAUB, A. (1995*a*). General formulation of the electric stratified problem with a boundary integral equation. *Geophysics*, *60*, 1656–1670.

STRAUB, A. (1995*b*). Properties of the kernel function in electric stratified problems. *Geophysics*, *60*, 1671–1681.

SZARKA, L. (1992). Comment on 'aspects of charge-accumulation in D.C. resistivity experiments' by Y. Li and D. W. Oldenburg. *Geophysical Prospecting*, *40*, 823–828.

TALWANI, M. (1965). Computation with the help of a digital computer of magnetic anomalies caused by bodies of arbitrary shape. *Geophysics*, *30*, 797–817.

TALWANI, M. et EWING, M. (1960). Rapid computation of gravitational attraction of three-dimensional bodies of arbitrary shape. *Geophysics*, *25*, 203–225.

TARANTOLA, A. et VALETTE, B. (1982). Generalized nonlinear inverse problems solved using the least squares criterion. *Reviews of Geophysics and Space Physics*, *20*, 219–232.

TELFORD, W. M., GELDART, L. P. et SHERIFF, R. E. (1990). Applied geophysics. Cambridge University Press, 2nd edition.

TIKHONOV, A. et ARSÉNINE, V. (1974). Méthodes de résolution de problèmes mal posés. Editions MIR . Moscou.

TING, S. et HOHMANN, G. (1981). Integral equation modeling of three-dimensional magnetotelluric response. *Geophysics*, *46*, 182–197.

TONG, L.-T. et YANG, C.-H. (1990). Incorporation of topography into two-dimensional resistivity inversion. *Geophysics*, *55*, 354–361.

TRIPP, A. C., HOHMANN, G. W. et JR., C. M. S. (1984). Two-dimensional resistivity inversion. *Geophysics*, *49*, 1708–1717.

VAN DER VORST, H. (1992). Bi-CGSTAB : A fast and smoothly converging variant of Bi-CG for the solution of nonsymmetric linear systems. *SIAM Journal on Scientific and Statistical Computation*, *13*, 631–644.

VAN NOSTRAND, R. (1953). Limitations on resistivity methods as inferred from the buried sphere problem. *Geophysics*, *18*, 423–433.

VANDECAR, J. et SNIEDER, R. (1994). Obtaining smooth solutions to large, linear, inverse problems. *Geophysics*, *59*, 818–829.

VAUHKONEN, M., VADASZ, D., KARJALAINEN, P., SOMERSALO, E. et KAIPIO, J. (1998). Tikhonov regularization and prior information in electrical impedance tomography. *IEEE Transactions on Medical Imaging*, *17*, 285–293.

VERPAELST, P., PELOQUIN, A., ADAM, E., BARNES, A., LUDDEN, J., DION, D.-J., HUBERT, C., MILKEREIT, B. et LABRIE, M. (1995). Seismic reflection profiles across the "Mines Series" in the Noranda camp of the Abitibi belt, eastern Canada. *Canadian Journal of Earth Science*, *32*, 167–176.

VOGEL, C. R. (1996). Non-convergence of the L-curve regularization parameter selection method. *Inverse Problems*, *12*, 535–547.

WAIT, J. R. (1982). Geo-electromagnetism. Ed. New York, Academic Press.

WANG, T. et MEZZATESTA, A. (2001). 3D DC resistivity modeling using the sweeping-seed conjugate gradient method. *Geophysics*, *66*, 441–447.

WANNAMAKER, P., HOHMANN, G. et SANFILIPO, W. (1984). Electromagnetic modeling of three-dimensional bodies in layered earths using integral equations. *Geophysics*, *49*, 60–74.

WEBB, J. H. (1931). The potential due to a buried spheroid. *Phys. Rev.*, *38*, 2056–2067.

WEIDELT, P. (1975). Inversion of two-dimensional conductivity structures. *Physics of the Earth and Planetary Interiors*, *10*, 282–291.

WEXLER, A., FRY, B. et NEUMAN, M. R. (1985). Impedance-computed tomography algorithm and system. *Applied Optics*, *24*, 3985–3992.

WHABA, G. (1990). Spline models for observational data. SIAM.

WILLIAMS, A. et BURRAGE, K. (1995). Surface fitting using GCV smoothing splines on supercomputers. *Supercomputing 1995, Association for Computing Machinery, Inc. (ACM).*, 871–885.

WURMSTICH, B. et MORGAN, F. D. (1994). Modeling of streaming potential responses caused by oil well pumping. *Geophysics*, *59*, 46–56.

XIA, J. et SPROWL, D. R. (1992). Inversion of potentiel-field data by iterative forward modeling in the wavenumber domain. *Geophysics*, *57*, 126–130.

XIONG, Z. (1989). Short note : Electromagnetic fields of electric dipoles embedded in a stratified anisotropic earth. *Geophysics*, *54*, 1643–1646.

XIONG, Z. (1992*a*). Electromagnetic modeling of 3-D structures by the method of system iteration using integral equations. *Geophysics*, *57*, 1556–1561.

XIONG, Z. (1992*b*). Short note : Symmetry properties of the scattering matrix in 3-D electromagnetic modeling using the integral equation method. *Geophysics*, *57*, 1199–1202.

XU, S., GAO, Z. et ZHAO, S. (1988). An integral formulation for three-dimensional terrain modeling for resistivity surveys. *Geophysics*, *53*, 546–552.

YANG, X. et LABRECQUE, D. J. (1998). Stochastic inversion of 3D ERT data. Dans *SAGEEP , Chicago, Illinois.*

YORKEY, T., WEBSTER, J. G. et TOMPKINS, W. (1987). Comparing reconstruction algorithms for electrical impedance tomography. *IEEE Transactions on Biomedical Engineering, BME-34.*

ZEYEN, H. et POUS, J. (1991). A new 3-D inversion algorithm for magnetic total field anomalies. *Geophysical Journal International*, *104*, 583–591.

ZEYEN, H. et POUS, J. (1993). 3-D joint inversion of magnetic and gravimetric data with a priori information. *Geophysical Journal International*, *112*, 244–256.

ZHANG, J., MACKIE, R. L. et MADDEN, T. R. (1995). Three-dimensional resistivity forward modeling and inversion using conjugate gradients. *Geophysics*, *60*, 1313–1325.

ZHANG, J., RODI, W., MACKIE, R. L. et SHI, W. (1996). Regularization in 3-DC resistivity tomography. Dans *Proceeding of the Symposium on the Application of Geophysics to Engineering and Environmental Problems, SAGEEP 96, April 28, Keystone, Colorado*, EEGS, 687–694.

ZHAO, S. et YEDLIN, M. J. (1996). Some refinements on the finite-difference method for 3-D resistivity modeling. *Geophysics*, *61*, 1301–1307.

ZHDANOV, M. S. et KELLER, G. V. (1994). The geoelectrical methods in geophysical exploration, volume 31 of *Methods in geochemistry and geophysics*. Elsevier.

ZHOU, W., BECK, B. F. et STEPHENSON, J. B. (2000). Reliability of dipole-dipole electrical resistivity tomography for defining depth to bedrock in covered karst terranes. *Environmental Geology*, *39*, 760–766.